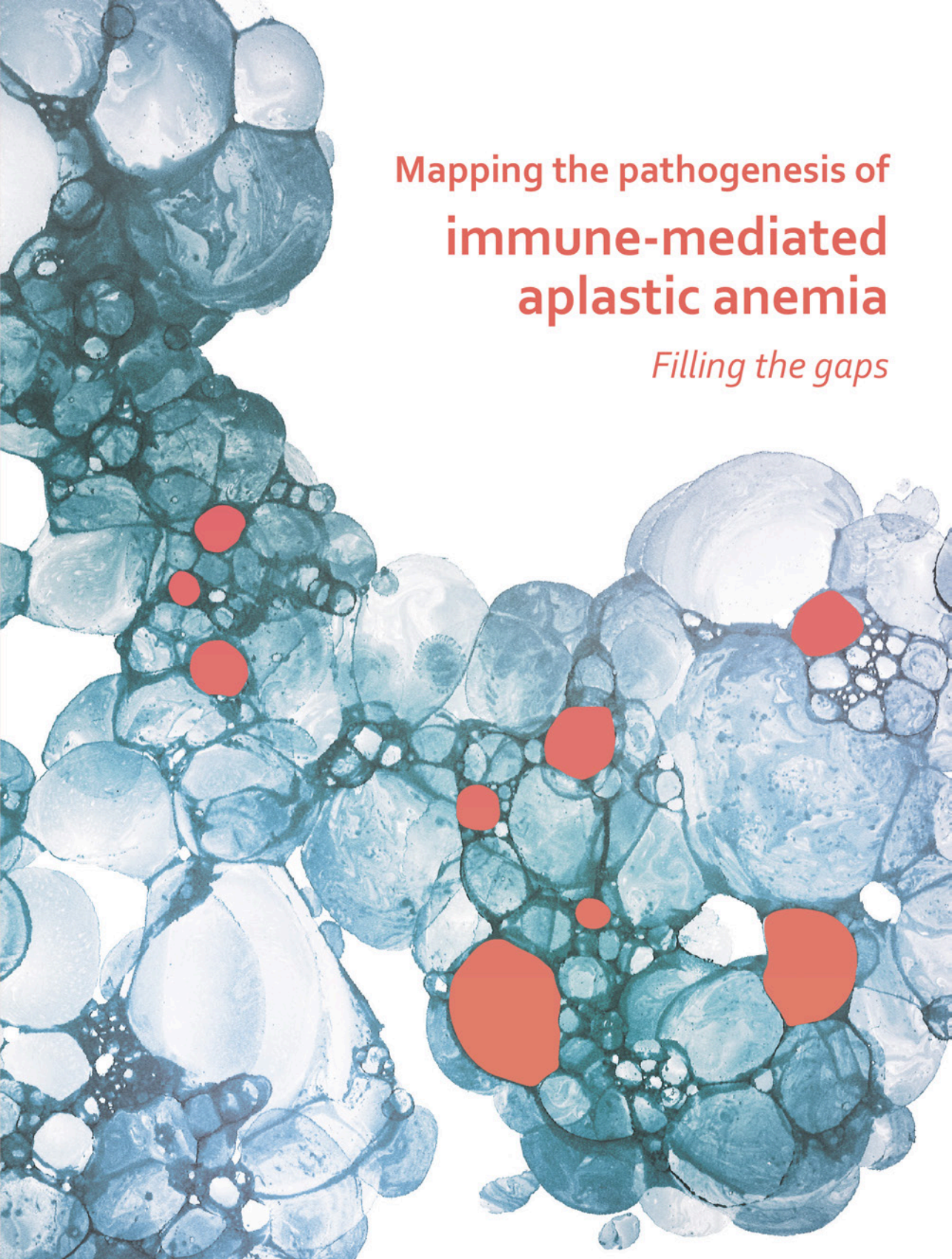
Mapping the pathogenesis of immune-mediated aplastic anemia

Filling the gaps



Emma Pool

Mapping the pathogenesis of immune-mediated aplastic anemia: *filling the gaps*

Emma Simone Pool

Cover and chapter illustrations: Marijke Pool and Emma Pool
Layout: Parntawan Kidtam | www.ridderprint.nl
Printing: Ridderprint | www.ridderprint.nl

ISBN: 978-94-6537-685-1

The research presented in this thesis was performed at the Department of Hematology of the Leiden University Medical Center in the Netherlands.

© 2026, Emma Simone Pool. All rights reserved. No part of this thesis may be reproduced, stored in a retrieval system, or transmitted in any form or by any means, electronically, mechanically, by photocopy, by recording, or otherwise without prior written permission from the author.

Mapping the pathogenesis of immune-mediated aplastic anemia: *filling the gaps*

Proefschrift

ter verkrijging van

de graad van doctor aan de Universiteit Leiden,

op gezag van rector magnificus prof.dr. S. de Rijcke,

volgens besluit van het college voor promoties

te verdedigen op donderdag 24 september 2026

klokke 13:00 uur

door

Emma Simone Pool

geboren te Terneuzen

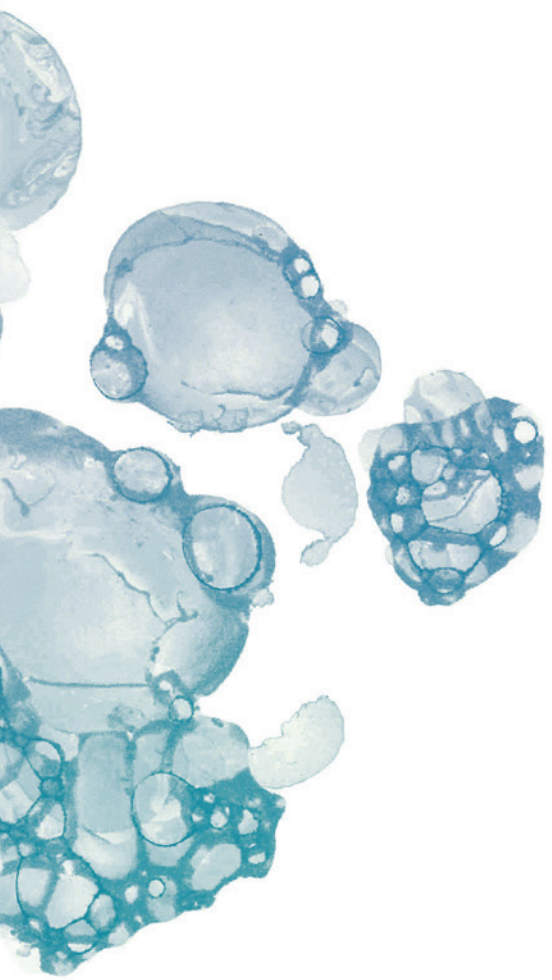
in 1996

Promotores:	Prof. dr. M.H.M. Heemskerk
	Prof. dr. F. Koning
Co-promotor:	Dr. J.M-L. Tjon
Leden promotiecommissie:	Prof. dr. A.C. Lankester
	Prof. dr. N.F.C.C. de Miranda
	Dr. S.M.C. Langemeijer (Radboudumc)
	Prof. dr. M.H.G.P. Raaijmakers (Erasmus MC)

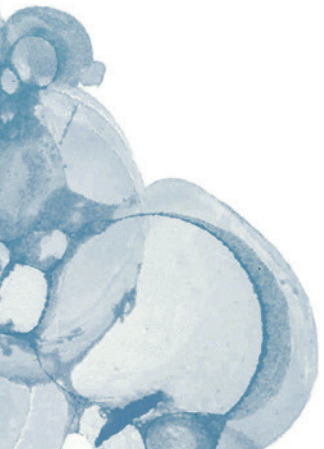
Table of contents

Chapter 1	Introduction	9
Chapter 2	Mass cytometric analysis unveils a disease-specific immune cell network in the bone marrow in acquired aplastic anemia	29
Chapter 3	Imaging mass cytometry reveals the order of events in the pathogenesis of immune-mediated aplastic anemia	61
Chapter 4	Selective lymphodepletion underlies the efficacy of horse anti-thymocyte globulin-based immunosuppressive therapy in aplastic anemia	111
Chapter 5	Longitudinal spatial mapping of the bone marrow in an aplastic anemia patient progressing to acute myeloid leukemia	167
Chapter 6	Summary and general discussion	181
Appendices	Nederlandse samenvatting	210
	About the author	217
	List of publications	218
	Acknowledgements	221





Introduction 1



Hematopoiesis

The bone marrow is the primary site for blood cell production, hematopoiesis[1]. The bone marrow produces erythroid cells (red blood cells), leukocytes (white blood cells) and thrombocytes (platelets), responsible for oxygen transport, protection against infections and blood clotting, respectively.

The hematopoietic stem cell is the most primitive cell in the bone marrow and maintains normal hematopoiesis. It has the ability to develop new 'daughter' hematopoietic stem cells through self-renewal, or to differentiate into committed precursor cells that can develop into one of two hematopoietic cell lineages: myeloid or lymphoid[1] (Figure 1).

Commitment to the myeloid lineage gives rise to the common myeloid progenitor, which can differentiate into three major groups of myeloid cells, depending on its development into the megakaryocyte-erythrocyte precursor or the granulocyte-monocyte precursor[1] (Figure 1). The first group of myeloid cells consists of erythroid cells and megakaryocytes, the latter of which are responsible for the production of thrombocytes. The second group of myeloid cells consists of monocytes and dendritic cells of the innate immune system. These cells can activate immune responses by antigen presentation in peripheral blood or tissues. Monocytes are also the precursor cells for macrophages, which can clear pathogens through phagocytosis, or regulate immune responses through antigen presentation and cytokine production. The last group of myeloid cells are the granulocytes, which include the neutrophils, the main effector cells of the innate immune system. These cells provide a first line of defense in case of infections by their ability to capture, engulf and kill pathogens[1].

Commitment to the lymphoid lineage gives rise to the common lymphoid progenitor, which can differentiate into the innate lymphoid cells (ILCs) of the innate immune system, or the T- and B-cells of the adaptive immune system[1]. The ILCs include natural killer (NK)-cells, which have the ability to kill infected and stressed cells without any prior antigenic exposure through the secretion of cytotoxic cytokines and granules. This is how NK-cells differ from T- or B-cells, which depend on the recognition of a specific antigen via the T-cell receptor (TCR) or B-cell receptor (BCR) on their cell surface for their activation. The development of T- and B-cells occurs through two distinct pathways that both involve a highly controlled screening process. Progenitor T-cells migrate from the bone marrow to the thymus for maturation. There, T-cells undergo positive selection to select those T-cells with TCRs that moderately bind antigens, and negative selection to eliminate all T-cells with self-reactive TCRs to prevent autoimmunity. After maturation and selection, naïve T-cells enter the circulation and acquire an effector function upon activation through interactions with antigen-presenting cells. In contrast, B-cell development occurs completely in the bone marrow. Similar to T-cells, B-cell

progenitors undergo a selection process to remove any B-cells with self-reactive BCRs. After selection, mature B-cells circulate in the blood, and following their activation by the binding of an antigen to the BCR, they can differentiate into either memory B-cells, which help prevent future infections, or effector B-cells called plasma cells, which secrete antibodies that can bind and protect against pathogens[1].

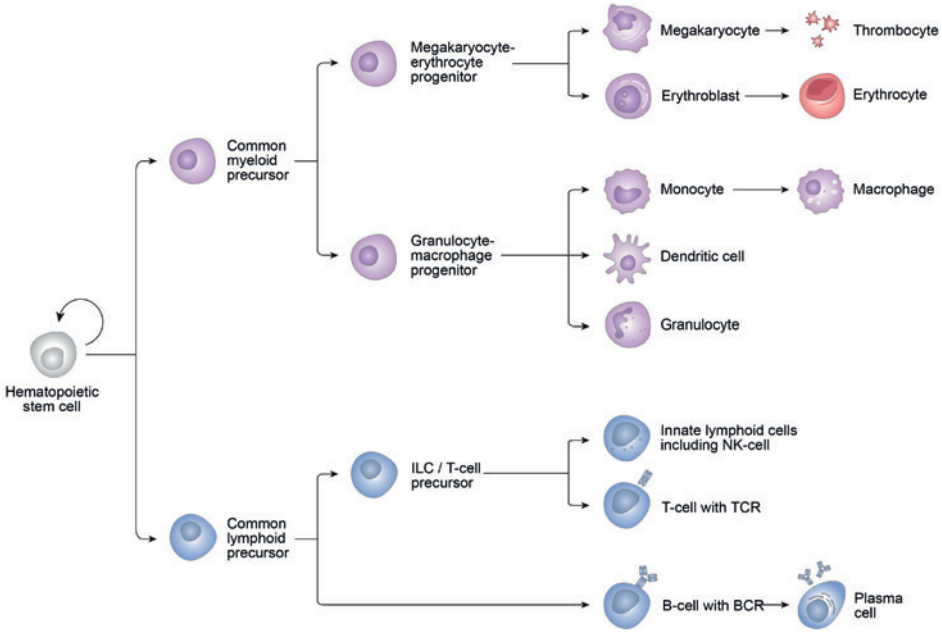


Figure 1. Overview of normal hematopoiesis in the human bone marrow. Figure adapted from The Immune System by Peter Parham[1].

The lifespan of myeloid and lymphoid cells differs considerably: while lymphoid cells can survive for weeks to a lifetime, most myeloid cells have a short half-life of only a few hours or months[1]. Therefore, hematopoiesis needs to be a continuous process to replenish these cells. The bone marrow microenvironment provides signals that support and regulate normal hematopoiesis[2,3]. This microenvironment consists of a complex network of mostly non-hematopoietic cells that can regulate the hematopoietic stem cells through the production of growth factors and chemokines. This includes the adipocytes, which cover most of the bone marrow tissue, are specialized in storing fat, and give the bone marrow its characteristic sponge-like structure (white round 'holes' in Figure 2, left). Other cells of the bone marrow microenvironment that can control stem cell function include the osteoblasts lining the bone, endothelial cells, mesenchymal stromal cells and sympathetic nerve fibers[2].

Bone marrow failure syndromes and aplastic anemia

If the bone marrow fails to produce a sufficient number of leukocytes, erythrocytes and/or thrombocytes, it may be termed bone marrow failure. The complications of bone marrow failure are the result of this decreased hematopoiesis and can involve potentially life-threatening bleeding, bruising, infections and/or fatigue, depending on which branches of the hematopoietic tree are affected.

Bone marrow failure syndromes are non-malignant conditions that result from a profound decrease in the hematopoietic stem cells in the bone marrow. This depletion leads to a characteristic hypocellular bone marrow, where the hematopoietic tissue (purple area in Figure 2, left) is replaced by adipocytes (white areas in Figure 2, right). This 'empty' bone marrow results in pancytopenia with decreased numbers of leukocytes, erythrocytes and/or thrombocytes in peripheral blood. Bone marrow failure can be either inherited or acquired[4]. Immune-mediated aplastic anemia (hereafter referred to as AA) is an acquired bone marrow failure syndrome caused by an autoimmune response targeting the hematopoietic stem cells in the bone marrow[4], and will be the focus of this thesis.

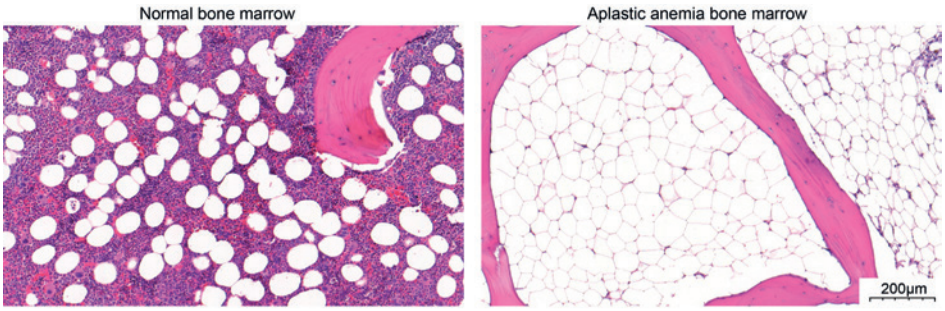


Figure 2. Histology of normal (left) and 'empty' aplastic anemia (right) bone marrow. White areas are adipocytes, long pink structures are bone, and dark purple areas represent hematopoietic tissue.

Immune-mediated aplastic anemia

AA is a rare hematological disorder with an estimated incidence of two per million[5]. Approximately 30 adults in the Netherlands are diagnosed with AA each year based on bone marrow hypocellularity without dysplasia, and pancytopenia (<100 g/L hemoglobin, $<50{\cdot}10^9$ thrombocytes/L and/or $<1.5{\cdot}10^9$ neutrophils/L)[6,7]. Diagnosing AA can be challenging since there are no biomarkers available to definitively confirm the disease. Therefore, the diagnosis of AA primarily relies on the exclusion of other causes of pancytopenia[6]. Clinically, AA is classified as non-severe (NSAA), severe (SAA) and very severe (VSAA) depending on peripheral blood counts[6]. AA can develop at any age but is most often diagnosed in young adults and

older individuals over the age of 60 years[5]. This thesis will focus on adult AA (patients ≥18 years of age). The strongest evidence for an immune-mediated cause is the recovery of the bone marrow and peripheral blood counts following immunosuppressive therapy. The widely accepted view is that the hematopoietic stem and progenitor cells (HSPCs) in the bone marrow are targeted by an autoreactive T-cell response[4]. However, the precise mechanisms leading to AA development remain poorly understood.

Treatment of AA

There are two potentially curative treatment options for AA: allogeneic hematopoietic stem cell transplantation (allo-HSCT) or immunosuppressive therapy (IST). The international treatment guidelines recommend allo-HSCT as the first-line approach in AA patients aged ≤40 years for whom a HLA-matched sibling donor is available[6]. In recent years, allo-HSCT with a HLA-matched unrelated donor has also been applied in younger AA patients with severe cytopenias that require rapid recovery of peripheral blood counts to reduce the risk of infections[6]. However, the advantages of allo-HSCT decline with age, since older age associates with a higher risk of toxicity, graft-versus-host disease and mortality[8]. Therefore, IST is the recommended first-line treatment option in AA patients aged ≥40 years, or for patients under the age of 40 years who are ineligible for allo-HSCT due the lack of a matched donor[6]. This applies to the majority of AA patients.

Immunosuppressive therapy

The aim of IST is to deplete the autoreactive immune cells that target the hematopoietic stem cells in the bone marrow in order to enable the recovery of hematopoiesis and peripheral blood counts[4]. The discovery of IST as a possible treatment for AA occurred unintentionally in the 1970s, when it was found that patients who underwent allo-HSCT and did not engraft their donor still experienced bone marrow recovery[9]. This suggested a therapeutic effect of the immunosuppression that was used with allo-HSCT. Subsequent studies confirmed the efficacy of immunosuppression as a treatment for AA by demonstrating recovery of peripheral blood counts in 40-60% of patients[10-13].

Based on these findings, IST with four consecutive days of 40 mg/kg/day anti-thymocyte globulin (ATG) and long-term ciclosporin is still the golden standard in the treatment of AA[6]. ATG is a polyclonal preparation of primarily IgG antibodies that can be produced by immunizing horses or rabbits with cells from the human thymus (also referred to as thymocytes). In the treatment of AA, both horse-derived ATG (hATG; ATGAM®, Pfizer) and rabbit-derived ATG (rATG; Thymoglobulin®, Sanofi) have been applied. In a study comparing

hATG to rATG, it was believed that rATG would be superior to hATG in the treatment of AA since it 1) induces more profound lymphodepletion; 2) induces the expansion of regulatory T-cells that can dampen pro-inflammatory immune responses; and 3) is effective in patients who relapse after first-line hATG-based IST[14,15]. Unexpectedly, however, response rates were higher with hATG-based IST compared to rATG-based IST[14,16,17]. Therefore, hATG has been the preferred source since.

Horse-derived anti-thymocyte globulin (hATG)

Although IST is the golden standard the treatment of most AA patients, its precise effects are poorly characterized. The short course of hATG is widely believed to induce rapid lymphodepletion, mainly T-cell depletion. However, data on the immunological effects of hATG in AA patients is limited, and experience from other settings is scarce since hATG is almost exclusively used to treat AA. Furthermore, although hATG and other ATG preparations share some characteristics due to similarities in the way they are produced, data from other preparations presumably do not apply to hATG since they are not the same drug[14,18].

hATG is a purified antibody preparation that is made by immunizing horses against cells from the human thymus, the primary site of T-cell development[1]. Therefore, it can be assumed that hATG contains antibodies against surface molecules presented on immature and mature T-cells. However, it is likely that hATG also targets other immune and stromal cells since 1) many surface markers are not exclusive to T-cells (e.g. HLA and CD45), and 2) the thymus is made up of a spectrum of (supportive) cells beyond T-cells[19]. The clinical study that demonstrated the efficacy of hATG has confirmed that hATG binds T-cells and induces T-cell depletion in AA patients treated with first-line hATG-based IST[14,15]. This study further showed that hATG affects other immune lineages, although the relevance of these findings remained unclear[15]. Thus, while these findings suggest hATG exerts a broad impact on the immune landscape, the immunomodulatory mechanisms associated with its therapeutic effects and the mechanisms by which hATG induces immune cell depletion remain to be determined.

Ciclosporin

While hATG is considered the main element of IST, it is not the only component. Long-term ciclosporin is added to standard IST since higher response rates are observed with hATG + ciclosporin-based IST compared to hATG alone[6,7,20]. This implies that ciclosporin could be important by suppressing residual immune cells that remain after hATG and/or by preventing the activation of reconstituted immune cells post-hATG. Ciclosporin is a calcineurin inhibitor that largely exerts its immunosuppressive effects by inhibiting T-cell activation by blocking IL-2 release, a cytokine required for T-cell proliferation[21]. Through this mechanism, ciclosporin

may also indirectly reduce other cytokines such as IFN-γ and TNF-α and therefore influence other immune cells, including antibody-secreting B-cells, macrophages and dendritic cells[22-25]. Therefore, it can have a broad immunosuppressive effect. Ciclosporin is a well-characterized drug commonly used in patients requiring immunosuppression. However, how it modulates the immune landscape in AA has not been studied in detail.

The need for improved treatment strategies for AA

While hATG-based IST can be successful in the treatment of AA, it comes with two major issues. First, bone marrow recovery after IST is delayed, with recovery of peripheral blood counts typically occurring three to six months after start of hATG[6,7]. Therefore, response to IST is determined six months after start of IST. Second, IST is not universally effective. Most patients responding to IST only achieve partial hematological recovery, with few reaching complete normalization of peripheral blood counts[6,7]. In addition, one-third of patients do not respond to IST and face prolonged pancytopenia with the accompanied risk of severe bleeding and infectious complications[6,7].

Since IST is not successful in all AA patients, there is a need to improve the treatment of AA. For this reason, alternative treatment strategies have been investigated. First, the optimal dose of hATG has been studied since it remains poorly defined[26]. Studies have compared the recommended dose of four consecutive days of 40 mg/kg/day hATG[6] to lower or higher dosing regimens[12,27,28], but no improvements in response rates have been observed so far. Second, the efficacy of alternative immunosuppressive drugs has been explored. However, no benefits of other commonly used immunosuppressive drugs such as alemtuzumab[29] or cyclophosphamide[6,30,31] have been reported. Finally, the use of combination therapies have been investigated. A recent approach that combines hATG-based IST with eltrombopag (Revolade®, Novartis) has shown some success. Eltrombopag is a thrombopoietin receptor agonist that was studied due to its ability to stimulate hematopoiesis by inducing the differentiation of the hematopoietic stem and progenitor cells in the bone marrow[32]. In 2022, a multicenter clinical trial showed improved response rates and faster hematologic response with hATG-based IST plus eltrombopag[32]. As a result, treatment guidelines have since recommended adding eltrombopag to standard first-line hATG-based IST, or as a second-line treatment starting six months after the start of IST[6].

Despite these efforts, IST, even in combination with eltrombopag, comes with numerous issues beyond the challenges regarding the suboptimal response rates described above. IST is a nonspecific therapy and therefore is associated with toxicities and adverse events, both in the short- and long-term[32]. Another concerning complication is clonal evolution to

secondary hematological malignancies including acute myeloid leukemia, which occurs in approximately 10-15% of AA patients treated with IST[33,34]. Despite efforts to identify high-risk patients and to delineate the underlying cause[35-38], the precise mechanisms driving clonal evolution are not clear and predicting its occurrence remains challenging.

Towards targeted treatment in AA

Targeted therapy would be the golden ticket to improve the treatment of AA. Such therapies could specifically deplete the immune cells that are believed to target the hematopoietic stem cells in the bone marrow without causing off-target effects. However, the development of targeted therapies is currently impossible because it remains unclear which immune cells are precisely involved in the pathogenesis of AA and which antigen(s) on the surface of hematopoietic stem and progenitor cells is targeted. Unraveling the immune-mediated pathogenesis of AA is essential to identify pathogenic immune cell populations that could serve as therapeutic targets for targeted therapy. Furthermore, it could help improve patient classification to individualize treatment. The overarching aim of this thesis is to decipher the immune-mediated pathogenesis of AA.

The immune system in AA: what do we know?

To better understand the immune mechanisms involved, several studies already have aimed to delineate the immune cells mediating bone marrow destruction in AA. Historically, AA has been regarded as a T-cell mediated autoimmune disorder, mainly due to the efficacy of hATG, which is generated against T-cells and T-cell precursors (thymocytes)[4,18]. As a result, there has been a focus on T-cells in research investigating the immune response in AA. The earliest studies demonstrating T-cell abnormalities date from the 1980s, when altered $CD4^+/CD8^+$ T-cell ratios and increased HLA-DR expression by T-cells hinted towards activation of the T-cell compartment[39]. Around the same time, activated lymphocytes from AA patients were found to produce the pro-inflammatory cytokine interferon and to suppress hematopoiesis when cultured with normal bone marrow *in vitro*[40,41]. Additional evidence supporting a T cell-mediated immune response was provided when studies identified a significant expansion of activated cytotoxic $CD8^+$ T-cells that was more prominent in bone marrow compared to peripheral blood[42].

By making use of the advancements in immune profiling techniques, more recent studies have taken a deeper dive into the T-cell compartment to identify the precise effector cells driving bone marrow destruction. These studies can be divided into two groups based on their two distinct approaches. The first group has used immunophenotyping to explore the frequencies

of CD8+ T-cell subpopulations, based on the hypothesis that effector T-cells mediating stem cell destruction would be more abundant in AA patients compared to healthy controls. Early immunophenotyping studies pointed towards a relative increase of effector memory and terminally differentiated memory T-cells in both peripheral blood and bone marrow in AA[43]. Further analysis demonstrated that these terminally differentiated memory CD8+ T-cells often co-expressed CD57 and contained cytotoxic granules loaded with granzyme B and perforin, emphasizing their strong cytotoxic potential[44].

The second group of studies has investigated the clonality of the TCR, and reasoned that pathogenic T-cells mediating bone marrow destruction could be detected by their clonal expansion following antigen recognition and activation. Despite the technical difference, this approach has complemented the findings from the immunophenotyping studies by demonstrating that clonally expanded CD8+ T-cells are present in AA[45,46], can kill patient-derived hematopoietic progenitor cells, co-express CD57[47,48], and are primarily found within the terminally differentiated memory T-cell population[45]. However, the cellular interactions and antigenic specificity, and therefore the precise relevance, of these T-cells remain largely unknown. There is recent evidence that suggests that the pathogenic T-cells in AA are virus-specific T-cells cross-reactive for an antigen presented by hematopoietic stem and progenitor cells[47]. However, data from a large cohort of AA patients are missing. Furthermore, while CD57+ CD8+ T-cells may appear as the key effector cells, the possibility that other CD8+ T-cell populations play a role in the pathogenesis of AA cannot be excluded.

CD4+ T-cells

Although CD8+ T-cells have been the primary focus in studies on AA, there has been a growing interest in the CD4+ T-cell compartment, mainly due to the importance of CD4+ T-cells in other autoimmune diseases. CD4+ T-cells include various helper T-cell populations that provide support for other cells of the immune system including cytotoxic T-cells and B-cells through cytokine release[1]. This includes T-helper 1 (Th1) cells that secrete interferon, Th2 cells that produce IL-4, and Th17 cells that release IL-17[1]. In contrast, regulatory T-cells of the CD4+ T-cell compartment can dampen immune responses by producing immunosuppressive cytokines such as IL-10 and TGF-β[1]. In AA, total CD4+ T-cell counts do not significantly differ from controls[49,50]. However, early research on CD4+ T-cells demonstrated a shift in the Th1/Th2 balance[51], and a profound decrease of regulatory T-cells[52], consistent with a state of inflammation. Subsequent work on the CD4+ T-cell compartment confirmed these findings and further showed that regulatory T-cells tend to correlate with disease severity[49] and IST-response[53]. Intriguingly, Th1 cells are clonally expanded in AA patients[49], but like CD8+ T-cells, their antigenic specificity and precise role remain unknown in AA. Data suggest that these

cells may be recruited during the early stages of bone marrow failure by pro-inflammatory Th17 cells[49,54], although the precise relevance of these phenotypes as well as the full complexity of the $CD4^+$ T-cell compartment remain poorly defined.

B-cells

Given the focus on T-cells in the pathogenesis of AA, there is little data supporting a role for other immune cell populations. Autoantibodies have been detected in AA[4,55,56], indicating potential B-cell involvement in AA, even though the functional relevance of these antibodies is debated. Direct evidence supporting a role for B-cells in AA is limited. The most comprehensive analysis of the B-cell compartment to date showed no significant differences in total $CD19^+$ B-cell counts nor frequencies in peripheral blood between AA patients and healthy controls[50]. Analyses at the cell subpopulation level did reveal significantly lower frequencies of $CD24^{high}CD38^{high}$ regulatory B-cells, which have since been confirmed in multiple analyses[57,58]. The biological meaning of this finding is yet to be determined. Some studies suggest that this decrease in regulatory B-cells could contribute to the inflammatory environment in AA through a decline in the anti-inflammatory cytokine IL-10, which suppresses cytotoxic T-cells and T-helper 1 responses under normal conditions[50].

Beyond these regulatory B-cells, no significant differences have been reported in mature naïve B-cell, memory B-cell or plasma cell frequencies between AA patients and controls[50]. However, functional markers were not studied and therefore the state of the B-cell compartment remains unclear. Notably, there is a recent study that found an increase of a B-cell subpopulation with pro-inflammatory properties[59]. This could suggest an inflammation-associated shift in the B-cell compartment in AA.

Innate immune cells

Adaptive immune cells including T- and B-cells depend on innate immune cells for activation[1]. Therefore, it is unsurprising that there has been an interest in the role of innate immune cells in AA. Among these, NK-cells have been of particular interest due to their ability to kill aberrant cells without needing prior exposure, and to secrete high quantities of pro-inflammatory cytokines[1,57,60-63]. Dendritic cells and macrophages have also gained interest due to their capacity to present antigens and to control inflammation, respectively[64-68]. However, interpreting the presence of innate immune cells in AA is complex. Increased frequencies of these cells may not necessarily be pathogenic but may instead result from reduced hematopoiesis, given their short half-life, typically of a few days. Additionally, if pathogenic, it remains unclear whether innate immune cells are primary players contributing to stem cell destruction or rather have a supportive function.

Immunological questions in AA

There is substantial data suggesting that the development of AA results from an autoimmune response against the hematopoietic stem cells in the bone marrow. However, after 50 years of research, the precise identity of the effector cells driving bone marrow destruction remains unknown. The growing body of research described above strongly suggests that AA results from an autoimmune response involving a spectrum of immune cells, rather than just a T-cell mediated attack. However, four critical limitations in prior research have obstructed a comprehensive understanding of the immune response underlying the disease.

First, most studies have focused on specific immune cell populations, rather than characterizing the full immune landscape in AA patients. This is mostly due to technical limitations in the number of immune cell subpopulations that could be analyzed simultaneously. As a result, potentially pathogenic immune cell subpopulations most likely have been overlooked.

Second, most studies have analyzed peripheral blood instead of bone marrow, mostly due to the scarce availability of bone marrow samples. Consequently, the presence and function of potentially pathogenic immune cell populations at the site of hematopoietic stem cell destruction remain unclear. Since immune cell composition and function can differ considerably between blood and bone marrow[69-71], it is plausible that critical immune cell populations that only occur at the site of stem cell destruction have been missed.

Third, even in studies that have studied bone marrow samples, analyses have mostly been performed on bone marrow aspirates instead of bone marrow biopsies. The few studies that have investigated bone marrow biopsies have relied on conventional imaging techniques without the possibility to characterize neighboring cells[54,68]. As a result, the interactions between potentially pathogenic immune cell populations and their cellular target remain within the bone marrow microenvironment remain unclear.

Fourth, the precise effects of hATG-based IST have not been delineated. Therefore, it remains unclear how successful IST reshapes the immune landscape and which immune cells must be eliminated in order to enable bone marrow recovery.

The need for high-dimensional analyses of the immune response in AA

The limitations of prior research illustrate the need for comprehensive approaches to analyze the immune landscape in AA to 1) delineate which immune cell subpopulations precisely are involved in the pathogenesis of AA, and 2) elucidate the cellular interactions and processes leading to stem cell destruction within the bone marrow microenvironment.

Recent developments of high-dimensional single-cell analysis techniques have enabled such comprehensive analyses of the immune landscape in both liquid and tissue biopsies. This includes mass cytometry (cytometry by time of flight; CyTOF), which allows for the simultaneous detection of over 40 cell markers and therefore facilitates in-depth phenotyping of immune cell subpopulations within one sample[72]. Suspension mass cytometry is an advanced version of flow cytometry that uses metal isotope-tagged antibodies instead of fluorochrome-conjugated antibodies to study liquid biopsies. By detecting these metal tags, mass cytometry is not limited by autofluorescence. This enables the detection of large antibody panels and the identification of both common and rarer immune cell subpopulations that may be difficult to distinguish with flow cytometry. Unlike single-cell RNA sequencing, which quantifies gene expression, mass cytometry measures protein expression, which offers a more detailed view of the immune landscape and its functional state. As a result, the use of mass cytometry has led to the discovery of new immune cell subpopulations and has provided unique insight into disease mechanisms, including cancer and autoimmunity.

A recent adaptation of mass cytometry is the development of imaging mass cytometry to study in-depth phenotyped cells within their native tissue microenvironment in tissue biopsies[73]. Imaging mass cytometry differs from more conventional imaging techniques such as immunohistochemistry or immunofluorescence by enabling the detection of a larger number of cellular markers at a single-cell resolution. Therefore, imaging mass cytometry facilitates comprehensive analyses of both the spatial localization and cellular interactions of in-depth phenotyped cells within the tissue. Recently, imaging mass cytometry has improved our understanding of the spatial organization of immune response in both health and disease, including autoimmunity[74-79]. However, its application on bone marrow tissue samples remains limited and comes with significant challenges due to the need for tissue decalcification.

Aims of this thesis

AA is a rare immune-mediated bone marrow failure syndrome that results from a profound decrease of hematopoietic stem cells in the bone marrow. The exact immunological mechanisms underlying the development of the disease remain poorly understood. This impedes the development of targeted therapies that could improve clinical outcome. The research described in this thesis aims to unveil the immunological mechanisms leading to bone marrow destruction.

In **Chapter 2**, we construct a comprehensive map of the immune landscape in bone marrow aspirates from AA patients to investigate which immune cell subpopulations may contribute

to the pathogenesis of AA. Using mass cytometry, we discover that AA is characterized by a disease-specific immune cell network that is significantly enriched in AA patients compared to healthy donors. We find that this network is composed of a spectrum of cells from multiple immune lineages, consistent with a state of chronic inflammation. Specifically, it includes $CD16^{+}$ myeloid cells, $CCR6^{high}$ B-cells, Th17-like $CCR6^{+}$ memory $CD4^{+}$ T-cells, $CD45RA^{+}CCR7^{+}CD38^{+}$ $CD8^{+}$ T-cells and $KLRG1^{+}$ terminally differentiated $CD8^{+}$ T-cells. Importantly, this network shows a trend toward normalization after successful IST, suggesting a pathogenic role. These observations provide the foundation for new research questions that are studied in **Chapter 3** and **Chapter 4**.

In **Chapter 3**, we investigate the immune response in AA within its native microenvironment in the bone marrow. This analysis aims to elucidate the chronological order of events occurring during disease development and to define the interactions between potential pathogenic immune cells and their cellular target. Using imaging mass cytometry on bone marrow biopsies, we generate a spatially-resolved single-cell atlas of the bone marrow in AA both before and six months after hATG-based IST. We confirm the presence of the identified immune cell network from **Chapter 2** in the bone marrow pre-treatment. Additionally, we identify immune 'hotspots' within the hypocellular bone marrow, where cells from the immune cell network and other activated immune cells colocalize with remaining progenitor cells. In bone marrow regions depleted of progenitor cells, these immune hotspots are nearly absent and more differentiated cells remain. Combined, these observations provide a unique visualization of the immune response during bone marrow destruction and reveal which immune cell interactions are critical in AA.

In **Chapter 4**, we perform an in-depth analysis of hATG-based IST to elucidate its precise effects *in vivo* and to evaluate how successful IST reshapes the immune landscape to enable bone marrow recovery. Since ATGAM (commercially available hATG produced by Pfizer) is generated in horses, it is a polyclonal antibody preparation with both human and non-human specificities. Therefore, we apply flow cytometry to focus on the 'active' ATGAM fraction capable of binding to human lymphocytes and inducing its therapeutic lymphodepleting effect. We provide evidence there is significant between-patient variability in active ATGAM exposure that may influence hematologic recovery. By interrogating the immunomodulatory effects of ATGAM exposure, we find that ATGAM exerts differential effects across T-, NK- and B-cells. Intriguingly, we also discover that successful treatment with ATGAM-based IST does not require a full immune 'reset' but rather depends on the selective depletion of the potentially pathogenic immune cell populations identified in **Chapter 2**. This depletion occurs either immediately upon ATGAM infusion, or through sustained immunosuppression with long-term ciclosporin use. Overall, these findings provide unique insight into the impact

of ATGAM-based IST and confirm the relevance of populations described in **Chapters 2 and 3**.

In **Chapter 5**, we explore how AA treated with first-line hATG-based IST impacts the biology of the bone marrow in the long term. We use a case study to investigate the biological mechanisms underlying clonal evolution to acute myeloid leukemia, a common and concerning long-term complication occurring in approximately 10-15% of patients who survive AA[6]. We propose a model in which the development of secondary acute myeloid leukemia is the result of the uncontrolled expansion of a preleukemic clone that may thrive in the bone marrow microenvironment created by the initial bone marrow failure. These findings underscore the added value of studying bone marrow biopsies as shown in **Chapter 3** and propose a potential role of the bone marrow microenvironment in determining long-term outcome.

In **Chapter 6**, we summarize the main findings of this thesis, discuss the autoimmune response in AA in a broader context, and explore future perspectives.

References

1. Parham P. The Immune System (ed 4). New York: Garland Science, Taylor & Francis Group, LLC; 2014.
2. Morrison SJ, Scadden DT. The bone marrow niche for haematopoietic stem cells. *Nature*. 2014;505(7483):327-334.
3. Wei Q, Frenette PS. Niches for Hematopoietic Stem Cells and Their Progeny. *Immunity*. 2018;48(4):632-648.
4. Young NS. Aplastic Anemia. *N Engl J Med*. 2018;379(17):1643-1656.
5. Young NS, Kaufman DW. The epidemiology of acquired aplastic anemia. *Haematologica*. 2008;93(4):489-492.
6. Kulasekararaj A, Cavenagh J, Dokal I, et al. Guidelines for the diagnosis and management of adult aplastic anaemia: A British Society for Haematology Guideline. *Br J Haematol*. 2024;204(3):784-804.
7. Tjon JM-L, Hussen-Dassen LGMv, Nur E, et al. Dutch guidelines for diagnostics and treatment of acquired aplastic anemia in adults. *Nederlands Tijdschrift voor Hematologie*. 2024.
8. Gupta V, Eapen M, Brazauskas R, et al. Impact of age on outcomes after bone marrow transplantation for acquired aplastic anemia using HLA-matched sibling donors. *Haematologica*. 2010;95(12):2119-2125.
9. Mathe G, Amiel JL, Schwarzenberg L, et al. Bone marrow graft in man after conditioning by antilymphocytic serum. *Br Med J*. 1970;2(5702):131-136.
10. Speck B, Gluckman E, Haak HL, van Rood JJ. Treatment of aplastic anaemia by antilymphocyte globulin with and without allogeneic bone-marrow infusions. *Lancet*. 1977;2(8049):1145-1148.
11. Speck B, Gratwohl A, Nissen C, et al. Treatment of severe aplastic anaemia with antilymphocyte globulin or bone-marrow transplantation. *Br Med J (Clin Res Ed)*. 1981;282(6267):860-863.
12. Young N, Griffith P, Brittain E, et al. A multicenter trial of antithymocyte globulin in aplastic anemia and related diseases. *Blood*. 1988;72(6):1861-1869.
13. Gluckman E, Devergie A, Poros A, Degoulet P. Results of immunosuppression in 170 cases of severe aplastic anaemia. Report of the European Group of Bone Marrow Transplant (EGBMT). *Br J Haematol*. 1982;51(4):541-550.
14. Scheinberg P, Nunez O, Weinstein B, et al. Horse versus rabbit antithymocyte globulin in acquired aplastic anemia. *N Engl J Med*. 2011;365(5):430-438.
15. Feng X, Scheinberg P, Biancotto A, et al. In vivo effects of horse and rabbit antithymocyte globulin in patients with severe aplastic anemia. *Haematologica*. 2014;99(9):1433-1440.
16. Marsh JC, Bacigalupo A, Schrezenmeier H, et al. Prospective study of rabbit antithymocyte globulin and cyclosporine for aplastic anemia from the EBMT Severe Aplastic Anaemia Working Party. *Blood*. 2012;119(23):5391-5396.
17. Halkes CJ, Veelken H, Falkenburg JH. Horse versus rabbit antithymocyte globulin in aplastic anemia. *N Engl J Med*. 2011;365(19):1842-1843; author reply 1843-1844.
18. Mohty M. Mechanisms of action of antithymocyte globulin: T-cell depletion and beyond. *Leukemia*. 2007;21(7):1387-1394.
19. Yayon N, Kedlian VR, Boehme L, et al. A spatial human thymus cell atlas mapped to a continuous tissue axis. *Nature*. 2024;635(8039):708-718.
20. Frickhofen N, Kaltwasser JP, Schrezenmeier H, et al. Treatment of aplastic anemia with antilymphocyte globulin and methylprednisolone with or without cyclosporine. The German Aplastic Anemia Study Group. *N Engl J Med*. 1991;324(19):1297-1304.

21. Elliott JF, Lin Y, Mizel SB, Bleackley RC, Harnish DG, Paetkau V. Induction of interleukin 2 messenger RNA inhibited by cyclosporin A. *Science*. 1984;226(4681):1439-1441.

22. Heidt S, Roelen DL, Eijsink C, et al. Calcineurin inhibitors affect B cell antibody responses indirectly by interfering with T cell help. *Clin Exp Immunol*. 2010;159(2):199-207.

23. Palay DA, Cluff CW, Wentworth PA, Ziegler HK. Cyclosporine inhibits macrophage-mediated antigen presentation. *J Immunol*. 1986;136(12):4348-4353.

24. Varey AM, Champion BR, Cooke A. Cyclosporine affects the function of antigen-presenting cells. *Immunology*. 1986;57(1):111-114.

25. Lee YR, Yang IH, Lee YH, et al. Cyclosporin A and tacrolimus, but not rapamycin, inhibit MHC-restricted antigen presentation pathways in dendritic cells. *Blood*. 2005;105(10):3951-3955.

26. Walter J, Rolles B, Schumacher Y, et al. Analysis of the Impact of Body Mass Index (BMI) on the Durability of Response in Patients with Aplastic Anemia Treated with Weight-Adjusted Horse Anti-Thymocyte Globulin (hATG). *Blood*. 2023;142.

27. Champlin R, Ho W, Gale RP. Antithymocyte globulin treatment in patients with aplastic anemia: a prospective randomized trial. *N Engl J Med*. 1983;308(3):113-118.

28. Scott A, Morris K, Butler J, Mills AK, Kennedy GA. Treatment of aplastic anaemia with lower-dose anti-thymocyte globulin produces similar response rates and survival as per standard dose anti-thymocyte globulin schedules. *Intern Med J*. 2016;46(10):1198-1203.

29. Scheinberg P, Nunez O, Weinstein B, Scheinberg P, Wu CO, Young NS. Activity of alemtuzumab monotherapy in treatment-naive, relapsed, and refractory severe acquired aplastic anemia. *Blood*. 2012;119(2):345-354.

30. Brodsky RA, Chen AR, Dorr D, et al. High-dose cyclophosphamide for severe aplastic anemia: long-term follow-up. *Blood*. 2010;115(11):2136-2141.

31. Tisdale JF, Dunn DE, Geller N, et al. High-dose cyclophosphamide in severe aplastic anaemia: a randomised trial. *Lancet*. 2000;356(9241):1554-1559.

32. Peffault de Latour R, Kulasekararaj A, Iacobelli S, et al. Eltrombopag Added to Immunosuppression in Severe Aplastic Anemia. *N Engl J Med*. 2022;386(1):11-23.

33. Scheinberg P, Young NS. How I treat acquired aplastic anemia. *Blood*. 2012;120(6):1185-1196.

34. Patel BA, Groarke EM, Lotter J, et al. Long-term outcomes in patients with severe aplastic anemia treated with immunosuppression and eltrombopag: a phase 2 study. *Blood*. 2022;139(1):34-43.

35. Babushok DV. A brief, but comprehensive, guide to clonal evolution in aplastic anemia. *Hematology Am Soc Hematol Educ Program*. 2018;2018(1):457-466.

36. Kulasekararaj AG, Jiang J, Smith AE, et al. Somatic mutations identify a subgroup of aplastic anemia patients who progress to myelodysplastic syndrome. *Blood*. 2014;124(17):2698-2704.

37. Negoro E, Nagata Y, Clemente MJ, et al. Origins of myelodysplastic syndromes after aplastic anemia. *Blood*. 2017;130(17):1953-1957.

38. Yoshizato T, Dumitriu B, Hosokawa K, et al. Somatic Mutations and Clonal Hematopoiesis in Aplastic Anemia. *N Engl J Med*. 2015;373(1):35-47.

39. Zoumbos NC, Ferris WO, Hsu SM, et al. Analysis of lymphocyte subsets in patients with aplastic anaemia. *Br J Haematol*. 1984;58(1):95-105.

40. Zoumbos NC, Gascon P, Djeu JY, Young NS. Interferon is a mediator of hematopoietic suppression in aplastic anemia in vitro and possibly in vivo. *Proc Natl Acad Sci U S A*. 1985;82(1):188-192.

41. Zoumbos NC, Gascon P, Djeu JY, Trost SR, Young NS. Circulating activated suppressor T lymphocytes in aplastic anemia. *N Engl J Med*. 1985;312(5):257-265.

42. Maciejewski JP, Hibbs JR, Anderson S, Katevas P, Young NS. Bone marrow and peripheral blood lymphocyte phenotype in patients with bone marrow failure. *Exp Hematol*. 1994;22(11):1102-1110.

43. Hu X, Gu Y, Wang Y, Cong Y, Qu X, Xu C. Increased CD4+ and CD8+ effector memory T cells in patients with aplastic anemia. *Haematologica*. 2009;94(3):428-429.

44. Kook H, Zeng W, Guibin C, Kirby M, Young NS, Maciejewski JP. Increased cytotoxic T cells with effector phenotype in aplastic anemia and myelodysplasia. *Exp Hematol*. 2001;29(11):1270-1277.

45. Risitano AM, Maciejewski JP, Green S, Plasilova M, Zeng W, Young NS. In-vivo dominant immune responses in aplastic anaemia: molecular tracking of putatively pathogenetic T-cell clones by TCR beta-CDR3 sequencing. *Lancet*. 2004;364(9431):355-364.

46. Risitano AM, Kook H, Zeng W, Chen G, Young NS, Maciejewski JP. Oligoclonal and polyclonal CD4 and CD8 lymphocytes in aplastic anemia and paroxysmal nocturnal hemoglobinuria measured by V beta CDR3 spectratyping and flow cytometry. *Blood*. 2002;100(1):178-183.

47. Ben Hamza A, Welters C, Stadler S, et al. Virus-reactive T cells expanded in aplastic anemia eliminate hematopoietic progenitor cells by molecular mimicry. *Blood*. 2024.

48. Giudice V, Feng X, Lin Z, et al. Deep sequencing and flow cytometric characterization of expanded effector memory CD8(+)CD57(+) T cells frequently reveals T-cell receptor Vbeta oligoclonality and CDR3 homology in acquired aplastic anemia. *Haematologica*. 2018;103(5):759-769.

49. Kordasti S, Marsh J, Al-Khan S, et al. Functional characterization of CD4+ T cells in aplastic anemia. *Blood*. 2012;119(9):2033-2043.

50. Zaimoku Y, Patel BA, Kajigaya S, et al. Deficit of circulating CD19(+) CD24(hi) CD38(hi) regulatory B cells in severe aplastic anaemia. *Br J Haematol*. 2020;190(4):610-617.

51. Tsuda H, Yamasaki H. Type I and type II T-cell profiles in aplastic anemia and refractory anemia. *Am J Hematol*. 2000;64(4):271-274.

52. Solomou EE, Rezvani K, Mielke S, et al. Deficient CD4+ CD25+ FOXP3+ T regulatory cells in acquired aplastic anemia. *Blood*. 2007;110(5):1603-1606.

53. Kordasti S, Costantini B, Seidl T, et al. Deep phenotyping of Tregs identifies an immune signature for idiopathic aplastic anemia and predicts response to treatment. *Blood*. 2016;128(9):1193-1205.

54. de Latour RP, Visconte V, Takaku T, et al. Th17 immune responses contribute to the pathophysiology of aplastic anemia. *Blood*. 2010;116(20):4175-4184.

55. Kelkka T, Tyster M, Lundgren S, et al. Anti-COX-2 autoantibody is a novel biomarker of immune aplastic anemia. *Leukemia*. 2022;36(9):2317-2327.

56. Hirano N, Butler MO, Von Bergwelt-Baildon MS, et al. Autoantibodies frequently detected in patients with aplastic anemia. *Blood*. 2003;102(13):4567-4575.

57. Vissers LTW, van Ostaijen-Ten Dam MM, Melsen JE, et al. Potential role of B- and NK-cells in the pathogenesis of pediatric aplastic anemia through deep phenotyping. *Front Immunol*. 2024;15:1328175.

58. Gu L, Fu B, Sui X, Xu H. Abnormal expression of b10 cell frequencies: possible relation to pathogenesis and disease severity of aplastic anemia. *Rev Assoc Med Bras (1992)*. 2019;65(5):637-646.

59. Solomou EE, Kattamis A, Symeonidis A, et al. Increased age-associated B cells in patients with acquired aplastic anemia correlate with IFN-gamma. *Blood Adv*. 2024;8(2):399-402.

60. Liu C, Chen Y, Lu D, et al. Single-cell transcriptomic analysis of PB and BM NK cells from severe aplastic anaemia patients. *Clin Transl Med*. 2022;12(12):e1092.

61. Chen T, Zhang T, Liu C, et al. NK cells suppress CD8(+) T cell immunity via NKG2D in severe aplastic anemia. *Cell Immunol*. 2019;335:6-14.

62. Liu C, Li Z, Sheng W, et al. Abnormalities of quantities and functions of natural killer cells in severe aplastic anemia. *Immunol Invest*. 2014;43(5):491-503.

63. Lundgren S, Huuhtanen J, Keranen M, et al. Single-cell analysis of aplastic anemia reveals a convergence of NK and NK-like CD8(+) T cells with a disease-associated TCR signature. *Sci Transl Med*. 2025;17(787):eadl6758.

64. Sun Y, Wu C, Liu C, et al. Myeloid dendritic cells in severe aplastic anemia patients exhibit stronger phagocytosis. *J Clin Lab Anal*. 2021;35(12):e24063.

65. Zonghong S, Meifeng T, Huaquan W, et al. Circulating myeloid dendritic cells are increased in individuals with severe aplastic anemia. *Int J Hematol*. 2011;93(2):156-162.

66. Liu B, Shao Y, Liang X, et al. CTLA-4 and HLA-DQ are key molecules in the regulation of mDC-mediated cellular immunity by Tregs in severe aplastic anemia. *J Clin Lab Anal*. 2020;34(10):e23443.

67. Sun W, Wu Z, Lin Z, et al. Macrophage TNF-alpha licenses donor T cells in murine bone marrow failure and can be implicated in human aplastic anemia. *Blood*. 2018;132(26):2730-2743.

68. Vaht K, Brenner J, Ednersson SB, Ljungman P, Brune M, Andersson PO. Bone marrow expression of CD68/CD163 macrophages, IL-17 and FOXP3 cells in aplastic anemia and their relation to prognosis. *Eur J Haematol*. 2023;110(3):313-321.

69. Caliskan G, Pawitan Y, Vu TN. Similarities and differences of bone marrow and peripheral blood samples from acute myeloid leukemia patients in terms of cellular heterogeneity and ex-vivo drug sensitivity. *EJHaem*. 2024;5(4):721-727.

70. Yang C, Siebert JR, Burns R, et al. Heterogeneity of human bone marrow and blood natural killer cells defined by single-cell transcriptome. *Nat Commun*. 2019;10(1):3931.

71. Glass DR, Tsai AG, Oliveria JP, et al. An Integrated Multi-omic Single-Cell Atlas of Human B Cell Identity. *Immunity*. 2020;53(1):217-232 e215.

72. Spitzer MH, Nolan GP. Mass Cytometry: Single Cells, Many Features. *Cell*. 2016;165(4):780-791.

73. Giesen C, Wang HA, Schapiro D, et al. Highly multiplexed imaging of tumor tissues with subcellular resolution by mass cytometry. *Nat Methods*. 2014;11(4):417-422.

74. Krop J, van der Zwan A, Ijsselsteijn ME, et al. Imaging mass cytometry reveals the prominent role of myeloid cells at the maternal-fetal interface. *iScience*. 2022;25(7):104648.

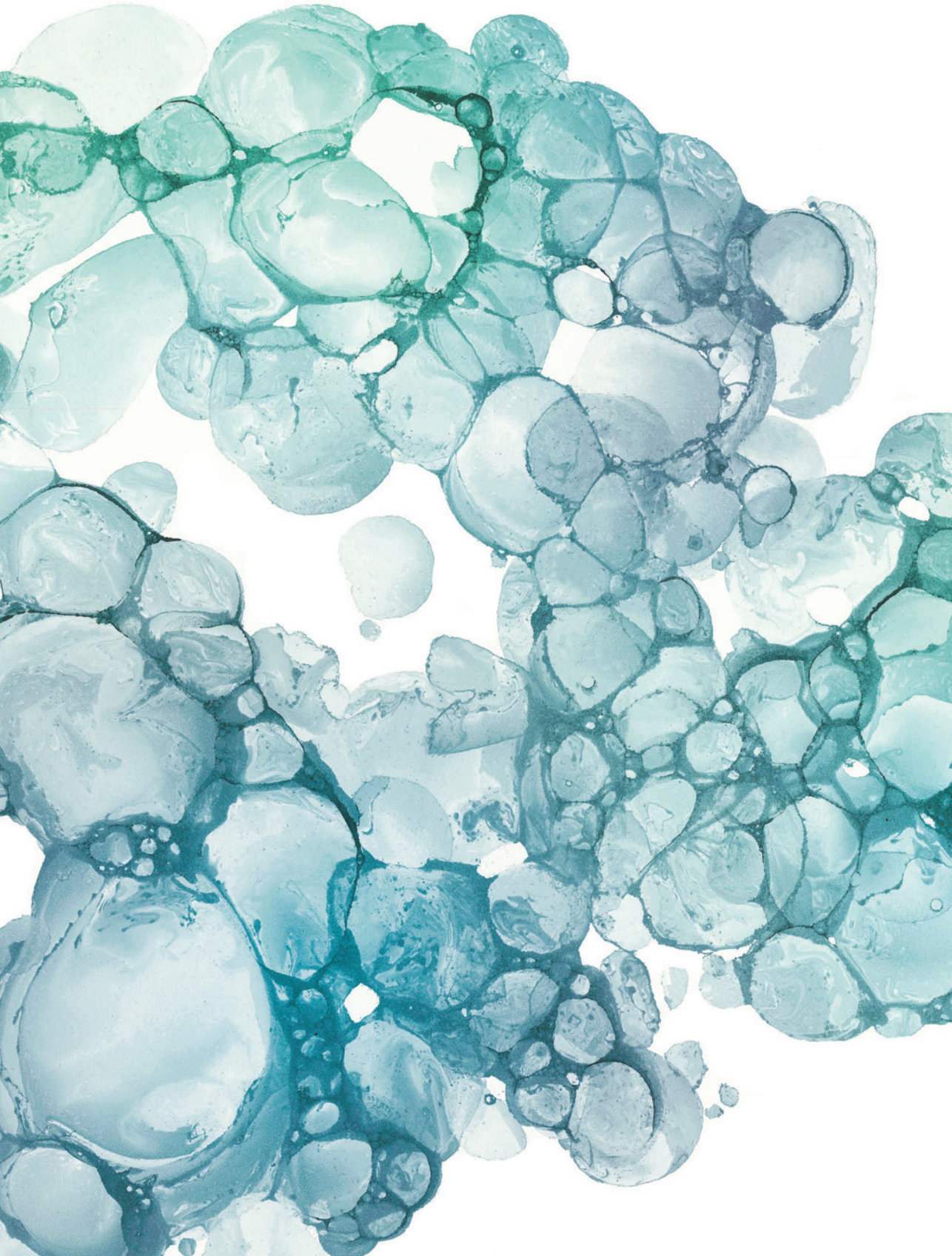
75. Ouboter LF, Lindelauf C, Jiang Q, et al. Activated HLA-DR+CD38+ Effector Th1/17 Cells Distinguish Crohn's Disease-associated Perianal Fistulas from Cryptoglandular Fistulas. *Inflamm Bowel Dis*. 2024.

76. Dieckman T, Schreurs M, Mahfouz A, et al. Single-Cell Analysis of Refractory Celiac Disease Demonstrates Inter- and Intra-Patient Aberrant Cell Heterogeneity. *Cell Mol Gastroenterol Hepatol*. 2022;14(1):173-192.

77. Krop J, van der Meeren LE, van der Hoorn MP, et al. Identification of a unique intervillous cellular signature in chronic histiocytic intervillositis. *Placenta*. 2023;139:34-42.

78. Jia L, Li N, Abdelaal TRM, et al. High-Dimensional Mass Cytometry Reveals Emphysema-associated Changes in the Pulmonary Immune System. *Am J Respir Crit Care Med*. 2024;210(8):1002-1016.

79. de Vries NL, van de Haar J, Veninga V, et al. gammadelta T cells are effectors of immunotherapy in cancers with HLA class I defects. *Nature*. 2023;613(7945):743-750.



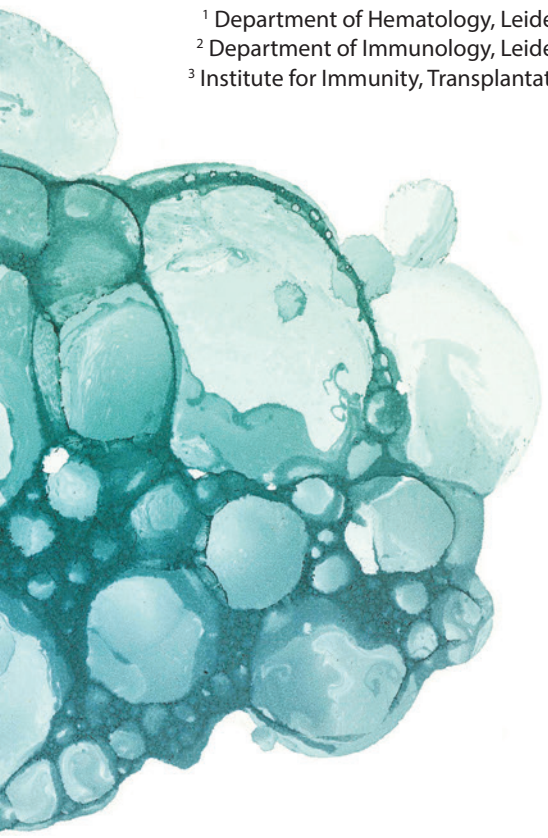
2

Mass cytometric analysis unveils a disease-specific immune cell network in the bone marrow in acquired aplastic anemia

Emma S. Pool[1], Yvonne Kooy-Winkelaar[2], Vincent van Unen[2,3], J.H. Frederik Falkenburg[1], Frits Koning[2], Mirjam H.M. Heemskerk[1] and Jennifer M-L. Tjon[1]

[1] Department of Hematology, Leiden University Medical Center, Leiden, The Netherlands
[2] Department of Immunology, Leiden University Medical Center, Leiden, The Netherlands
[3] Institute for Immunity, Transplantation and Infection, Stanford University, California, USA

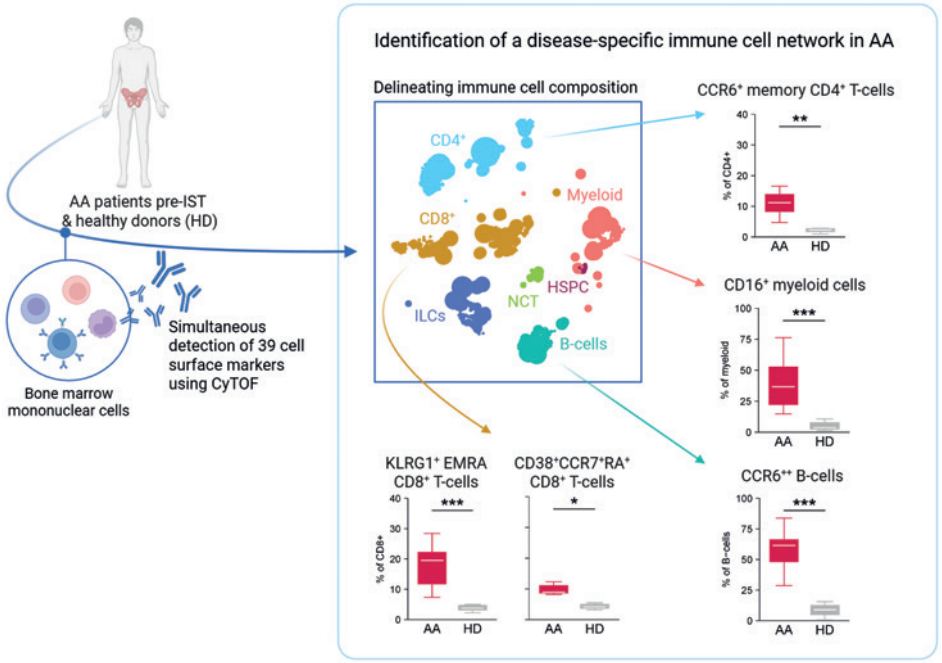
Frontiers in Immunology (2023)
DOI: 10.3389/fimmu.2023.1274116



Key points

- Broad immunophenotyping by mass cytometry provides a detailed overview of the immune landscape in the bone marrow in aplastic anemia
- A disease-specific immune cell network that shows a trend toward normalization after successful treatment was identified.

Visual abstract



Abstract

Idiopathic acquired aplastic anemia (AA) is considered an immune-mediated syndrome of bone marrow failure since approximately 70% of patients respond to immunosuppressive therapy (IST) consisting of a course of anti-thymocyte globulin (ATG) followed by long-term use of ciclosporin. However, the immune response that underlies the pathogenesis of AA remains poorly understood. In this study, we applied high-dimensional mass cytometry on bone marrow aspirates of AA patients pre-ATG, AA patients post-ATG and healthy donors to decipher which immune cells may be implicated in the pathogenesis of AA. We show that the bone marrow of AA patients features an immune cell composition distinct from healthy donors, with significant differences in the myeloid, B-cell, $CD4^+$ and $CD8^+$ T-cell lineages. Specifically, we discovered that AA pre-ATG is characterized by a disease-specific immune cell network with high frequencies of $CD16^+$ myeloid cells, $CCR6^{++}$ B-cells, Th17-like $CCR6^+$ memory $CD4^+$ T-cells, $CD45RA^+CCR7^+CD38^+$ $CD8^+$ T-cells and $KLRG1^+$ terminally differentiated effector memory (EMRA) $CD8^+$ T-cells, compatible with a state of chronic inflammation. Successful treatment with IST strongly reduced the levels of $CD16^+$ myeloid cells and showed a trend towards normalization of the frequencies of $CCR6^{++}$ B-cells, $CCR6^+$ memory $CD4^+$ T-cells and $KLRG1^+$ EMRA $CD8^+$ T-cells. Altogether, our study provides a unique overview of the immune landscape in the bone marrow in AA at a single-cell level and proposes CCR6 as a potential new therapeutic target in AA.

Introduction

Idiopathic acquired aplastic anemia (AA) is characterized by bone marrow hypocellularity due to a profound decrease in hematopoiesis resulting in pancytopenia[1]. Symptoms of AA relate to the severity of pancytopenia and severe cases of AA are potentially fatal, mainly due to bleeding and infectious complications.

Two effective treatments can result in recovery of hematopoiesis: allogeneic hematopoietic stem cell transplantation (allo-HSCT) and immunosuppressive therapy (IST)[1-3]. First-line allo-HSCT leads to rapid recovery of hematopoiesis but has a risk of graft-versus-host disease and transplant-related mortality and is therefore only recommended for patients under the age of 40 with an HLA-identical sibling donor[4]. Accordingly, IST is the preferred first-line treatment in most AA patients.

Standard IST for AA combines ciclosporin and anti-thymocyte globulin (ATG), a polyclonal IgG antibody preparation that is manufactured by immunizing animals with human thymocytes. In the setting of AA both rabbit-derived ATG (rATG) and horse-derived ATG (hATG) have been applied. However, hATG is preferred since hematological response to hATG is superior to rATG[5,6]. In patients responsive to IST, peripheral blood counts gradually recover within several months. Therefore, international guidelines recommend response evaluation 3-6 months after the start of IST. Consequently, non-responding patients are identified after months of prolonged cytopenia and remain at risk for bleeding and infectious complications. One-third of patients fail to recover sufficiently after IST[6]. At present, it is not possible to predict at diagnosis which patients will respond to IST.

Better understanding of the pathogenesis of AA could aid in timely identifying patients that are less likely to respond to IST. Bone marrow recovery after IST strongly implies an immune-mediated pathogenesis in AA. Because ATG results in lymphocyte depletion and effector T-cells are expanded in AA[7], a widely accepted view is that hematopoietic stem and progenitor cells (HSPCs) in the bone marrow are targeted by autoreactive T-cells. However, if AA would only be mediated by T-cells, it is surprising that hATG is superior to rATG, since hATG is less potent at depleting lymphocytes[5,6]. Therefore, we include the possibility that the therapeutic effect of hATG goes beyond T-cell depletion and involves an effect on other immune cell populations as well.

Previous research extensively investigated immune cells in peripheral blood in AA and suggested a role for T-cell[8,9] and B-cell[10] subpopulations in its pathogenesis. However, a detailed overview of the immune landscape at the site of HSPC destruction, the bone marrow, is lacking. The few studies that reported T-cell abnormalities in the bone marrow could not

provide a full overview of the immune cell composition due to limitations in the size of flow cytometry antibody panels. In recent years, high-dimensional discovery tools like single-cell RNA sequencing (scRNA-seq) or mass cytometry offered new possibilities to study the immune system in tissues[11]. Mass cytometry, in contrast to scRNA-seq, quantifies protein expression levels on single-cells and therefore allows for the exploration of both common and rarer immune subpopulations. In the present study, we applied mass cytometry on bone marrow aspirates of AA patients. This enabled us to reveal a considerable shift in the immune cell composition in bone marrow from AA patients and to identify a disease-specific immune cell network. Our study contributes to our understanding of AA as an immune-mediated form of bone marrow failure and shows that not only T-cells, but also myeloid cells and B-cells are likely involved in its pathogenesis.

Methods

Patients and samples

Bone marrow aspirates and peripheral blood samples were collected from 7 adult AA patients at diagnosis (pre-ATG; AA^{PRE}) and 7 age- and sex-matched healthy donors (HDs). In addition, bone marrow aspirates from 3 of 7 AA patients were collected six months after the start of first-line IST (post-ATG; AA^{POST}), which consisted of 4 days of 40 mg/kg ATGAM® (hATG; Pfizer) and 5 mg/kg/day ciclosporin for at least six months. Bone marrow and peripheral blood collection were performed after given informed consent in accordance with the Declaration of Helsinki. Clinical characteristics of patients and HDs are outlined in Table 1. All patients were treatment-naïve at diagnosis, had an indication for treatment, did not have an additional underlying disease and were diagnosed and treated according to Dutch guidelines[3]. Patients under the age of 40 were screened for Fanconi anemia to rule out a congenital form of bone marrow failure. One patient was classified as non-severe AA (NSAA), two patients as severe AA (SAA) and four patients as very severe AA (VSAA), defined as described in international guidelines[2]. Complete response to IST was defined as complete normalization of peripheral blood counts. Partial response was defined as transfusion independence and a neutrophil count of at least $0.5 \cdot 10^9$ neutrophils/L. This study was approved by the Medical Ethical Committee of the Leiden University Medical Center (protocol number B20.037).

Table 1. Characteristics of patients and response to IST.

Characteristic	AA^{PRE}	AA^{POST}	HD
Patients (n)	7	3	7
Age (median, range in years)	31 (23-42)	28 (27-40)	31 (24-44)
Sex (n, M:F)	4:3	2:1	4:3
Severity of disease (n)			
Non-severe AA	1	0	NA
Severe AA	2	1	NA
Very severe AA	4	2	NA

AA indicates aplastic anemia; F: female; IST: immunosuppressive therapy; M: male; NA: not applicable.

Mass cytometry antibody staining, data acquisition and data analysis

Bone marrow mononuclear cells (BMMCs) or peripheral blood mononuclear cells (PBMCs) were isolated from bone marrow aspirates or peripheral blood, stained with a panel of 39 validated[12-14] metal-isotope tagged antibodies and measured as described in Supplemental Methods. For each acquired mass cytometry data file, single, live $CD45^+$ cells were gated in FlowJo version 10.7.1 (BD Biosciences) as shown in Figure S1. A median of $0.5{\cdot}10^6$ (range 0.4-$0.9{\cdot}10^6$) cells was gated for each AA^{PRE} sample. For every HD or AA^{POST} sample, a median of $0.5{\cdot}10^6$ (range 0.3-$0.9{\cdot}10^6$) or $0.3{\cdot}10^6$ (range 0.3-$0.6{\cdot}10^6$) cells was gated respectively.

The single, live $CD45^+$ cells were studied using two analyses. In the first analysis, BMMC samples from all AA^{PRE} and HDs were studied. $7.7{\cdot}10^6$ single, live $CD45^+$ cells were sample-tagged, hyperbolic arcsinh transformed with a cofactor of 5 and imported into Cytosplore[15] for dimensionality reduction. A five-level hierarchical stochastic neighbor embedding (HSNE) analysis was performed with default perplexity and iterations (30 and 1000, respectively; see Figure S2 for outline of HSNE analysis pipeline). Three of 39 markers in the mass cytometry panel (HLA-DR, CD5 and KLRG1) were not used in the HSNE clustering analysis due to small variations in marker distribution between experiments (data not shown). Major immune lineages were identified at the overview level of the HSNE analysis and were defined as: $CD4^+CD3^+CD7^+$ $CD4^+$ T-cells, $CD8a/b^+CD3^+CD7^+$ $CD8^+$ T-cells, $CD7^-CD20/IgM^+$ B-cells, $CD3^+CD7^+TCRgd^+$ non-conventional T-cells (NCTs), $CD3^-CD7^+$ innate lymphoid cells (ILCs) including NK-cells and Lin^-cKit^+ HSPCs. All remaining cells were considered myeloid cells. Subsequently, each major immune lineage was selected for detailed analysis at the data level of the HSNE analysis using t-distributed stochastic neighbor embedding (tSNE) analyses with up to $0.5{\cdot}10^6$ landmarks. Clusters with distinct surface marker expression were identified within each major immune lineage by Gaussian mean shift (GMS) clustering at the data level. Each cluster consisted of at least 1000 cells (Figure S2).

In the second analysis, paired BMMC samples from 3 AA^{PRE} and AA^{POST} were analyzed using a comparable approach, for detailed description, see Supplemental Methods.

After clustering in both analyses, .fcs files of major immune lineages and clusters were exported from Cytosplore and loaded into R version 4.0.5 for data visualization and analysis. Cytofast[16] was used to generate heatmaps and to compare lineage or cluster frequencies between groups. Principal component analyses (PCA) and a Spearman's rank correlation analysis were performed using the packages factoextra version 1.0.7[17] and corrplot version 0.92[18], respectively.

Statistical analysis

Mann-Whitney *U* tests performed in R version 4.0.5 were used to compare immune cell frequencies between two groups. *P*-values ≤ 0.05 were considered statistically significant. Since this was an exploratory study, no adjustments for multiple testing were applied. **P* ≤ 0.05; ***P* ≤ 0.01; ****P* ≤ 0.001.

Results

The immune cell composition in bone marrow of AA patients pre-ATG is distinct from healthy donors

First, we studied the immune cell composition in the bone marrow of the 7 AA^{PRE} and 7 age- and sex-matched HDs. A five-level HSNE analysis was performed to visualize all $7.7{\cdot}10^6$ $CD45^+$ cells (median $0.5{\cdot}10^6$ $CD45^+$ cells per sample). At the overview level of the HSNE analysis, all major immune lineages and HSPCs could be identified by clustering based on lineage markers and cKit (Figure 1A). All AA^{PRE} and HD samples were homogeneously distributed per group over the HSNE analysis (Figure S3). Visualization of the AA^{PRE} and HDs in the overview level already revealed clear differences in the immune cell composition.

An unsupervised PCA confirmed a clear separation in the immune cell composition of AA^{PRE} and HDs (Figure 1B). Next, the immune cell composition was studied in further detail at the major immune lineage level. Since we aimed to uncover how the immune cell composition differs in bone marrow from AA^{PRE} and HDs and total cell counts are decreased in the bone marrow in AA, we studied relative cell frequencies instead of absolute cell counts. Major immune lineage frequencies of $CD45^+$ cells were determined (Figure 1C). HSPCs could not be distinguished enough at this level of the HSNE analysis and were therefore merged with myeloid cells. In agreement with disease characteristics, myeloid cells were scarce in AA^{PRE} compared to HDs (median 0.6% *versus* 33% of $CD45^+$ cells). B-cells were also reduced in AA^{PRE} compared to HDs (median 9% *versus* 16% of $CD45^+$ cells). In contrast, $CD4^+$ and $CD8^+$ T-cells were increased in AA^{PRE} compared to HDs, which could be due to the relative decrease in myeloid and B-cells. Finally, non-conventional T-cell (NCT) and innate lymphoid cell (ILC) frequencies did not significantly differ between AA^{PRE} and HDs.

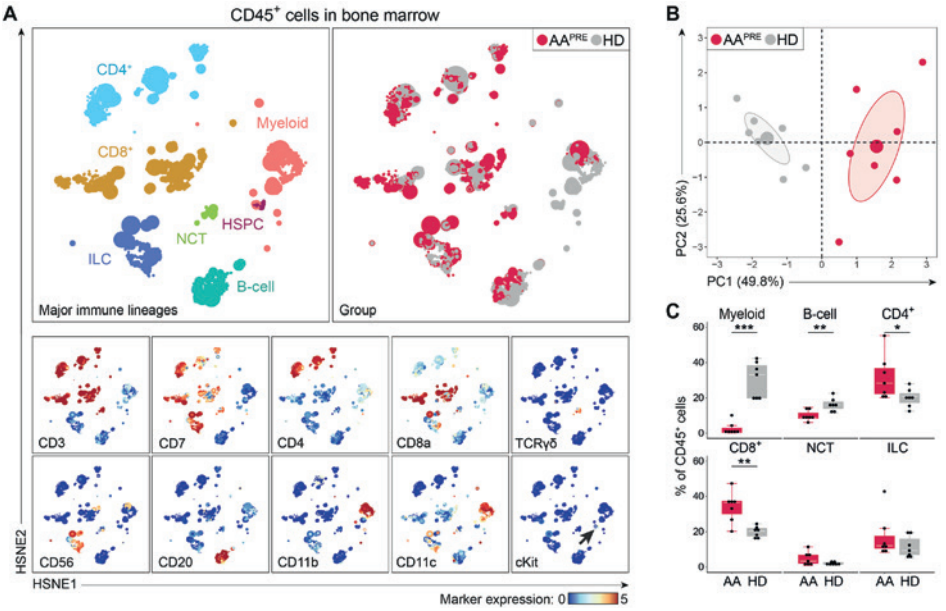


Figure 1. Major immune lineages in bone marrow in AA pre-ATG and HD. Colors indicate major immune lineages (HSPCs, myeloid cells, B-cells, CD4$^+$ T-cells, CD8$^+$ T-cells, NCT-cells and ILCs), groups (AA^{PRE} in red and HDs in gray) or median ArcSinh-transformed marker expression values. (A) Major immune lineages in bone marrow of 7 AA^{PRE} and 7 HDs, visualized at the overview level of a five-level HSNE analysis. $7.8{\cdot}10^3$ HSNE landmarks represented all $7.7{\cdot}10^6$ CD45$^+$ cells in the analysis. The size of each landmark reflects the number of cells represented by the landmark. cKit$^+$ cells are indicated by an arrow. Major immune lineages were defined as follows: CD4$^+$CD3$^+$CD7$^+$ CD4$^+$ T-cells, CD8a/b$^+$CD3$^+$CD7$^+$ CD8$^+$ T-cells, CD7$^-$CD20/IgM$^+$ B-cells, CD3$^+$CD7$^+$TCRγδ$^+$ non-conventional T-cells (NCTs), CD3$^-$CD7$^+$ innate lymphoid cells (ILCs) including NK-cells and Lin$^-$cKit$^+$ HSPCs. All remaining cells were considered myeloid cells. (B) Principal component analysis of the 7 AA^{PRE} and 7 HD bone marrow samples. Each larger dot represents the group mean. Each smaller dot represents a sample. (C) Major immune lineage frequencies in AA^{PRE} and HDs, shown as a percentage of all CD45$^+$ cells in bone marrow. Each black dot represents a sample. Box plots present the median with the interquartile range (IQR), error bars present 1.5*IQR.

Stem cell depletion and high frequencies of CD16$^+$ myeloid cells in AA pre-ATG

Since myeloid, B-cell, CD4$^+$ T-cell and CD8$^+$ T-cell frequencies were significantly different in the bone marrow from AA^{PRE} compared to HDs, we studied each of these lineages at the immune subpopulation level. First, the myeloid cells including HSPCs were selected and analyzed at the four successive levels of the HSNE analysis (Figure 2; Figure S2). In this manner, multiple HSPC and myeloid cell populations could be distinguished based on the expression of defining cell surface markers (Figure 2A, right panels). Twenty phenotypically distinct clusters were identified (Figure 2B), 8 of which were significantly different in AA^{PRE} compared to HDs, 1 had a p-value of 0.053 and 11 clusters did not significantly differ between both groups. Analysis of the 8 significant clusters and cluster 9 showed a strong reduction in all cKit$^{+/dim}$ clusters (cluster #9-11) in AA^{PRE}, confirming HSPC depletion in AA^{PRE} (Figure 2C). Furthermore, we observed a decrease of myeloid cells compatible with CD123$^+$ plasmacytoid dendritic cells

(cluster #13), CD163^{+} macrophages (cluster #16), CD11c^{+} conventional dendritic cells (cluster #17) and CD14^{+}CD16^{-} classical monocytes (cluster #18) in AA^{PRE}. The most striking observation was a substantial increase in CD16^{+} myeloid cells in AA^{PRE}, which lacked expression of the neutrophil marker CD15 and represented a median of 41% (range 16-83%) of all myeloid cells (Figure S4A-B cluster #14 and 19-20 combined; arrows in Figure 2A). Two CD16^{+} myeloid cell clusters (cluster #19-20) resembling CD14^{-}CD16^{+} non-classical and CD14^{+}CD16^{+} intermediate monocytes were significantly increased in AA^{PRE} (Figure 2D). In contrast, CD16^{+} myeloid cells only comprised a median of 5% (range 2-19%) of all myeloid cells in HDs (Figure S4A-B).

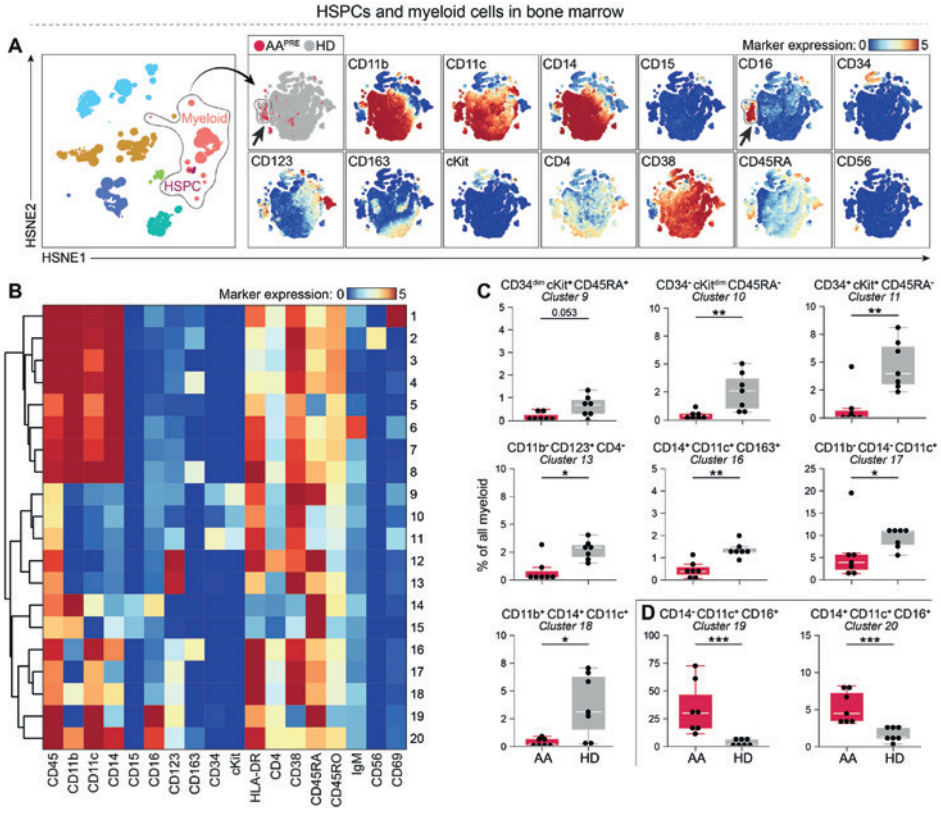


Figure 2. Myeloid cell compartment including HSPCs in bone marrow in AA pre-ATG and HD. Colors indicate major immune lineages (HSPCs, myeloid cells, B-cells, CD4^{+} T-cells, CD8^{+} T-cells, NCT-cells and ILCs), groups (AA^{PRE} in red or HDs in gray) or median arcsinh-transformed marker expression values. (A) HSPCs and myeloid cells isolated from bone marrow of 7 AA^{PRE} and 7 HDs, visualized at level four of a five-level HSNE analysis. $2.4{\cdot}10^{5}$ landmarks represent $1.3{\cdot}10^{6}$ cells. The size of each landmark reflects the number of cells represented by the landmark. Arrows indicate CD16^{+} myeloid cells. (B) Heatmap presenting median arcsinh-transformed marker expression values for the 20 clusters identified within the HSPC and myeloid cell compartment. The relationships of similarity between clusters are depicted by the dendrogram. (C) HSPC and myeloid cell clusters reduced in AA^{PRE}. (D) HSPC and myeloid cell clusters increased in AA^{PRE}. Cluster frequencies are presented as a percentage of all HSPCs and myeloid cells in bone marrow from each respective patient or HD. Each black dot represents a sample. Box plots present the median with the interquartile range (IQR), error bars present 1.5*IQR. Only clusters that significantly differed in frequency between AA^{PRE} and HDs are shown.

CCR6^{++} B-cells predominate in AA pre-ATG

Detailed analysis of all B-cells revealed phenotypical heterogeneity within the B-cell compartment (Figure 3A). 20 B-cell clusters were identified (Figure S4C). CD20^{+}IgM^{-}CD127^{+} B-cells (cluster #2) and CD20^{-}IgM^{-} B-cells expressing variable levels of CD127 (cluster #3-4), compatible with a group of early B-cells[19,20], were markedly reduced in AA^{PRE} compared to HDs (Figure 3B). We also observed a decrease in B-cells with absent or low expression of the chemokine receptor CCR6 (Figure 3B, cluster #14 and 17-20). Strikingly, B-cells expressing high levels of CCR6 were strongly increased in AA^{PRE} compared to HDs (Figure 3C, cluster #12-13 and 16). Combined, CCR6^{++} B-cells constituted a median of 64% (range 38-86%) of all B-cells in AA^{PRE} and only a median of 10% (range 1-26%) of all B-cells in HDs (Figure S4C-D, cluster #5, 9, 12-13 and 16 combined). Clusters 12 and 16 co-expressed CD27 in line with previous descriptions of memory B-cells[21-23] (Figure S4C). In contrast, cluster 13 lacked expression of CD27, compatible with a population of immature or mature B-cells[24]. In addition, the CCR6^{++} B-cells expressed different levels of IgM, indicating that these cells were in multiple stages of development.

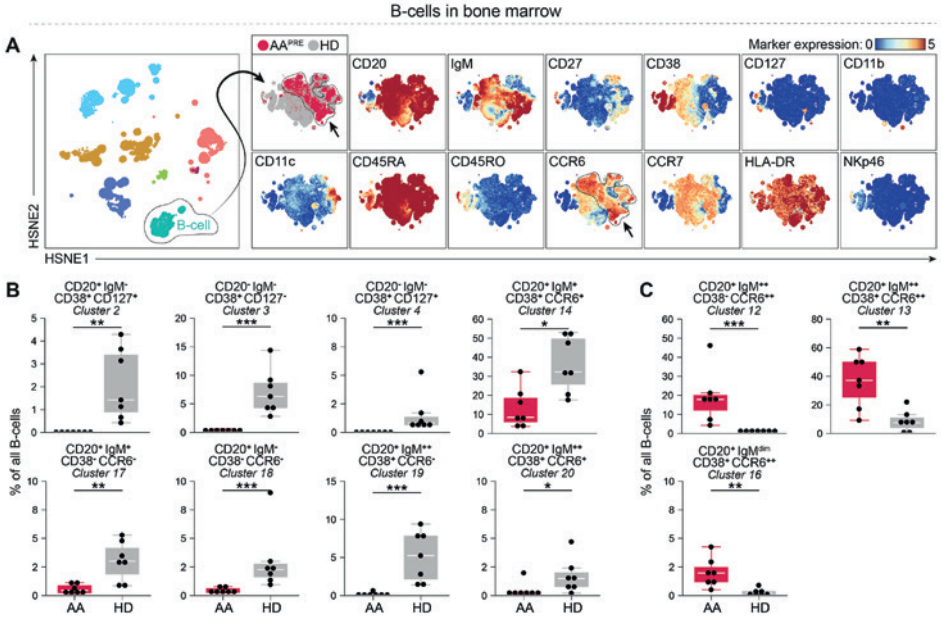


Figure 3. B-cell compartment in bone marrow in AA pre-ATG and HD. Colors indicate major immune lineages (HSPCs, myeloid cells, B-cells, CD4^{+} T-cells, CD8^{+} T-cells, NCT-cells and ILCs), groups (AA^{PRE} in red or HDs in gray) or median arcsinh-transformed marker expression values. (A) B-cells isolated from bone marrow of 7 AA^{PRE} and 7 HDs, visualized at level four of a five-level HSNE analysis. The HSNE depicts $1.6{\cdot}10^{5}$ landmarks for $0.9{\cdot}10^{6}$ B-cells. The size of each landmark reflects the number of cells represented by the landmark. Arrows indicate CCR6^{++} B-cells. (B) B-cell clusters reduced in AA^{PRE}. (C) B-cell clusters increased in AA^{PRE}. Cluster frequencies are presented as a percentage of all B-cells in bone marrow from each respective patient or HD. Each black dot represents a sample. Box plots present the median with the interquartile range (IQR), error bars present 1.5*IQR. Only clusters that significantly differed in frequency between AA^{PRE} and HDs are shown.

Th17-like CCR6^{+}CD4^{+} T-cells are increased in AA pre-ATG

Hierarchical clustering of all CD4^{+} T-cells classified 35 phenotypically distinct CD4^{+} T-cell clusters in different stages of development (Figures S4E-G). No significant differences were observed in naïve (CD45RA^{+}CCR7^{+}) CD4^{+} T-cell clusters. In contrast, multiple central memory (CM; CD45RO^{+}CCR7^{+}) and effector memory (EM; CD45RO^{+}CCR7^{-}) CD4^{+} T-cell clusters were significantly reduced in AA^{PRE} (Figure 4A). The most remarkable difference was an increase in CM and EM CD4^{+} T-cells with a Th17-like phenotype based on the co-expression of CCR6 and/or CD161[25], suggestive of Th17-skewing in AA^{PRE}. Six CCR6^{+}CD4^{+} T-cell clusters were significantly increased in AA^{PRE} compared to HDs (Figure 4B). Together, the CCR6^{+}CD4^{+} T-cells represented a median of 11% (range 5-18%) of CD4^{+} T-cells in AA^{PRE}, compared to a median of 2% (range 2-6%) of CD4^{+} T-cells in HDs (Figure S4F-G, cluster #13, 16, 18, 20, 22 and 34-35 combined).

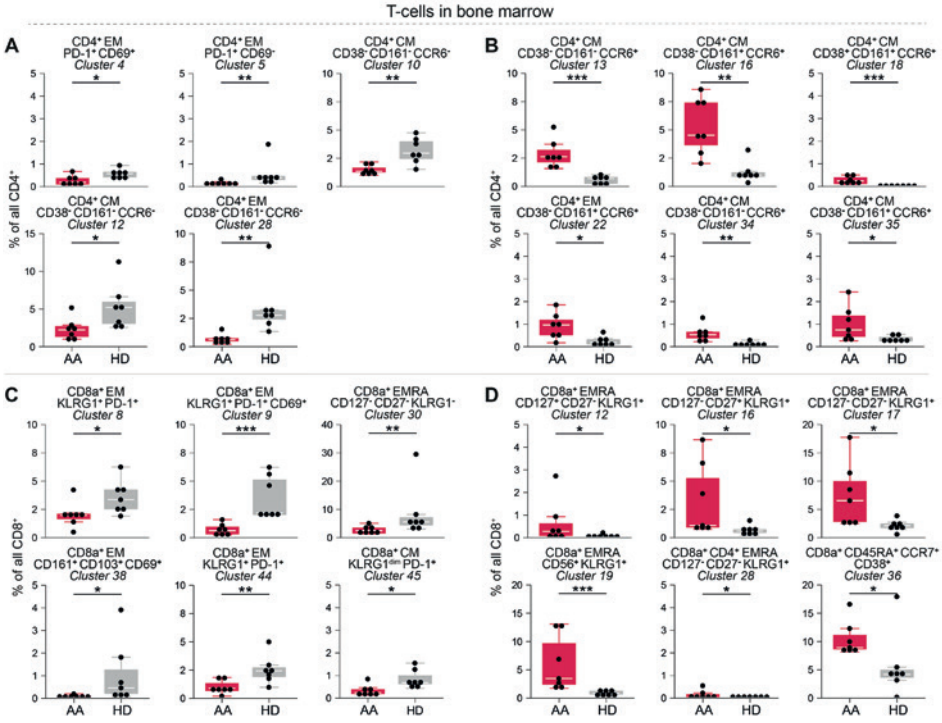


Figure 4. CD4^{+} T-cell and CD8^{+} T-cell compartment in bone marrow in AA pre-ATG and HD. Colors indicate groups (AA^{PRE} in red or HDs in gray). (A) CD4^{+} T-cell clusters reduced in AA^{PRE}. (B) CD4^{+} T-cell clusters increased in AA^{PRE}. (C) CD8^{+} T-cell clusters reduced in AA^{PRE}. (D) CD8^{+} T-cell clusters increased in AA^{PRE}. Cluster frequencies are presented as a percentage of all CD4^{+} T-cells or CD8^{+} T-cells in bone marrow from each respective patient or HD. Each black dot represents a sample. Box plots present the median with the interquartile range (IQR), error bars present 1.5*IQR. Only clusters that significantly differed in frequency between AA^{PRE} and HDs are shown.

Increase of KLRG1$^+$ terminally differentiated effector memory CD8$^+$ T-cells in AA pre-ATG

Hierarchical clustering of all CD8$^+$ T-cells identified 45 phenotypically distinct CD8$^+$ T-cell clusters (Figures S4H-J). CM and EM CD8$^+$ T-cells were predominantly reduced in AA^{PRE} (Figure 4C; Figure S4I-J). A cluster of CD8$^+$ T-cells (cluster #36) resembling a population of naïve but activated (CD38$^+$) T-cells was significantly increased in AA^{PRE} (Figure 4D). The most striking observation within the CD8$^+$ T-cell compartment in AA^{PRE} was an increase of EMRA CD8$^+$ T-cells positive for KLRG1 resembling highly differentiated cytotoxic T-cells[26]. These KLRG1$^+$ EMRA CD8$^+$ T-cells constituted a median of 29% (range 15-45%) of all CD8$^+$ T-cells in AA^{PRE}, but only a median of 9% (range 7-33%) of all CD8$^+$ T-cells in the HDs (cluster #10-22, 24-26 and 28-29 combined; Figure S4I-J). Five KLRG1$^+$EMRA CD8$^+$ T-cell clusters (cluster #12, 16-17, 19 and 28) were significantly elevated in AA^{PRE} compared to HDs (Figure 4D).

A disease-specific immune cell network characterizes AA pre-ATG

To capture the relationships across the immune cell clusters that characterize AA^{PRE}, we performed a Spearman's rank correlation analysis on the myeloid, B-cell and T-cell clusters with significant differential presence between AA^{PRE} and HDs. A matrix of Spearman's correlation coefficients visualized two large networks of immune cells (Figure 5A). In line with the analysis of the major immune lineages above, network 1 showed a correlation between CD16$^+$ myeloid cells, CCR6^{++} B-cells, CCR6$^+$ memory CD4$^+$ T-cells, CD45RA$^+$CCR7$^+$CD38$^+$ CD8$^+$ T-cells and KLRG1$^+$EMRA CD8$^+$ T-cells, and was significantly more abundant in AA^{PRE} compared to HDs (median 22% *versus* 5% of CD45$^+$ cells, Figure 5B). In contrast, network 2 was significantly reduced in AA^{PRE} compared to HDs (median 6% *versus* 23% of CD45$^+$ cells). Analysis of paired peripheral blood and bone marrow samples from all 7 AA^{PRE} demonstrated that all subpopulations of network 1 are detectable in peripheral blood (Figure S5).

IST normalizes the immune cell composition in patients with adequate hematological improvement six months post-ATG

Since IST can result in recovery of hematopoiesis, we investigated the effect of IST on the immune cell composition in the bone marrow of 3 AA patients pre- and six months post-ATG. All patients still received ciclosporin and were transfusion-independent six months post-ATG. All patients had improvement of peripheral blood counts and eventually responded to IST, however, only one patient (AA3) showed complete response six months post-ATG (8.3 mmol hemoglobin/L, 149·10^9 platelets/L and 1.8·10^9 neutrophils/L). One patient (AA2) had major partial response six months post-ATG (5.8 mmol hemoglobin/L, 87·10^9 platelets/L and 1.9·10^9 neutrophils/L), while the third patient (AA1) showed minor partial response six months post-ATG (5.4 mmol hemoglobin/L, 18·10^9 platelets/L and 0.3·10^9 neutrophils/L).

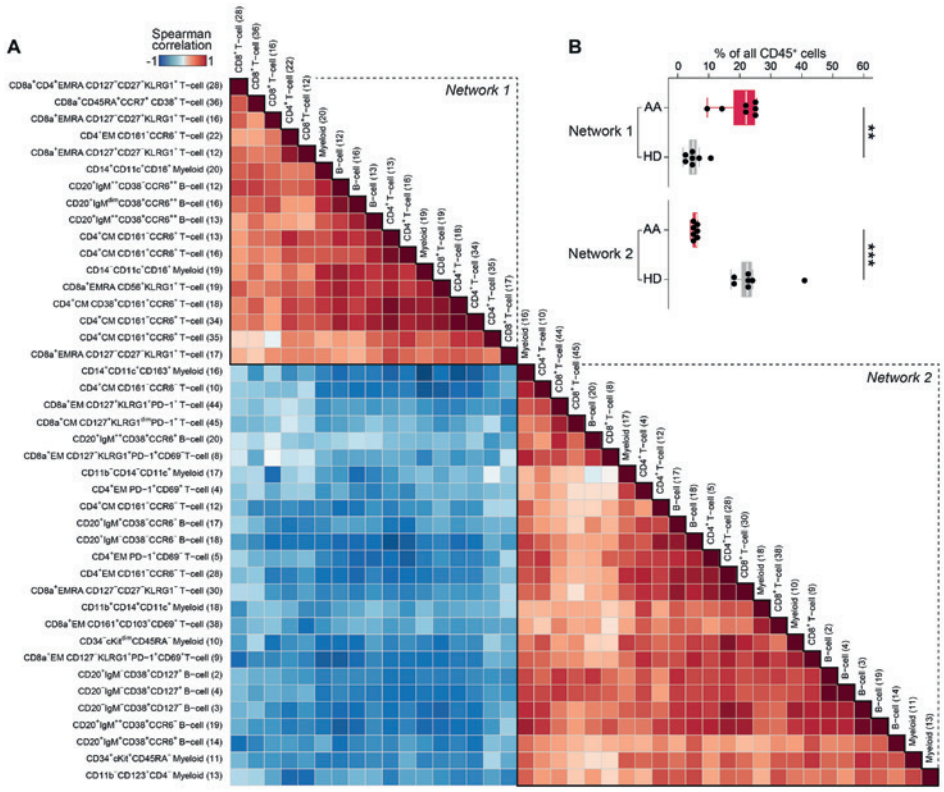


Figure 5. Spearman's rank correlation analysis of differentially present myeloid, B-cell and T-cell clusters in bone marrow in AA pre-IST and HD. (A) Spearman's rank correlation analysis based on the frequencies of all differentially present cell clusters in AA^{PRE} compared to HDs. All AA^{PRE} (n=7) and HDs (n=7) samples were included in the analysis. The strength of the correlations is presented in color (blue to red). The phenotype of each cell cluster is presented left of the correlation matrix. The number of each cell cluster is shown between brackets and corresponds to the cell cluster numbers used in Figures 2 and 3 and Supplemental Figure 3. (B) Total frequency of all cell clusters in networks 1 or 2, expressed as a percentage of all $CD45^+$ cells in bone marrow from each respective patient or HD. Colors indicate groups (AA^{PRE} in red or HDs in gray). Each black dot represents a sample. Box plots present the median with the interquartile range (IQR), error bars present 1.5*IQR.

A total of $3.0{\cdot}10^6$ $CD45^+$ cells (median $0.5{\cdot}10^6$ or $0.3{\cdot}10^6$ cells per AA^{PRE} or AA^{POST}, respectively) were analyzed using a four-level HSNE analysis. At the overview level, the global immune cell composition in AA^{PRE} and AA^{POST} was visualized and all major immune lineages were identified (Figure 6A). HSPCs were not observed, suggesting that the frequency of HSPCs was too low to be detected. Unsupervised PCA presented a clear separation of AA^{PRE} and AA^{POST} (Figure 6B), indicative of a considerable shift in the immune cell composition in the bone marrow six months post-ATG. Analyses at the major immune lineage level demonstrated that myeloid cells were strongly increased or normalized in all AA^{POST} (Figure 6C). In addition, $CD4^+$ T-cells were normalized, while B-cells were still below normal levels in all AA^{POST}. $CD8^+$ T-cells remained high in the patient (AA1) with the lowest blood counts six months post-ATG (Figure 6C).

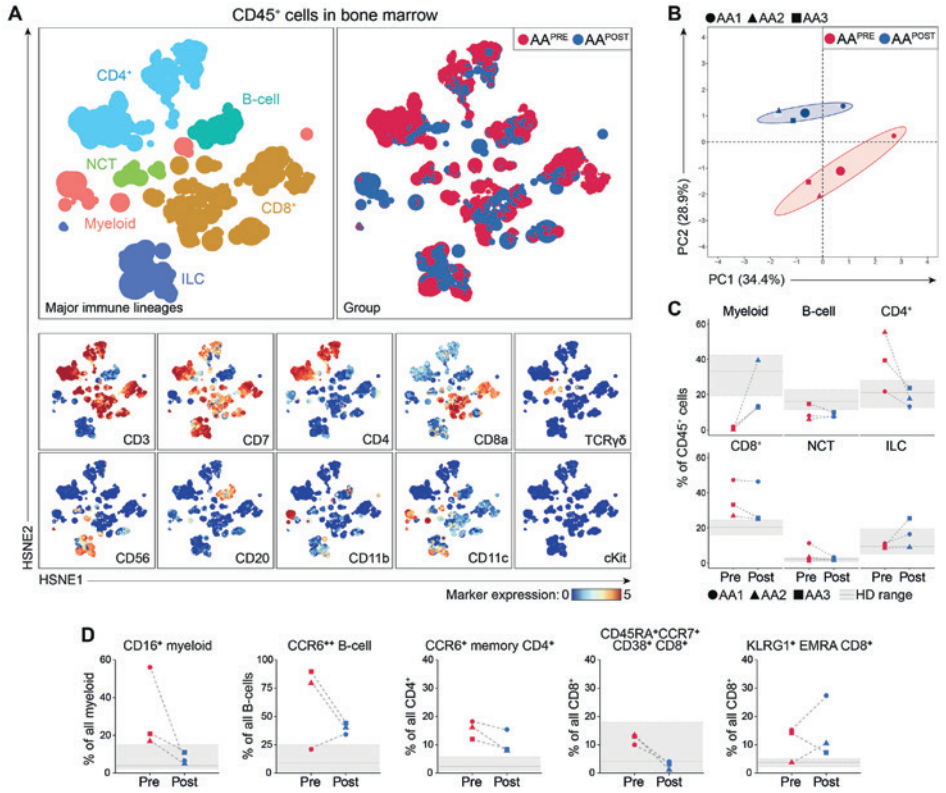


Figure 6. Identification and frequencies of major immune lineages in bone marrow in AA pre- and post-ATG. Colors indicate major immune lineages (myeloid cells, B-cells, $CD4^+$ T-cells, $CD8^+$ T-cells, NCT-cells and ILCs), groups (AA^{PRE} in red and AA^{POST} in blue) or median ArcSinh-transformed marker expression values. (A) Major immune lineages visualized at the overview level of a four-level HSNE analysis with $3.0{\cdot}10^6$ $CD45^+$ cells isolated from paired bone marrow samples collected from 3 AA patients before and six months post-ATG. $1.7{\cdot}10^4$ landmarks represented all $3.0{\cdot}10^6$ $CD45^+$ cells in the analysis. The size of each landmark reflects the number of cells represented by the landmark. (B) Principal component analysis of the 3 AA^{PRE} and 3 AA^{POST} samples. Each larger dot represents the group mean. Each smaller dot represents a sample. (C) Major immune lineage frequencies in the AA^{PRE} and AA^{POST} samples, shown as a percentage of all $CD45^+$ cells in bone marrow from each respective patient or HD. (D) Total pre- and post-ATG frequencies of the $CD16^+$ myeloid cell, $CCR6^{++}$ B-cell, $CCR6^+$ CM or EM $CD4^+$ T-cell, $CD45RA^+CCR7^+CD38^+$ $CD8^+$ T-cell and $KLRG1^+$ EMRA $CD8^+$ T-cell clusters representing the immune cell network that was significantly increased in AA^{PRE} compared to HDs. Pre- and post-ATG samples of every AA patient are connected by a dotted line. Minimum and maximum ranges of shaded regions depict the minimum and maximum lineage or subpopulation frequencies in the 7 HDs. Median frequencies in HDs are depicted by a solid gray line. Respective patients are represented by different shapes (AA1 closed circle, AA2 triangle, AA3 square). No P-values are shown because of the small group size.

To analyze the effect of IST on the disease-specific immune cell network identified in AA^{PRE} (network 1), we studied the presence of its corresponding immune cell subtypes in AA^{POST}. Cluster frequencies were compared to frequencies observed in the HDs. Strikingly, this revealed that $CD16^+$ myeloid cell frequencies normalized in all AA^{POST} and $CD45RA^+CCR7^+CD38^+$ $CD8^+$ T-cell frequencies decreased in all AA^{POST} (Figure 6D). $CCR6^{++}$ B-cell, $CCR6^+$ memory $CD4^+$

T-cell and KLRG1^{+} EMRA frequencies showed a trend towards normalization in the two patients (AA2 and AA3) with complete response or major partial response six months post-ATG. In contrast, these clusters were still frequent or increased in the patient (AA1) with minor partial response six months post-ATG (Figure 6D).

Discussion

The present study provides a comprehensive comparison of the immune landscape in the bone marrow from AA^{PRE} and HDs with the aim to decipher which immune cells may be implicated in the pathogenesis of AA. We demonstrate that the bone marrow from AA^{PRE} harbors a distinct immune cell composition compared to HDs, with significant differences in the myeloid, B-cell, CD4^{+} T-cell and CD8^{+} T-cell lineages. Detailed analyses at the immune subpopulation level identified a disease-specific immune cell network of CD16^{+} myeloid cells, CCR6^{++} B-cells, Th17-like CCR6^{+}CD4^{+} T-cells, CD45RA^{+}CCR7^{+}CD38^{+} CD8^{+} T-cells and KLRG1^{+} EMRA CD8^{+} T-cells that distinguishes AA^{PRE} from HDs. This network showed a trend towards normalization in patients with hematological improvement six months post-ATG, which implies a pathogenic role of the network in AA.

To date, cytotoxic T-cells have been the focus of immunophenotyping studies in AA. The present study shows CD4^{+} and CD8^{+} T-cell derangements in AA^{PRE}, consistent with the view that AA is mediated by an autologous T-cell response. The identified disease-specific immune cell network featured a group of KLRG1^{+}EMRA CD8^{+} T-cells, which accords with previous reports on autoimmune disorders[27,28] where KLRG1^{+}CD8^{+} T-cells accumulate at inflammatory sites. Although CD57 expression was not evaluated in our study, the KLRG1^{+}CD8^{+} T-cells could resemble previous descriptions of CD57^{+}CD28^{-} CD8^{+} T-cells, which commonly express KLRG1[29] and are expanded in peripheral blood [30] in AA where their presence seems to correlate with disease activity[31]. We assume, therefore, that the identified KLRG1^{+}CD8^{+} T-cells have cytotoxic capacity. The target of this immune response remains presently unknown and would be an interesting topic for future studies.

Within the CD4^{+} T-cell compartment, we observed increased frequencies of CCR6^{+} Th17-like cells in the bone marrow of AA^{PRE} compared to HDs. Previous studies postulated a role for Th17 cells in the pathogenesis of AA and identified Th17 cells based on the expression of IL-17[8,32] or CD161[9]. Our data are in line with these studies and add CCR6 as a new marker to delineate Th17 cells in AA. Functionally, Th17 cells may contribute to the immune response in AA through their ability to secrete pro-inflammatory cytokines including IL-17 and IL-21 which can trigger macrophage recruitment and activation.

Interestingly, B-cells are not well characterized in AA, even though B-cell involvement is increasingly recognized in autoimmune disorders. We identified high proportions of $CCR6^{++}$ B-cells that have not been described in AA before but are profoundly increased in autoimmune disorders[33]. Together with the identification of Th17-like $CCR6^{+}CD4^{+}$ T-cells, this presents CCR6 as a potentially important marker in the pathogenesis of AA. CCR6 is a chemokine receptor expressed on various immune cell types and mediates immune cell recruitment to inflammatory sites through CCL20, its sole ligand[34]. Increased levels of CCL20 have been described in the bone marrow in AA[35]. Hence, it is tempting to speculate that the CCR6-CCL20 axis fuels an immune response in AA, as proposed in other autoimmune disorders[36,37], by recruiting pro-inflammatory immune cells to the bone marrow.

Autoimmune responses are generally characterized by an expansion of effector T-cells, rather than an accumulation of polyclonal, antigen-inexperienced naïve T-cells. Therefore, it is surprising that our results point to the importance of a cluster of $CD45RA^{+}CCR7^{+}CD38^{+}$ $CD8^{+}$ T-cells with a naïve phenotype. Since previous work has demonstrated the increased presence of $CD95^{+}$ stem cell-like memory T-cells (T_{SCM}) within the naïve $CD8^{+}$ T-cell compartment in AA[38], we consider the possibility that the $CD45RA^{+}CCR7^{+}CD38^{+}$ $CD8^{+}$ T-cells are $CD8^{+}$ T_{SCM}. T_{SCM} are endowed with an enhanced capacity for self-renewal and control immune responses through their ability to generate memory and effector T-cells[39]. However, because our panel did not include T_{SCM}-specific markers, the precise identity of the $CD45RA^{+}CCR7^{+}CD38^{+}$ $CD8^{+}$ T-cells remains unclear.

The presence of $CD16^{+}$ myeloid cells in the identified immune cell network is striking because AA is characterized by a profound reduction of the myeloid compartment in peripheral blood. Therefore, it would be interesting to determine whether these cells are expanded or are the only myeloid cells left in the bone marrow after immune-mediated destruction in AA. Higher percentages of $CD16^{+}$ macrophages, defined by the expression of CD68 and lower levels of CD14, have been reported in bone marrow in AA, and were suggested to exert bone marrow destructive effects by stimulating effector T-cells through the secretion of TNF-α[40]. We characterized the $CD16^{+}$ myeloid cells in further detail and identified two populations that expressed different levels of CD11b and CD14 and did not express the M2-macrophage marker CD163. Based on this expression profile, these $CD16^{+}$ myeloid cells could represent a population of $CD14^{+}CD16^{+}$ intermediate and $CD14^{-}CD16^{+}$ non-classical monocytes, which can express CD68[20], produce TNF-α[41] and contribute to autoimmune disorders[42,43]. Regarding the function of these cells, one could speculate whether these cells have a direct role in HSPC destruction, e.g. by cytokine secretion, or that they are recruited to clear dead and dying cells, e.g. by antibody-dependent cell-mediated cytotoxicity, and merely reflect a consequence of the immune response.

Altogether, the disease-specific immune cell network identified in the bone marrow from AA^{PRE} is compatible with a state of chronic inflammation. Although this study did not aim to

interrogate the functional role of the network, our post-ATG data could indicate a distinct role of CD16^{+} myeloid cells compared to CCR6^{++} B-cells, Th17-like CCR6^{+}CD4^{+} T-cells and KLRG1^{+}EMRA CD8^{+} T-cells. ATG-based IST can result in the recovery of hematopoiesis, which implies that IST intervenes with the immune response that underlies the pathogenesis of AA. We demonstrate that CD16^{+} myeloid cells were normalized six months post-ATG, but that CCR6^{++} B-cells, CCR6^{+} Th17-like CD4^{+} T-cells and KLRG1^{+}EMRA CD8^{+} T-cells remained elevated in patients with hematological improvement, despite a trend towards normalization. A possible explanation for the fact that only CD16^{+} myeloid cells were strongly reduced six months post-ATG could be that these cells are charged with clearing dead and dying cells in the bone marrow in AA, which would explain the decrease in these cells once the initiating immune response has resolved. However, the decrease in CD16^{+} myeloid cells could also indicate that these cells carry out an effector function in the immune response in AA via cytokine secretion. This would explain the recovery of hematopoiesis after the depletion of CD16^{+} myeloid cells six months post-ATG. As ciclosporin suppresses B-cell[44] and T-cell development[45], we hypothesize that ciclosporin suppresses the CCR6^{++} B-cells, Th17-like CCR6^{+}CD4^{+} T-cells and KLRG1^{+}EMRA CD8^{+} T-cells that are still elevated six months post-ATG to maintain stable hematopoiesis. The fact that ciclosporin suppression is needed beyond six months could implicate a role for these cells in the initiation of the inflammatory process. Regarding the potential significance of CCR6^{++} B-cells, it is tempting to speculate that hATG-based IST, the preferred first-line treatment in AA, may be more potent at depleting CCR6^{++} B-cells than rATG-based IST and is, therefore, superior in the setting of AA. Based on the potential importance of CCR6^{++} B-cells and CCR6^{+} Th17-like CD4^{+} T-cells, our study proposes CCR6 as a new potential therapeutic target. Blockade of CCR6 and disruption of the CCR6-CCL20 interaction have been shown to reduce severity of several autoimmune disorders[46,47]. Multiple reports describe CCR6 blockade therapies targeting pathogenic Th17 T-cells[46,48] and show improvement in diseases such as psoriasis[47] through the inhibition of T-cell recruitment to inflammatory sites, illustrating that CCR6 blockade could be effective in treating T-cell mediated autoimmune disorders. Another report proposes a small molecule inhibitor of CCR6 as a potential therapy for autoimmune disorders through its ability to inhibit CCR6-dependent B-cell migration[49]. Whether anti-CCR6 treatment may be used to control inflammation and symptoms in the active phase of AA could be subject of further studies.

To investigate the clinical applicability of our work, we analyzed peripheral blood for the presence of the disease-specific immune cell network and found that all subpopulations of the immune cell network are detectable in paired peripheral blood and bone marrow samples from AA^{PRE} The fact that the disease-specific immune cell network can be measured in peripheral blood offers possibilities for its clinical use as a marker of disease activity to evaluate the success of IST and possible disease progression.

In summary, we identified a disease-specific immune cell network in the bone marrow from AA^{PRE}. While inflammation-associated immune cells were expected in AA, our approach shows for the first time an association between $CD16^+$ myeloid cells, Th17-like cells, $CD45RA^+CCR7^+CD38^+$ $CD8^+$ T-cells and $KLRG1^+$ EMRA $CD8^+$ T-cells and adds $CD16^+$ myeloid cells and $CCR6^{++}$ B-cells as a potentially important populations in AA. Successful treatment with IST strongly reduced the levels of $CD16^+$ myeloid cells and showed a trend toward normalization of the frequencies of $CCR6^{++}$ B-cells, $CCR6^+$ memory $CD4^+$ T-cells and $KLRG1^+$EMRA $CD8^+$ T-cells. The identified network has the potential to be used as a marker for disease activity at diagnosis and during treatment of AA. Together, our study sets the stage for further exploration of the functional relevance and cellular spatial interactions of this immune cell network within the bone marrow microenvironment.

Conflict of interest

The authors declare no competing financial interests.

Author contributions

E.S.P. analyzed results, interpreted the data, made the figures and wrote the manuscript. Y.K-W. performed experiments. V.vU. designed the experimental set-up. J.H.F.F. interpreted the data. F.K. and M.H.M.H. interpreted the data and supervised the project. J.M.L.T. conceptualized the study, recruited patients, interpreted data and supervised the project. All authors critically edited and reviewed the manuscript. All authors approved the final manuscript.

Funding

This work was supported by a research grant from Dioraphte Foundation (grant number 20010406).

Acknowledgements

We thank dr. Tamim Abdelaal of the Department of Radiology of the Leiden University Medical Center for assistance in the data normalization and the network analysis. We acknowledge the Flow Cytometry Core Facility (FCF) of the Leiden University Medical Center for assistance with the generation of the mass cytometry data.

Data availability statement

Mass cytometry data acquired in this study have been deposited to https://flowrepository.org.

Supplemental methods

Mononuclear cell isolation and cryopreservation

Bone marrow mononuclear cells (BMMCs) or peripheral blood mononuclear cells (PBMCs) were isolated from fresh bone marrow aspirates or peripheral blood using Ficoll separation gradient or CPT Cell Preparation Tubes (BD, cat 362780). Subsequently, cells were cryopreserved in liquid nitrogen until further use.

Mass cytometry antibodies

Mass cytometry antibodies and antibody specifications are listed in Supplementary Table 1. The antibodies were either purchased from Standard Biotools or conjugated in-house using Maxpar® X8 Antibody Labeling Kits (Standard Biotools) according to the manufacturer's instructions. After conjugation, antibodies were eluted in 200mL of antibody stabilizer PBS (Candor Biosciences, 131125) containing 0.05% sodium azide and stored at 4°C. All antibodies were previously validated by our group[12-14].

Mass cytometry antibody staining and data acquisition

Cryopreserved BMMC or PBMC samples were measured in six batches. Samples collected from AA^{PRE} and HDs were paired and measured across five batches. BMMC samples taken from AA^{POST} were measured in the sixth batch. A cryopreserved PBMC reference sample was included in batches one and six to account for technical variation. All samples were stained and measured as previously described[14,50]. In brief, cryopreserved BMMCs or PBMCs were thawed, washed, resuspended in 2mL of cell staining buffer (Standard Biotools, cat 201068) and incubated with 1mL of 1:500 Cell-ID™ Intercalator-^{103}Rh 500µM (Standard Biotools, cat 201103A) for 15 minutes at room temperature (RT) to label dead cells. Subsequently, cells were washed, incubated with 5µL of Fc block™ (BD Biosciences, cat 564219) and stained with the 39 metal-isotope tagged antibodies of the mass cytometry panel in a volume of 100µL at RT. After a 45-minute incubation, cells were washed and 1mL of 1:1000 125nM of Cell-ID™ Intercalator-Ir (Standard Biotools, cat 201192A) in fix and perm buffer (Standard Biotools, cat 201067) was added to label nucleated cells. Cells were then stored at 4°C for up to 48 hours. On the day of data acquisition, cells were washed twice in staining buffer and once in MilliQ water. Finally, pelleted cells were resuspended in MilliQ water containing 1:10 EQ Four Element Calibration Beads (Standard Biotools, cat 201078) at a concentration of 0.5-0.75·10^6 cells/mL and acquired on the Helios™ mass cytometer (Standard Biotools). At least 0.59·10^6 (median 0.88·10^6) events were measured per sample. After measurement, all mass cytometry data were normalized using the EQ bead signal and the reference EQ passport P13H2302.

Analysis of pre- and post-ATG samples

To compare the immune cell composition in bone marrow pre- and post-ATG, paired BMMC samples collected from AA^{PRE} (n=3) and AA^{POST} (n=3) were studied. First, marker distributions across all data files with single, live $CD45^+$ cells were aligned using CytoNorm[51] in R version 4.0.5 (R foundation for Statistical Computing) and the PBMC reference samples to correct for a batch effect observed in the data of all post-ATG samples (data not shown). Outputs were checked and confirmed in FlowJo. Next, $3.0 \cdot 10^6$ single, live $CD45^+$ cells were sample-tagged, hyperbolic arcsinh transformed with a cofactor of 5 and imported into Cytosplore for dimensionality reduction. A four-level HSNE analysis was performed with default perplexity and iterations (30 and 1000, respectively). Three of 39 markers in the mass cytometry panel (HLA-DR, CD20 and CD8a) did not show clear separation between positive and negative populations and thus were not used in the HSNE clustering analysis. Major immune lineages were identified at the overview level of the HSNE analysis by clustering. $CD4^+$ T-cells were defined as $CD3^+CD7^+CD4^+$ cells, $CD8^+$ T-cells were defined as $CD3^+CD7^+CD8a/b^+$ cells, B-cells were defined as $CD7^-CD20/IgM^+$ cells, non-conventional T-cells (NCTs) were defined as $CD3^+CD7^+TCR\gamma\delta^+$ cells, innate lymphoid cells (ILCs) including NK-cells were defined as $CD3^-CD7^+$ cells and HSPCs were defined as Lin^-cKit^+ cells. All remaining cell clusters were considered myeloid cells. Subsequently, each major immune lineage was selected for detailed analysis at the data level of the HSNE analysis using t-distributed stochastic neighbor embedding (tSNE) analyses with up to $0.5 \cdot 10^6$ landmarks. Clusters with distinct surface marker expression were identified within each major immune lineage by performing Gaussian mean shift (GMS) clustering at the data level in Cytosplore. Each cluster consisted of at least 1000 cells.

Supplemental tables

Supplemental table 1. 39-marker mass cytometry panel.

Metal	Marker	Clone	Vendor	Dilution
89Y	CD45	HI30	Standard Biotools	1:100
Qdot800	CD14	TuK4	Invitrogen	1:1000
115In	CD15	W6D3	BioLegend	1:50
141Pr	CCR6	G034E3	Standard Biotools	1:100
142Nd	CD34	HIB19	BioLegend	1:100
143Nd	cKit (CD117)	104D2	Standard Biotools	1:100
144Nd	CD69	FN50	Standard Biotools	1:100
145Nd	CD4	RPA-T4	Standard Biotools	1:100
146Nd	CD8a	RPA-T8	Standard Biotools	1:200
147Sm	NKp44 (CD336)	253415	R&D systems	1:40
148Nd	CD16	3G8	Standard Biotools	1:100
149Sm	CD25	2A3	Standard Biotools	1:100
150Nd	IgM	MHM88	BioLegend	1:100
151Eu	CD123	6H6	Standard Biotools	1:100
152Sm	TCRgd	11F2	Standard Biotools	1:50
153Eu	CD7	CD7-6B7	Standard Biotools	1:100
154Sm	CD163	GHI/61	Standard Biotools	1:100
155Gd	CD103	Ber-ACT8	BioLegend	1:100
156Gd	CRTH2 (CD294)	BM16	BioLegend	1:100
158Gd	CD122	TU27	BioLegend	1:50
159Tb	CCR7	G043H7	Standard Biotools	1:100
160Gd	CD5	UCHT2	BioLegend	1:50
161Dy	KLRG1	REA261	MACS	1:50
162Dy	CD11c	Bu15	Standard Biotools	1:200
163Dy	CD20	2H7	BioLegend	1:200
164Dy	CD161	HP-3G10	Standard Biotools	1:100
165Ho	CD127	AO19D5	Standard Biotools	1:200
166Er	CD8b	SIDI8BEE	eBioscience	1:50
167Er	CD27	O323	Standard Biotools	1:100
168Er	HLA-DR	L243	BioLegend	1:300
169Tm	CD45RA	HI100	Standard Biotools	1:100
170Er	CD3	UCHT1	Standard Biotools	1:100
171Yb	CD28	CD28.2	BioLegend	1:100
172Yb	CD38	HIT2	Standard Biotools	1:200
173Yb	CD45RO	UCHL1	BioLegend	1:100
174Yb	NKp46 (CD335)	9E2	BioLegend	1:40
175Lu	PD-1 (CD279)	EH 12.2H7	Standard Biotools	1:100
176Yb	CD56	NCAM16.2	Standard Biotools	1:100
209Bi	CD11b	ICRF44	Standard Biotools	1:100

CCR indicates chemokine receptor; CD: cluster of differentiation; CRTH2: Chemoattractant Receptor-Homologous molecule expressed on T-Helper Type 2 cells; HLA: Human Leukocyte Antigen; Ig: immunoglobulin; KLRG: Killer Cell Lectin-like Receptor; NKp44: Natural Killer Cell P44-related Protein; TCR: T-cell receptor; NKp46: Natural Killer Cell P46-related Protein; PD: Programmed Cell Death Protein.

Supplemental figures

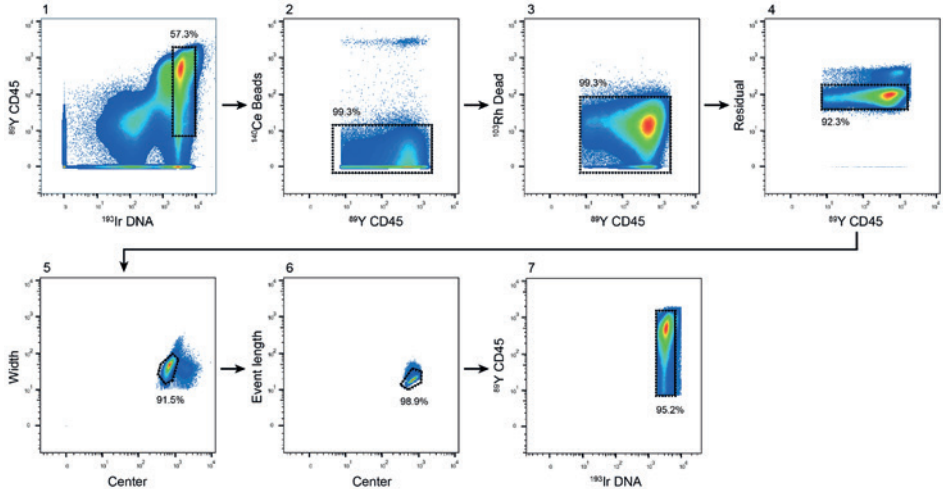


Figure S1. Mass cytometry gating strategy used to identify single, live CD45⁺ cells in bone marrow aspirates. CD45⁺ cells were first gated using CD45 and a DNA marker (panel 1). Subsequently, beads (panel 2), dead cells (panel 3) and doublets and debris (panels 4-6) were eliminated and single, live CD45⁺ cells (panel 7) were exported for analysis. The gating strategy on a representative HD bone marrow aspirate sample is shown.

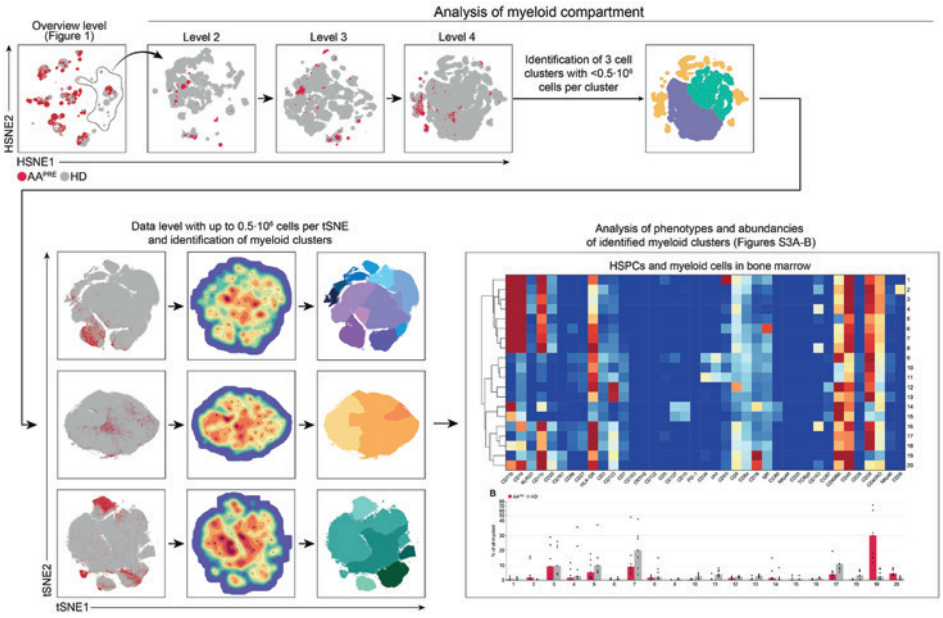


Figure S2. Approach used to analyze each major immune lineage at the immune subset level. HSPCs and myeloid cells are shown as an example. $1.3{\cdot}10^6$ HSPCs and myeloid cells isolated from bone marrow aspirates of 7 AA^{PRE} and 7 HDs were captured at the overview level of the five-level HSNE analysis (Figure 1) and visualized in more detail at levels two ($0.7{\cdot}10^5$ landmarks for $1.3{\cdot}10^6$ cells), three ($4.2{\cdot}10^5$ landmarks for $1.3{\cdot}10^6$ cells) and four ($2.4{\cdot}10^5$ landmarks for $1.3{\cdot}10^6$ cells) of the HSNE analysis. Subsequently, all HSPCs and myeloid cells were divided into three clusters of $\leq 0.5{\cdot}10^6$ cells and studied at the data level. Next, distinct HSPCs and myeloid cell clusters were classified by Gaussian mean shift (GMS) clustering in Cytosplore based on cell densities and differences in marker expression. Finally, marker expression profiles and frequencies of identified clusters were studied in R. Each cluster consisted of at least 1000 cells.

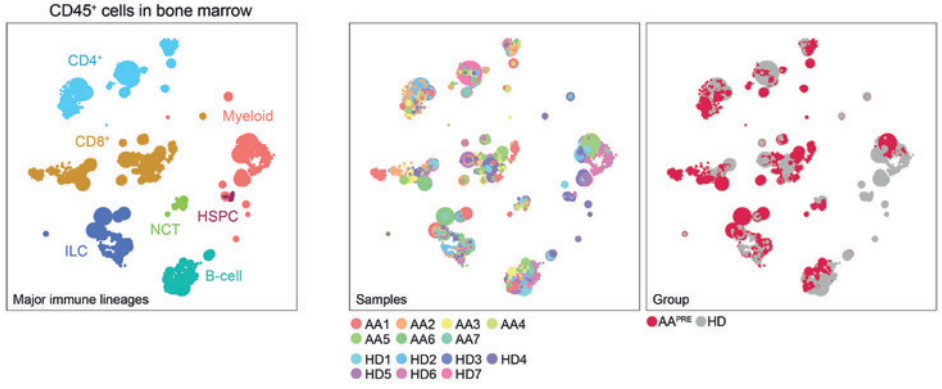
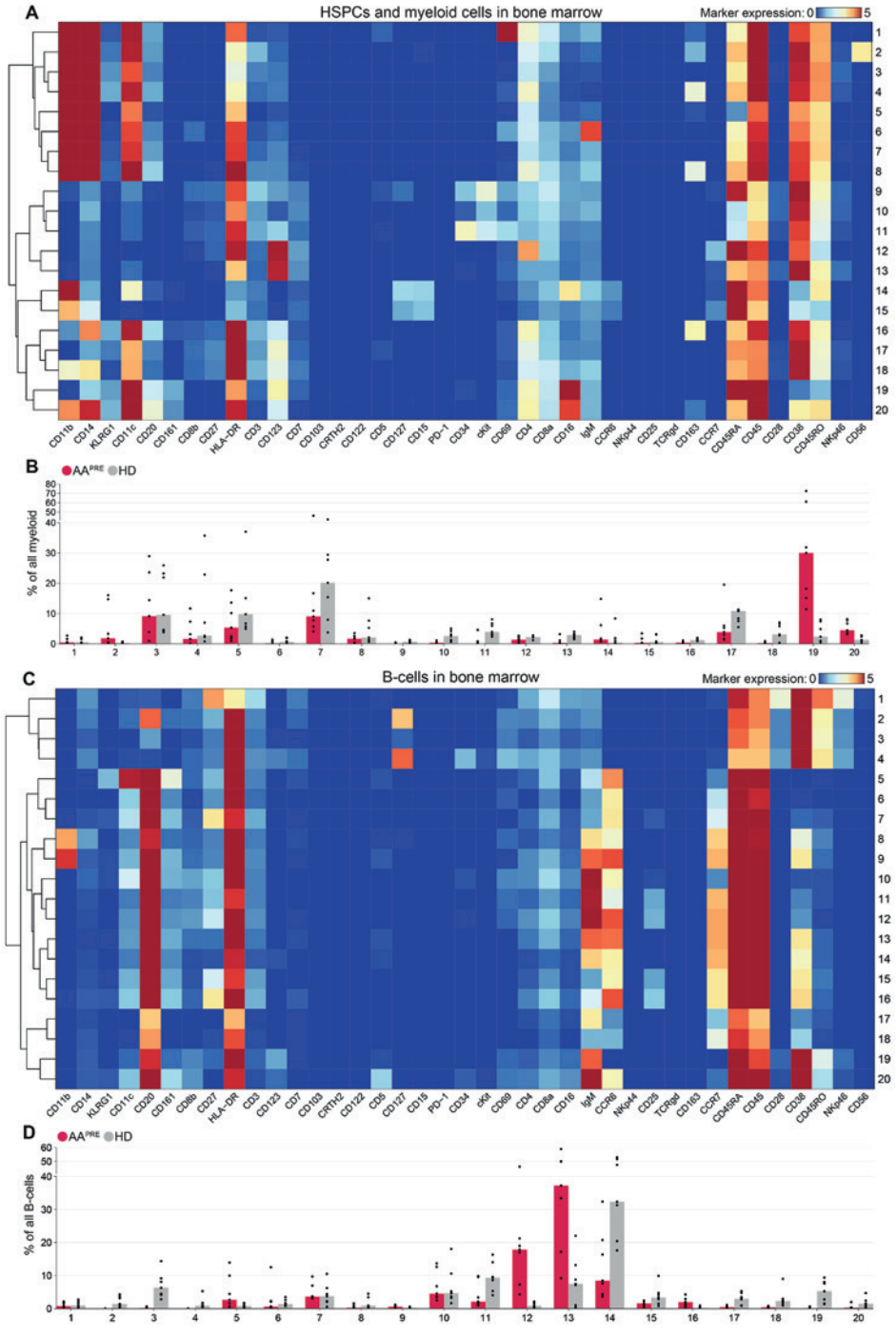
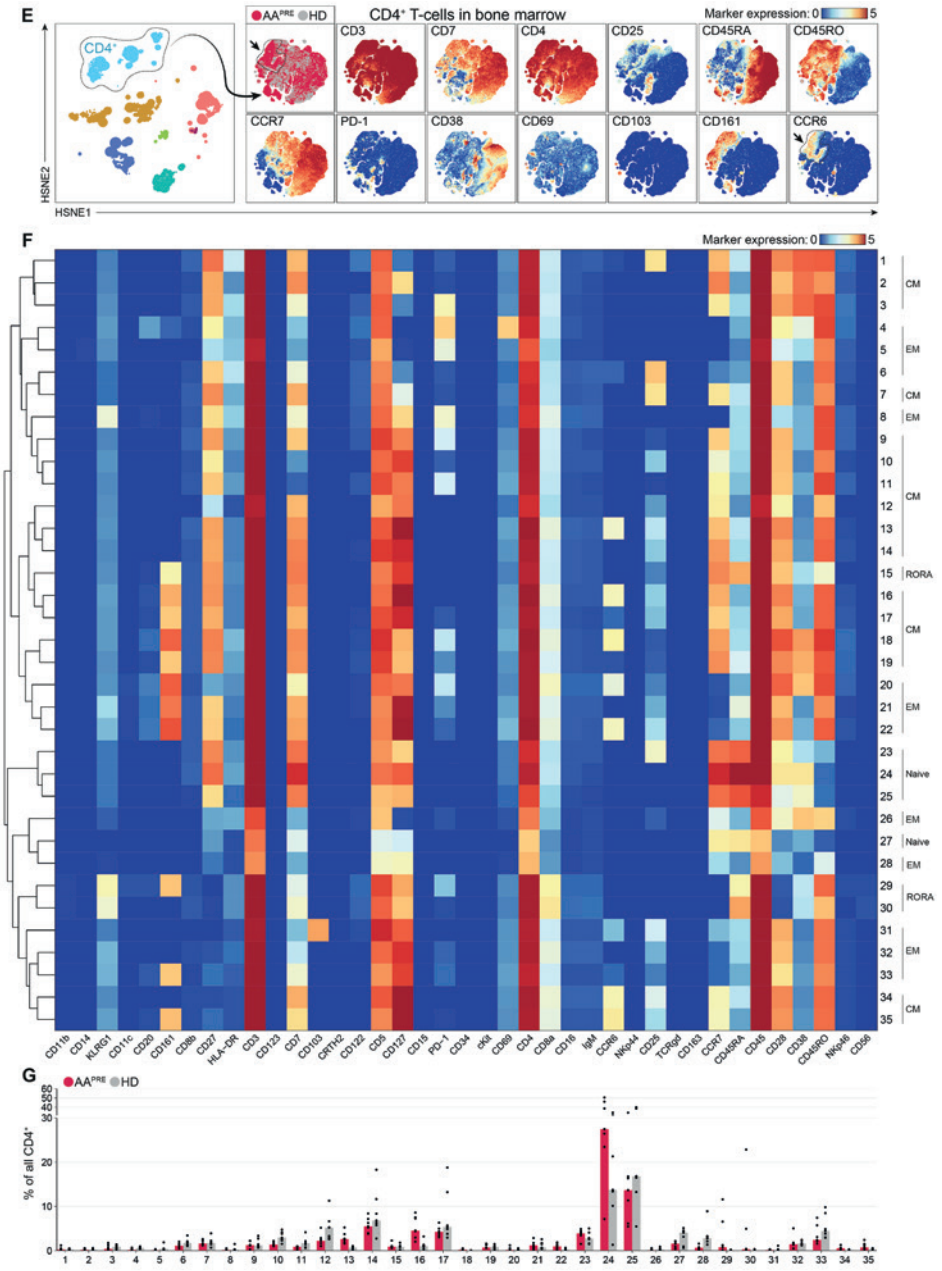
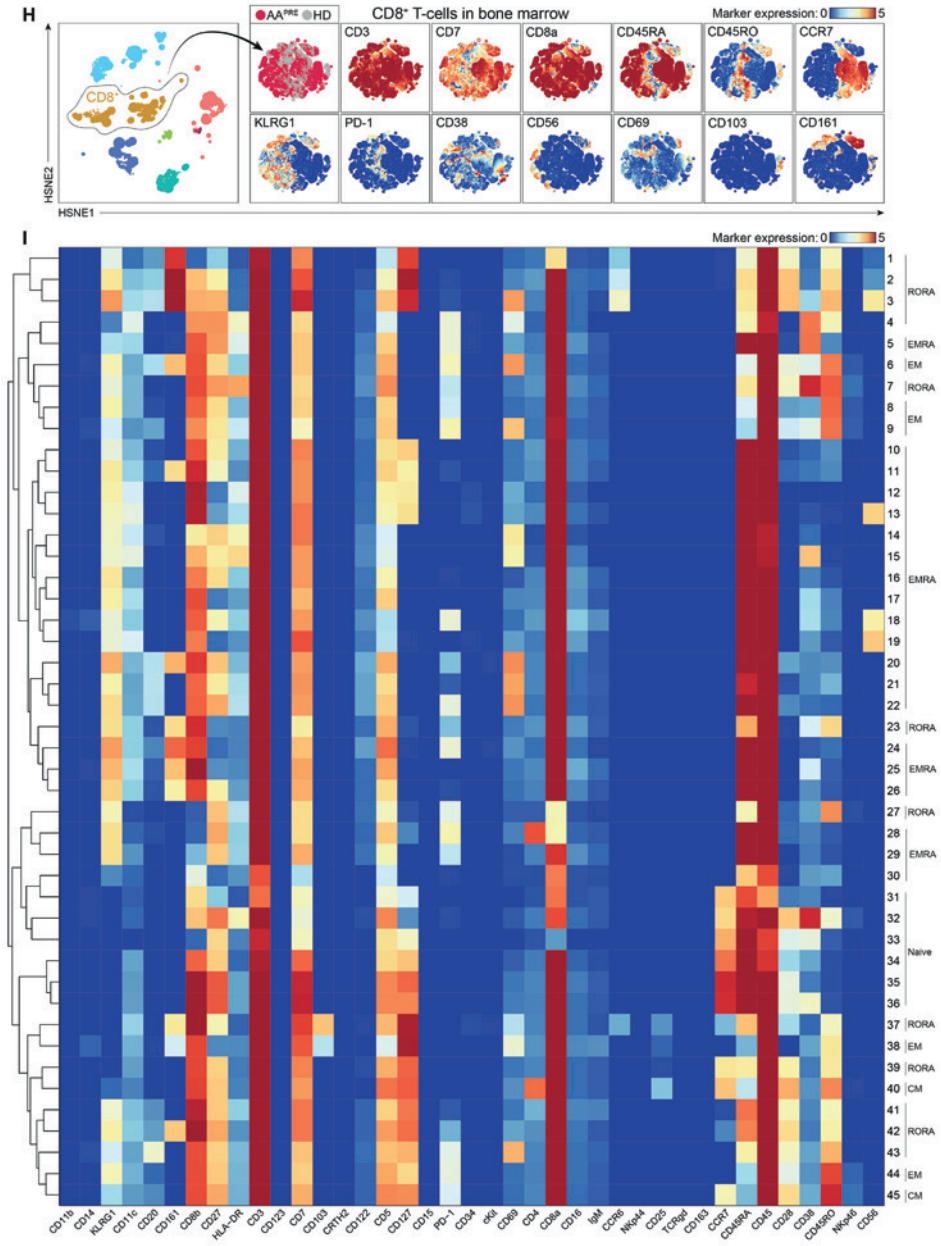


Figure S3. AA^{PRE} and HDs samples visualized at the overview level of the five-level HSNE analysis. Colors indicate major immune lineages (HSPCs, myeloid cells, B-cells, $CD4^+$ T-cells, $CD8^+$ T-cells, NCT-cells and ILCs), samples (7 AA^{PRE} and 7 HDs) or groups (AA^{PRE} in red and HDs in gray). $7.8{\cdot}10^3$ HSNE landmarks represented all $7.7{\cdot}10^6$ $CD45^+$ cells in the analysis. The size of each landmark reflects the number of cells represented by the landmark.


A
HSPCs and myeloid cells in bone marrow
Marker expression: 0 5
CD11b CD14 KLRG1 CD11c CD20 CD161 CD8b CD27 HLA-DR CD3 CD123 CD7 CD103 CRTH2 CD122 CD5 CD127 CD15 PD-1 CD34 cKit CD69 CD4 CD8a CD16 IgM CCR6 NKp44 CD25 TCRgd CD163 CCR7 CD45RA CD45 CD28 CD38 CD45RO NKp46 CD56
B
AA PRE HD
% of all myeloid
C
B-cells in bone marrow
Marker expression: 0 5
CD11b CD14 KLRG1 CD11c CD20 CD161 CD8b CD27 HLA-DR CD3 CD123 CD7 CD103 CRTH2 CD122 CD5 CD127 CD15 PD-1 CD34 cKit CD69 CD4 CD8a CD16 IgM CCR6 NKp44 CD25 TCRgd CD163 CCR7 CD45RA CD45 CD28 CD38 CD45RO NKp46 CD56
D
AA PRE HD
% of all B-cells


E
AA^PRE HD
CD4+ T-cells in bone marrow
Marker expression: 0 5
CD4+
HSNE2
HSNE1
CD3
CD7
CD4
CD25
CD45RA
CD45RO
CCR7
PD-1
CD38
CD69
CD103
CD161
CCR6
F
Marker expression: 0 5
CM
EM
CM
EM
CM
RORA
CM
EM
Naive
EM
Naive
EM
RORA
EM
CM
CD11b CD14 KLRG1 CD11c CD20 CD161 CD8b CD27 HLA-DR CD3 CD123 CD7 CD103 CRTH2 CD122 CD5 CD127 CD15 PD-1 CD34 cKit CD69 CD4 CD8a CD16 IgM CCR6 NKp44 CD25 TCRgd CD163 CCR7 CD45RA CD45 CD28 CD38 CD45RO NKp46 CD56
G
AA^PRE HD
% of all CD4+


H
AA^PRE
HD
CD8+ T-cells in bone marrow
Marker expression: 0 5
CD3
CD7
CD8a
CD45RA
CD45RO
CCR7
KLRG1
PD-1
CD38
CD56
CD69
CD103
CD161
CD8+
HSNE2
HSNE1
I
Marker expression: 0 5
RORA
EMRA
EM
RORA
EM
EMRA
RORA
EMRA
RORA
EMRA
Naive
RORA
EM
RORA
CM
RORA
EM
CM
CD11b CD14 KLRG1 CD11c CD20 CD161 CD8b CD27 HLA-DR CD3 CD123 CD7 CD103 CRTH2 CD122 CD5 CD127 CD15 PD-1 CD24 cKit CD69 CD4 CD8a CD16 IgM CCR6 NKp44 CD25 TCRgd CD163 CCR7 CD45RA CD45 CD28 CD38 CD45RO NKp46 CD56

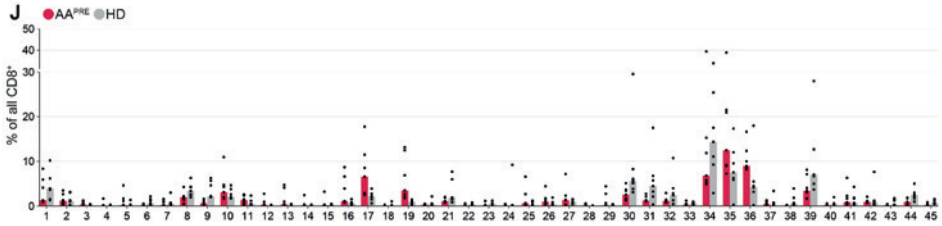


Figure S4. Overview of the myeloid cell, B-cell, CD4$^+$ T-cell and CD8$^+$ T-cell lineages. Colors indicate major immune lineages (HSPCs, myeloid cells, B-cells, CD4$^+$ T-cells, CD8$^+$ T-cells, NCT-cells and ILCs), groups (AA^{PRE} or HDs) or median arcsinh-transformed marker expression values. A, C, F, I) Phenotypes of the cell clusters identified within the myeloid, B-cell, CD4$^+$ T-cell and CD8$^+$ T-cell compartments, respectively. Heatmaps present median arcsinh-transformed marker expression values. The relationships of similarity between cell clusters are depicted by the dendrogram. B, D, G, J) Frequencies of the cell clusters identified within the myeloid cell, B-cell, CD4$^+$ T-cell and CD8$^+$ T-cell compartments, respectively. Frequencies are presented per group and are shown as a percentage of all cells within a lineage. E, H) CD4$^+$ T-cells and CD8$^+$ T-cells isolated from bone marrow of 7 AA^{PRE} and 7 HDs, visualized at level four of a five-level HSNE analysis. HSNEs depict $3.4{\cdot}10^5$ landmarks for $1.9{\cdot}10^6$ CD4$^+$ T-cells and $3.9{\cdot}10^5$ landmarks for $2.1{\cdot}10^6$ CD8$^+$ T-cells. The size of each landmark reflects the number of cells represented by the landmark. Arrows in (E) indicate CCR6$^+$ CM and EM CD4$^+$ T-cells. RORA: T-cells co-expressing CD45RA and CD45RO.

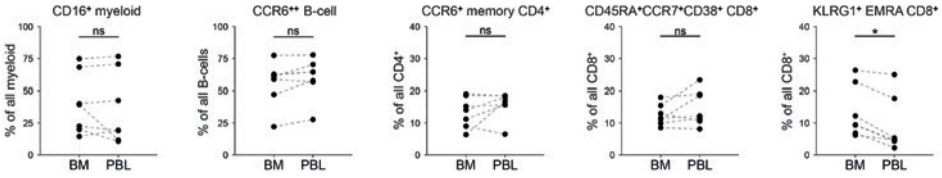


Figure S5. Disease-specific immune cell network can be detected in peripheral blood. Frequencies of the five cell clusters within the identified disease-specific immune cell network, shown in bone marrow and peripheral blood. Paired bone marrow and peripheral blood samples from AA^{PRE} are connected by a dotted line. Bone marrow and peripheral blood samples were compared in an independent analysis to avoid an influence of peripheral blood cells on clustering of bone marrow cells from AA^{PRE} and HDs. Therefore, small differences in cell percentages may be observed between the data presented here and in Figures 2, 3, 4 and 5. The paired bone marrow and peripheral blood samples were compared in a five-level HSNE analysis with default perplexity and iterations (30 and 1000, respectively) and a total of $11.5{\cdot}10^6$ single, live CD45$^+$ cells (bone marrow samples from AA^{PRE} and HDs, and peripheral blood samples from AA^{PRE} only). Three of 39 markers in the mass cytometry panel (HLA-DR, CD5 and KLRG1) were not used to generate the HSNE due to small variations in marker distribution between experiments. Major immune lineages were identified at the overview level of the HSNE analysis by clustering based on the phenotypes described in the methods. Subsequently, each major immune lineage was selected for detailed analysis at the data level using tSNE analyses with up to $0.5{\cdot}10^6$ landmarks. Immune cells that matched the phenotypes of the CD16$^+$ myeloid cells, CCR6^{++} B-cells, CCR6$^+$ memory CD4$^+$ T-cells and CD45RA$^+$CCR7$^+$CD38$^+$ CD8$^+$ T-cells and KLRG1$^+$EMRA CD8$^+$ T-cells that were significantly elevated in AA^{PRE} were captured in Cytosplore. Subsequently, their total frequencies were compared between bone marrow and peripheral blood for each individual patient.

References

1. Young NS. Aplastic Anemia. *N Engl J Med*. 2018;379(17):1643-1656.
2. Killick SB, Bown N, Cavenagh J, et al. Guidelines for the diagnosis and management of adult aplastic anaemia. *Br J Haematol*. 2016;172(2):187-207.
3. Tjon JM-L, Zeerleder SS, Groot MRd, et al. Diagnostiek en behandeling verworven aplastische anemie bij volwassenen. *Nederlandse Vereniging voor Hematologie*. 2019.
4. Bacigalupo A, Giammarco S, Sica S. Bone marrow transplantation versus immunosuppressive therapy in patients with acquired severe aplastic anemia. *Int J Hematol*. 2016;104(2):168-174.
5. Halkes CJ, Veelken H, Falkenburg JH. Horse versus rabbit antithymocyte globulin in aplastic anemia. *N Engl J Med*. 2011;365(19):1842-1843; author reply 1843-1844.
6. Scheinberg P, Nunez O, Weinstein B, et al. Horse versus rabbit antithymocyte globulin in acquired aplastic anemia. *N Engl J Med*. 2011;365(5):430-438.
7. Young NS. Pathophysiologic mechanisms in acquired aplastic anemia. *Hematology Am Soc Hematol Educ Program*. 2006:72-77.
8. Kordasti S, Marsh J, Al-Khan S, et al. Functional characterization of CD4+ T cells in aplastic anemia. *Blood*. 2012;119(9):2033-2043.
9. Kordasti S, Costantini B, Seidl T, et al. Deep phenotyping of Tregs identifies an immune signature for idiopathic aplastic anemia and predicts response to treatment. *Blood*. 2016;128(9):1193-1205.
10. Zaimoku Y, Patel BA, Kajigaya S, et al. Deficit of circulating CD19(+) CD24(hi) CD38(hi) regulatory B cells in severe aplastic anaemia. *Br J Haematol*. 2020;190(4):610-617.
11. Bandura DR, Baranov VI, Ornatsky OI, et al. Mass cytometry: technique for real time single cell multitarget immunoassay based on inductively coupled plasma time-of-flight mass spectrometry. *Anal Chem*. 2009;81(16):6813-6822.
12. Li N, van Unen V, Hollt T, et al. Mass cytometry reveals innate lymphoid cell differentiation pathways in the human fetal intestine. *J Exp Med*. 2018;215(5):1383-1396.
13. van der Zwan A, van Unen V, Beyrend G, et al. Visualizing Dynamic Changes at the Maternal-Fetal Interface Throughout Human Pregnancy by Mass Cytometry. *Front Immunol*. 2020;11:571300.
14. van Unen V, Li N, Molendijk I, et al. Mass Cytometry of the Human Mucosal Immune System Identifies Tissue- and Disease-Associated Immune Subsets. *Immunity*. 2016;44(5):1227-1239.
15. Hollt T, Pezzotti N, van Unen V, et al. Cytosplore: Interactive Immune Cell Phenotyping for Large Single-Cell Datasets. *Computer Graphics Forum*. 2016;35(3):171-180.
16. Beyrend G, Stam K, Hollt T, Ossendorp F, Arens R. Cytofast: A workflow for visual and quantitative analysis of flow and mass cytometry data to discover immune signatures and correlations. *Comput Struct Biotechnol J*. 2018;16:435-442.
17. Kassambara A, Mundt F. factoextra: Extract and Visualize the Results of Multivariate Data Analyses. *Version 107*. 2020:CRAN.R-project.org/package=factoextra.
18. Taiyun Wei, Simko V. R package 'corrplot': Visualization of a Correlation Matrix (Version 0.92). 2021.
19. Ryan DH, Nuccie BL, Ritterman I, Liesveld JL, Abboud CN, Insel RA. Expression of interleukin-7 receptor by lineage-negative human bone marrow progenitors with enhanced lymphoid proliferative potential and B-lineage differentiation capacity. *Blood*. 1997;89(3):929-940.

20. Uhlen M, Karlsson MJ, Zhong W, et al. A genome-wide transcriptomic analysis of protein-coding genes in human blood cells. *Science*. 2019;366(6472).

21. Suan D, Krautler NJ, Maag JLV, et al. CCR6 Defines Memory B Cell Precursors in Mouse and Human Germinal Centers, Revealing Light-Zone Location and Predominant Low Antigen Affinity. *Immunity*. 2017;47(6):1142-1153 e1144.

22. Grimsholm O, Piano Mortari E, Davydov AN, et al. The Interplay between CD27(dull) and CD27(bright) B Cells Ensures the Flexibility, Stability, and Resilience of Human B Cell Memory. *Cell Rep*. 2020;30(9):2963-2977 e2966.

23. Agematsu K, Hokibara S, Nagumo H, Komiyama A. CD27: a memory B-cell marker. *Immunol Today*. 2000;21(5):204-206.

24. Sims GP, Ettinger R, Shirota Y, Yarboro CH, Illei GG, Lipsky PE. Identification and characterization of circulating human transitional B cells. *Blood*. 2005;105(11):4390-4398.

25. Annunziato F, Cosmi L, Santarlasci V, et al. Phenotypic and functional features of human Th17 cells. *J Exp Med*. 2007;204(8):1849-1861.

26. Herndler-Brandstetter D, Ishigame H, Shinnakasu R, et al. KLRG1(+) Effector CD8(+) T Cells Lose KLRG1, Differentiate into All Memory T Cell Lineages, and Convey Enhanced Protective Immunity. *Immunity*. 2018;48(4):716-729 e718.

27. Greenberg SA, Pinkus JL, Kong SW, Baecher-Allan C, Amato AA, Dorfman DM. Highly differentiated cytotoxic T cells in inclusion body myositis. *Brain*. 2019;142(9):2590-2604.

28. Li Y, Li B, You Z, et al. Cytotoxic KLRG1 expressing lymphocytes invade portal tracts in primary biliary cholangitis. *J Autoimmun*. 2019;103:102293.

29. Ibegbu CC, Xu YX, Harris W, Maggio D, Miller JD, Kourtis AP. Expression of killer cell lectin-like receptor G1 on antigen-specific human CD8+ T lymphocytes during active, latent, and resolved infection and its relation with CD57. *J Immunol*. 2005;174(10):6088-6094.

30. Kook H, Zeng W, Guibin C, Kirby M, Young NS, Maciejewski JP. Increased cytotoxic T cells with effector phenotype in aplastic anemia and myelodysplasia. *Exp Hematol*. 2001;29(11):1270-1277.

31. Giudice V, Feng X, Lin Z, et al. Deep sequencing and flow cytometric characterization of expanded effector memory CD8(+)CD57(+) T cells frequently reveals T-cell receptor Vbeta oligoclonality and CDR3 homology in acquired aplastic anemia. *Haematologica*. 2018;103(5):759-769.

32. de Latour RP, Visconte V, Takaku T, et al. Th17 immune responses contribute to the pathophysiology of aplastic anemia. *Blood*. 2010;116(20):4175-4184.

33. Lee AYS, Bannan JL, Adams MJ, Korner H. Expression of CCR6 on B cells in systemic lupus erythematosus patients. *Clin Rheumatol*. 2017;36(6):1453-1456.

34. Ito T, Carson WFt, Cavassani KA, Connett JM, Kunkel SL. CCR6 as a mediator of immunity in the lung and gut. *Exp Cell Res*. 2011;317(5):613-619.

35. Ge M, Zheng Y, Li X, et al. Differential expression profile of Th1/Th17/Th2-related chemokines and their receptors in patients with acquired bone marrow failure syndromes. *Hum Immunol*. 2013;74(2):176-180.

36. Meitei HT, Jadhav N, Lal G. CCR6-CCL20 axis as a therapeutic target for autoimmune diseases. *Autoimmun Rev*. 2021;20(7):102846.

37. Ruth JH, Shahrara S, Park CC, et al. Role of macrophage inflammatory protein-3alpha and its ligand CCR6 in rheumatoid arthritis. *Lab Invest*. 2003;83(4):579-588.

38. Hosokawa K, Muranski P, Feng X, et al. Memory Stem T Cells in Autoimmune Disease: High Frequency of Circulating CD8+ Memory Stem Cells in Acquired Aplastic Anemia. *J Immunol*. 2016;196(4):1568-1578.

39. Gattinoni L, Lugli E, Ji Y, et al. A human memory T cell subset with stem cell-like properties. *Nat Med*. 2011;17(10):1290-1297.

40. Sun W, Wu Z, Lin Z, et al. Macrophage TNF-alpha licenses donor T cells in murine bone marrow failure and can be implicated in human aplastic anemia. *Blood*. 2018;132(26):2730-2743.

41. Mukherjee R, Kanti Barman P, Kumar Thatoi P, Tripathy R, Kumar Das B, Ravindran B. Non-Classical monocytes display inflammatory features: Validation in Sepsis and Systemic Lupus Erythematous. *Sci Rep*. 2015;5:13886.

42. Rossol M, Kraus S, Pierer M, Baerwald C, Wagner U. The CD14(bright) CD16+ monocyte subset is expanded in rheumatoid arthritis and promotes expansion of the Th17 cell population. *Arthritis Rheum*. 2012;64(3):671-677.

43. Narasimhan PB, Marcovecchio P, Hamers AAJ, Hedrick CC. Nonclassical Monocytes in Health and Disease. *Annu Rev Immunol*. 2019;37:439-456.

44. Hannam-Harris AC, Taylor DS, Nowell PC. Cyclosporin A directly inhibits human B-cell proliferation by more than a single mechanism. *J Leukoc Biol*. 1985;38(2):231-239.

45. Jenkins MK, Schwartz RH, Pardoll DM. Effects of cyclosporine A on T cell development and clonal deletion. *Science*. 1988;241(4873):1655-1658.

46. Bouma G, Zamuner S, Hicks K, et al. CCL20 neutralization by a monoclonal antibody in healthy subjects selectively inhibits recruitment of CCR6(+) cells in an experimental suction blister. *Br J Clin Pharmacol*. 2017;83(9):1976-1990.

47. Getschman AE, Imai Y, Larsen O, et al. Protein engineering of the chemokine CCL20 prevents psoriasiform dermatitis in an IL-23-dependent murine model. *Proc Natl Acad Sci U S A*. 2017;114(47):12460-12465.

48. Robert R, Juglair L, Lim EX, et al. A fully humanized IgG-like bispecific antibody for effective dual targeting of CXCR3 and CCR6. *PLoS One*. 2017;12(9):e0184278.

49. Tawaraishi T, Sakauchi N, Hidaka K, et al. Identification of a novel series of potent and selective CCR6 inhibitors as biological probes. *Bioorg Med Chem Lett*. 2018;28(18):3067-3072.

50. Bendall SC, Simonds EF, Qiu P, et al. Single-cell mass cytometry of differential immune and drug responses across a human hematopoietic continuum. *Science*. 2011;332(6030):687-696.

51. Van Gassen S, Gaudilliere B, Angst MS, Saeys Y, Aghaeepour N. CytoNorm: A Normalization Algorithm for Cytometry Data. *Cytometry A*. 2020;97(3):268-278.





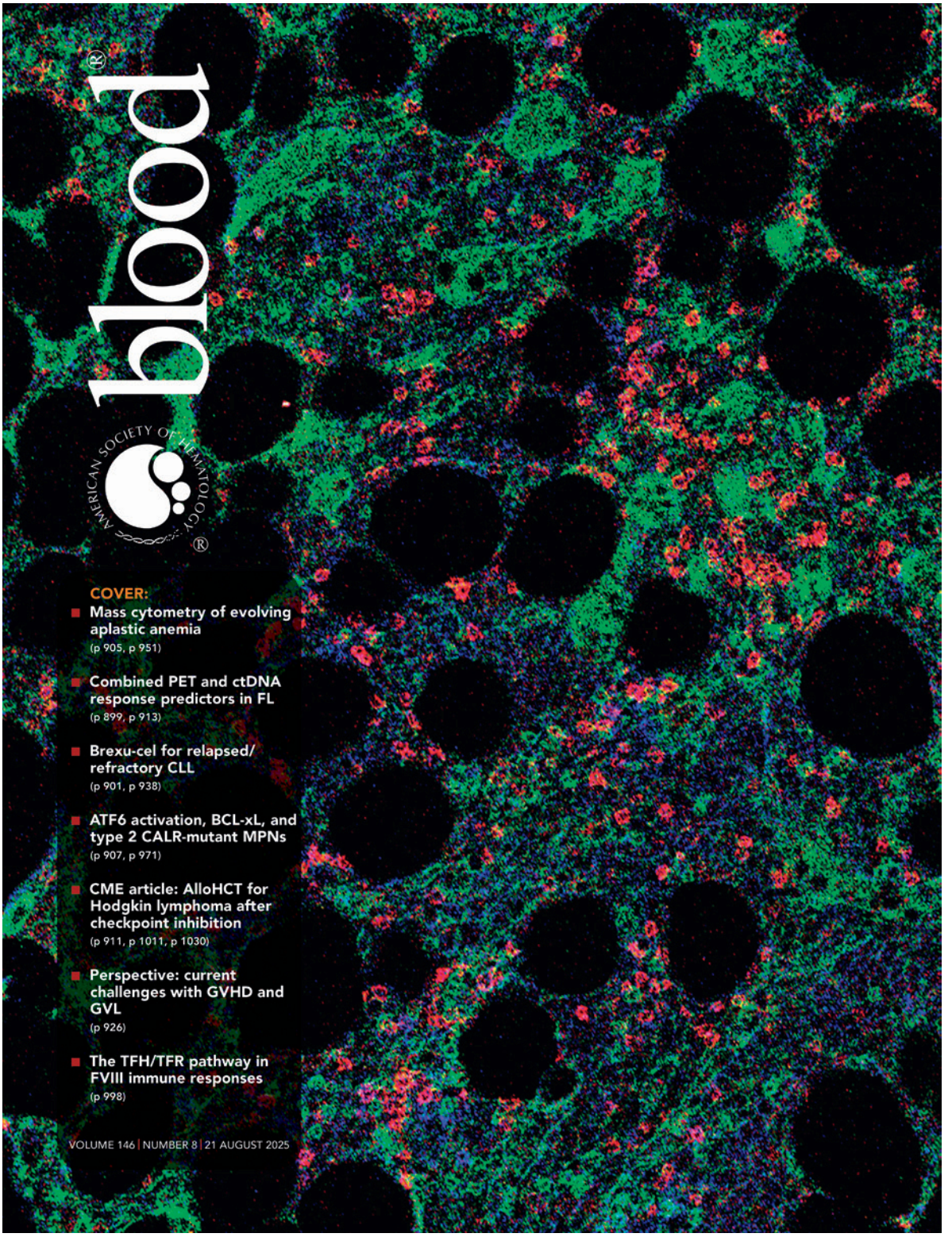
3

Imaging mass cytometry reveals the order of events in the pathogenesis of immune-mediated aplastic anemia

Emma S. Pool[1], Sietse J. Luk[1], Marieke E. IJsselsteijn[2], Vincent van Unen[3], Noel F.C.C. de Miranda[2], J.H. Frederik Falkenburg[1], Frits Koning[3], Mirjam H.M. Heemskerk[1] and Jennifer M-L. Tjon[1]

[1] Department of Hematology, Leiden University Medical Center, Leiden, The Netherlands
[2] Department of Pathology, Leiden University Medical Center, Leiden, The Netherlands
[3] Department of Immunology, Leiden University Medical Center, Leiden, The Netherlands

Blood (2025)
DOI: 10.1182/blood.2025028723



COVER:

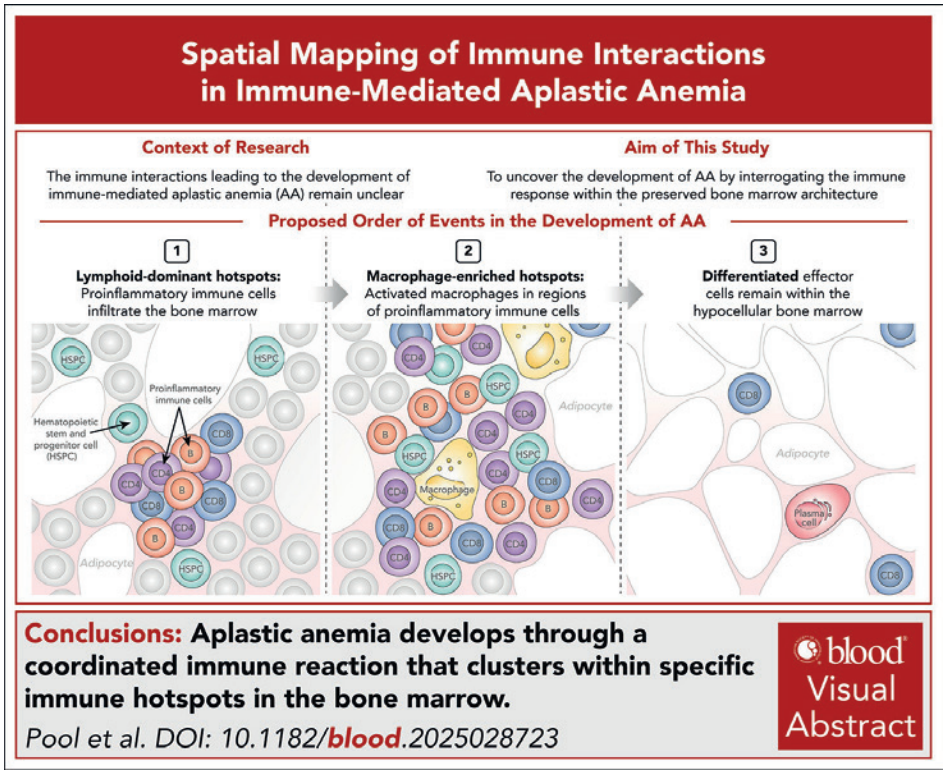
- **Mass cytometry of evolving aplastic anemia**
  (p 905, p 951)
- **Combined PET and ctDNA response predictors in FL**
  (p 899, p 913)
- **Brexu-cel for relapsed/refractory CLL**
  (p 901, p 938)
- **ATF6 activation, BCL-xL, and type 2 CALR-mutant MPNs**
  (p 907, p 971)
- **CME article: AlloHCT for Hodgkin lymphoma after checkpoint inhibition**
  (p 911, p 1011, p 1030)
- **Perspective: current challenges with GVHD and GVL**
  (p 926)
- **The TFH/TFR pathway in FVIII immune responses**
  (p 998)

VOLUME 146 | NUMBER 8 | 21 AUGUST 2025

Key points

- Development of AA is the result of a coordinated immune reaction that concentrates within immune hot spots in the bone marrow.
- During bone marrow destruction, the immune response gradually shifts from an activated to a more differentiated phenotype.

Visual abstract



Abstract

The autoimmune response driving hematopoietic stem and progenitor cell (HSPC) destruction in immune-mediated aplastic anemia (AA) remains incompletely understood. We previously identified a disease-specific immune cell network involving T-, B-, and myeloid cells. However, the interactions within this network, the interaction with the microenvironment and the chronological events in AA development, remain unclear. In this study, we aimed to characterize the changes occurring during disease development and to define the interactions between potential autoreactive cells and their target. Using imaging mass cytometry, we analyzed bone marrow biopsies from AA patients at diagnosis and after treatment with horse-derived anti-thymocyte globulin (hATG), and six controls. Within the hypocellular bone marrow architecture, we identified lymphoid-dominant 'immune hot spots' with high densities of pro-inflammatory lymphocytes, and macrophage-enriched hot spots that additionally contained activated macrophages in proximity to progenitors. These immune hot spots potentially represent sites where the active immune response resulting in HSPC destruction takes place. In bone marrow regions depleted of progenitors, effector cells with a differentiated phenotype remain. Our data indicate that HSPC destruction in AA is mediated by coordinated interactions among specific immune cell subpopulations. As the immune response progresses and HSPCs are depleted, the immune composition shifts, with activated T- and B-cells differentiating into terminally differentiated T-cells and plasma cells. In patients with normalizing bone marrow post-hATG treatment, most immune hot spots were depleted, underscoring their potential pathogenic role. Collectively, our study visualizes the complex interactions among immune cell subpopulations and, for the first time, reveals the order of events in the immune-mediated pathogenesis of AA.

Introduction

Immune-mediated acquired aplastic anemia (AA) is characterized by bone marrow hypocellularity due to a loss of hematopoietic stem and progenitor cells (HSPCs), leading to pancytopenia and life-threatening bleeding and infectious complications[1]. Immunosuppressive therapy (IST) with horse-derived anti-thymocyte globulin (hATG) and long-term ciclosporin results in gradual improvement of peripheral blood counts within 6 months in approximately 70% of patients[2-4]. Response rates to IST can be increased by adding eltrombopag to first-line IST[5] or as second-line treatment 6 months after start of IST. However, hematological recovery is partial in most patients, with few reaching complete normalization of blood counts. One-third of patients do not respond to IST and face prolonged pancytopenia with the accompanying risk of bleeding and infections[4].

Better understanding of the pathogenesis of AA may lead to improved therapeutic strategies by identifying new treatment targets. Previously, by analyzing bone marrow aspirates from AA patients using mass cytometry, we identified an AA-specific immune cell network, containing $CCR6^{++}$ B-cells, Th17-like $CCR6^{+}$ memory $CD4^{+}$ T-cells, and $KLRG1^{+}$ terminally differentiated $CD8^{+}$ T-cells[6]. This provided strong evidence that AA results from immune-mediated HSPC destruction involving specific immune cells associated with inflammation. These subpopulations were significantly increased in AA patients at diagnosis compared to healthy donors, and showed a trend toward normalization after successful IST. Additionally, we observed $CD163^{+}$ macrophages in the bone marrow at diagnosis, despite depletion of the myeloid compartment, suggesting macrophage recruitment to clear apoptotic cells.

Although our previous work provides a strong indication of the cells involved, the precise interactions of these cells and their microenvironment cannot be deduced from studying bone marrow aspirates. Previous research demonstrated that bone marrow biopsies offer the unique possibility to analyze spatial cellular interactions in AA while overcoming issues of selective cell loss generally observed with bone marrow aspirates[7]. In this study, we aimed to define the interactions between potential autoreactive cells and their cellular target, and to reveal the order of events in AA development. To achieve this, we studied the spatial orientation of the immune response within its native microenvironment in bone marrow biopsies from AA patients at diagnosis (AA^{Dx}) and 6 months post-hATG (AA^{6M}) using imaging mass cytometry (IMC). Our study provides unique insight into the spatial biology of the bone marrow in AA. We confirmed the presence of the previously identified immune cell network *in situ*. Importantly, we identified immune 'hot spots' within the hypocellular bone marrow, where cells from the immune cell network and other activated immune cells colocalize with remaining progenitor cells. In bone marrow regions depleted of progenitors, these immune

hot spots are nearly absent and more differentiated cells remain. Collectively, our study sheds light on the possible chronological order of events in the pathogenesis of AA.

Methods

Patients and bone marrow biopsies

Bone marrow biopsies were collected from 16 AA patients at diagnosis (AA^{Dx}), with paired biopsies available for 12 of 16 patients 6 months after start of first-line IST (AA^{6M}) (Table 1, S1). As a proxy for normal bone marrow, bone marrow biopsies were collected from six age-, sex-, CMV- and EBV status-matched diffuse large B-cell lymphoma patients without bone marrow localization. Bone marrow collection was performed after given informed consent. All patients were treatment-naïve at diagnosis, did not have an additional underlying disease and were diagnosed and treated according to standard Dutch guidelines[8]. Patients <40 years were screened for Fanconi anemia to rule out a congenital form of bone marrow failure. IST consisted of 4 days of 40 mg/kg/day ATGAM® (hATG; Pfizer) and 5 mg/kg/day ciclosporin for ≥6 months. All biopsies collected 6M post-hATG were taken before the start of eltrombopag. This study was approved by the Medical Ethical Committee of the Leiden University Medical Center (protocol B20.037).

Table 1. Characteristics of patients and response to IST.

Characteristic	Dx	6M post-hATG	Controls
Patients (n)	16	12	6
Age (median, range in years)*	42 (23-79)	53 (24-79)	54 (44-83)
Sex (n, M:F)	9:7	6:6	5:1
Severity of disease at diagnosis (n)			
Non-severe AA	2	-	NA
Severe AA	8	7	NA
Very severe AA	6	5	NA
Response to IST (n)#			
≤ 6 months post-hATG	8	5	NA
≥ 6 months post-hATG	5	5	NA
Non-responder to IST	3	2	NA

AA indicates aplastic anemia; hATG: horse-derived anti-thymocyte globulin; F: female; M: male; NA: not applicable. *: at diagnosis. #: response to IST was defined as transfusion independence and a neutrophil count of $\geq 0.5 \cdot 10^9$ neutrophils/L. Response to IST ≥ 6 months post-hATG occurred either spontaneously or after eltrombopag (Revolade®, Novartis).

Acquisition and analysis of imaging mass cytometry images

Bone marrow tissue sections were stained with 37 metal isotope-tagged antibodies to detect both hematopoietic cells and non-hematopoietic cells of the bone marrow microenvironment (Table S2). For panel development and staining details, see supplementary methods[9-14]. High-dimensional images with 1 μm^2 resolution were acquired on the Hyperion™ Imaging

System (Standard BioTools) by laser-ablation at 200Hz. Data inspection showed clear cellular staining in bone marrow and control tonsil (Figures S1-2).

Bone marrow images were analyzed by quantifying tissue surface areas, cell segmentation and downstream clustering analyses[15-20]. Detailed description is provided in the supplementary methods and is visualized in Figures S3-6.

Statistical analyses

Dunn's tests performed in R v4.3.0 were used for comparisons between groups, with *P*-values ≤0.05 considered statistically significant. Since this was an exploratory study, no adjustments for multiple testing were applied. *$P \leq 0.05$; **$P \leq 0.01$; ***$P \leq 0.001$; ****$P \leq 0.0001$.

Results

Bone marrow from AA patients at diagnosis features Ki-67$^+$ regions with activated macrophages

The immune response in AA was studied using IMC (Figure 1A). Bone marrow biopsies from 16 AA patients at diagnosis (AA^{Dx}), 12 paired AA patients 6M post-hATG (AA^{6M}) and six age-matched controls were stained with a 37-marker IMC panel and imaged. 79 regions of interest (ROIs; 2-3 per biopsy; median 1.5mm^2) were acquired across all sections.

AA is characterized by bone marrow hypocellularity at diagnosis, which can improve after IST (Figure 1B, upper row; 1C). The extent of hypocellularity varied between patients, suggesting the bone marrow was captured at different stages of bone marrow destruction. In line with previous observations[21], the cellularity of the bone marrow did not significantly differ between disease severities (non-severe, severe and very severe AA median 1236, 1216 and 1010 cells/mm^2 respectively, Figure 1C; global bone marrow structure per patient in Figure S7). To enable quantitative comparisons between samples, we determined the surface areas of three major compartments in the bone marrow: 1) the hematopoietic compartment containing hematopoietic cells and their microenvironment, 2) adipocytes, and 3) bone (Figure 1B, lower row). The area of the hematopoietic compartment was determined based on pixels positive for DNA (nuclei), Vimentin (cytoplasm, cell membrane, microenvironment) and/or CD31 (cytoplasm of Vimentin$^-$ CD31$^+$ megakaryocytes) using Cytosplore[18] Imaging (Figure S3). For the surface areas of bone and adipocytes, areas of CollagenI$^+$ bone trabeculae and remaining surface areas (adipocytes) were quantified in ImageJ. Consistent with the observed bone marrow hypocellularity, the hematopoietic compartment was significantly decreased and replaced by adipocytes at diagnosis, while bone area was not affected (Figure 1D). 6M post-hATG, the area of the hematopoietic compartment increased in most patients, reflecting bone marrow recovery (Figure 1D).

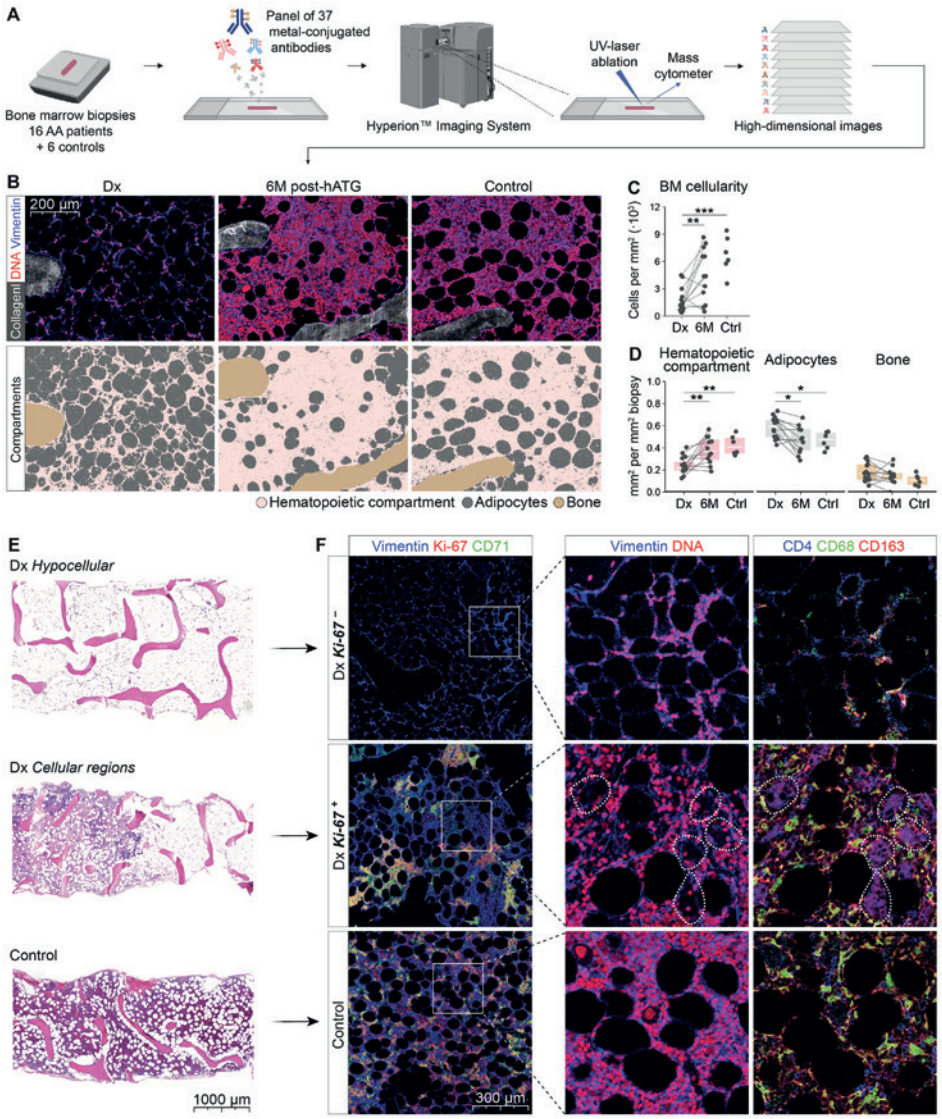


Figure 1. Histology of the bone marrow from AA patients and controls. [A] Experimental approach. Tissue sections of FFPE EDTA-decalcified bone marrow biopsies were cut, stained with a 37-marker IMC panel and measured on the Hyperion Imaging System, resulting in a dataset of 79 high-dimensional images. [B] Top row: global histology of the bone marrow, visualized for a representative AA^{Dx}, AA^{6M} and control ROI. CollagenI (white) stains bone, Vimentin (blue) stains all hematopoietic cells and their microenvironment and DNA (red) stains all cellular nuclei. Bottom row: Defined tissue compartments visualized within the representative images: hematopoietic compartment (pink), adipocytes (gray) and bone (tan). [C] Bone marrow cellularity, quantified as the total number of cells per mm^2 of bone marrow biopsy. [D] Surface areas of the three compartments in AA^{Dx}, AA^{6M} and controls. [E] H&E stainings of 1) a representative completely hypocellular bone marrow biopsy lacking expression of Ki-67 at diagnosis, 2) a bone marrow biopsies containing cellular regions with islands of $Ki\text{-}67^+$ progenitor cells at diagnosis and 3) a control bone marrow biopsy. [F] IMC images for a $Ki\text{-}67^-$ region from a representative AA^{Dx}, a $Ki\text{-}67^+$ region from a representative AA^{Dx} and a control ROI. Single cells, hematopoietic progenitor cells and tissue structure are visualized using DNA, CD71 and Ki-67, and Vimentin. Macrophages are visualized using the markers CD4, CD68 and CD163. Box plots present the median with the interquartile range (IQR), error bars present 1.5*IQR.

To capture the immune response, we assessed the hematopoietic compartment of all AA^{Dx} biopsies. The proliferation marker Ki-67 was used to detect sites of active hematopoiesis. This distinguished bone marrow regions in which all Ki-67$^+$ progenitors were cleared (Ki-67$^-$ regions) and regions that still contained pockets of hematopoiesis, including CD71$^+$Ki-67$^+$ erythroid precursors (Ki-67$^+$ regions) (Figure 1E-F). Importantly, Ki-67$^+$ and Ki-67$^-$ bone marrow regions co-existed within bone marrow biopsies from several AA^{Dx}. Comparison of Ki-67$^-$ and Ki-67$^+$ regions from AA^{Dx} with control bone marrow revealed the presence of CD68$^+$CD163$^+$ macrophages in Ki-67$^+$ regions from AA^{Dx} and controls, but not in Ki-67$^-$ regions (Figure 1F, yellow cells). Strikingly, activated and enlarged CD68$^-$CD163$^+$CD4$^+$ macrophages were exclusively found in Ki-67$^+$ regions from AA^{Dx}, where they surrounded sites of active hematopoiesis (Figure 1F, purple cells within white circles). Notably, these macrophages were engulfing hematopoietic cells including a mixture of CD7$^+$ T-cells and innate lymphoid cells, CD20$^+$ B-cells, CD14$^+$ monocytes and CD71$^+$Ki-67$^+$ erythroid precursors, as illustrated in Figure S8.

These data show that the differences in bone marrow cellularity between AA^{Dx} stem from the presence of Ki-67$^+$ regions that still contain hematopoietic progenitors. Importantly, in AA^{Dx}, only these Ki-67$^+$ regions contain enlarged, activated macrophages, suggesting the active immune response resulting in AA occurs in these regions.

Lymphoid cells predominate in the bone marrow from AA patients at diagnosis

To perform detailed analyses of the hematopoietic compartment in AA^{Dx} at the single-cell level, cell segmentation was applied to all ROIs (Figure S4). This generated a dataset of $0.5 \cdot 10^6$ cells with the spatial localization and the marker expression profile for each segmented cell. A median of 4,137 cells (range 2,028-19,622) were segmented for each AA^{Dx}, compared to a median of 12,913 cells (range 1,212-37,336) for each AA^{6M} and a median of 29,523 cells (range 11,094-54,334) for each control.

All segmented cells were visualized in an optSNE analysis (Figure 2A), which discriminated five major cell types based on marker expression: 1) lymphoid cells including CD7$^+$ T-cells, CD7$^+$ innate lymphoid cells, CD20$^+$ B-cells, CD138$^+$ plasma cells and CD7$^-$CD20$^-$CD127$^+$ cells that could represent a population of early lymphoid cells due to their expression of CD127 in the absence of CD3, CD20 and HLA-DR[22,23]; 2) mature myeloid cells including CD14$^+$ monocytes, CD15$^+$ neutrophils and CD68$^+$ macrophages; 3) stroma including CD271$^+$ stromal cells, osteoblasts and endothelium; 4) CD71$^+$ erythroid precursors and 5) myeloid progenitors including CD31$^-$CD34$^+$ hematopoietic progenitor cells (HPCs) (Figure 2A). $0.04 \cdot 10^6$ cells divided across all ROIs were unclassifiable and thus were excluded from

downstream analyses. Visualization of all AA^{Dx} and controls in the optSNE analysis showed clear differences in the cellular composition of the hematopoietic compartment between groups, with lymphoid cells predominating in AA^{Dx} (Figure 2B). Visualization of each patient separately revealed heterogeneity within the hematopoietic compartment between all AA^{Dx} (Figure 2C, top row). 6M post-hATG, a trend towards normalization was observed for all patients, except for patients AA8 and AA17 whose hematopoietic composition remained comparable to diagnosis (Figure 2C, red box).

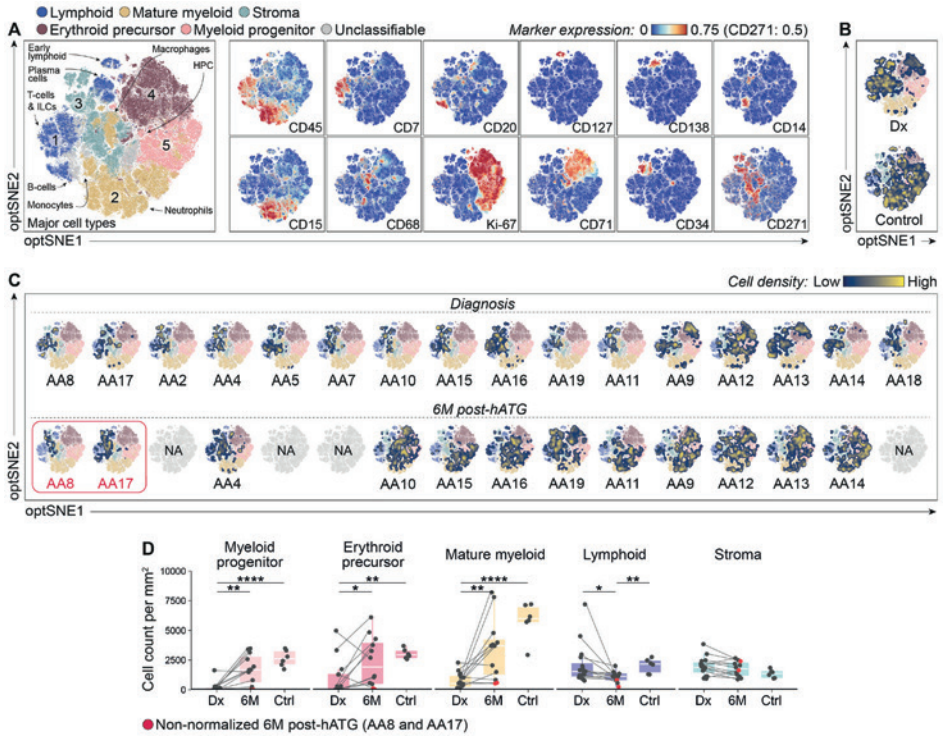


Figure 2. Global cellular composition of the hematopoietic compartment in bone marrow from AA patients and controls. Colors indicate major cell types (lymphoid cells, mature myeloid cells, myeloid progenitors, erythroid precursors, stroma and unclassifiable cells), groups (AA^{Dx}, AA^{6M} and controls) or marker expression values, where a marker expression value of 0.75 indicates that 75% of pixels of a segmented cell are positive for the corresponding marker. [A] $0.46{\cdot}10^6$ cells segmented from 79 ROIs from AA^{Dx} (n=16 patients), AA^{6M} (n=12 patients) or controls (n=6 controls) visualized using an optSNE analysis. [B] Contour plots showing the cellular composition of the bone marrow in all ROIs collected from all AA^{Dx} (n=16) and controls (n=6). [C] Contour plots showing the cellular composition of the bone marrow in all ROIs collected from all AA^{Dx} and AA^{6M}, shown per patient per time point. The red box presents the patients with a non-normalized bone marrow 6M post-hATG (AA8 and AA17). [D] Abundance of the major cell types, shown as an absolute cell count per mm^2 of hematopoietic compartment. Each dot represents the mean of all ROIs collected from a patient or control. Box plots present the median with the interquartile range (IQR), error bars present 1.5*IQR.

To correct for myeloid cell depletion and bone marrow hypocellularity, we quantified the major cell types as an absolute count per mm^2 of hematopoietic compartment. As expected, we observed a profound decrease in precursor/progenitor and mature myeloid cells in all AA^{Dx} (Figure 2D). Consistent with the presence of Ki-67$^+$ regions, precursor/progenitor cells were still present in the bone marrow from 7 AA^{Dx} (AA9, AA12-14, AA16-18), with most cells exhibiting a CD71$^+$ erythroid precursor phenotype (Figure 2C). In contrast, absolute numbers of lymphoid cells and stroma did not differ between AA^{Dx} and controls, again indicating that they are the predominant cell types remaining in the bone marrow from AA^{Dx}.

Quantification of all major cell types 6M post-hATG confirmed a trend towards normalization of the precursor/progenitor, mature myeloid and lymphoid compartments in all patients, except for the two patients with a non-normalized bone marrow (Figure 2D).

Increase of pro-inflammatory lymphocytes in Ki-67$^+$ regions in AA at diagnosis

Since activated CD68$^-$CD163$^+$CD4$^+$ macrophages were exclusively present in Ki-67$^+$ regions from AA^{Dx} (Figure 1F), we hypothesized that the active immune response resulting in HSPC destruction is best detectable in these Ki-67$^+$ regions. Because patients can have both Ki-67$^+$ and Ki-67$^-$ regions at diagnosis, groups were defined by the presence of Ki-67$^+$ cells, and the bone marrow was analyzed per ROI instead of per patient.

Clustering of cells from the hematopoietic compartment, excluding stroma, identified 40 distinct subpopulations of which the phenotypes were confirmed in the raw images (Figure S6). Identified phenotypes were clearly separable, except for CCR6$^+$ B-cells (Figure 3A, magenta cells) and CCR6$^+$CD45RO$^+$CD4$^+$ T-cells (Figure 3A, cyan cells) which were too close to be separated and thus were captured as one cluster.

15 progenitor and mature myeloid subpopulations (Figure 3B) and 25 lymphoid subpopulations were distinguished (Figure 3C). The absolute counts of all subpopulations (per mm^2 of hematopoietic compartment) across all ROIs were visualized as z-scores. ROIs were grouped according to disease status (patient versus control), treatment status (diagnosis or 6M post-hATG) and the presence of Ki-67. Consistent with the depletion of the progenitor compartment, CD31$^-$CD34$^+$ HPCs, CD31$^+$CD34$^-$ megakaryocytes, CD71$^+$ erythroid precursors and other Ki-67$^+$ myeloid progenitors were markedly reduced in AA^{Dx} compared to controls (Figure 3B, statistics in Figure S9). In line with reduced myelopoiesis in AA, all CD15$^+$ neutrophils or CD14$^+$ monocytes were decreased in AA^{Dx}. The presence of CD68$^+$CD163$^+$ macrophages in both Ki-67$^+$ regions from AA^{Dx} and controls was confirmed in this analysis. Furthermore, a cluster of CD68^{dim}CD163$^+$ macrophages was enriched in AA^{Dx} compared to controls. This cluster included the activated and enlarged CD68$^-$CD163$^+$CD4$^+$ macrophages

exclusively found in Ki-67$^+$ regions from AA^{Dx} (Figure 1F). Remarkably, CD11c$^+$ mature myeloid cells fitting with a population of dendritic cells were abundant in the Ki-67$^+$ regions from AA^{Dx}, a feature not observed in most Ki-67$^-$ regions and controls. CD11b$^+$ myeloid cells with differential expression of cKit were also abundant in the bone marrow from AA^{Dx}. CD11b$^+$cKit$^-$ cells resembling basophils[24] were prevalent in both Ki-67$^+$ and Ki-67$^-$ regions at diagnosis, whereas CD11b$^+$cKit$^+$ cells fitting with a population of mast cells[25] predominated across the Ki-67$^-$ regions at diagnosis.

Within the lymphoid compartment (Figure 3C), we distinguished T- and B-cells in multiple differentiation stages. We observed a decrease of CD7$^-$CD20$^-$CD127$^+$ early lymphoid-like cells in both Ki-67$^+$ and Ki-67$^-$ regions from AA^{Dx} compared to controls. The presence of other lymphoid subpopulations was heterogeneous among AA^{Dx}, with notable differences between Ki-67$^+$ and Ki-67$^-$ regions. All CD4$^+$ T-cell, CD8a$^+$ T-cell and CD56$^+$ NK-cell populations were increased in Ki-67$^+$ regions, whereas Ki-67$^-$ regions mainly contained the expanded terminally differentiated (CD45RA$^+$CD27$^-$) CD8a$^+$ T-cells from our previously identified immune cell network[6]. CCR6$^+$ B-cells and CCR6$^+$CD45RO$^+$CD4$^+$ T-cells, corresponding to the expanded CCR6$^+$ lymphoid cells identified in our previous study[6], were found in both Ki-67$^+$ and Ki-67$^-$ regions at diagnosis. B-cells with differential expression of the memory marker CD27[26] were increased in Ki-67$^+$ regions but rarely observed in Ki-67$^-$ regions at diagnosis. A cluster of CD20$^-$CD138$^-$CD27$^+$CD38$^+$ plasmablasts was decreased in all AA^{Dx}, with the exception of a few Ki-67$^+$ regions. Plasma cells, reflecting a population of differentiated B-cells, were strongly increased in almost all AA^{Dx} and predominated in Ki-67$^-$ regions at diagnosis. An exception to these patterns was observed for the Ki-67$^-$ regions from AA8, which contained many T- and B-cell subpopulations across all differentiation stages.

These data indicate that the Ki-67$^+$ regions are characterized by an influx of T-cells (green/cyan/yellow CD3$^+$ T-cells in Figure 3D, top panel), ILCs and B-cells (red CD20$^+$ B-cells in Figure 3D, lower panel) with a pro-inflammatory phenotype including the previously identified CCR6$^+$ B-cells and CCR6$^+$CD45RO$^+$CD4$^+$ T-cells. This observation fits with our hypothesis that Ki-67$^+$ regions are the site of an active immune response in AA. In contrast, Ki-67$^-$ regions from AA^{Dx} contain cells of a more terminally differentiated phenotype based on the presence of CD45RA$^+$CD27$^-$CD8a$^+$ T-cells (cyan cells in Figure 3E, top panel) and plasma cells (green CD138$^+$ cells in Figure 3E, lower panel) fitting with a more advanced stage of bone marrow destruction where the active immune response has waned. Collectively, this suggests a shift in the immune cell composition of the bone marrow during the development of AA. 6M post-hATG, a trend towards normalization of progenitors and immune cells was observed in patients with normalizing bone marrow, suggesting successful IST restores the balance in the bone marrow (Figure 3B-C).

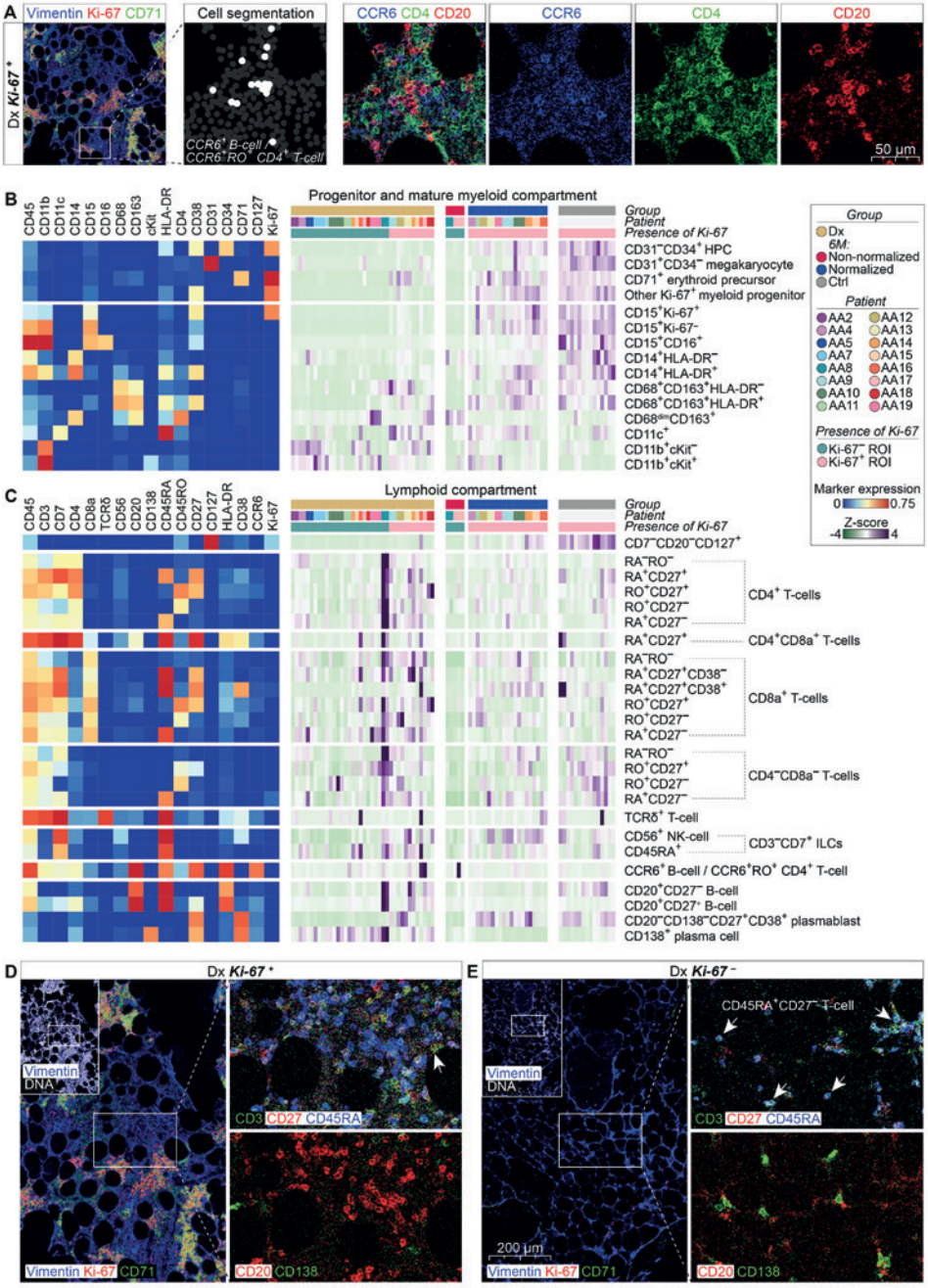


Figure 3. Subpopulation analysis of the myeloid and lymphoid compartments. [A] CCR6+ B-cells and CCR6+CD45RO+ CD4+ T-cells, visualized in a representative Ki-67+ ROI from an AA^{Dx}. CD4, CD20 visualize CD4+ T-cells and B-cells, respectively. [B-C] Heatmaps presenting the composition of the mature myeloid and progenitor compartments [B] or lymphoid compartment [C] across all AA^{Dx}, AA^{6M} and control ROIs at the subpopulation level. Left: heatmap showing the marker expression profiles of the identified

subpopulations, where a marker expression value of 0.75 indicates that 75% of pixels of a segmented cell are positive for the corresponding marker. Right: Heatmap visualizing the absolute cell counts of the identified cell subpopulations per mm^2 of hematopoietic compartment, shown as a z-score (green = less abundant; purple = more abundant compared to other ROIs). Colors indicate 1) groups, 2) patients or 3) the presence of Ki-67$^+$ progenitor cells. Data are shown per ROI. [D] CD3$^+$ T-cells in multiple differentiation stages; CD20$^+$ B-cells and CD138$^+$ plasma cells visualized in a representative Ki-67$^+$ (left) and Ki-67$^-$ (right) ROI from AA^{Dx}.

Pro-inflammatory lymphocytes colocalize with progenitors in the bone marrow in AA

To determine whether immune cells colocalize with precursors in Ki-67$^+$ regions from AA^{Dx}, we examined the interactions of all identified subpopulations using cellular neighborhood analyses. This approach identified neighborhoods by clustering segmented cells from all groups based on the cellular phenotypes in their direct neighborhood (Figure 4A). Nine distinct neighborhoods were identified (Figure 4B). Neighborhoods 1 and 2, enriched for erythroid precursors, aligned with the CD71$^+$ erythroblastic islands (Figure 4C). Neighborhoods 3-6, enriched for HPCs and/or mature myeloid cells, represented regions of progenitors and myelopoiesis. Neighborhood 7 and 8 were highly enriched for immune cells, with neighborhood 8 showing a more differentiated phenotype based on the presence of plasma cells. Neighborhood 9 mainly included stroma and aligned with blood vessels or osteoblasts lining the bone. Visualization of all neighborhoods in all AA^{Dx} and AA^{6M} is shown in Figure S10.

Neighborhoods 7 and 8, enriched for immune cells, were more abundant in the bone marrow from AA^{Dx} compared to controls (Figure 4D). 6M post-hATG, neighborhoods 7 and 8 decreased in patients with a normalizing bone marrow, suggesting a pathogenic role. Interestingly, multiple T-cell, ILC and B-cell subpopulations with a pro-inflammatory phenotype were also present in neighborhoods 3-6, suggesting a possible interaction between immune cells and progenitors in the bone marrow. In contrast, these activated immune subpopulations were absent in the erythroblastic islands (neighborhoods 1-2), indicating their interactions with erythroid precursors may be limited.

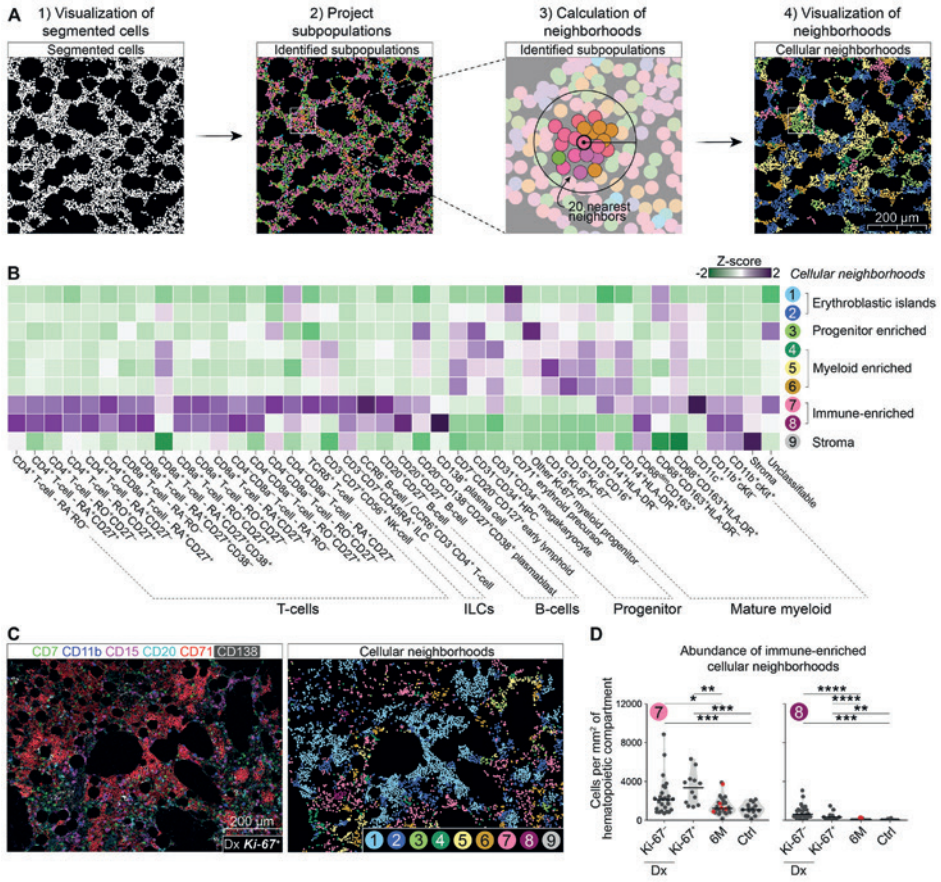


Figure 4. Identification of cellular neighborhoods in the bone marrow. Colors indicate identified subpopulations or cellular neighborhoods. [A] Approach used to identify neighborhoods. Step 1: The spatial location of each segmented cell was determined. Step 2: The phenotype of each segmented cell as identified in Figure 3 was visualized. Step 3: The neighborhoods were calculated. For each segmented cell in every ROI, the phenotypes of its 20 nearest neighbors within a 25-pixel distance were determined. Subsequently, all segmented cells were clustered into 9 neighborhoods based on the cellular composition of their direct microenvironment. [B] Cellular composition of the identified neighborhoods. Relative frequencies of all identified subpopulations within the neighborhoods are shown as a z-score (green = less frequent; purple = highly frequent compared to other neighborhoods). [C] IMC stainings and neighborhoods, visualized in a Ki-67$^+$ region from an AA^{Dx} (patient AA9). CD7 stains T-cells and ILCs; CD11b stains myeloid cells; CD15 stains neutrophils; CD20 stains B-cells; CD71 stains erythroid precursors; CD138 stains plasma cells. [D] Abundance of neighborhoods 7 and 8 in the bone marrow across all groups, shown as an absolute cell count per mm^2 of the hematopoietic compartment. Data are shown per ROI. ROIs from patients with a non-normalized bone marrow 6M post-hATG are shown in red and were excluded from statistical analysis.

Development of AA can be visualized within the bone marrow

To investigate the interactions between immune cells and HSPCs, we examined the spatial distribution of the identified neighborhoods within the bone marrow. This discriminated four areas: 1) areas exclusively composed of erythroblastic islands (neighborhoods 1-2); 2) areas containing lymphoid cells from neighborhoods 7-8 along with progenitors; 3) areas where myeloid cells including progenitors (neighborhoods 3-6) were interspersed with lymphoid cells from neighborhoods 7-8 and 4) areas predominantly containing cells from neighborhood 8 (representative Ki-67$^+$ region from AA^{Dx} in Figure 5A, all AA^{Dx} in Figure S10).

Each area represented a distinct stage in the development of AA. In the CD71$^+$ erythroblastic islands (area 1), T- and B-cells were present in small numbers, similar to controls, indicating limited immune cell interactions with erythroid precursors in AA^{Dx} (Figure 5A-B, area 1, control in Figure S11). In contrast, area 2 included CD15$^+$Ki-67$^+$ neutrophil progenitors (green cells with blue nucleus in panel Bi) and was predominantly composed of pro-inflammatory T- and B-cell subpopulations in close proximity (Figure 5B, area 2). Therefore, we defined area 2 as a 'lymphoid-dominant' immune hot spot. This area included early effector T-cells (white CD3$^+$CD45RA$^+$CD27$^+$ cells in panel Bii), memory T-cells (green/yellow CD3$^+$CD45RA$^-$CD45RO$^+$ cells in panel Bii) and B-cells (red CD20$^+$ cells in panel Biv), as well as the CCR6$^+$ B-cells and CCR6$^+$CD45RO$^+$CD4$^+$ T-cells (magenta CCR6$^+$CD20$^+$ / cyan CCR6$^+$CD4$^+$ cells in panel Biv) and terminally differentiated CD8a$^+$ T-cells (cyan CD3$^+$CD45RA$^+$CD27$^-$ in panel Bii) from our previously identified immune cell network[6]. The close proximity and highly activated state of the cells could represent the initial stage of immune activation in AA.

In area 3 (Figure 5A-B, area 3), the activated lymphoid cells and CD15$^+$Ki-67$^+$ neutrophil progenitors were accompanied by the activated and enlarged CD68$^-$CD163$^+$CD4$^+$ macrophages (purple cells in panel Bv). Therefore, we defined these areas as 'macrophage-enriched immune hot spots', which may represent areas where the immune response has reached its maximum. Finally, in area 4 (Figure 5A-B, area 4), we observed high densities of terminally differentiated T-cells (cyan cells in panel Bii) and plasma cells (yellow cells in panel Biii), along with a few remaining CD68$^-$CD163$^+$CD4$^+$ macrophages but no Ki-67$^+$ progenitors.

We quantified the four identified tissue areas across all bone marrow regions using spatial context analyses previously described[19]. This confirmed the presence of the pro-inflammatory immune hot spots in all Ki-67$^+$ regions from AA^{Dx} and demonstrated that Ki-67$^+$ regions contained fewer immune-differentiated areas (area 4) compared to Ki-67$^-$ regions (Figure 5C).

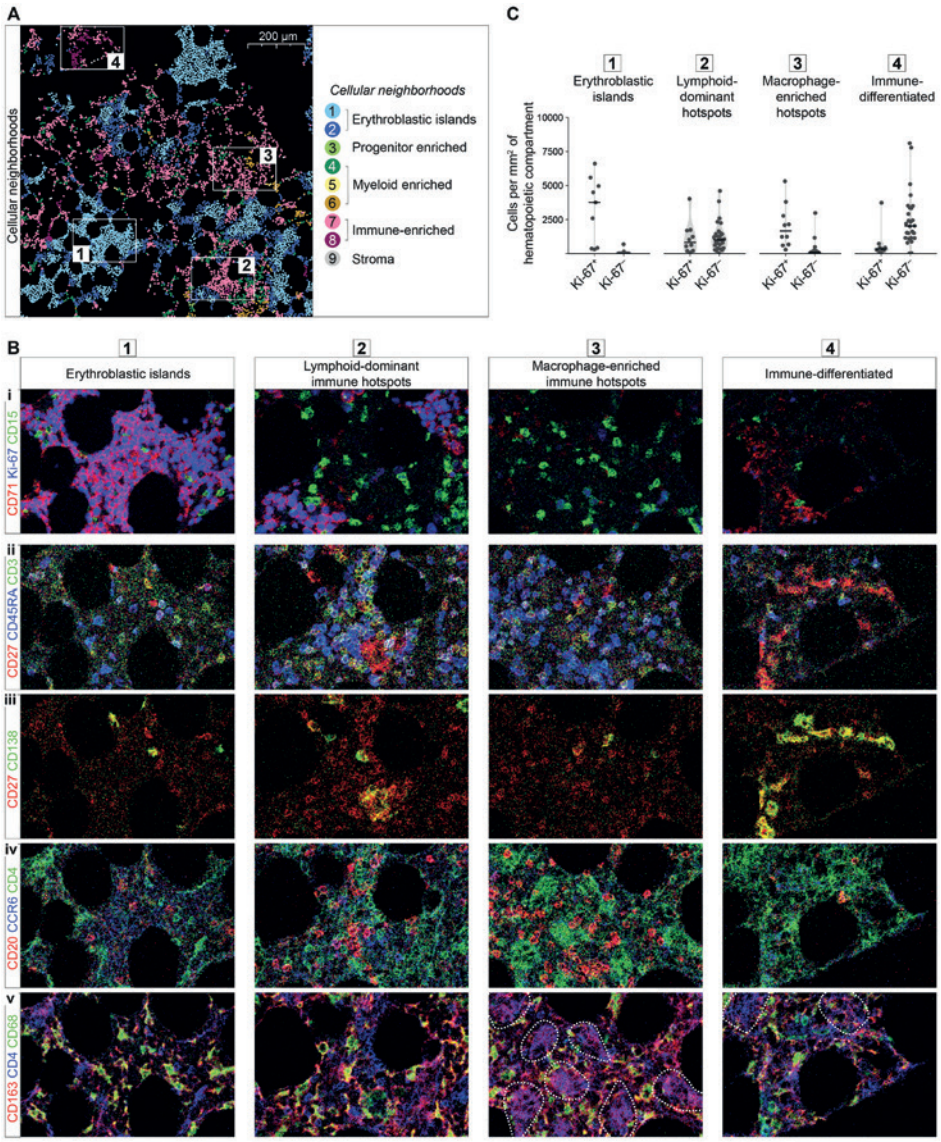


Figure 5. Cellular composition of four distinct microenvironments within the Ki-67⁺ regions from AA patients at diagnosis. [A] Visualization of cellular neighborhoods in a representative Ki-67⁺ region at diagnosis (patient AA13), revealing four distinct tissue areas: 1) erythroblastic islands; 2) lymphoid-dominant immune hot spots; 3) macrophage-enriched immune hot spots and 4) immune-differentiated tissue areas. [B] Presence of immune cell subpopulations, visualized in the four identified tissue areas. Panel Bi: Visualization of CD71⁺Ki-67⁺ erythroid precursors (red cells with blue nucleus) or CD15⁺Ki-67⁺ neutrophil progenitors (green cells with blue nucleus) in each tissue area. Panel Bii: Visualization of CD3⁺ T-cell populations in multiple differentiation stages in each tissue area. Panel Biii: Visualization of CD138⁺CD27⁺ plasma cells in each tissue area. Panel Biv: Visualization of (CCR6⁺) CD20⁺ B-cells and CD4⁺ T-cells in each tissue area. Panel Bv: Visualization of macrophages in each tissue area. CD4⁺CD68⁻ CD163⁺ macrophages are circled. [C] Presence of the four identified tissue areas across all Ki-67⁺ and Ki-67⁻ ROIs from all AA^{Dx}, shown as an absolute count per mm^2 of the hematopoietic compartment. Each dot represents a Ki-67⁺ or Ki-67⁻ ROI from an AA^{Dx}. Horizontal bars present group median.

Bone marrow normalization is associated with a decrease in immune hot spots

Since IST can restore hematopoiesis, we investigated its effect on the immune response by studying the spatial distribution of the immune hot spots 6M post-hATG (Figure 6; all patients in Figure S10). In the two patients with a non-normalized bone marrow 6M post-hATG (AA8 and AA17), we observed a striking difference in the abundance of the hot spots. In AA8, the bone marrow was completely hypocellular and all hot spots were depleted, while in AA17 immune hot spots were still highly abundant (Figure 6A). Ten patients showed a trend toward normalization 6M post-hATG. In five of these patients, the hot spots were nearly absent (AA9, AA13: Figure 6B, top row; AA11, AA15, AA16: Figure S10). In the other five patients, hot spots persisted but were reduced in number compared to diagnosis, and activated $CD68^{-}CD163^{+}CD4^{+}$ macrophages were absent (AA10, AA14: Figure 6B, bottom row; AA4, AA12, AA19: Figure S10). No differences were observed between complete or partial responders to IST (Table S1). These findings indicate that bone marrow normalization 6M post-hATG is associated with changes in immune hot spots and can occur in all patients, regardless of the extent of hypocellularity of the bone marrow at diagnosis.

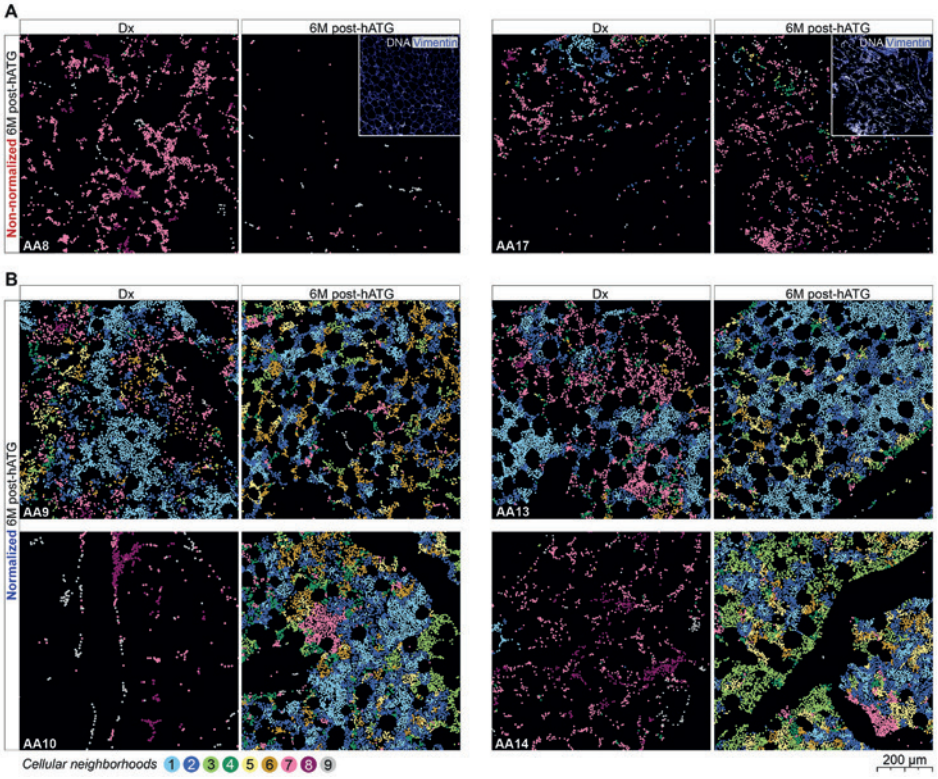


Figure 6. Effect of IST on the spatial cellular composition of the bone marrow. [A] Cellular neighborhoods, visualized in the bone marrow from the two patients with a non-normalized bone marrow 6M post-hATG (AA8 and AA17). [B] Cellular neighborhoods visualized in the bone marrow from four representative patients with a normalizing bone marrow 6M post-hATG (AA9, AA10, AA13, AA14). Colors indicate cellular neighborhoods.

Discussion

In this study, we aimed to interrogate the chronological order of events in the immune-mediated pathogenesis of AA by examining the spatial orientation of the immune response within the preserved bone marrow architecture. Previously, using suspension mass cytometry on bone marrow aspirates, we identified an AA-specific immune cell network enriched for CCR6^{++} B-cells, Th17-like[27-29] CCR6^{+} memory CD4^{+} T-cells, and KLRG1^{+} terminally differentiated CD8^{+} T-cells[6]. We also observed CD163^{+} macrophages in the AA bone marrow, despite depletion of the myeloid compartment, suggesting macrophage recruitment to clear apoptotic cells. Building on these findings, we used imaging mass cytometry to study the spatial composition of the bone marrow microenvironment in AA. Our study expands upon early studies of the AA bone marrow[7] and complements recent mappings of normal human and murine bone marrow using fluorescence-based imaging techniques[23,30]. The present study extends our previous findings by confirming the presence of network populations in the AA bone marrow and demonstrating their spatial proximity. We show that CCR6^{+} B-cells and CCR6^{+}CD45RO^{+}CD4^{+} T-cells are organized in immune 'hot spots' in Ki-67^{+} regions where the active immune response in AA is concentrated. Remarkably, these CCR6^{+} cells are so closely located that they could not be separated in the clustering analysis, indicating strong pathogenic interactions of CCR6^{+} T- and B-cells in AA. Throughout both Ki-67^{-} and Ki-67^{+} regions from AA^{Dx} we observed terminally differentiated CD8^{+} T-cells representing the KLRG1^{+} terminally differentiated CD8^{+} T-cells with potential cytotoxic capacity[31]. These findings further support their involvement in AA and suggest these cells accumulate in the bone marrow following activation and differentiation due to repeated antigenic stimulation.

Building on our previous work, we exclusively observed CD68^{-}CD163^{+}CD4^{+} macrophages in Ki-67^{+} regions from AA^{Dx}, distinguishing them from other macrophage populations in AA^{Dx} and controls. These macrophages are activated, enlarged and are engulfing other hematopoietic cells, suggesting involvement in an active process within the AA bone marrow. CD163^{+} macrophages have been described in AA before, and have been associated with improved overall survival, particularly in non-severe AA patients[21]. It was suggested that these CD163^{+} macrophages could be beneficial through an immunosuppressive M2 macrophage-like state. Our results provide an alternative explanation. We found that CD68^{-}CD163^{+}CD4^{+} macrophages are organized in immune hot spots with high immune activity in Ki-67^{+} regions, where they are interspersed with activated lymphoid cells and progenitors. Whether CD68^{-}CD163^{+}CD4^{+} macrophages are direct contributors to HSPC destruction in AA or are mainly involved in the clearance of apoptotic cells cannot be deducted from our data and would be an important topic for future research.

Beyond the network populations, we demonstrate the presence of pro-inflammatory immune subpopulations in the Ki-67$^+$ regions harboring the active immune response in AA. This underscores the importance of analyzing bone marrow biopsies, as relying solely on bone marrow aspirates may overlook potentially pathogenic populations and does not allow the analysis of cellular interactions within the bone marrow. Consistent with the view that AA is mediated by an autoreactive T-cell response[1], we identified various memory CD4$^+$ and CD8$^+$ T-cell subpopulations in the Ki-67$^+$ regions, which could correspond to previous descriptions of expanded T-cell populations in peripheral blood and bone marrow aspirates[28,32]. The presence of these activated and differentiated CD4$^+$ and CD8$^+$ T-cell subpopulations indicates ongoing T-cell responses and extends the previous observation demonstrating T-cell infiltration and clustering in the AA bone marrow, particularly around blood vessels[7]. In line with previous studies describing a profound decrease of regulatory T-cells in peripheral blood from AA patients[28,29], Tregs were not detected within the AA bone marrow. Beyond T-cells, we observed high numbers of ILCs including NK-cells in Ki-67$^+$ regions from AA^{Dx}, contrasting with studies showing decreased NK-cell counts in peripheral blood[33-35]. Additionally, we detected high numbers of B-cells within Ki-67$^+$ regions from AA^{Dx}, while B-cell counts were lower or comparable in peripheral blood between patients and controls[33,35]. This suggests recruitment of specific immune subpopulations to the bone marrow in AA. This adds complexity to the immune response in AA, and suggests that the autoimmune response resulting in HSPC destruction is more diverse than previously recognized, and involves a broad spectrum of immune cell phenotypes rather than being only T-cell mediated.

Our findings raise important questions regarding the antigenic target(s) of the immune cells within the AA bone marrow. Despite advances in evaluating expanded T-cell clones in AA[36], the targeted antigen(s) and progenitor population(s) remain incompletely defined. Using IMC, we observed that Ki-67$^+$ regions from AA^{Dx} contained fewer stem cells and myeloid progenitors, but similar numbers of erythroid precursors compared to controls. This could indicate the immune response in AA targets antigens confined to stem cells and myeloid progenitors. Erythroid precursors, further along in the hematopoietic tree, may evade depletion.

Our study provides a stepwise view of the immune response in AA development. Our data indicate the active immune response resulting in HSPC destruction in AA is mediated by a spectrum of T-, B- and myeloid cell subpopulations that interact within the bone marrow in a coordinated manner. We propose that the disease begins in 'lymphoid-dominant' immune hot spots within Ki-67$^+$ regions, where interactions such as antigen presentation by B-cells and T-cell-mediated activation of B-cells activate the immune cascade. As the response progresses, 'macrophage-enriched' immune hot spots develop that are characterized by activated and enlarged CD68$^-$CD163$^+$CD4$^+$ macrophages, which presumably are phagocytosing apoptotic

cells. In addition, activated T- and B-cells are still present that may orchestrate targeted immune responses through cytokine secretion and cytotoxic attack. After all HSPCs are depleted, only differentiated effector cells including terminally differentiated $CD8^+$ T-cells and plasma cells remain. These terminally differentiated T-cells likely correspond to the clonally expanded[36] and cytotoxic[32,36] T-cells identified in AA, contributing to continuous inflammation in the bone marrow. B-cell differentiation into plasma cells is also observed. Their differentiation and presence within the immune hot spots, alongside the detection of autoantibodies[1], suggests their active contribution to the immune response in AA, potentially through antigen presentation and antibody production. How the immune interactions lead to the actual bone marrow destruction would be an important topic for future *in vitro* studies.

To confirm the relevance of the immune hot spots in the pathogenesis of AA, we studied their presence 6M post-hATG and found a decrease in hot spots in all patients with a normalizing bone marrow. This suggests that IST works through a gradual process: hATG disrupts the coordinated immune cell interactions in the tissue, while ciclosporin remains needed to suppress remaining immune cells. Non-response to IST may result from AA not being immune-mediated, irreversible stem cell depletion pre-hATG or insufficient immunosuppression. In our study, two non-normalized patients showed distinct patterns: in AA8 immune hot spots were depleted, but bone marrow normalization may have been hindered by complete HSPC deletion due to the hyperactive immune response observed pre-hATG. In AA17, hot spots persisted 6M post-hATG, suggesting insufficient immunosuppression.

Collectively, our study provides the first visualization of the chronological order of events in the development of AA, mapping the complex interactions among immune cell subpopulations within the bone marrow microenvironment. These findings underscore the potential of both established and previously overlooked immune cell populations as possible therapeutic targets, and pave the way for research on more precise and effective treatment strategies for AA.

Acknowledgements

We thank the Flow Cytometry Core Facility of the Leiden University Medical Center for assistance with the acquisition of the imaging mass cytometry data. Figure 1A was created with BioRender.com. This work was supported by a research grant from Dioraphte Foundation.

Authorship contributions

E.S.P. designed the experimental set-up, performed experiments, analyzed results, interpreted the data, made the figures and wrote the manuscript. S.J.L. designed the experimental set-up, performed experiments and assisted with data analysis. M.E.IJ. designed the experimental set-up. V.vU. and J.H.F.F. interpreted the data. N.F.dM. designed the experimental set-up. F.K. and M.H.M.H. interpreted the data and supervised the project. J.M-L.T. conceptualized the study, recruited patients, interpreted the data, supervised the project and wrote the manuscript. All authors critically edited and reviewed the manuscript. All authors approved the final manuscript.

Conflicts of interest

The authors declare no competing financial interests.

Data availability statement

Imaging mass cytometry data are available from the corresponding author on reasonable request. Contact: Jennifer M-L Tjon, MD PhD; j.m.l.tjon@lumc.nl.

Supplemental methods

IMC panel design, antibody conjugation and antibody validation

A 37-marker IMC antibody panel for formalin-fixed paraffin-embedded (FFPE) EDTA-decalcified bone marrow biopsies was designed and optimized to capture both hematopoietic cells and non-hematopoietic cells of the bone marrow microenvironment. Antigens were selected based on publicly available RNA sequencing[13] and our published suspension mass cytometry data of bone marrow aspirates from AA patients[6]. 31 of 37 antibodies of the IMC panel were selected from validated IMC panels published by our institute[9-11] and applied on FFPE EDTA-decalcified bone marrow in screening experiments with FFPE non-decalcified tonsil and FFPE EDTA-decalcified tonsil as a control to confirm antibody performance after tissue decalcification. For the other 6 antibodies of the IMC panel (CD34, CD59, CD71, CD271, CXCL12 and cKit), BSA and carrier-free formulated antibodies were purchased from multiple vendors and tested for performance on control FFPE non-decalcified tonsil, control FFPE EDTA-decalcified tonsil and FFPE EDTA-decalcified bone marrow using immunohistochemistry (IHC). All IHC stainings showed adequate signal-to-noise ratios and matched the staining patterns of publicly available tissue protein expression data in both non-decalcified and decalcified tissue[14]. The 6 antibodies were then conjugated in-house to heavy metal isotopes using Maxpar® X8 Antibody Labeling Kits (Standard BioTools) according to the manufacturer's instructions. After conjugation, the antibodies were eluted in 200mL of antibody stabilizer PBS (Candor Biosciences, cat 131125) containing 0.05% sodium azide. Subsequently, the metal-conjugated IMC antibodies were titrated for performance on FFPE EDTA-decalcified bone marrow and tonsil at 1:50 or 1:100 at 5 hours at room temperature (RT) or overnight at 4°C. All 37 IMC antibodies were stored at 4°C at all times. Since KLRG1$^+$ EMRA CD8$^+$ T-cells were part of our previously identified disease-specific immune cell network in AA[6], we evaluated several KLRG1 antibodies but did not find a suitable clone and therefore did not add KLRG1 to our IMC panel.

Tissue staining

All bone marrow biopsies were fixed in 4% formalin, decalcified overnight in 10% EDTA and embedded in paraffin after collection. To perform IMC, the FFPE EDTA-decalcified bone marrow biopsies were cut at a thickness of 5µm and mounted on FLEX IHC Microscope Slides (Dako, cat K8020). Subsequently, slides were baked overnight at 37°C and stored at 4°C until further use. Slides were sealed in paraffin to reduce oxidation if stored at 4°C for longer than four weeks.

Bone marrow tissue sections were stained with the 37-marker IMC panel over three days as previously described[9]. Briefly, tissue sections were deparaffinized in xylol, rinsed in ethanol and boiled for 10 minutes in IHC Antigen Retrieval Solution 10x Low Ph (Invitrogen, cat 00495558). Subsequently, slides were cooled to RT and blocked for 30 minutes at RT with Superblock Blocking Buffer (ThermoFisher, cat 37515). Next, excess blocking solution was removed and slides were stained overnight at 4°C with the unconjugated primary antibodies for CD4 and TCRδ in a volume of 100µL. The following morning, slides were washed and stained with the two secondary antibodies conjugated to 145Nd and 148Nd in a volume of 100µL in PBS with 1% BSA and 0.05% Tween. All washes were performed 3 times for 5 minutes in PBS with 1% BSA and 0.05% Tween. After a one hour incubation at RT, slides were washed and stained with 17 of 35 primary IMC antibodies for 5 hours at RT in a volume of 100µL (Table S2). Subsequently, slides were washed and stained overnight with the remaining 18 primary IMC antibodies at 4°C in a volume of 100µL. On the morning of the third day, slides were washed and stained with DNA intercalator-Ir (Standard BioTools, cat 201192A) for 5 minutes at RT in a volume of 100µL. Lastly, slides were washed and dried under an air flow. Slides were stored at 4°C until measurement.

Definition of three histological compartments in the bone marrow tissue

AA is characterized by severe damage to the bone marrow, leading to an 'empty' bone marrow. Therefore, large differences in bone marrow histology were observed between AA^{Dx}, AA^{6M} and controls. To enable quantitative comparison between biopsies we quantified the surface areas of three major compartments in the bone marrow: the hematopoietic compartment, adipocytes and bone.

The hematopoietic compartment was defined as hematopoietic cells including their direct microenvironment. To determine the surface area of the hematopoietic compartment, for each ROI, multi-page .tiff images were exported from MCD viewer, hyperbolic arcsinh transformed with a cofactor of 5 and loaded into Cytosplore Imaging software v3.2.6 (unpublished, adapted from Cytosplore[18]) for dimensionality reduction. Subsequently, a 2-level hierarchical stochastic neighbor embedding (HSNE) analysis was performed for all pixels (1 pixel = $1\mu m^2$) in each ROI with default settings and 500 iterations. All markers of the IMC panel and the DNA stain were used to generate the HSNE. At the overview level of each HSNE analysis, all pixels in an ROI were summarized into landmarks based on similarities in marker expression intensities and the spatial localization of each landmark in each ROI could be evaluated. Next, we selected all landmarks corresponding to the hematopoietic compartment. DNA^+ landmarks were selected to capture the nucleus of all cells within the hematopoietic compartment. $Vimentin^+$ landmarks were selected to capture the cytoplasm

and cell membrane of all cells and their microenvironment. Vimentin was chosen over CD45 in this process to capture all pixels corresponding to both non-hematopoietic cells and hematopoietic cells (visualized in Figure S3). Additionally, $CD31^+$ landmarks were selected to capture the cytoplasm of $Vimentin^-CD31^+$ megakaryocytes. The combined selection of these DNA^+, $Vimentin^+$ and/or $CD31^+$ pixels enabled us to determine the total number of pixels within the hematopoietic compartment (where 1 pixel = $1\mu m^2$). A few ROIs in the IMC dataset included unrepresentative regions with few cells and poor tissue quality due to blood clots, which therefore were subtracted from the surface area of the hematopoietic compartment. To determine the surface areas of these unrepresentative regions, .tiff images of these ROIs were exported from MCD Viewer and loaded into ImageJ v1.53q (Fiji). Subsequently, the surface area of the blood clots was manually selected, calculated and subtracted from the total surface area of the hematopoietic compartment using the Vimentin and DNA stains. A visualization of the approach used to determine the surface area of the hematopoietic compartment in Cytosplore Imaging is shown in Figure S3.

Bone was defined as the part of the bone marrow section that consists of Collagen I^+ bone trabeculae. To determine the surface area of bone, for each ROI, .tiff images were exported from MCD Viewer and loaded into ImageJ v1.53q (Fiji). Subsequently, surface areas corresponding to bone were identified, selected and calculated using the Collagen I, Vimentin and DNA stains.

The surface area of adipocytes was defined by subtracting the surface areas of the hematopoietic compartment, blood clots and bone from the total ROI surface area. A few ROIs were ablated at the edge of a bone marrow biopsy and therefore included 'empty' regions without bone marrow tissue. If present, the surface areas of these empty regions were calculated by manual selection in ImageJ and also subtracted from the total ROI surface area to obtain the surface area of adipocytes.

Cell segmentation and background removal

To enable detailed interrogations of single cells in the images we applied a cell segmentation pipeline as shown in Figure S4 to all acquired ROIs. First, a single-cell mask was generated for each acquired ROI as previously described[16]. To ensure proper segmentation of cells with different shapes, namely megakaryocytes and stromal cells, a multi-layer cell segmentation mask was applied.

To generate the cell segmentation mask, Ilastik v1.3.2[37] was used to generate three probability maps based on the signal of the DNA stain, the stromal cell marker CD271 and megakaryocytes ($CD31^+Vimentin^-$) for each ROI. Subsequently, the three probability maps

were loaded into CellProfiler v4.2.1[17], where each respective map was used to identify primary objects in each ROI. The size of each DNA object was increased by 1 pixel (1 pixel = 1μm^2) to accurately capture the marker expression on the cells' membrane in downstream analyses. The holes in all identified megakaryocyte objects, corresponding to the megakaryocyte nuclei, were filled using the fill holes strategy in CellProfiler to avoid separate segmentation of the megakaryocyte cytoplasm and nucleus.

Next, the three sets of primary objects (DNA$^+$, CD271$^+$ and CD31$^+$Vimentin$^-$ objects) were combined using the preservation strategy for overlapping objects in CellProfiler. Since the primary aim of this study was to interrogate the immune response in the bone marrow in AA, DNA$^+$ objects were favored over stromal cell objects if these objects overlapped. Megakaryocyte objects were placed over DNA objects to avoid the separate segmentation of the megakaryocyte cytoplasm and nucleus (described above). Finally, the 3-layer single-cell mask with DNA$^+$, CD271$^+$ and CD31$^+$Vimentin$^-$ objects was exported from CellProfiler for each ROI and compared to the raw IMC images. Since CD271$^+$ objects were placed under DNA$^+$ and CD31$^+$Vimentin$^-$ objects in the cell segmentation mask, stromal cells were regularly split into multiple objects in the final 3-layer mask.

To optimize the quality of the recovered data and to reduce noise, semi-automated background removal by an interactive machine learning algorithm in Ilastik v1.3.2 was used to remove background signals from true signals and to create binary signal masks for each marker in the IMC panel. Background removal was performed as previously described[16] and returned binary signal masks for each marker in the IMC panel for every acquired ROI. To ensure proper noise removal, exported binary signal masks were compared to the original IMC images (unthresholded stainings) before proceeding to the next step in the segmentation pipeline.

Finally, to retrieve single-cell information from the IMC images, the 3-layer segmentation masks and corresponding binary signal masks were loaded into ImaCytE v1.0 and aligned for each ROI. Subsequently, a .fcs file with marker expression values for all identified cells was generated and exported for each ROI.

Cell clustering analysis

.fcs files of all $0.50 \cdot 10^6$ segmented cells from all acquired ROIs were loaded into OMIQ (Dotmatics) for data inspection. $0.04 \cdot 10^6$ cells were positive or negative for all markers of the IMC panel and/or were positive for the background channel ^{208}Pb and thus were excluded from the analysis. Subsequently, .fcs files of all remaining $0.46 \cdot 10^6$ cells were exported, ROI-tagged and imported in Cytosplore[18] for dimensionality reduction. A three-level hierarchical stochastic neighbor embedding (HSNE) clustering analysis was performed with default

perplexity and iterations (30 and 1000, respectively; see Figure S5 for HSNE analysis pipeline). Three of 37 markers in the IMC panel (CD19, CD57 and CD59) were not used in the HSNE clustering analysis; CD19 and CD59 stainings were suboptimal and CD57 staining was not performed on all bone marrow sections. Three major groups of cells of $\leq 0.5 \cdot 10^6$ cells were distinguished at the overview level of the HSNE analysis by Gaussian mean shift (GMS) clustering. Group 1 included cells expressing Collagen I, CXCL12, CD31, CD71 and/or CD271. Group 2 consisted of cells expressing CD3, CD7, CD20, CD27, CD127 and/or CD138. Group 3 included all remaining cells. Subsequently, each group of cells was selected for detailed analysis at the data level using t-distributed stochastic neighbor embedding (tSNE) analyses with up to $0.5 \cdot 10^6$ landmarks. A total of 236 clusters with distinct marker expression were identified within the three tSNEs by Gaussian mean shift (GMS) clustering. Next, .fcs files of all 236 phenotypes were exported and projected back onto the cell segmentation masks in ImaCytE to verify their marker expression profile in the unthresholded IMC stainings. All clusters except for a cluster of Collagen I$^+$ bone cells were then manually merged to 5 major cell types or to 42 cell subpopulations based on similarities in marker expression profile using Cytofast[15] in R v4.3.0 for analyses at the major cell type or cell subpopulation level, respectively. The phenotypes of all clusters of hematopoietic cells were confirmed in the raw images (Figure S6). To compare marker expression profiles and abundancies of all cell types between groups, .fcs files of major cell types or cell subpopulations were loaded into R and studied using the Cytofast pipeline[15]. Identified cell clusters were visualized using optSNE analyses performed in OMIQ (Dotmatics).

Identification of cellular neighborhoods and spatial context analyses

To evaluate the spatial distribution of cell subpopulations in the bone marrow from AA^{Dx}, AA^{6M} and controls, we performed cellular neighborhood analyses. XY coordinates of all segmented cells were extracted from CellProfiler and added to the .fcs files of the cell clusters identified in the HSNE analysis by aligning the data in R. Cellular neighborhood analyses were then performed for all acquired ROIs using the R package imcRtools[19]. Cells were grouped into 10 cellular neighborhoods by unbiased k-means clustering based on the phenotypes of their 20 nearest neighbors within a 25-pixel distance. Two of the identified neighborhoods were comparable in cellular composition and therefore were merged, resulting in a total of 9 neighborhoods. To interrogate the interactions of distinct neighborhoods, we performed spatial context analyses downstream of the cellular neighborhood analyses using default settings and a 50-nearest neighbor graph for spatial context detection, also with imcRtools. All further analyses and visualization of the neighborhoods were performed in R.

Supplemental tables

Table S1. Studied time points and patient characteristics.

Patient	Studied time points		Disease severity	Peripheral blood counts at diagnosis				Days between marrow sampling and start hATG	Response to IST	
	Dx	6M post-hATG		Hb (mmol/L)	Reticulocytes (·10⁹/L)	Thrombocytes (·10⁹/L)	Neutrophils (·10⁹/L)		6M post-hATG	>6M post-hATG if NR at 6M
AA2		NA	VSAA	4.2	5.3	20	0.02	7	PR	-
AA4			VSAA	4.9	4.6	15	0.01	17	NR	PR (9 months post-hATG)
AA5		NA	NSAA	5.9	39.2	31	2.73	30	PR	-
AA7		NA	SAA	5.7	13.6	24	0.37	49	NR	NA (underwent allo-HSCT)
AA8			VSAA	5.8	2.2	23	0.00	33	NR	NR
AA9			SAA	4.1	38.0	26	0.32	33	PR	-
AA10			VSAA	4.0	4.7	10	0.03	16	PR	-
AA11			VSAA	5.8	6.7	15	0.16	19	NR	PR (9 months post-hATG)
AA12			SAA	6.4	20.7	22	0.81	13	NR	PR (12 months post-hATG)
AA13			SAA	5.2	37.3	15	0.50	30	NR	PR (9 months post-hATG)
AA14			SAA	4.4	11.9	38	0.23	16	PR	-
AA15			SAA	5.3	10.0	15	0.35	6	CR	-
AA16			SAA	5.7	4.7	132	0.61	20	CR	-
AA17			SAA	4.8	4.2	38	0.02	133	NR	NR
AA18		NA	NSAA	3.9	60.0	14	0.81	52	PR	-
AA19			VSAA	5.4	5.8	12	0.04	56	NR	PR (9 months post-hATG)

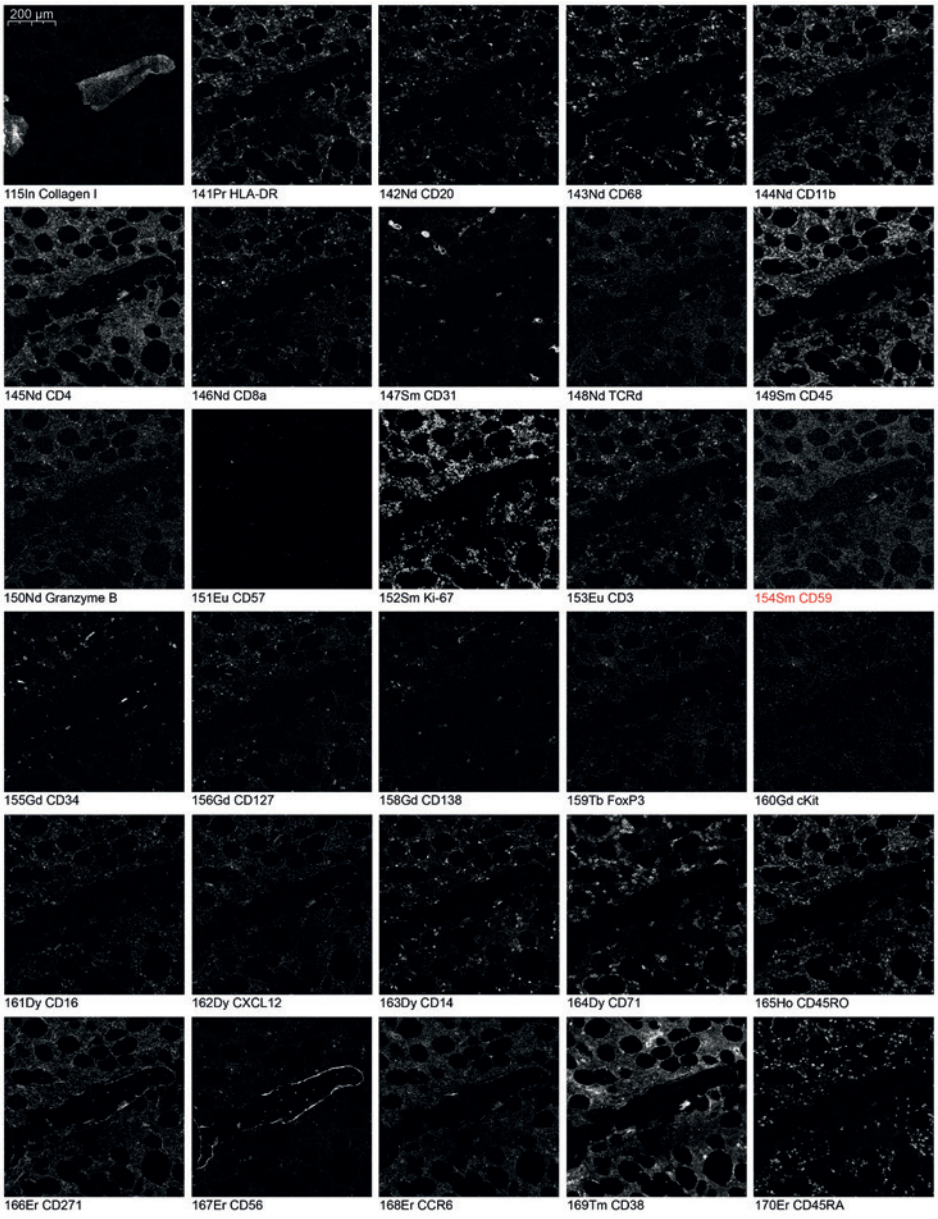
AA indicates aplastic anemia; CR: complete response; hATG: horse-derived anti-thymocyte globulin; Hb: hemoglobin; IST: immunosuppressive therapy; M: months; NA: not available; NR: no response; NSAA: non-severe AA; PR: partial response; SAA: severe AA; VSAA: very severe AA. Response to IST was defined as transfusion independence and a neutrophil count of ≥0.5·10^9 neutrophils/L. The distinction between partial and complete response to IST was made in accordance with the Dutch treatment guidelines. Response to IST ≥ 6 months post-hATG occurred either spontaneously or after eltrombopag (Revolade®, Novartis).

Table S2. 37-marker imaging mass cytometry panel.

Metal	Marker	Clone	Vendor	Dilution	Condition
115In	CollagenI	EPR7785	Abcam	1:100	ON 4°C
141Pr	HLA-DR	TAL-1B5	ThermoFisher	1:100	5H RT
142Nd	CD20	H1	BD Biosciences	1:100	ON 4°C
143Nd	CD68	D4B9C	Cell Signaling Technology	1:100	ON 4°C
144Nd	CD11b	D6X1N	Cell Signaling Technology	1:100	5H RT
145Nd	CD4	EPR6855	Abcam	1:200	Indirect
146Nd	CD8a	D8A8Y	Cell Signaling Technology	1:50	5H RT
147Sm	CD31	89C2	Cell Signaling Technology	1:100	ON 4°C
148Nd	TCRd	H-41	Santa Cruz	1:50	Indirect
149Sm	CD45	D9M8I	Cell Signaling Technology	1:50	ON 4°C
150Nd	Granzyme B	D6E9W	Cell Signaling Technology	1:100	5H RT
151Eu	CD57	HNK-1/Leu-7	Abcam	1:100	ON 4°C
152Sm	Ki-67	8D5	Cell Signaling Technology	1:100	ON 4°C
153Eu	CD3	D7A6E	Cell Signaling Technology	1:50	ON 4°C
154Sm	CD59	MEM-43/5	Exbio	1:50	ON 4°C
155Gd	CD34	QBEND/10	ThermoFisher	1:100	5H RT
156Gd	CD127	EPR23747-333	Abcam	1:50	5H RT
158Gd	CD138	MI15	BioLegend	1:100	5H RT
159Tb	FoxP3	D6O8R	Cell Signaling Technology	1:50	ON 4°C
160Gd	cKit (CD117)	D3W6Y	Cell Signaling Technology	1:50	5H RT
161Dy	CD16	D1N9L	Cell Signaling Technology	1:100	ON 4°C
162Dy	CXCL12 (SDF-1)	79018	R&D Systems	1:50	ON 4°C
163Dy	CD14	D7A2T	Cell Signaling Technology	1:100	5H RT
164Dy	CD71	H68.4	Invitrogen	1:100	5H RT
165Ho	CD45RO	UCHL1	Cell Signaling Technology	1:100	ON 4°C
166Er	CD271 (NGFR)	NGFR5	Abcam	1:50	ON 4°C
167Er	CD56	E7X9M	Cell Signaling Technology	1:100	5H RT
168Er	CCR6	EPR22259	Abcam	1:50	5H RT
169Tm	CD38	EPR4106	Abcam	1:100	ON 4°C
170Er	CD45RA	HI100	BioLegend	1:100	5H RT
171Yb	CD15	BRA-4F1	Cell Signaling Technology	1:100	ON 4°C
172Yb	CD19	D4V4B	Cell Signaling Technology	1:100	5H RT
173Yb	CD163	EPR14643-36	Abcam	1:50	5H RT
174Yb	CD7	EPR4242	Abcam	1:100	5H RT
175Lu	CD27	EPR8569	Abcam	1:100	ON 4°C
176Yb	CD11c	EP1347Y	Abcam	1:100	5H RT
194Pt	Vimentin	D21H3	Cell Signaling Technology	1:50	ON 4°C
191-193Ir	DNA	NA	Standard BioTools	1:100	5min RT

CCR indicates chemokine receptor; CD: cluster of differentiation; CXCL: C-X-C motif chemokine; HLA: Human Leukocyte Antigen; ON 4°C: overnight at 4°C; RT: room temperature; TCR: T-cell receptor; 5H RT: 5 hours at room temperature.

Supplemental figures



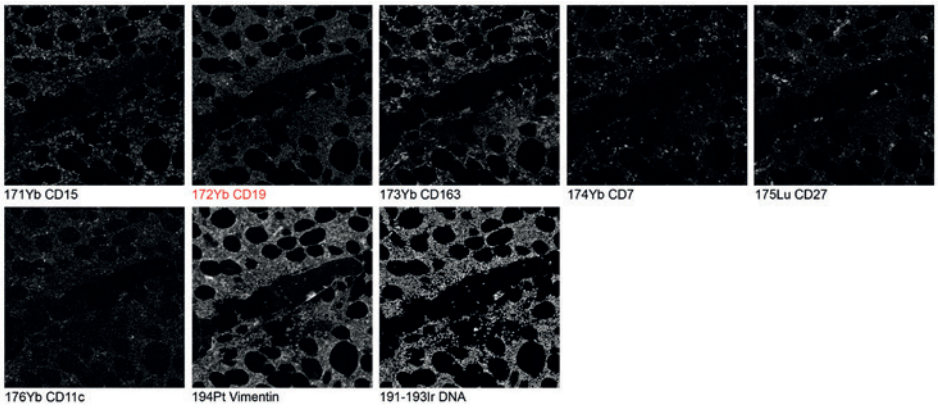
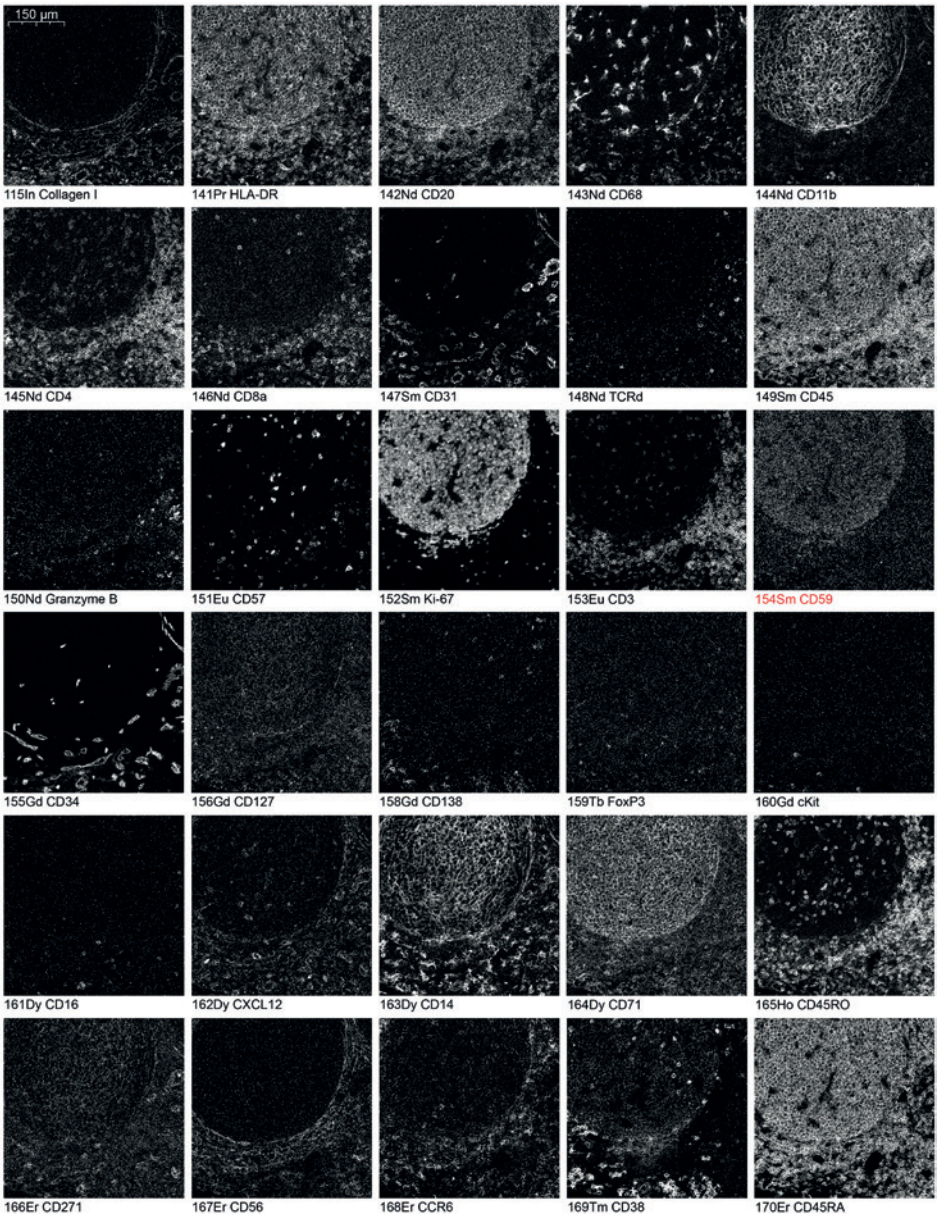


Figure S1. Performance of the 37-marker IMC panel for bone marrow on FFPE EDTA-decalcified bone marrow. Thresholded images of the staining results are shown for a representative control bone marrow ROI (Control5) with a surface area of 0.56mm^2. Suboptimal stainings excluded from downstream analyses are highlighted in red. CD59 stainings were weak and could not distinguish between CD59$^+$ and CD59$^-$ cells, as evaluated on a FFPE EDTA-decalcified bone marrow biopsy from a PNH patient with 98% GPI-negative clones in peripheral blood. CD19 stainings showed co-expression of CD19 and CD20 in FFPE EDTA-decalcified tonsil, but did not produce a similar result in FFPE EDTA-decalcified bone marrow.


150 µm
115In Collagen I
141Pr HLA-DR
142Nd CD20
143Nd CD68
144Nd CD11b
145Nd CD4
146Nd CD8a
147Sm CD31
148Nd TCRd
149Sm CD45
150Nd Granzyme B
151Eu CD57
152Sm Ki-67
153Eu CD3
154Sm CD59
155Gd CD34
156Gd CD127
158Gd CD138
159Tb FoxP3
160Gd cKit
161Dy CD16
162Dy CXCL12
163Dy CD14
164Dy CD71
165Ho CD45RO
166Er CD271
167Er CD56
168Er CCR6
169Tm CD38
170Er CD45RA

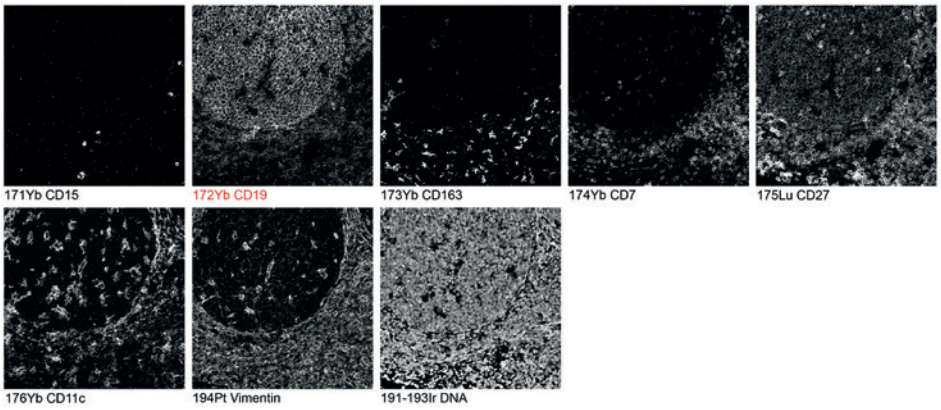


Figure S2. Performance of the 37-marker IMC panel for bone marrow on FFPE EDTA-decalcified tonsil. Thresholded images of the staining results are shown for FFPE EDTA-decalcified human tonsil with a surface area of 0.25mm^2, which was used as a positive control to confirm panel performance on decalcified tissue. Suboptimal stainings excluded from downstream analyses are highlighted in red. CD59 stainings were weak and could not distinguish between CD59$^+$ and CD59$^-$ cells, as evaluated on a FFPE EDTA-decalcified bone marrow biopsy from a PNH patient with 98% GPI-negative clones in peripheral blood. CD19 stainings showed co-expression of CD19 and CD20 in FFPE EDTA-decalcified tonsil, but did not produce a similar result in FFPE EDTA-decalcified bone marrow.

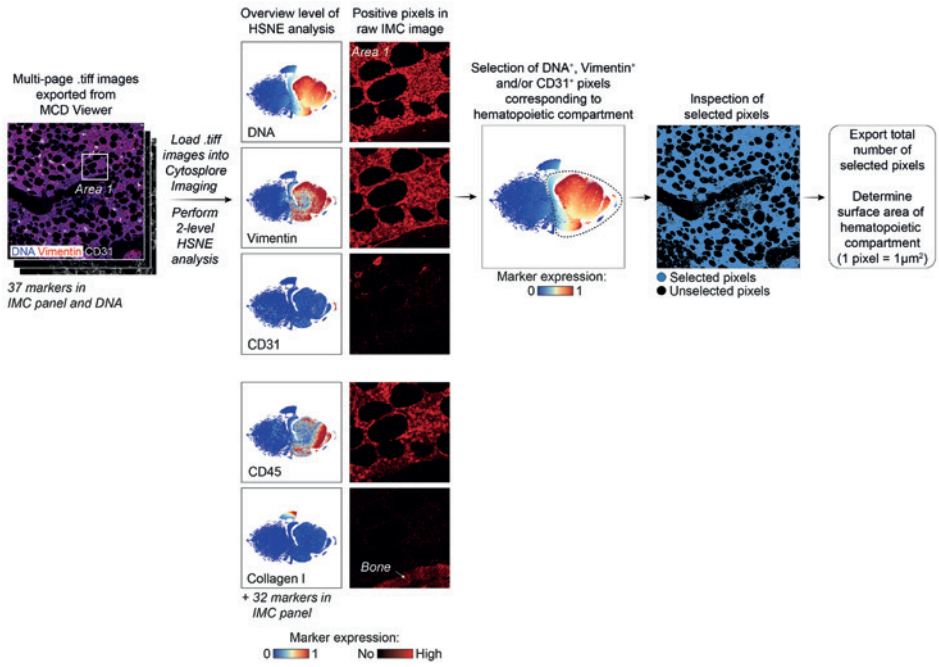


Figure S3. Approach used to determine the surface area of the hematopoietic compartment in Cytosplore Imaging. The analysis pipeline is illustrated for a representative control ROI (Control5). For each ROI, multi-page .tiff files were exported from MCD Viewer and loaded into Cytosplore Imaging for dimensionality reduction. A 2-level HSNE analysis was run for all pixels in each ROI. At the overview level of the 2-level HSNE analysis, all pixels in the ROI were summarized into landmarks based on similarities in marker expression intensities. Visualization of all markers of the 37-marker IMC panel and DNA in the HSNE showed the presence of DNA^+, $Vimentin^+$, $CD31^+$, $CD45^+$ and/or Collagen I^+ pixels in each ROI image. DNA^+ pixels captured cellular nuclei; $Vimentin^+$ pixels captured cytoplasm and cell membrane; $CD31^+$ pixels captured the $Vimentin^-$ cytoplasm of megakaryocytes. Vimentin stained both non-hematopoietic and hematopoietic cells and therefore captured a broader range of cells than the hematopoietic cell marker CD45. Next, DNA^+, $Vimentin^+$ and/or $CD31^+$ pixels were selected and inspected by projecting all selected pixels back on to the ROI image. Finally, the total number of selected pixels was determined and the surface area of the hematopoietic compartment was calculated (where 1 pixel = $1\mu m^2$).

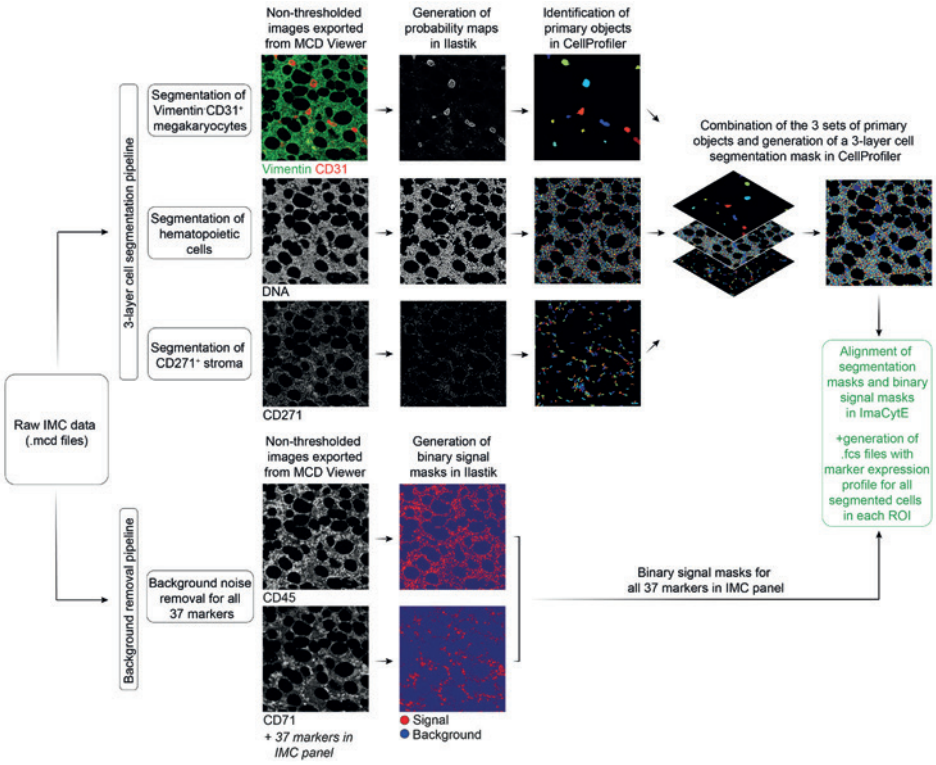


Figure S4. Cell segmentation pipeline. To extract single-cell information from the high-dimensional images, a 3-step cell segmentation pipeline was applied on all acquired ROIs. The pipeline is shown for a representative control ROI (Control5). Step 1) Generation of a cell segmentation mask. A 3-layer cell segmentation mask was generated for each ROI in the IMC dataset. For proper segmentation of megakaryocytes, hematopoietic cells and stromal cells separate cell segmentation masks were generated for each of these cell types. First, raw (non-thresholded) images of the Vimentin and CD31, DNA and CD271 stainings were exported from MCD Viewer and imported in Ilastik to generate probability maps by pixel classification. Subsequently, all probability maps were loaded into CellProfiler to create a segmentation mask for based on each probability map, which were then stacked to generate the final 3-layer cell segmentation mask. Step 2) Generation of binary signal masks for background noise removal. Raw (non-thresholded) images were exported from MCD Viewer for all 37 markers in the IMC panel and all ROIs in the IMC dataset. Next, true marker signals were distinguished from background noise by performing pixel classification in Ilastik. Subsequently, the generated thresholded binary signal masks were exported. Step 3) Alignment of segmentation masks and binary signal masks. Finally, to generate .fcs files with marker expression values for every segmented cell in each ROI, 3-layer segmentation masks and their corresponding thresholded binary signal masks were imported in ImaCytE and aligned. .fcs files were exported for each acquired ROI separately.

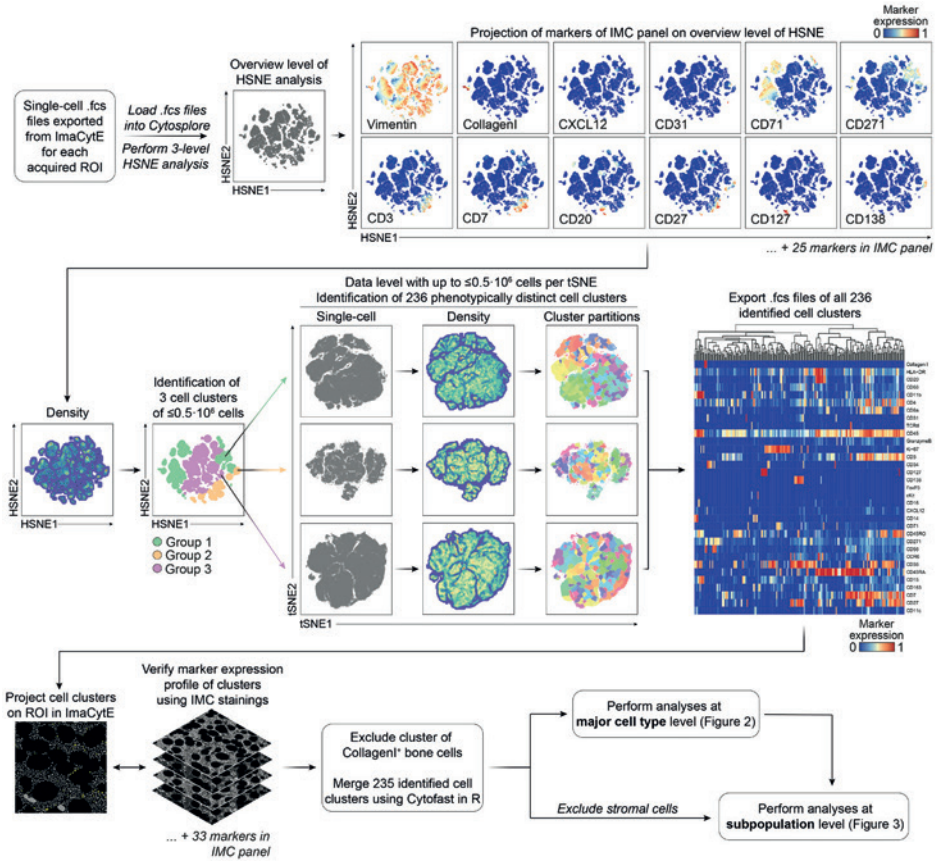
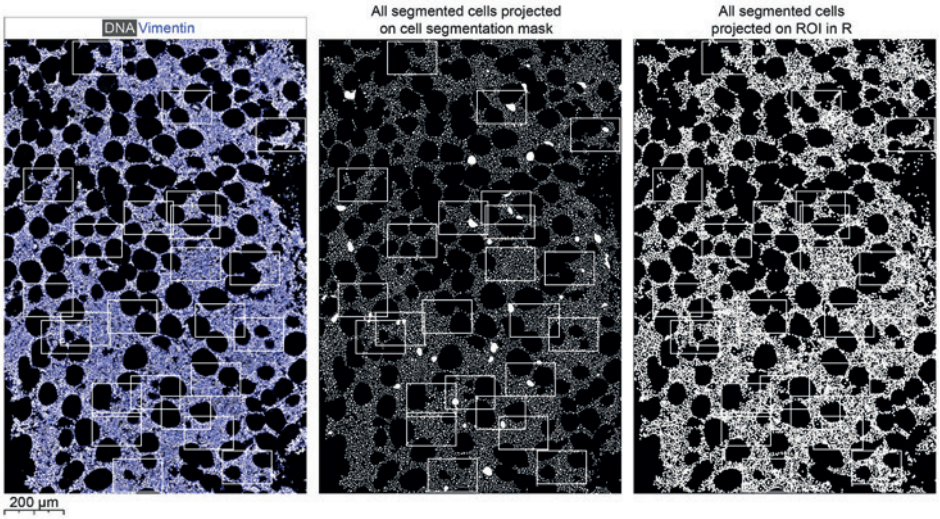
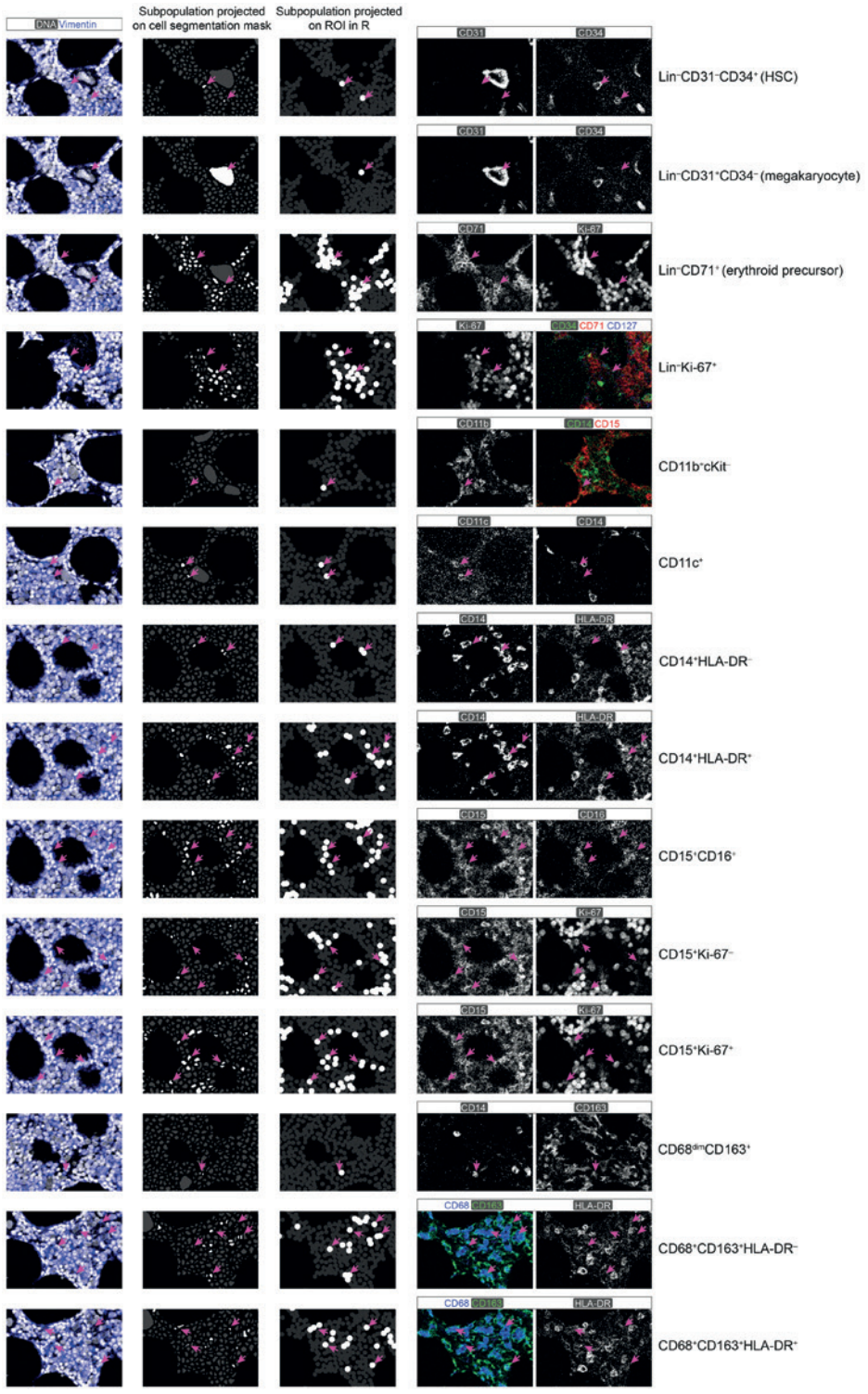
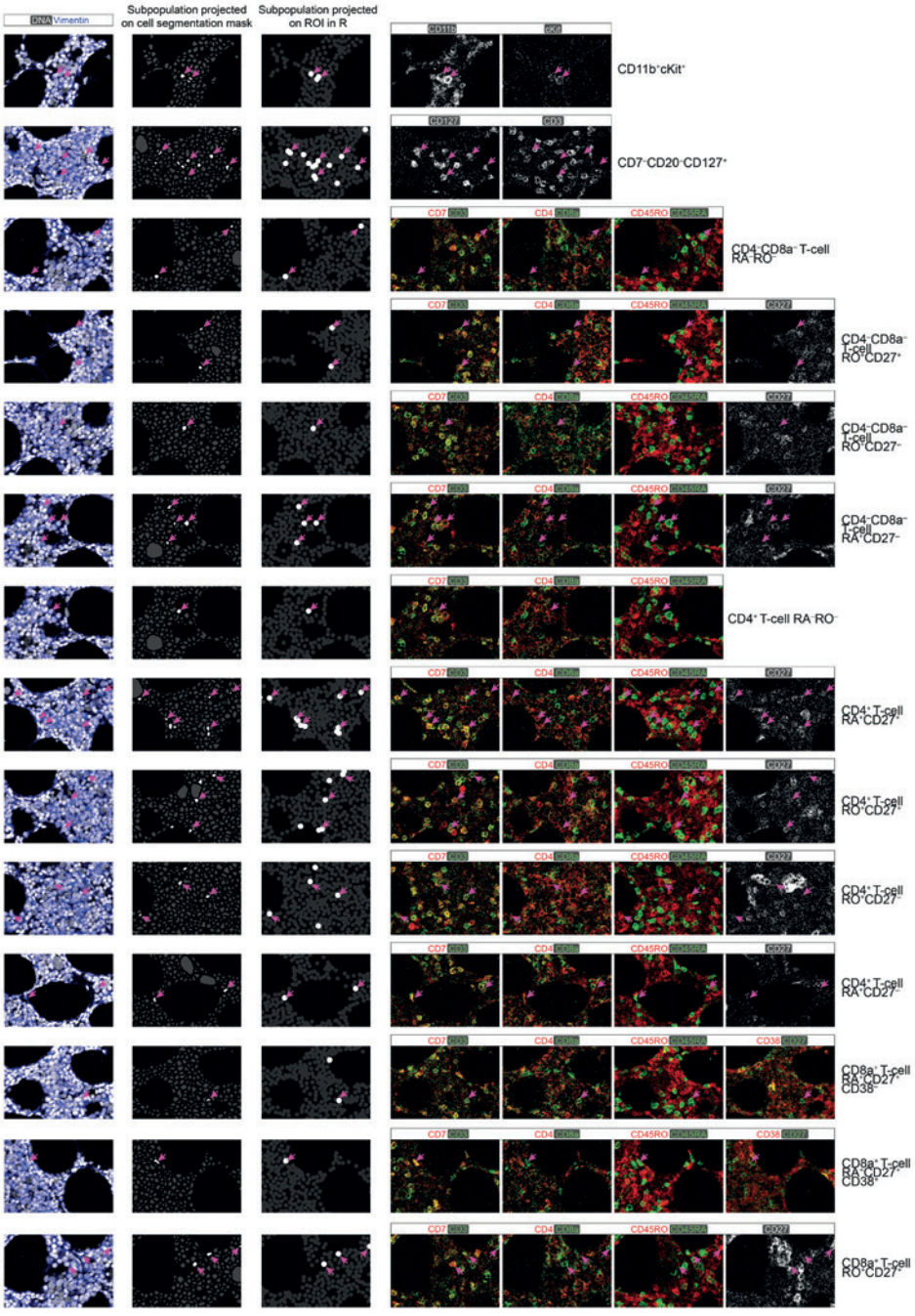


Figure S5. Cell clustering analysis pipeline. To compare the cellular composition of the bone marrow from AA patients at diagnosis, AA patients post-hATG and controls, the $0.52 \cdot 10^6$ cells segmented from all ROIs were analyzed using a 3-level HSNE analysis in Cytosplore. At the overview level of the HSNE analysis, the $0.52 \cdot 10^6$ cells were clustered into three groups of cells. Group 1 included cells expressing Collagen I, CXCL12, CD31, CD71 and/or CD271. Group 2 consisted of cells expressing CD3, CD7, CD20, CD27, CD127 and/or CD138. Group 3 included all remaining cells. Next, each group of cells was studied and clustered at the data level of the 3-level HSNE analysis. 236 phenotypically distinct cell clusters were identified. To verify the marker expression profile of each identified cell cluster, all clusters were projected back onto the cell segmentation mask in ImaCytE. Subsequently, the ImaCytE images were compared to the unthresholded IMC stainings. Finally, the 236 identified cell clusters were merged in R for downstream analysis at the major cell type or subpopulation level.


DNA Vimentin
All segmented cells projected on cell segmentation mask
All segmented cells projected on ROI in R
200 µm


DNA Vimentin
Subpopulation projected on cell segmentation mask
Subpopulation projected on ROI in R
CD31
CD34
Lin⁻CD31⁻CD34⁺ (HSC)
CD31
CD34
Lin⁻CD31⁺CD34⁻ (megakaryocyte)
CD71
Ki-67
Lin⁻CD71⁺ (erythroid precursor)
Ki-67
CD34 CD71 CD127
Lin⁻Ki-67⁺
CD11b
CD15 CD15
CD11b⁺cKit⁻
CD11c
CD14
CD11c⁺
CD14
HLA-DR
CD14⁺HLA-DR⁻
CD14
HLA-DR
CD14⁺HLA-DR⁺
CD15
CD16
CD15⁺CD16⁺
CD15
Ki-67
CD15⁺Ki-67⁻
CD15
Ki-67
CD15⁺Ki-67⁺
CD14
CD163
CD68dimCD163⁺
CD68 CD163
HLA-DR
CD68⁺CD163⁺HLA-DR⁻
CD68 CD163
HLA-DR
CD68⁺CD163⁺HLA-DR⁺


DNA Vimentin
Subpopulation projected on cell segmentation mask
Subpopulation projected on ROI in R
CD11b
cKit
CD11b+cKit+
CD127
CD3
CD7-CD20-CD127+
CD7
CD20
CD4
CD8a
CD45RO
CD45RA
CD4-CD8a- T-cell RA-RO-
CD27
CD4-CD8a- T-cell RO+CD27+
CD4-CD8a- T-cell RO+CD27-
CD4-CD8a- T-cell RA+CD27-
CD4+ T-cell RA-RO-
CD4+ T-cell RA+CD27+
CD4+ T-cell RO+CD27+
CD4+ T-cell RO+CD27-
CD4+ T-cell RA+CD27-
CD38
CD8a+ T-cell RA-CD27+CD38-
CD8a+ T-cell RA-CD27+CD38+
CD8a+ T-cell RO+CD27+

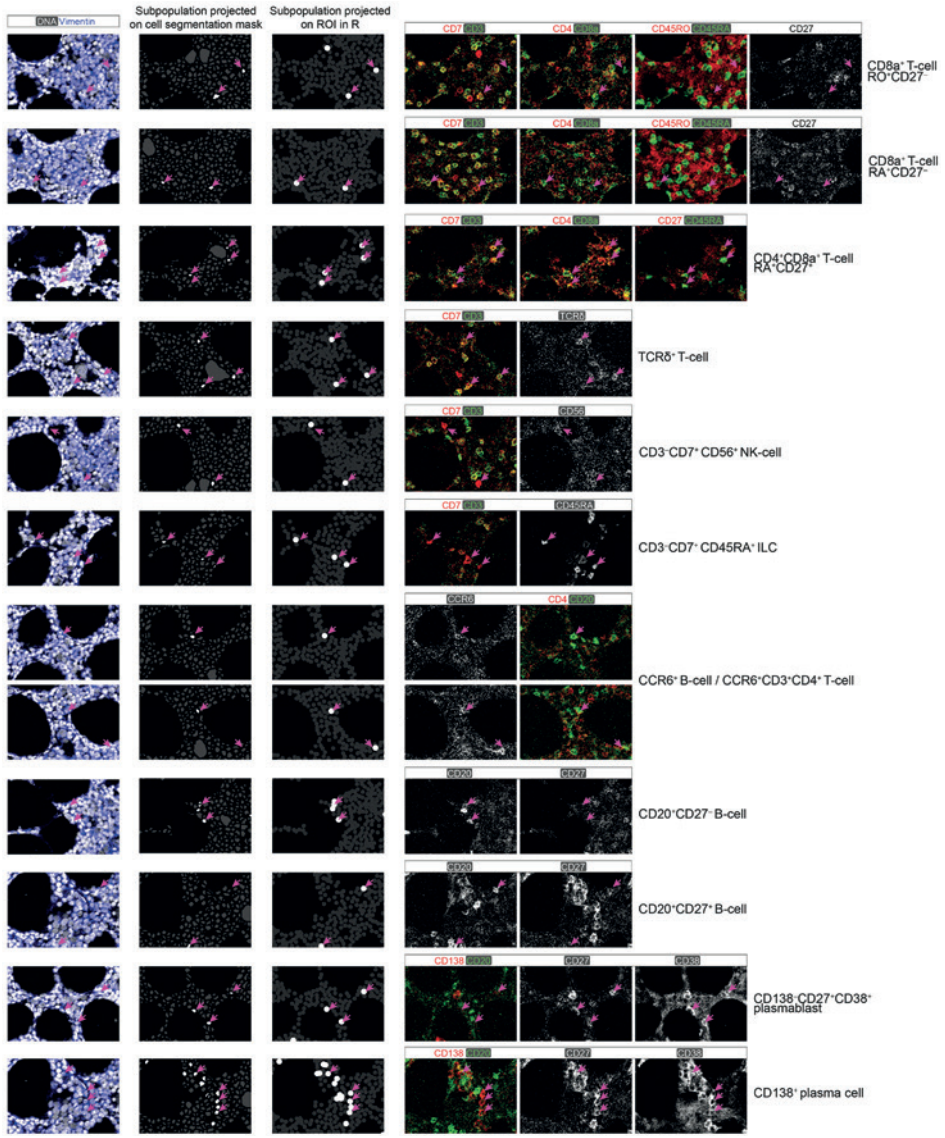


Figure S6. Confirmation of identified phenotypes in raw IMC stainings. Raw IMC stainings and identified hematopoietic cell subpopulations are shown throughout different regions of a representative control ROI (Control5). Identified subpopulations are visualized in both the cell segmentation mask and the images acquired during the data analysis pipeline in R.

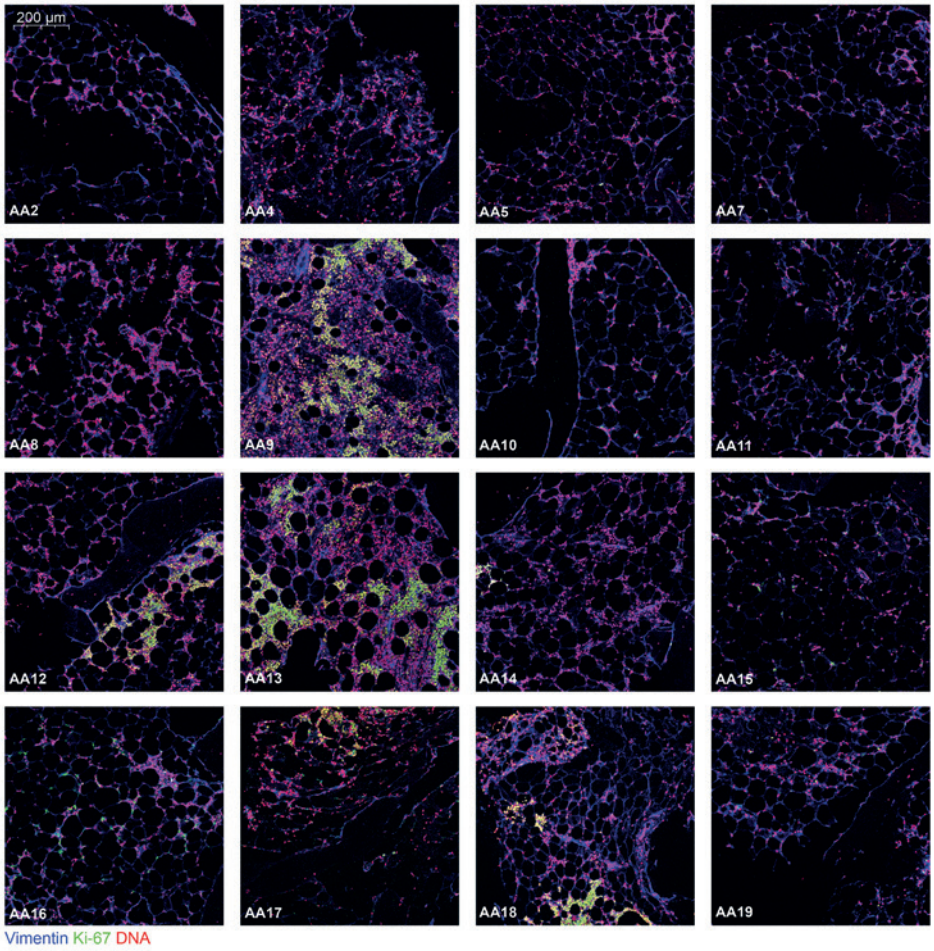


Figure S7. Global architecture of the bone marrow from all AA patients at diagnosis. Vimentin (blue) stains all hematopoietic cells and their microenvironment, DNA (red) stains all cellular nuclei, Ki-67 stains all proliferating cells. One imaged region of interest (ROI) is shown for each patient.

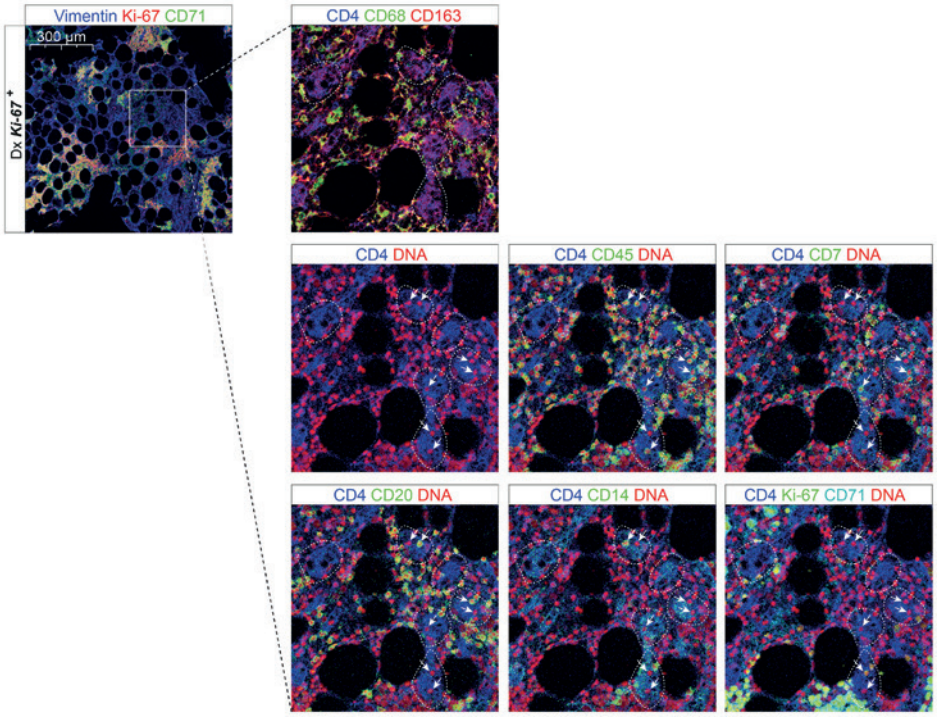


Figure S8. Hematopoietic cell populations within the CD4^{+}CD68^{-}CD163^{+} macrophages in Ki-67^{+} regions from AA^{Dx}. CD4^{+}CD68^{-}CD163^{+} macrophages in the bone marrow from a representative AA^{Dx} are indicated with white dotted circles. Cells within the CD4^{+}CD68^{-}CD163^{+} macrophages are indicated by arrows. DNA stains cellular nuclei; CD45 stains all hematopoietic cells; CD7 stains T-cells and innate lymphoid cells; CD20 stains B-cells; CD14 stains monocytes; Ki-67 and CD71 stain erythroid precursors.

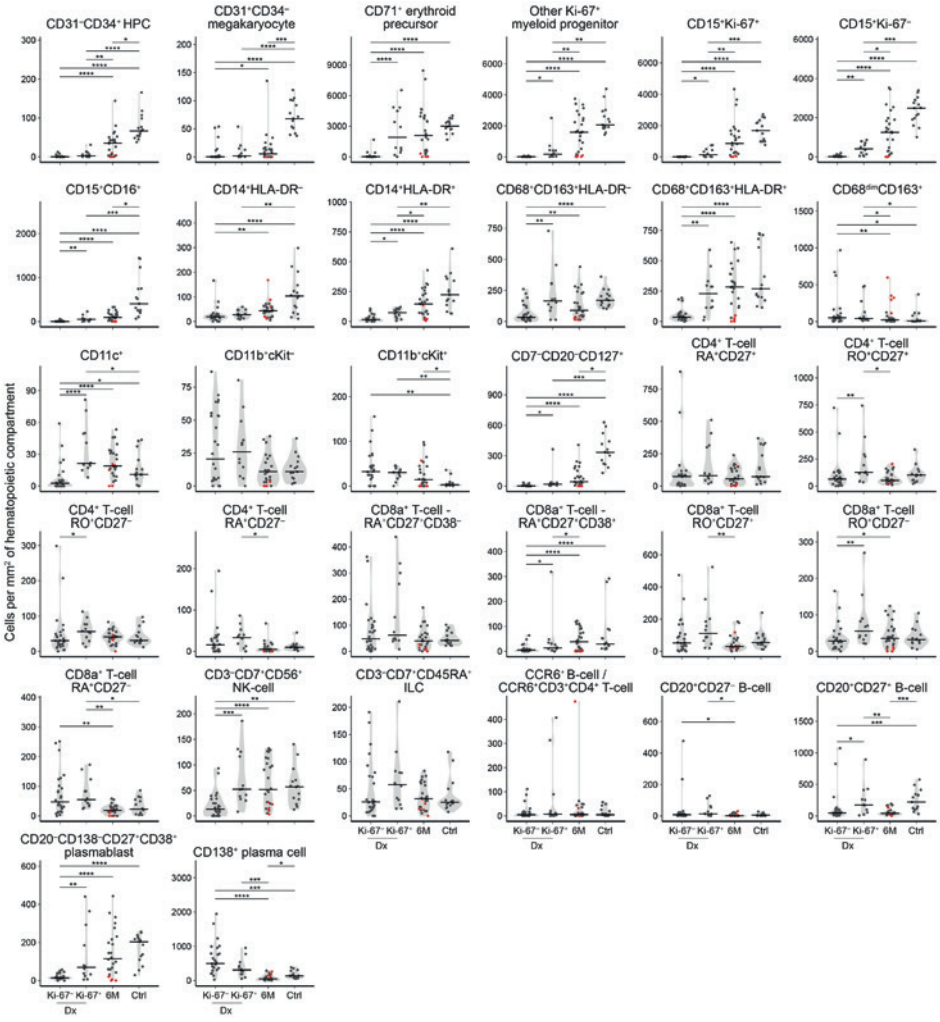
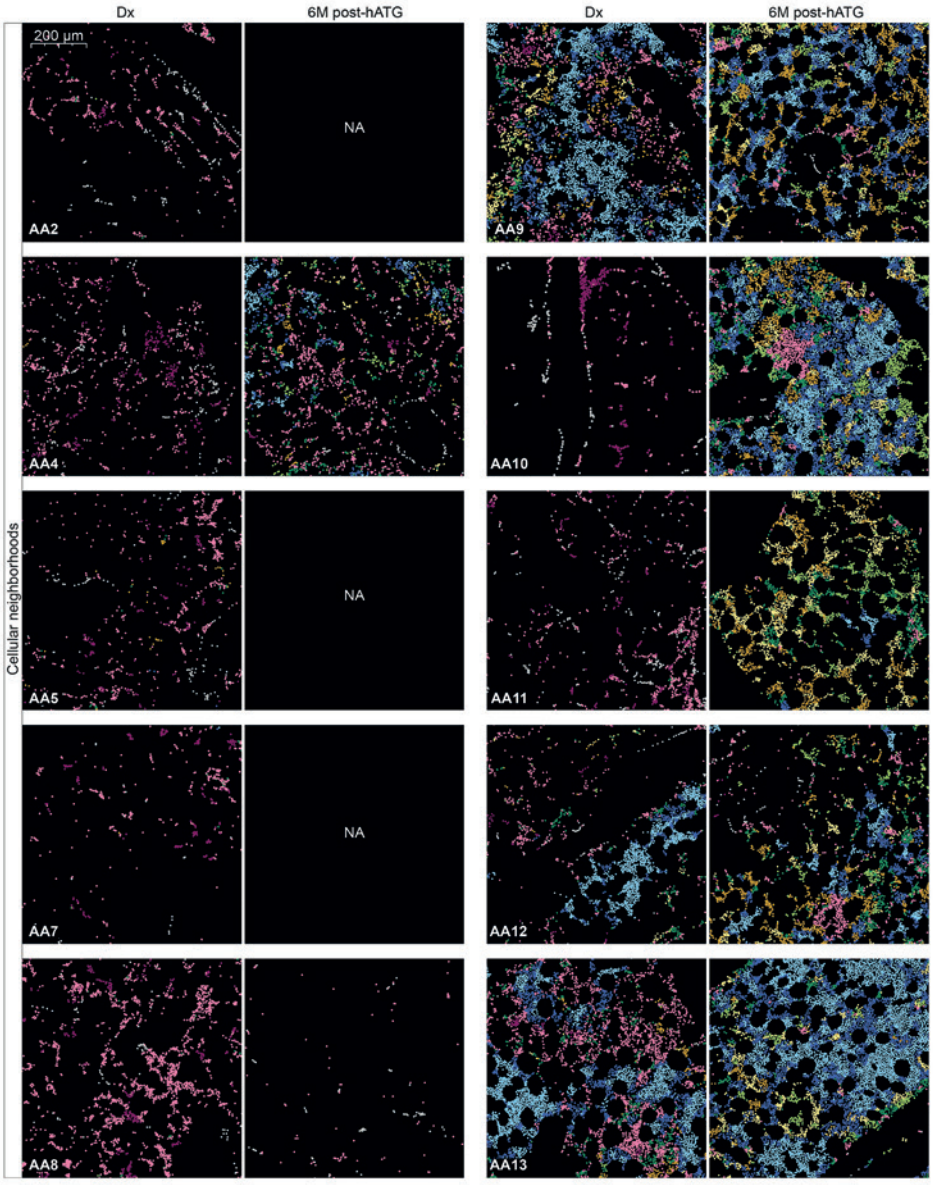


Figure S9. Abundancies of identified phenotypes in ROIs. Abundancies of identified progenitor, mature myeloid, CD4⁺ T-cell, CD8⁺ T-cell, ILC, B-cell and plasma cell subpopulations are shown as an absolute count per mm^2 of hematopoietic compartment. Each dot represents one ROI; red dots represent patients with a non-normalized bone marrow 6M post-hATG. Horizontal bars present group median.


Dx
6M post-hATG
Dx
6M post-hATG
200 µm
NA
AA2
AA9
AA4
AA10
NA
AA5
AA11
NA
AA7
AA12
AA8
AA13
Cellular neighborhoods

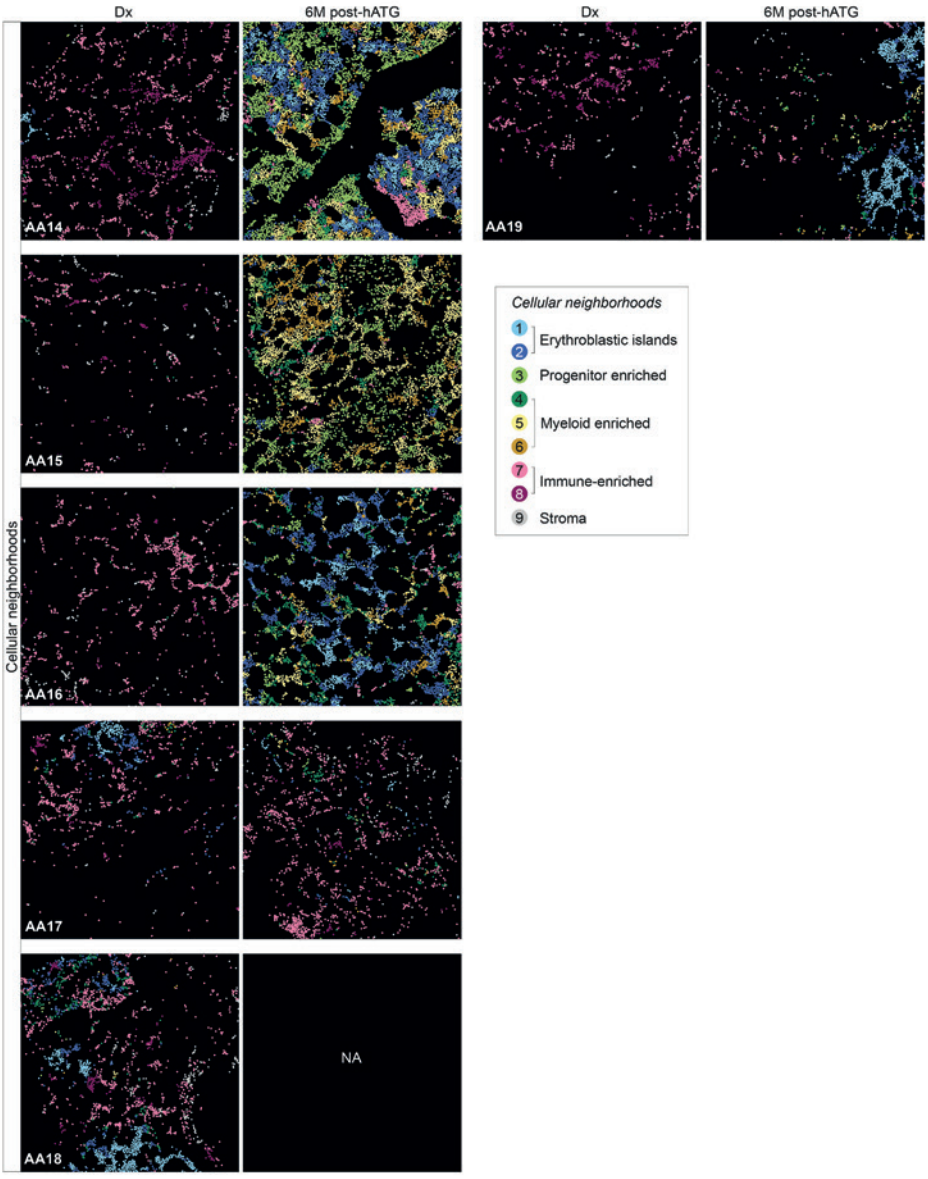


Figure S10. Visualization of all identified cellular neighborhoods in all AA patients at diagnosis and 6M post-hATG. Cellular neighborhoods visualized in a representative ROI from each AA^{Dx} (n=16) and AA^{6M} (n=12). Bone marrow tissue samples were not studied for 4 of 16 AA patients 6M post-hATG. Colors indicate cellular neighborhoods, each dot represents one segmented cell.

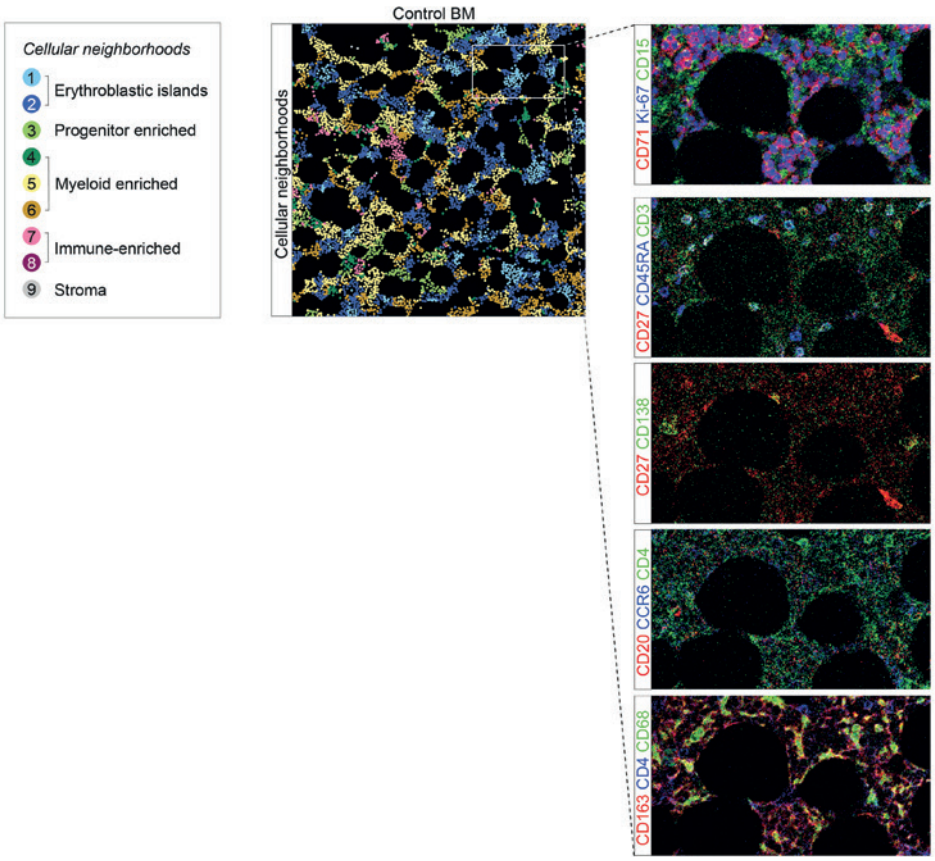


Figure S11. Immune cells subpopulations within the erythroblastic islands in control bone marrow. Left: Cellular neighborhoods visualized in a representative control ROI. Colors indicate cellular neighborhoods, each dot represents one segmented cell. Right: Cell subpopulations visualized within the erythroblastic islands in the control ROI. Top panel: Visualization of $CD71^{+}Ki\text{-}67^{+}$ erythroid precursors (red cells with blue nucleus) or $CD15^{+}Ki\text{-}67^{+}$ neutrophil progenitors (green cells with blue nucleus). Second panel: Visualization of $CD3^{+}$ T-cell populations in multiple differentiation stages. Third panel: Visualization of $CD138^{+}CD27^{+}$ plasma cells. Fourth panel: Visualization of ($CCR6^{+}$) $CD20^{+}$ B-cells and $CD4^{+}$ T-cells. Fifth panel: Visualization of macrophages using CD4, CD68 and CD163.

References

1. Young NS. Aplastic Anemia. *N Engl J Med*. 2018;379(17):1643-1656.
2. Halkes CJ, Veelken H, Falkenburg JH. Horse versus rabbit antithymocyte globulin in aplastic anemia. *N Engl J Med*. 2011;365(19):1842-1843; author reply 1843-1844.
3. Scheinberg P, Nunez O, Weinstein B, et al. Horse versus rabbit antithymocyte globulin in acquired aplastic anemia. *N Engl J Med*. 2011;365(5):430-438.
4. Kulasekararaj A, Cavenagh J, Dokal I, et al. Guidelines for the diagnosis and management of adult aplastic anaemia: A British Society for Haematology Guideline. *Br J Haematol*. 2024;204(3):784-804.
5. Peffault de Latour R, Kulasekararaj A, Iacobelli S, et al. Eltrombopag Added to Immunosuppression in Severe Aplastic Anemia. *N Engl J Med*. 2022;386(1):11-23.
6. Pool ES, Kooy-Winkelaar Y, van Unen V, et al. Mass cytometric analysis unveils a disease-specific immune cell network in the bone marrow in acquired aplastic anemia. *Front Immunol*. 2023;14:1274116.
7. Takaku T, Malide D, Chen J, Calado RT, Kajigaya S, Young NS. Hematopoiesis in 3 dimensions: human and murine bone marrow architecture visualized by confocal microscopy. *Blood*. 2010;116(15):e41-55.
8. Tjon JM-L, Zeerleder SS, Groot MRd, et al. Diagnostiek en behandeling verworven aplastische anemie bij volwassenen. *Nederlandse Vereniging voor Hematologie*. 2019.
9. Ijsselsteijn ME, van der Breggen R, Farina Sarasqueta A, Koning F, de Miranda N. A 40-Marker Panel for High Dimensional Characterization of Cancer Immune Microenvironments by Imaging Mass Cytometry. *Front Immunol*. 2019;10:2534.
10. Krop J, van der Zwan A, Ijsselsteijn ME, et al. Imaging mass cytometry reveals the prominent role of myeloid cells at the maternal-fetal interface. *iScience*. 2022;25(7):104648.
11. Ouboter LF, Lindelauf C, Jiang Q, et al. Activated HLA-DR+CD38+ Effector Th1/17 Cells Distinguish Crohn's Disease-associated Perianal Fistulas from Cryptoglandular Fistulas. *Inflamm Bowel Dis*. 2024.
12. Dieckman T, Schreurs M, Mahfouz A, et al. Single-Cell Analysis of Refractory Celiac Disease Demonstrates Inter- and Intra-Patient Aberrant Cell Heterogeneity. *Cell Mol Gastroenterol Hepatol*. 2022;14(1):173-192.
13. Uhlen M, Karlsson MJ, Zhong W, et al. A genome-wide transcriptomic analysis of protein-coding genes in human blood cells. *Science*. 2019;366(6472).
14. Ponten F, Jirstrom K, Uhlen M. The Human Protein Atlas--a tool for pathology. *J Pathol*. 2008;216(4):387-393.
15. Beyrend G, Stam K, Hollt T, Ossendorp F, Arens R. Cytofast: A workflow for visual and quantitative analysis of flow and mass cytometry data to discover immune signatures and correlations. *Comput Struct Biotechnol J*. 2018;16:435-442.
16. Ijsselsteijn ME, Somarakis A, Lelieveldt BPF, Hollt T, de Miranda N. Semi-automated background removal limits data loss and normalizes imaging mass cytometry data. *Cytometry A*. 2021;99(12):1187-1197.
17. Stirling DR, Swain-Bowden MJ, Lucas AM, Carpenter AE, Cimini BA, Goodman A. CellProfiler 4: improvements in speed, utility and usability. *BMC Bioinformatics*. 2021;22(1):433.
18. Hollt T, Pezzotti N, van Unen V, et al. Cytosplore: Interactive Immune Cell Phenotyping for Large Single-Cell Datasets. *Computer Graphics Forum*. 2016;35(3):171-180.
19. Windhager J, Zanotelli VRT, Schulz D, et al. An end-to-end workflow for multiplexed image processing and analysis. *Nat Protoc*. 2023;18(11):3565-3613.

20. Somarakis A, Van Unen V, Koning F, Lelieveldt B, Hollt T. ImaCytE: Visual Exploration of Cellular Micro-Environments for Imaging Mass Cytometry Data. *IEEE Trans Vis Comput Graph*. 2021;27(1):98-110.

21. Vaht K, Brenner J, Ednersson SB, Ljungman P, Brune M, Andersson PO. Bone marrow expression of CD68/CD163 macrophages, IL-17 and FOXP3 cells in aplastic anemia and their relation to prognosis. *Eur J Haematol*. 2023;110(3):313-321.

22. Zhang X, Song B, Carlino MJ, et al. An immunophenotype-coupled transcriptomic atlas of human hematopoietic progenitors. *Nat Immunol*. 2024;25(4):703-715.

23. Wu Q, Zhang J, Kumar S, et al. Resilient anatomy and local plasticity of naive and stress haematopoiesis. *Nature*. 2024;627(8005):839-846.

24. Han X, Jorgensen JL, Brahmandam A, et al. Immunophenotypic study of basophils by multiparameter flow cytometry. *Arch Pathol Lab Med*. 2008;132(5):813-819.

25. Welker P, Grabbe J, Zuberbier T, Guhl S, Henz BM. Mast cell and myeloid marker expression during early in vitro mast cell differentiation from human peripheral blood mononuclear cells. *J Invest Dermatol*. 2000;114(1):44-50.

26. Agematsu K, Hokibara S, Nagumo H, Komiyama A. CD27: a memory B-cell marker. *Immunol Today*. 2000;21(5):204-206.

27. de Latour RP, Visconte V, Takaku T, et al. Th17 immune responses contribute to the pathophysiology of aplastic anemia. *Blood*. 2010;116(20):4175-4184.

28. Kordasti S, Marsh J, Al-Khan S, et al. Functional characterization of CD4+ T cells in aplastic anemia. *Blood*. 2012;119(9):2033-2043.

29. Kordasti S, Costantini B, Seidl T, et al. Deep phenotyping of Tregs identifies an immune signature for idiopathic aplastic anemia and predicts response to treatment. *Blood*. 2016;128(9):1193-1205.

30. Bandyopadhyay S, Duffy MP, Ahn KJ, et al. Mapping the cellular biogeography of human bone marrow niches using single-cell transcriptomics and proteomic imaging. *Cell*. 2024;187(12):3120-3140 e3129.

31. Kook H, Zeng W, Guibin C, Kirby M, Young NS, Maciejewski JP. Increased cytotoxic T cells with effector phenotype in aplastic anemia and myelodysplasia. *Exp Hematol*. 2001;29(11):1270-1277.

32. Hu X, Gu Y, Wang Y, Cong Y, Qu X, Xu C. Increased CD4+ and CD8+ effector memory T cells in patients with aplastic anemia. *Haematologica*. 2009;94(3):428-429.

33. Zaimoku Y, Patel BA, Kajigaya S, et al. Deficit of circulating CD19(+) CD24(hi) CD38(hi) regulatory B cells in severe aplastic anaemia. *Br J Haematol*. 2020;190(4):610-617.

34. Gascon P, Zoumbos N, Young N. Analysis of natural killer cells in patients with aplastic anemia. *Blood*. 1986;67(5):1349-1355.

35. Vissers LTW, van Ostaijen-Ten Dam MM, Melsen JE, et al. Potential role of B- and NK-cells in the pathogenesis of pediatric aplastic anemia through deep phenotyping. *Front Immunol*. 2024;15:1328175.

36. Ben Hamza A, Welters C, Stadler S, et al. Virus-reactive T cells expanded in aplastic anemia eliminate hematopoietic progenitor cells by molecular mimicry. *Blood*. 2024.

37. Berg S, Kutra D, Kroeger T, et al. ilastik: interactive machine learning for (bio)image analysis. *Nat Methods*. 2019;16(12):1226-1232.



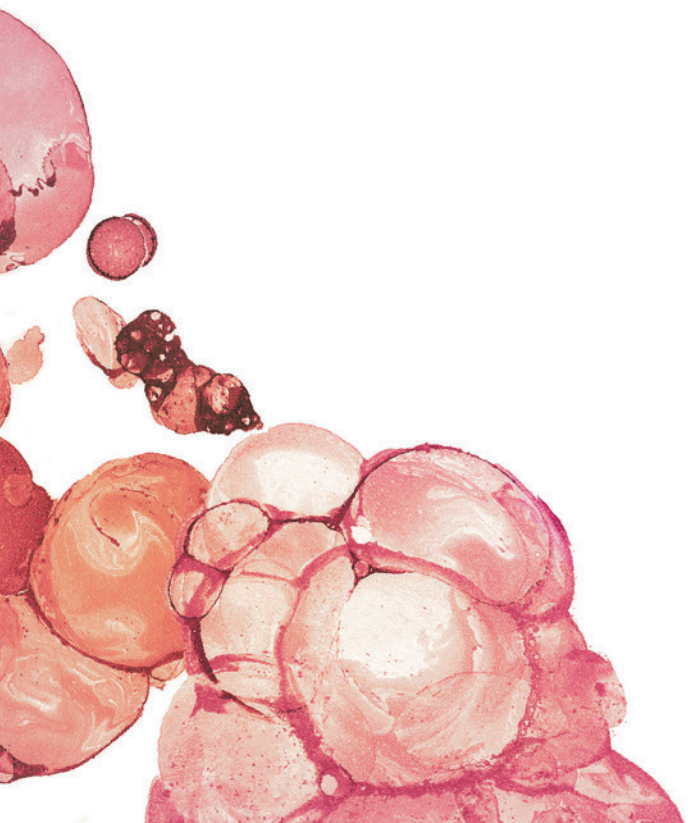
4

Selective lymphodepletion underlies the efficacy of horse anti-thymocyte globulin-based immunosuppressive therapy in aplastic anemia

Emma S. Pool[1], Cilia R. Pothast[1], Shannah M. Gennesse[1], Esther H.M. van Egmond[1], Julia M. Giezen[2], Sabrina A.J. Veld[1], René E.M. Toes[2], Frits Koning[3], Constantijn J.M. Halkes[1], Mirjam H.M. Heemskerk[1], Dirk Jan A.R. Moes[4] and Jennifer M-L. Tjon[1]

[1] Department of Hematology, Leiden University Medical Center, Leiden, The Netherlands
[2] Department of Rheumatology, Leiden University Medical Center, Leiden, The Netherlands
[3] Department of Immunology, Leiden University Medical Center, Leiden, The Netherlands
[4] Department of Clinical Pharmacy and Toxicology, Leiden University Medical Center, Leiden, The Netherlands

Haematologica (2026)
DOI: 10.3324/haematol.2025.300002



Key points

- ATGAM exposure varies substantially between AA patients, with higher exposure levels associating with earlier hematologic recovery
- Successful IST involves selective depletion of pathogenic T cells by ATGAM, and suppression of remaining CCR6^{+} T and B cells by ciclosporin

Abstract

Horse-derived anti-thymocyte globulin (ATGAM) in combination with long-term ciclosporin is the first-line treatment for most immune-mediated aplastic anemia (AA) patients. The exact impact of this immunosuppressive therapy (IST) on hematological recovery and the immune landscape, however, remains poorly understood. We report a longitudinal analysis of the pharmacodynamic effects of ATGAM-based IST in a cohort of 44 AA patients. With flow cytometry we quantified plasma levels of lymphocyte-binding ATGAM, which is believed to mediate the therapeutic effect. Population pharmacokinetic modeling revealed substantial between-patient variability in ATGAM exposure, with higher exposure levels associating to earlier hematologic recovery. ATGAM bound all lymphoid lineages and profoundly depleted T- and NK-cells at high plasma concentrations. Strikingly, ATGAM did not deplete B-cells but instead induced an increase of CD27^{+} B-cells. Deep immunophenotyping on series of peripheral blood samples collected up to three years after the start of IST demonstrated that ATGAM induced rapid depletion of T-cells, including KLRG1^{+} terminally differentiated CD8^{+} T-cells and Th17-like CCR6^{+}CD4^{+} T-cells. Although naïve and pathogen-specific T-cells were also depleted, they recovered quickly, indicating preservation of protective immunity. Notably, CCR6^{++} B-cells, implicated in AA pathogenesis, escaped ATGAM depletion but reduced gradually over time along with residual potentially pathogenic T-cells, including the CCR6^{+}CD4^{+} T-cells. This could explain the crucial contribution of long-term ciclosporin to successful IST. Collectively, our results identify ATGAM exposure as a factor influencing hematologic recovery, and indicate that the therapeutic effect of IST goes beyond total lymphodepletion but is rather the result of selective depletion and suppression of key lymphocyte subpopulations.

Introduction

Immune-mediated aplastic anemia (AA) is a bone marrow failure syndrome caused by an autoimmune attack on the hematopoietic stem and progenitor cells (HSPCs)[1]. The resulting peripheral cytopenias can lead to severe bleeding and infections. Effective treatments are allogeneic hematopoietic stem cell transplantation (allo-HSCT) or immunosuppressive therapy (IST). IST is the first-line treatment for most patients due to older age or lack of a matched donor[2].

Standard first-line IST for AA combines anti-thymocyte globulin (ATG) with long-term ciclosporin. ATG is a polyclonal antibody mixture that can be produced by immunizing horses or rabbits with human thymocytes. In AA, both horse-derived ATG (ATGAM®, Pfizer) and rabbit-derived ATG (Thymoglobulin®, Sanofi) have been applied. However, ATGAM is preferred since it results in superior response rates and overall survival[3,4]. Approximately 70% of patients show hematologic recovery after ATGAM-based IST, with a gradual improvement of peripheral blood counts over several months[2,4,5].

The pharmacodynamics of ATGAM-based IST are poorly understood. Its therapeutic effect is attributed to the depletion of autoreactive immune cells implicated in AA pathogenesis. ATGAM, administered at 40 mg/kg/day for four consecutive days[2], is thought to induce immediate lymphodepletion, possibly through complement-dependent lysis or activation-induced apoptosis[6,7]. Subsequently, long-term ciclosporin is believed to suppress residual and reconstituted lymphocytes through calcineurin and IL-2 blockade[8,9]. Since ATGAM is manufactured in horses, it contains antibodies against both non-human and human antigens. Therefore, only a small 'active' fraction can bind human immune cells and mediate its immunomodulatory effects. The precise specificities of this active ATGAM fraction are unknown and its activity differs from the more extensively studied rabbit-derived ATG[7,10], however, ATGAM has been shown to bind a spectrum of proteins on the surface of immune cells[11,12], and to reduce $CD4^+$, $CD8^+$ and regulatory T-cells *in vivo*[4,13]. Similarly, the relationship between active ATGAM exposure and lymphodepletion is unclear, and the impact of ATGAM plus ciclosporin on the immune landscape has not been characterized in detail. Previously, we identified potentially pathogenic T- and B-cell subpopulations in AA patients[14,15]. These $CCR6^{++}$ B-cells, Th17-like $CCR6^+CD4^+$ T-cells and $KLRG1^+$ terminally differentiated $CD8^+$ T-cells were enriched at diagnosis, colocalized in bone marrow, and significantly reduced six months post-ATGAM. This decrease could imply that IST selectively depletes specific lymphocyte subpopulations.

In this study, we aimed to delineate the effects of ATGAM exposure on hematologic recovery in 44 AA patients. For the first time, we quantified active ATGAM concentrations in patient

plasma using flow cytometry, and applied population pharmacokinetic (POPPK) modeling to estimate exposure. Furthermore, to elucidate the impact of IST with ATGAM plus ciclosporin on the immune landscape, we performed spectral flow cytometry on peripheral blood samples collected before and at multiple time points after the start of IST. Our results present active ATGAM exposure as a factor influencing hematologic recovery and reveal that successful IST involves selective removal and suppression of key lymphocyte subpopulations rather than a full immune 'reset'.

Methods

Patients and plasma samples

Plasma samples (n=381) were collected from 44 treatment-naïve AA patients before each ATGAM infusion and up to 82 days after the first infusion (median 9, range 4-13 samples/patient). PBMCs were collected from 3 of 44 patients at diagnosis and up to 3.5 years post-ATGAM (7-10 samples/patient), and 5 healthy donors. Patient characteristics are listed in Table 1. Patients <40 years were screened for Fanconi anemia to exclude congenital bone marrow failure. Patients received IST according to Dutch guidelines: four consecutive days of 40 mg/kg/day ATGAM and 5 mg/kg/day ciclosporin for at least six months[16]. Exceptions were UPN5 (two days ATGAM), UPN9 (four days ATGAM with two-day break after infusion two), and UPN46 (118 days ciclosporin). ATGAM was administered intravenously over 12 hours. 19 of 44 patients responded within six months after the start of IST, which was defined as becoming transfusion-independent and a neutrophil count of $\geq 0.5 \cdot 10^9/L$[2]. Plasma or PBMCs were stored at -80°C or -196°C until bioanalysis, respectively. This study was approved by the Medical Ethical Committee of the Leiden University Medical Center (B21.003).

ATGAM measurement and spectral flow cytometry

Flow cytometry was used to quantify active ATGAM concentrations in plasma, and to perform deep immunophenotyping in peripheral blood. For active ATGAM measurement, cryopreserved PBMCs from a single healthy donor were incubated with serial dilutions of patient plasma using a protocol based on a previously validated assay for quantifying lymphocyte-binding antibody concentrations[17], and stained with a six-marker antibody panel including anti-horse IgG. Subsequently, cells were measured by flow cytometry, and active ATGAM plasma concentrations were determined. For deep phenotyping of lymphocytes, cryopreserved PBMC samples were stained with a 25-marker panel (Table S1), measured by spectral flow cytometry, and analyzed by dimensionality reduction[18]. Detailed description of all methods, including the quantification of total ATGAM in plasma by ELISAs, is provided in the Supplementary methods and Figures S1-3.

Table 1. Patient characteristics.

Characteristic	Patients (n=44)
Age at diagnosis (median, range in years)	54 (20-79)
Sex (n)	
Male	26
Female	18
Weight at diagnosis (median, range in kg)	80 (51-120)
Body mass index at diagnosis (median, range)	24.7 (17.6-34.3)
Height at diagnosis (median, range in cm)	176 (156-198)
Severity of disease at diagnosis (n)	
Non-severe AA	7
Severe AA	23
Very severe AA	14
Total lymphocyte count pre-ATGAM ($\cdot 10^6$/L)*#	1375 (260-2890)
$CD4^+$ T-cell count pre-ATGAM ($\cdot 10^6$/L)*#	732 (21-1479)
$CD8^+$ T-cell count pre-ATGAM ($\cdot 10^6$/L)*#	363 (71-949)
NK-cell count pre-ATGAM ($\cdot 10^6$/L)*#	77 (4-291)
B-cell count pre-ATGAM ($\cdot 10^6$/L)*	124 (17-631)
Response to IST 6 months post-ATGAM (n)	
Non-response	21
Partial response	14
Complete response	5
Unknown (died <6 months after first ATGAM infusion)	4

**Cell counts between days -2 to 0 pre-ATGAM infusion; #Data missing for 2 patients.*

Exposure-response analyses

POPPK modelling was performed in NONMEM® to estimate ATGAM exposure as detailed in Supplementary methods, Tables S2-3 and Figure S4. Downstream exposure-response analyses used clinical data collected until day 180, because IST response is assessed 3-6 months post-ATGAM[2]. As a measure for hematologic recovery, we evaluated peripheral blood neutrophil and reticulocyte counts from routine measurements, generally taken at least weekly. Thrombocyte and hemoglobin levels were not analyzed to avoid potential bias caused by blood transfusions. To study lymphodepletion and immune reconstitution, we analyzed peripheral blood lymphocyte counts from routine measurements, typically collected once every two weeks. To correct for missing immune reconstitution data, non-linear mixed effect modeling was performed using SAEMIX[19], see Supplementary methods and Figure S5. Data visualization and statistical analyses were performed in R v4.4.1 (Rstudio v2023.03) using Mann-Whitney *U* (continuous variables), Fisher's Exact (categorical variables), and Spearman's correlation tests. P-values ≤ 0.05 were considered significant.

Results

Active ATGAM binds all major lymphoid lineages

To study the effects of ATGAM, the concentration of ATGAM capable of binding PBMCs from an unrelated healthy donor (active ATGAM hereafter) was quantified in plasma from 44 adult AA patients using flow cytometry (Figure 1A). In patients that received the standard regimen of four consecutive days of 40 mg/kg/day ATGAM, active ATGAM concentrations increased over the four days of infusion and reached a median peak concentration of 131AU/mL on day 4 (Figure 1B). After the last infusion, concentrations rapidly decreased, and typically fell below the concentration of 10AU/mL by day 20. The pharmacokinetics of active ATGAM varied considerably between patients in both peak concentrations (range 31-497AU/mL on day 4) and clearance rates (Figure 1B). Similar variability was observed in total ATGAM concentrations (e.g. active ATGAM and ATGAM binding to other (non)-human targets combined) quantified in the same plasma samples using ELISA (Figure S6A). Active ATGAM in patient plasma was detected on donor T-, NK- and B-cells. However, pharmacokinetics differed as B-cell binding active ATGAM was detected longer than T- or NK-cell binding active ATGAM (Figure 1C; all patients in Figure S6B).

Active ATGAM exposure is increased in AA patients with higher body weight

Given the variability in active ATGAM concentrations between patients, POPPK modeling was performed to estimate the full concentration-time curve of active ATGAM exposure. The POPPK of intravenously administered active ATGAM was best described by a two-compartment model with first-order linear elimination (structural model in Figure S7). The model showed adequate agreement between observed and model-estimated active ATGAM concentrations (Figure S8, individual patients in Figure S9). Exposure ($AUC_{0\text{-}inf}$) was defined as the estimated area under the concentration-time curve (Table S4). Since this study is the first to report on active ATGAM, we also validated the accuracy of our approach by performing POPPK modeling for total ATGAM (Figure S10-11, Table S5) to simulate the dosing regimens described in the manufacturer's brochure[20]. This revealed strong agreement between model-estimated and reported total ATGAM concentrations for an external cohort of AA patients (Figure S12).

To identify factors driving between-patient variability in active ATGAM pharmacokinetics, the impact of clinical covariates was evaluated. No significant effects of sex, age and lymphocyte counts pre-ATGAM were observed (Figure S13). Since ATGAM is dosed based on body weight, we anticipated clearance to increase with body weight to obtain similar ATGAM exposures across patients. However, we found that patients with higher body weights had higher

active ATGAM concentrations over time, resulting in higher exposures (Figure 1D), as neither clearance nor volume of distribution were influenced by weight (Figure 1E-F).

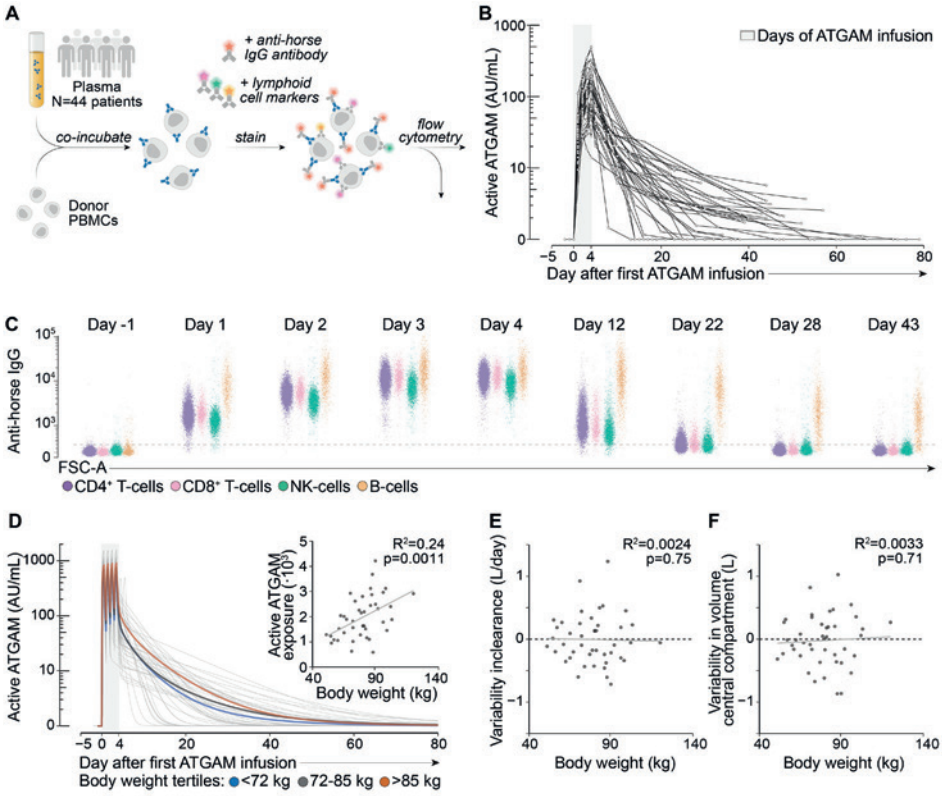


Figure 1. Active ATGAM binding specificities and concentration-time profiles in plasma from AA patients. [A] Experimental approach. Donor PBMCs were incubated with plasma samples collected pre- and post-ATGAM, stained and analyzed by flow cytometry to determine the plasma levels of free active ATGAM capable of binding to human lymphocyte lineages. [B] Measured active ATGAM levels in patient plasma (in arbitrary units/mL; n=44 patients) over time before, during and after ATGAM infusion on days 0-4. [C] Flow cytometric plots demonstrating the binding of active ATGAM in plasma from a representative patient (UPN33) to CD4⁺ T-cells, CD8⁺ T-cells, NK-cells or B-cells from a healthy donor, measured using an Alexa Fluor 488-conjugated anti-horse IgG antibody. [D] Model-estimated active ATGAM plasma concentrations over time before, during and after ATGAM infusion on days 0-4. Mean active ATGAM concentrations are presented for patients within the lowest (blue), medium (yellow) and highest (red) body weight quantiles, who received 4 consecutive days 40mg/kg/day ATGAM. Insert: Correlation between model-estimated active ATGAM exposure and body weight. [E-F] Covariate plots showing the relationship between body weight and the inter-individual variability in estimated active ATGAM clearance (E) or volume of distribution (F). Each dot represents one patient. Only patients that received the standard dosing regimen of 4 consecutive days 40mg/kg/day ATGAM are shown.

Higher active ATGAM exposure associates with earlier hematologic recovery

To investigate the effect of active ATGAM exposure on hematological recovery, patients were categorized into low, medium and high exposure groups based on the exposure tertiles of 1515 and 2216AU·day/L (Figure 2A). Neutrophil and reticulocyte counts served as a measure of bone marrow recovery. Two patients in the low-exposure group, one patient in the medium-exposure group and one in the high-exposure group were censored before day 180 due to death. Age, sex, disease severity, eltrombopag use and ciclosporin discontinuation did not significantly differ between the groups, and none of the patients started second-line treatment before day 180 (Table S6). In all three exposure groups, neutrophil and reticulocyte counts gradually increased post-ATGAM (Figure 2B-C). Reticulocyte counts peaked in a few patients within the first 120 days post-ATGAM. Notably, the high- and medium-exposure groups tended to have higher neutrophil and reticulocyte counts from day 60 onward, despite similar baseline counts compared to the low-exposure group (Figure 2B-C). This difference was most pronounced around day 90 (Figure 2B-C, box plots) and diminished 180 days post-ATGAM infusion, suggesting that increased active ATGAM exposure associates with earlier hematologic recovery but does not impact six-month response rates.

ATGAM induces profound depletion of T- and NK-cells but not of B-cells

As we showed that ATGAM binds all major lymphoid lineages, we studied the response of active ATGAM exposure on T-, NK- and B-cell counts in peripheral blood. To correct for missing immune reconstitution data, total lymphocyte, T-cell and NK-cell counts were estimated by non-linear mixed modeling. ATGAM induced a strong reduction of $CD4^+$ T-cells, $CD8^+$ T-cells and NK-cells, with no differences between the active ATGAM exposure groups (Figure 2D). Depletion of these lineages was short-lived and only observed immediately post-infusion, suggesting that T- and NK-cell depletion requires a minimal active ATGAM plasma concentration (+/-100AU/mL, estimated from Figure 2D). Strikingly, B-cell counts did not show a consistent trend between patients post-ATGAM and therefore could not be modelled. Interestingly, B-cell counts even peaked post-ATGAM before returning to baseline around day 30, indicating that although ATGAM binds all lymphoid lineages, it exerts differential effects among cell types.

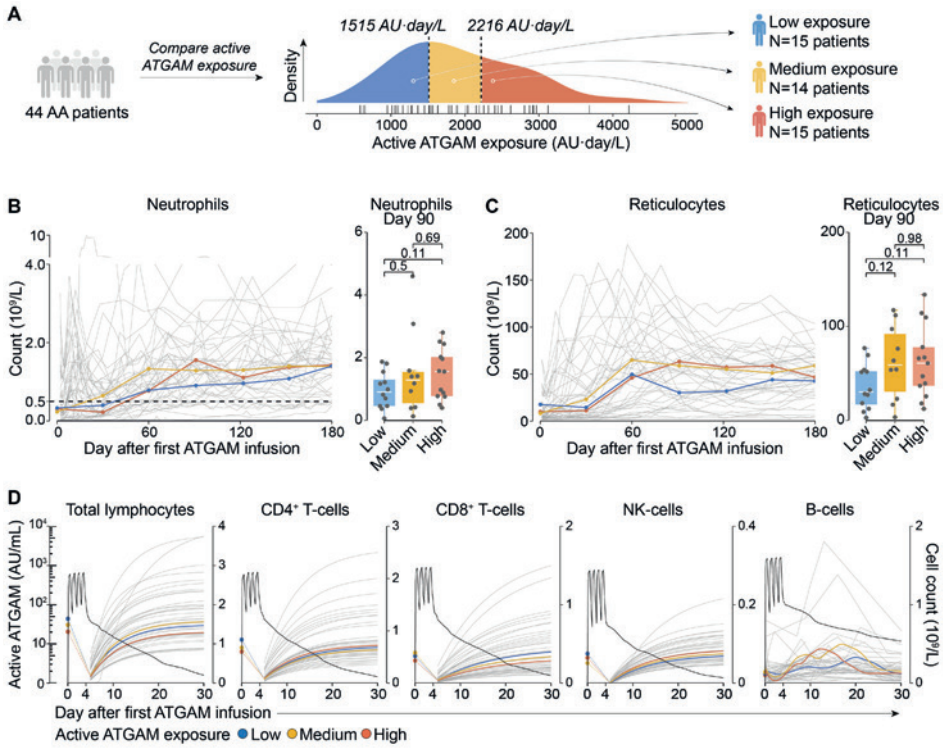


Figure 2. Impact of active ATGAM exposure on peripheral blood counts. [A] Histogram showing the distribution of active ATGAM exposure across the patient cohort. [B-C] Absolute neutrophil (B) and reticulocyte (C) counts over time up to 180 days after ATGAM infusion on days 0-4. Light gray lines present individual patients. Blue, yellow and red lines present group medians of low, medium and high active ATGAM exposure groups, on days 0, 30, 60, 91, 122, 152 and 180 +/- 7 days, respectively. Cell counts were unavailable for 2 (day 30), 5 (day 60), 9 (day 91), 9 (day 122), 7 (day 152) and 9 (day 180) patients divided across all exposure groups. Box plots represent the group median, whiskers represent 1.5 * interquartile range. [D] Median model-estimated active ATGAM concentrations capable of binding to all lymphocytes, CD4⁺ T-cells, CD8⁺ T-cells, NK-cells or B-cell plotted against absolute total lymphocyte, CD4⁺ T-cell, CD8⁺ T-cell, NK-cell or B-cell counts, respectively. Light gray lines present cell counts of individual patients. Blue, yellow and red lines present median cell counts of low, medium and high active ATGAM exposure groups, respectively. Model-estimated lymphocyte, CD4⁺ T-cell, CD8⁺ T-cell, NK-cell counts are presented, whereas observed B-cell counts are shown.

Detection of ATGAM on patient lymphocytes confirms B-cell binding *in vivo*

To study the paradox that ATGAM binds donor B-cells but does not induce B-cell depletion, we investigated the presence of ATGAM directly bound to patient PBMCs. Unique series of PBMC samples collected from three AA patients before and immediately after ATGAM infusion were studied. A 25-marker spectral flow cytometry panel including anti-horse IgG enabled the detection of ATGAM on the surface of in-depth phenotyped lymphocytes. To study the long-term effects of ATGAM plus ciclosporin, samples collected up to 3.5 years post-ATGAM were also analyzed (total of 7-10 samples/patient). Patients received 40 mg/kg/day ATGAM on four

consecutive days, responded to IST (peripheral blood counts in Figure S14) and were CMV seropositive. Ciclosporin was discontinued after tapering two years post-ATGAM in patient UPN31, and three years post-ATGAM in UPN13 and UPN15. As a reference, PBMCs from five age-, sex- and CMV status-matched healthy donors were included.

To directly compare the immune landscape between time points, UMAPs were generated after downsampling $0.1{\cdot}10^6$ single, live lymphocytes from each sample (Figure 3A). The following major lymphoid lineages were identified: 1) $CD3^+CD4^+$ T-cells; 2) $CD3^+CD8^+$ T-cells; 3) $CD3^+TCR\gamma\delta^+$ T-cells; 4) $CD3^+CD4^+FoxP3^+$ regulatory T-cells; 5) $CD3^-CD56^+$ NK-cells and 6) $CD19^+$ B-cells. Visualization of all samples from a representative patient in the UMAP revealed a shift in the lymphoid compartment over time, with the most obvious changes observed immediately after the last ATGAM infusion on day 4, when T-cells and NK-cells were reduced but B-cells were still present (Figure 3B).

Quantification of lineage frequencies confirmed the presence of the major lymphoid lineages at AA diagnosis, with some heterogeneity between patients and no considerable differences compared to controls (Figure 3C, $TCR\gamma\delta^+$ and regulatory T-cells in Figure S15A). Immediately after the last ATGAM infusion (day 4/5) the composition of the lymphoid compartment changed dramatically. In agreement with previous observations, percentages of $CD4^+$, $CD8^+$, $TCR\gamma\delta^+$ and regulatory T-cells and NK-cells decreased in all patients, whereas B-cell frequencies increased. A trend towards normalization was observed from two weeks post-ATGAM onwards. Normalization of the lymphoid compartment continued up to six months post-ATGAM.

With anti-horse IgG, ATGAM was best detectable on day 4, and could be detected until day 26 on all circulating lymphocytes from the representative patient post-infusion (Figure 3B,D). The amount of ATGAM bound to T-cells or B-cells did not differ (Figure S15B). To rule out a potential influence of ATGAM Fc-binding to the Fc-receptor on B-cells, Fc-receptor blockade experiments were performed and no Fc-binding was found (Figure S16). ATGAM binding to patient lymphocytes gradually decreased within one month post-infusion. Lower concentrations of ATGAM again correlated with T- and NK-cell recovery from two weeks post-infusion onwards. These findings confirm that while ATGAM binds to all lymphoid lineages, it does not induce B-cell depletion to the same extent as observed in T- and NK-cells.

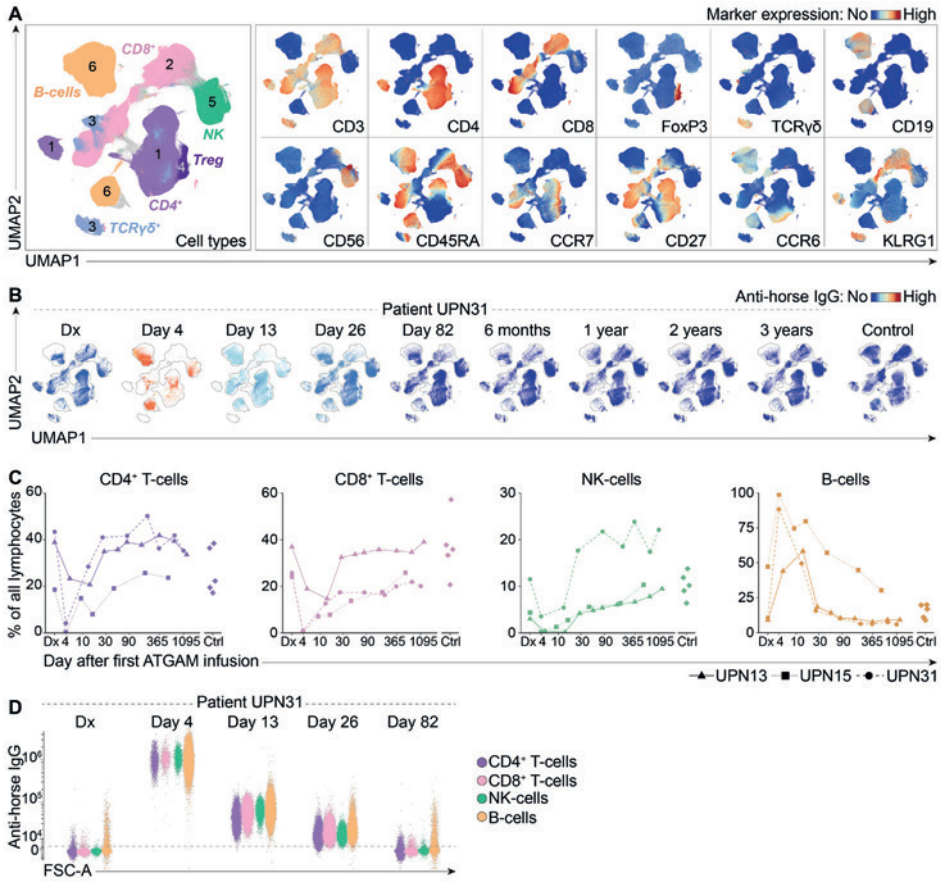


Figure 3. Binding of ATGAM and the impact of ATGAM-based IST on lymphocytes from AA patients. [A] $3{\cdot}10^6$ single, live lymphocytes downsampled from all PBMC samples (UPN13, UPN15, UPN31 and five controls) visualized using an UMAP analysis. Colors indicate major lymphoid lineages or marker expression values. [B] UMAP plots showing the cellular composition of the lymphoid compartment in peripheral blood from UPN31 before and over time following ATGAM infusion on days 0-4. The signal of the Alexa Fluor 488-conjugated anti-horse IgG antibody is shown. $0.1{\cdot}10^6$ single, live lymphocytes are shown per time point. [C] Frequencies of major lymphoid lineages, shown as a percentage of all single, live lymphocytes per time point. Each line represents an individual patient. [D] Flow cytometry plots visualizing the presence of ATGAM directly bound to T-, NK- or B-cells from UPN31 over time, detected using an Alexa Fluor 488-conjugated anti-horse IgG antibody incorporated into the spectral flow cytometry panel.

ATGAM profoundly depletes memory T-cells but induces an increase of CD27$^+$ B-cells

Next, we studied the immediate effects of ATGAM and long-term impact of ATGAM plus ciclosporin at the immune subpopulation level. In the representative patient, we observed a more profound decrease of memory T-cells compared to naïve T-cells post-ATGAM, with the strongest depletion of CD45RA$^+$CCR7$^-$ terminally differentiated effector memory (EMRA) CD8$^+$ T-cells (Figure 4A-B, quantification: Figure S15C-D). In contrast, we observed a striking increase of memory CD27$^+$ B-cells immediately post-ATGAM (Figure 4C, S15E).

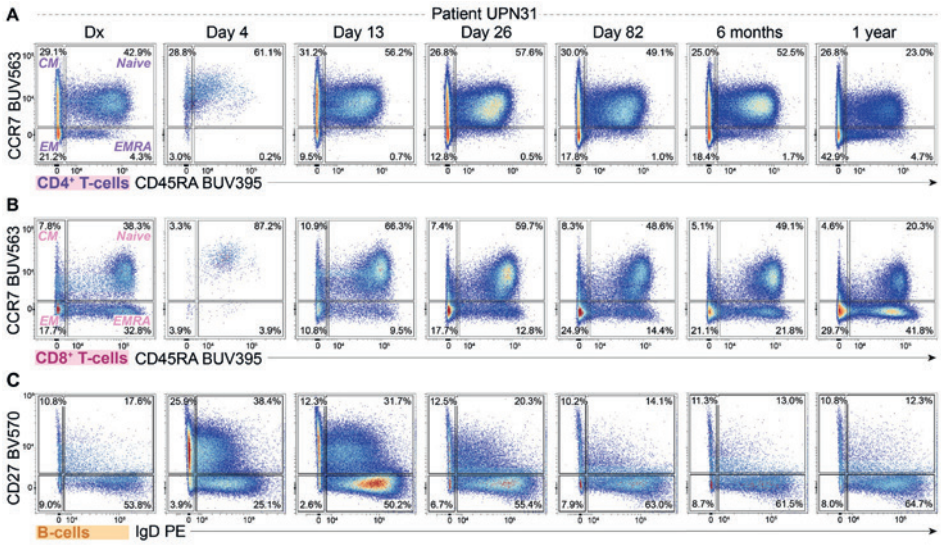


Figure 4. Impact of ATGAM-based IST at the immune subpopulation level in a representative AA patient. [A-C] Flow cytometry plots visualizing the composition of the [A] $CD4^+$ T-cell compartment, [B] $CD8^+$ T-cell compartment and [C] B-cell compartment from patient UPN31 before and over time following the start of ATGAM-based IST on day 0. CM: central memory, EM: effector memory, EMRA: terminally differentiated effector memory.

The profound depletion of memory T-cells and increase of memory $CD27^+$ B-cells was observable across all patients post-ATGAM (Figure 5A-C). Only in patient UPN15 memory T-cell frequencies remained high, which was attributable to the low number of analyzed T-cells, as this patient experienced the strongest T-cell depletion (Figure 3C). Within two weeks post-ATGAM, both memory T-cells and $CD27^+$ B-cells frequencies showed a trend towards normalization (Figure 5A-C). Notably, this normalization occurred independently of T-cell and B-cell proliferation, indicating that recovery was not driven by proliferation of remaining circulating cells (Figure S17).

To further characterize the increase of $CD27^+$ B-cells, we examined the identity of these cells in patient UPN31 on day 13 using a B-cell-oriented spectral flow cytometry panel. This revealed that the $CD27^+$ B-cells comprised of a heterogeneous population of both unswitched (IgM^+IgD^+) and switched (IgG^+, IgA^+) memory B-cells (Figure 5D). Compared to healthy controls, these cells preserved high levels of CD21 and CD24, compatible with a resting B-cell state (Figure 5E). Additionally, they did not differentially express the activation markers CD80, CD86 and CD95, and complement inhibitors CD46 and CD55 (Figure 5E-F), illustrating that the increase of $CD27^+$ B-cells is not the result of cell expansion or resistance to complement-mediated lysis. Consistent with these findings, the $CD27^+$ B-cells harbored

tetanus-specific cells, indicating their increase was driven by a recruitment of resting, pre-existing memory B-cells in circulation (Figure 5G).

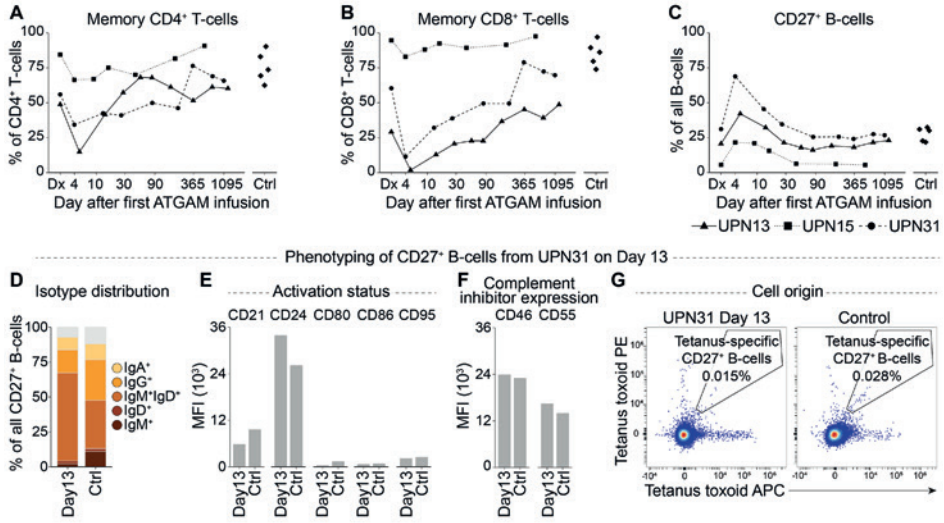


Figure 5. Dynamics of memory T-cells and CD27⁺ B-cells, and identity of CD27⁺ B-cells, post-ATGAM. [A-C] Frequencies of memory CD4⁺ T-cells, memory CD8⁺ T-cells or CD27⁺ B-cells over time, quantified in all three AA patients and controls. Memory T-cells include central memory, effector memory and terminally differentiated effector memory T-cells. [D] Isotype distribution of the CD27⁺ B-cells from UPN31 on day 13 after the first ATGAM infusion, and the mean of two age-matched controls. [E] Expression of CD21, CD24, CD80, CD86 and CD95 on CD27⁺ B-cells from patient UPN31 on day 13, and the mean of two age-matched controls. Median fluorescence intensities are shown. [F] Expression of complement inhibitors CD46 and CD55 on CD27⁺ B-cells from patient UPN31 on day 13, and the mean of two age-matched healthy controls. Median fluorescence intensities are shown. [G] Flow cytometry plots showing the presence of tetanus toxoid-specific CD27⁺ B-cells in patient UPN31 on day 13, and an age-matched healthy control. $0.1 \cdot 10^6$ CD27⁺ B-cells are shown per plot.

ATGAM-based IST depletes potentially pathogenic subpopulations while allowing the recovery of virus-specific lymphocytes

The rapid recovery of the T-cell compartment in the absence of proliferation, along with the persistence of pre-existing memory B-cells post-ATGAM, raises the question of how profoundly ATGAM depletes the T-cell compartment. Therefore, we investigated the origin of reconstituted T-cells by tracking the presence of CMV-specific CD8⁺ T-cells using CMV peptide-HLA tetramers incorporated into our spectral flow cytometry panel. In one of three patients (UPN13), these analyses were not possible due to HLA-incompatibilities between the patient and the tetramers. In the representative patient (UPN31), we detected CMV-specific CD8⁺ T-cells at diagnosis, which were no longer detectable immediately following ATGAM infusion, consistent with the observed T-cell depletion (day 4; Figure 6A). However, CMV-specific CD8⁺ T-cells were detectable from day 13 onwards, and a similar trend was observed in UPN15 (Figure 6B).

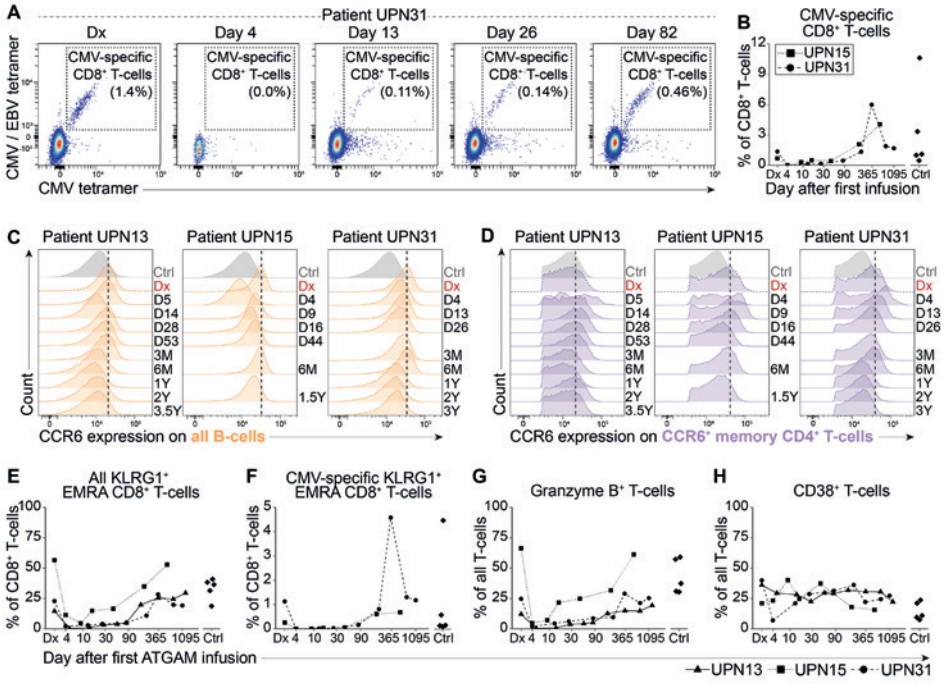


Figure 6. Effects of ATGAM on pre-existing and potentially pathogenic subpopulations. [A] Flow cytometry plots showing the presence of CMV-specific CD8$^+$ T-cells within the CD8$^+$ T-cell compartment at diagnosis and after the first ATGAM infusion in patient UPN31. [B] Frequencies of CMV-specific CD8$^+$ T-cells, quantified as a frequency of all CD8$^+$ T-cells in patients UPN15 and UPN31, and all controls. [C-D] Histograms showing CCR6 expression on all CD19$^+$ B-cells (C) or CCR6$^+$ memory CD4$^+$ T-cells (D) in the three AA patients over time following ATGAM infusion and ciclosporin treatment. [E-H] Frequencies of all KLRG1$^+$ EMRA CD8$^+$ T-cells, CMV-specific KLRG1$^+$ EMRA CD8$^+$ T-cells, Granzyme B$^+$ cytotoxic T-cells and CD38$^+$ activated T-cells in all three AA patients over time following ATGAM infusion.

Given that our results indicate the persistence of pre-existing T- and B-cells post-ATGAM, we reasoned that the therapeutic effect of IST, comprising ATGAM and long-term ciclosporin, may not depend on a full immune 'reset'. Instead, it may rely on the selective depletion and suppression of pro-inflammatory CCR6^{++} B-cells, CCR6$^+$ memory CD4$^+$ T-cells and KLRG1$^+$ EMRA CD8$^+$ T-cells, which we previously identified as part of a disease-specific immune cell network[14]. These subpopulations were enriched in AA patients at diagnosis, and co-localized in bone marrow regions harboring the active immune response[14,15]. In all three patients, we confirmed higher frequencies of CCR6^{++} B-cells at diagnosis compared to controls (Figure 6C). CCR6 expression on B-cells remained high immediately post-ATGAM but gradually decreased with long-term ciclosporin use, with the strongest decrease in CCR6 expression >6 months post-ATGAM. CCR6 expression remained reduced after ciclosporin was discontinued (≥3 years post-ATGAM). A similar decrease of CCR6 expression on CCR6$^+$ memory CD4$^+$ T-cells was observed (Figure 6D). In contrast, KLRG1$^+$ EMRA CD8$^+$ T-cells were strongly depleted

immediately post-ATGAM (Figure 6E), and their recovery was delayed compared to other CD8$^+$ T-cells (Figure 3C). Further analysis showed that only a small fraction of these KLRG1$^+$ EMRA CD8$^+$ T-cells were CMV-specific, suggesting depletion also affected potentially autoreactive T-cells within this population (Figure 6F). Over time, KLRG1$^+$ EMRA CD8$^+$ T-cell frequencies returned to pre-ATGAM levels, indicating a temporary rather than a permanent depletion. A depletive effect was also observed for Granzyme B$^+$ cytotoxic T-cells (Figure 6G), while expression of the activation marker CD38 remained unaffected by ATGAM plus ciclosporin (Figure 6H). These findings underscore that IST results in an immediate but selective depletion of key T-cell populations by ATGAM, while other potentially pathogenic populations are reduced over several months, possibly through selective suppression by ciclosporin.

Discussion

In this study, we investigated the pharmacodynamics of first-line IST with ATGAM plus long-term ciclosporin in AA patients. Our analysis is the first to focus on active ATGAM, the fraction capable of binding human lymphocytes and mediating the immunomodulatory effects that are believed to underlie its therapeutic efficacy. POPPK modeling revealed that active ATGAM exposure varies considerably among patients, and tends to correlate with hematologic recovery. At high plasma concentrations, ATGAM binds T- and NK-cells and drastically reduces their counts *in vivo*. Paradoxically, while ATGAM also binds B-cells, it does not induce their depletion but rather results in an increase of resting memory CD27$^+$ B-cells in circulation. Following ATGAM infusion, immune reconstitution occurs rapidly within two weeks, and is marked by the recovery of pre-existing cells alongside a selective suppression of specific pro-inflammatory subpopulations over time. Thus, the therapeutic effect of ATGAM-based IST goes beyond 'simple' lymphodepletion.

To date, ATGAM is administered at a fixed dose per kilogram bodyweight, although its optimal dose remains unclear since its exposure-response profile has not been characterized in detail[2,21,22]. This study provides unique insight into ATGAM pharmacokinetics and offers important considerations regarding dosing. Consistent with data on rabbit-derived ATG[23,24], we demonstrate that linear weight-based dosing causes variability in active ATGAM exposure between patients. In line with a previous report[25] that suggested a benefit of higher ATGAM exposures on relapse rates, we found that higher active ATGAM exposures tend to associate with increased neutrophil and reticulocyte counts starting 60 days post-ATGAM infusion. Although these associations did not reach statistical significance, the observed trend could be suggestive of a possible relationship between active ATGAM exposure and the timing of hematologic recovery. These findings may complement previous studies that identified patient- and disease-specific characteristics predicting response to IST, suggesting that

hematologic recovery may be controlled by multiple factors[26-32]. The biological mechanism by which active ATGAM exposure may influence hematologic recovery remains unclear. In our study, active ATGAM exposure was not significantly associated with the extent or duration of T- or NK-cell depletion. Although we did not assess ciclosporin levels, their impact seems limited, given that ciclosporin dosing was concentration-controlled to a pre-specified target[2]. Interestingly, it has been reported that ATGAM can stimulate progenitor cells[33] and the release of factors regulating hematopoiesis[13,34]. Thus, higher ATGAM exposures could have a favorable effect through a stronger influence on the progenitors in the bone marrow.

By applying flow cytometry, we provide a detailed description of both the short- and long-term immunological effects of ATGAM plus ciclosporin in AA patients. Although it is known that ATGAM results in less profound lymphodepletion compared to other ATG preparations[4], our findings show that immune reconstitution occurs early post-ATGAM while active ATGAM concentrations are still detectable. This indicates that a minimal level should be exceeded for adequate lymphodepletion, and that a better understanding of the exposure-response relationship of ATGAM is needed to optimize treatment across patients.

Importantly, our analyses revealed how successful IST may reshape the immune landscape to enable bone marrow recovery in AA patients. Our study therefore builds upon recent reports demonstrating the added value of high-dimensional single-cell techniques in deciphering the pathogenesis of AA[14,15,35,36], and complements a comprehensive review of their application in AA[37]. Previously, using (imaging) mass cytometry on bone marrow samples from AA patients, we identified a disease-specific immune cell network of CCR6^{++} B-cells, Th17-like[32,38,39] CCR6^{+} memory CD4^{+} T-cells and KLRG1^{+} EMRA CD8^{+} T-cells[14,15]. These immune cells were significantly enriched in AA patients at diagnosis compared to healthy donors, and showed a trend towards normalization six months after successful IST, implying a pathogenic role. In this study, we extend these findings by confirming their increased presence at diagnosis. Importantly, we further show how these cells are reduced with IST through an analysis of unique series of PBMC samples collected pre- and up to 3.5 years post-ATGAM. Our study thereby provides a more dynamic visualization of the reshaping of the immune landscape compared to previous reports that generally focused on samples collected pre- and six months post-ATGAM[14,15,36,39]. Although the analysis included only three patients, it allowed for a deeper investigation beyond the major immune lineages assessed in the full cohort of 44 AA patients, and sets the stage for more widely applied longitudinal analyses in future studies. We demonstrate that successful IST depletes potentially pathogenic populations via two distinct mechanisms: KLRG1^{+} EMRA CD8^{+} and CCR6^{+} memory CD4^{+} T-cells are depleted by ATGAM. In contrast, CCR6^{++} B-cells and residual T-cells, including CCR6^{+} memory CD4^{+} T-cells, gradually decrease within several months during long-term ciclosporin use. These data indicate the persistence

of potentially pathogenic immune cell subpopulations post-ATGAM, and could explain why long-term ciclosporin is needed to achieve durable response rates.

Based on prior studies[4,13], we expected ATGAM to bind T-cells and to cause rapid but short-lived T-cell depletion. Our data confirm this effect and further reveal important differences among T-cell subpopulations. Specifically, memory T-cells were more profoundly depleted than naïve T-cells, suggesting that ATGAM targets cytotoxic T-cells, while preserving part of the antigen-naïve T-cell repertoire that provides protection against future pathogen encounters. This effect is more pronounced among $CD8^+$ T-cells compared to $CD4^+$ T-cells, and remains detectable up to six months post-ATGAM, likely due to the inhibition of T-cell proliferation and differentiation by ciclosporin[40]. During this period, we observed reconstitution of CMV-specific $CD8^+$ T-cells, implying that ATGAM does not result in a full immune 'reset'. Although the recovery of pre-existing cells has been described with other ATG preparations[41], it raises questions on how successful IST eliminates potential autoreactive T-cells while preserving protective immune memory. We consider three possible explanations. First, ATGAM may exert a stronger effect on autoreactive T-cells compared to other memory T-cells, possibly due to differences in cellular state. Similarly, it is possible that, in the absence of infections, remaining autoreactive T-cells post-ATGAM may be more susceptible to ciclosporin compared to pathogenic-specific T-cells due to continued antigenic triggering. Finally, it could be that ATGAM depletes memory T-cells in the blood and bone marrow, while not affecting tissue-resident T-cells. This would suggest that autoreactive T-cells are limited to the blood and bone marrow, and that targeting these compartments alone could suffice to enable bone marrow recovery.

Since ATGAM has strong effects on T-cells, it is noteworthy that our data confirm that ATGAM does not have the same effect on B-cells[13]. Instead of depletion, we report a shift in the B-cell compartment, characterized by an increase of memory $CD27^+$ B-cells immediately post-ATGAM infusion, which gradually normalizes within one month. These $CD27^+$ B-cells comprised a heterogeneous population of both non-switched and switched memory B-cells in a resting state. The $CD27^+$ B-cell population included pre-existing pathogen-specific cells as evidenced by the presence of tetanus toxoid-specific B-cells and was not proliferating. Therefore, we believe that the observed increase of $CD27^+$ B-cells may reflect redistribution of memory B-cells from the lymphoid organs into the circulation. This could be driven by an imbalance of chemotactic factors released following T-cell apoptosis. How B-cells survive ATGAM binding to their cell surface while T-cells are depleted should be clarified by future studies. Our data revealed no increased resistance of B-cells to complement-mediated lysis, nor an influence of Fc-binding. Given that ATGAM is a polyclonal antibody preparation generated against thymocytes, it is possible that ATGAM induces T-cell apoptosis by triggering T-cell activation (e.g. via anti-CD3 or TCR binding), without activating apoptotic pathways in B-cells.

To conclude, we unveil active ATGAM exposure as a clinically relevant factor influencing hematologic recovery in AA. We further demonstrate that successful IST with ATGAM plus long-term ciclosporin exerts differential effects among major lymphoid lineages, leading to selective depletion and suppression of $CCR6^+$ and $KLRG1^+$ T- and B-cell subpopulations implicated in AA pathogenesis. These findings confirm their potential pathogenicity, and establish these subpopulations as promising targets for targeted treatment.

Acknowledgements

We thank the Laboratory for Special Hematology of the Leiden University Medical Center for processing all plasma samples. Furthermore, we thank Anja Jansen-Hoogendijk of the Department of Pediatrics of the Leiden University Medical Center for sharing her expertise on measuring active ATG concentrations in patient plasma. Flow cytometry was performed at the Flow Cytometry Core Facility of the Leiden University Medical Center. This work was supported by a research grant from Dioraphte Foundation.

Authorship contributions

E.S.P., C.R.P., S.M.G., E.H.M.v.E., J.M.G. and S.V. performed laboratory experiments. E.S.P. and D.J.A.R.M. performed pharmacokinetic modelling. E.S.P. analyzed the data. E.S.P., E.H.M.v.E., J.M.G., R.E.M.T, F.K., C.J.M.H., M.H.M.H., D.J.A.R.M. and J.M-L.T. interpreted the data. E.S.P wrote the first draft of the manuscript. C.J.M.H. and J.M-L.T. recruited patients and collected samples. D.J.A.R.M and J.M-L.T. conceptualized the study. M.H.M.H., D.J.A.R.M. and J.M-L.T. supervised the project. All authors critically reviewed the manuscript.

Conflicts of interest

The authors declare no competing financial interests.

Supplementary methods

Quantification of total ATGAM concentrations

Total ATGAM was defined as all horse IgG antibodies in the ATGAM preparation[42]. Total ATGAM concentrations in patient plasma were quantified by sandwich ELISA. 96-well plates were coated overnight at 4°C with goat anti-horse IgG antibodies at a dilution of 1:2500 in PBS (Jackson Immunoresearch, cat 108-005-003). Next, plates were blocked, washed using PBS with 0.005% Tween20, and incubated with diluted patient plasma samples for two hours at room temperature. Each sample was analyzed across eight serial dilutions. Subsequently, plates were washed five times using PBS with 0.005% Tween20 and incubated with a peroxidase-conjugated secondary goat anti-horse antibody at a dilution of 1:25,000. After a one hour incubation at room temperature, plates were washed five times using PBS with 0.005% Tween20 and stained with TMB substrate buffer for five minutes in the dark. Finally, staining was stopped and plates were measured at 450nm on a microplate photometer (ThermoFisher Multiskan FC). Total ATGAM concentrations in µg/mL in each plasma sample were calculated using the linear range of a standard curve, which was created by including serial dilutions of known ATGAM concentrations in each experiment.

Quantification of active ATGAM concentrations

Active ATGAM was defined as the fraction of ATGAM that is capable of binding to human lymphocytes. To quantify active ATGAM concentrations in plasma, flow cytometry was performed based on a validated protocol for the quantification of alemtuzumab levels in patient plasma[17], which since has been optimized for the measurement of rabbit-derived anti-thymocyte globulin plasma concentrations[43]. Recent work shows this assay resulted in high-quality pharmacokinetic data for a cohort of 121 acute lymphoblastic leukemia patients who received rabbit-derived anti-thymocyte globulin as part of the conditioning regimen pre-HSCT[24]. In our study, first, cryopreserved PBMCs isolated from a healthy donor were thawed and plated in 96-well plates. PBMCs from the same donor were used in all experiments to enable comparisons between experiments. Subsequently, cells were incubated with non-diluted and 3x, 9x, and 27x diluted patient plasma for 30 minutes at 4°C. Afterwards, cells were washed twice in PBS and incubated with an AlexaFluor 488-conjugated goat anti-horse antibody diluted at 1:100 in a volume of 10µL for 30 minutes at 4°C (Jackson Immunoresearch, cat 108-545-003). Next, cells were washed twice in PBS and stained with a panel of six fluorochrome-conjugated antibodies in a volume of 10µL to distinguish all major immune lineages. The following antibodies were used: APC-H7 anti-human CD3 antibody diluted at 1:60 (BD Biosciences, cat 641406); PE-Cy7 anti-human CD4 antibody diluted at 1:3000 (Beckman Coulter, cat 6607101); Pacific Blue anti-human CD8 antibody diluted

at 1:2000 (BioLegend, cat 301026); PerCP anti-human CD14 antibody diluted at 1:50 (BD Biosciences, cat 563372); APC anti-human CD19 antibody diluted at 1:50 (BD Biosciences, cat 555415) and BV510 anti-human CD56 antibody at 1:50 (BD Biosciences, cat 563041). After a 30 minute incubation at 4°C, cells were washed and measured immediately on the BD LSRFortessa™ cell analyzer (BD Biosciences). Data were analyzed in FlowJo (BD Biosciences) or OMIQ (Dotmatics). The gating strategy presented in Figure S1 determined the geometric mean fluorescence intensity of AlexaFluor 488-stained total lymphocytes, $CD4^+$ T-cells, $CD8^+$ T-cells, B-cells, NK-cells and monocytes in each acquired sample. Concentrations of ATGAM capable of binding to all lymphocytes (active ATGAM), $CD4^+$ T-cells ($CD4^+$ T-cell-binding active ATGAM), $CD8^+$ T-cells ($CD8^+$ T-cell-binding active ATGAM), $CD19^+$ B-cells (B-cell-binding active ATGAM) and $CD56^+$ NK-cells (NK-cell-binding active ATGAM) were then calculated using the mean of two reference curves, which were created by exposing the PBMCs to known concentrations of ATGAM in each experiment. To ensure consistency between experiments, the reference curves were aliquoted and stored at -20°C to enable their use across experiments. Active ATGAM concentrations were calculated in arbitrary units (AU), and the concentration of 1mg/mL ATGAM was arbitrarily set as 1000 AU/mL. The lower limit of quantification (LLoQ) of the assay was 0.02 AU/mL. At high ATGAM concentrations of >200 AU/mL in patient plasma, accurate gating of NK-cells could not be performed. As a result, concentrations of NK-cell-binding active ATGAM were not determined on days 3 and/or 4 after the first ATGAM dose for a few patients. To confirm the robustness of the assay, we analyzed the duplicate measurement of undiluted patient plasma included in each experiment, and evaluated duplicate measurements of serial dilutions of ATGAM. This revealed strong correlations between technical duplicates ($p<0.001$), underscoring within-experiment reproducibility (Figure S2A). To confirm reproducibility between experiments, plasma samples collected from several AA patients pre- and post-ATGAM were measured in duplicate in independent experiments, which resulted in highly comparable results (Figure S2B).

Population pharmacokinetic modelling and estimation of ATGAM exposure

To estimate the full concentration *versus* time profile of total and active ATGAM, non-linear mixed-effects modeling was performed using the acquired total or active ATGAM concentration-time data. Model development was performed in NONMEM version 7.4.4 (Icon Development Solutions, Ellicott City, MD). Pirana version 2.9.8 (Certara, Princeton, NJ) was used as a modeling platform, while R version 4.4.1 run in RStudio version 2023.03 was used for data visualization. Pharmacokinetic parameters were estimated using a first-order conditional estimation with interaction approach (FOCE+I). To identify the model with the best fit for the concentration-time data, both one- and two-compartment models,

incorporating linear, non-linear or parallel linear and non-linear elimination, were evaluated. Inter-individual variability (IIV) in parameter estimates was evaluated using an exponential error model, while residual unexplained variability was characterized by testing additive, proportional and combined error models. Inter-occasion variability was examined for all pharmacokinetic parameters to determine whether pharmacokinetics varied between different ATGAM infusions. A detailed overview of the steps taken during model development is shown in Tables S2 and S3.

To find the model that best described the concentration-time data, we compared each candidate model using the objective function value (OFV; -2 log likelihood). A lower OFV indicated a better fit, and a model was considered to have a significantly improved fit if its OFV decreased by at least 6.63 ($p \leq 0.01$; based on 1 degree of freedom, and assuming a chi-square distribution). Models were also assessed visually using goodness-of-fit (GOF) plots. These plots compared observed (measured) ATGAM concentrations against both individual predicted (IPRED) and population predicted (PRED) ATGAM concentrations to assess how well the model captured the measured concentration-time data. Other GOF plots compared conditional weighted residuals (CWRES) against time or PRED. The aim of these plots was to identify any systematic differences between the predicted and observed (measured) ATGAM concentrations. Other considerations in model selection included model pharmacokinetic parameter stability, inter-individual variability (IIV) and shrinkage, to ensure the model was well structured and not too complex for the available data.

To better understand the differences in the concentration-time profile of ATGAM between patients and to improve the predictive power of the model, we studied the influence of clinical covariates on the population pharmacokinetics of ATGAM. Potential covariates were selected based on physiological plausibility, and included age, sex and body weight. The effect of the selected covariates on ATGAM pharmacokinetics was initially evaluated visually, by examining how clearance (CL) or volume of distribution (V) were influenced by these covariates across all patients. Eta CL and V *versus* covariate plots were used. Given that ATGAM includes antibodies that can bind lymphocytes, we also assessed whether CL or V were influenced by differences in lymphocyte count pre-ATGAM between patients.

The final population pharmacokinetic models for total or active ATGAM were validated using prediction-corrected visual predictive checks (pcVPC)[44]. This approach relied on running the model 500 times to simulate new datasets, which were then compared to the observed (measured) ATGAM concentrations to confirm the performance of the model in predicting the ATGAM concentrations between patients. In addition, non-parametric bootstraps with 1000 simulations were performed to evaluate the precision of the final parameter estimates.

To estimate the full concentration *versus* time curve of the active ATGAM fractions capable of binding to $CD4^+$ T-cells, $CD8^+$ T-cells, B cells or NK cells, we ran the final population pharmacokinetic model (posthoc estimation) for active ATGAM using the concentration *versus* time data of each of these active ATGAM fractions.

To enable correlation analyses between ATGAM exposure and clinical parameters, we used the final population pharmacokinetic models that best described the concentration *versus* time data for total or active ATGAM to estimate individual pharmacokinetic parameters. These estimates were then used to calculate patients' cumulative exposure to total or active ATGAM, which was defined as the area under the concentration *versus* time curve ($AUC_{0\text{-}inf}$).

Immune reconstitution data

To correct for missing immune reconstitution data, we performed non-linear mixed effect modeling using the SAEMIX package[19] in R version 4.4.1. We used exponential models to predict total lymphocyte, $CD4^+$ T-cell, $CD8^+$ T-cell and NK-cell counts on each day between days 4 and 40 after start of ATGAM infusion in each patient. These models considered both the general trend across all patients and inter-individual differences. Predictions were only made for patients who had at least one measurement available between days 4 and 40 following infusion (n=43 patients), and are presented in Figure S5. B-cell reconstitution was not modeled using SAEMIX since no consistent trends were observed in the B-cell count-time data shortly after ATGAM administration between patients.

Spectral flow cytometry data acquisition and analysis

For deep immunophenotyping both before and at various time points after start of IST, spectral flow cytometry was performed. A 25-marker panel was designed to immunophenotype all major lymphoid lineages and to examine the binding of ATGAM to in-depth phenotyped immune cell subpopulations (Table S1). Cryopreserved PBMC samples from 3 AA patients, collected at AA diagnosis and up to 3.5 years after ATGAM infusion were studied (patients UPN13, UPN15 and UPN31; 7-10 samples per patient). All patients had very severe AA (VSAA), received four consecutive days 40 mg/kg/day ATGAM, responded to IST and were CMV seropositive at time of AA diagnosis. As a reference, cryopreserved PBMC samples from 5 age-, sex- and CMV status-matched healthy donors were studied. PBMC samples were thawed, plated into 96-well plates and rested at 37°C overnight. The next morning, cells were stained for viability with Zombie-NIR. Subsequently, cells were washed and stained with AlexaFluor 488-conjugated goat anti-horse IgG (Jackson Immunoresearch) diluted at 1:100 in a volume of 10µL for 30 minutes at room temperature to detect ATGAM-bound cells. Next, cells were washed and stained for 7 of 25 markers of the panel extracellularly in a volume of 10µL.

This included BUV615-, PE- or APC-conjugated peptide-HLA tetramers, which were produced in-house and were added to evaluate the presence of CMV- and EBV-specific $CD8^+$ T-cells over time. After a 30 minute incubation at room temperature, cells were washed, fixed and stained intracellularly for the remaining 17 markers of the flow cytometry panel using the FoxP3/Transcription Factor Staining Buffer Set (Invitrogen; cat 00-5523-00) according to the manufacturer's instructions. As many markers as possible were stained intracellularly to avoid potential issues in detecting key cell surface markers, which could theoretically be masked for detection by the binding of ATGAM to these cell surface markers *in vivo*. Cells were then measured on the Aurora spectral flow cytometer (Cytek Biosciences). For each acquired flow cytometry data file, single, live lymphocytes were gated in OMIQ as shown in Figure S3. A median of $0.3 \cdot 10^6$ (range $0.02\text{-}0.5 \cdot 10^6$) single, live lymphocytes were gated for each sample, resulting in a dataset of $9.3 \cdot 10^6$ cells. To compare the cellular composition between samples, $0.1 \cdot 10^6$ cells were selected from each sample by downsampling, and visualized by performing UMAP dimensionality reduction analyses in OMIQ based on 15 neighbors, a minimum distance of 0.3 and 400 epochs. Only for the day 5 sample from patient UPN13 less cells were available ($0.02 \cdot 10^6$ cells), due lymphodepletion caused by ATGAM infusion. CD3, CD19 and anti-horse IgG stainings were not used generate the UMAP due to differences in marker expression intensities between samples. To distinguish all major lymphoid lineages, all single, live lymphocytes were clustered into 150 cell clusters using FlowSOM[18] in OMIQ, which were then merged into 6 clusters based on similarities in marker expression. Major lymphoid lineages were defined as follows: $CD3^+CD4^+$ T-cells, $CD3^+CD8^+$ T-cells, $CD3^+TCR\gamma\delta^+$ T-cells, $FoxP3^+$ regulatory T-cells, $CD3^-CD56^+$ NK-cells and $CD19^+$ B-cells. Analyses at the subpopulation level were performed by manual gating in OMIQ. R version 4.4.1 ran in RStudio version 2023.03 was used for data visualization and analysis.

For detailed characterization of $CD27^+$ B-cells post-ATGAM, cryopreserved PBMCs collected from UPN31 on day 13 after the first ATGAM infusion were stained with a 16-marker spectral flow cytometry antibody panel directed against B-cell surface markers. This panel enabled analysis of B-cell isotype distribution, activation status and expression of complement inhibitors. The panel also incorporated PE- and APC-conjugated tetanus toxoid to allow for the detection of tetanus-specific B-cells. Cryopreserved PBMC samples from two sex- and age-matched healthy donors (also included in the larger spectral flow cytometry analysis) were included as a reference. Cells were fixed prior to acquisition on the Aurora spectral flow cytometer. Single, live B-cells were gated using the forward and side scatter, and by selecting $CD19^+$ B-cells while excluding all cells positive for the live dead stain. $0.2 \cdot 10^6$ cells single, live B-cells were gated from the day 13 sample from UPN31, while $0.5 \cdot 10^6$ and $1.1 \cdot 10^6$ single, live B-cells were acquired for the controls.

Supplementary tables

Table S1. Spectral flow cytometry panel for phenotyping of all lymphoid lineages.

Marker	Fluorochrome	Clone	Manufacturer	Dilution	Extracellular / intracellular staining
CD45RA	BUV395	HI100	BD	600	Intracellular
CCR7	BUV563	3D12	BD	100	Extracellular
Tetramers CMV	BUV615	NA	In-house	75	Extracellular
Tetramers EBV	BUV615	NA	In-house	75	Extracellular
CD19	BV421	HIB19	BioLegend	160	Intracellular
CD56	BV510	NCAM16.2	BD	30	Intracellular
CD27	BV570	O323	BioLegend	30	Extracellular
CD38	BV605	HIT2	BD	75	Intracellular
CCR6	BV711	G034E3	BioLegend	40	Extracellular
TCRγδ	BV750	11F2	BD	75	Extracellular
CD24	BV786	ML5	BioLegend	100	Intracellular
Goat anti-horse IgG	AF488	NA	Jackson Immunoresearch	100	Extracellular
CD3	RB545	UCHT1	BD	1000	Intracellular
FoxP3	RB744	259D/C7	BD	75	Intracellular
CD69	RB780	FN50	BD	2000	Intracellular
IgD	PE	IADB6	Beckman Coulter	1000	Extracellular
Tetramers EBV	PE	NA	In-house	100	Extracellular
Granzyme B	PE-CF594	GB11	BD	1500	Intracellular
CD28	PE-Cy5	CD28.2	BD	200	Intracellular
CD8	PE-fire 700	SK1	BioLegend	1000	Intracellular
Ki-67	PE-Cy7	B56	BD	400	Intracellular
CD4	PE-fire 810	SK3	BD	800	Intracellular
IgM	APC	MHM-88	BioLegend	160	Intracellular
Tetramers CMV	APC	NA	In-house	50	Extracellular
KLRG1	Spark NIR 685	SA231A2	BioLegend	50	Intracellular
HLA-DR	AF700	G46-6	BD	75	Intracellular
Live/dead	Zombie-NIR	NA	BioLegend	500	NA
Perforin	APC-fire 750	B-D48	BioLegend	300	Intracellular

Table S2. Model building process for active ATGAM.

Model number	Description	Model	Compared against	OFV	ΔOFV	Comments
1	One-compartment with linear elimination	CL = Θ1 × EXP(IIV) V= Θ2 × EXP(IIV)	-	84.063	-	Additive error fixed to 0.0001 (rounding errors without fixation)
2	One-compartment with parallel linear and non-linear elimination	CL = Θ1 × EXP(IIV) V= Θ2 × EXP(IIV) Vmax= Θ3 × EXP(IIV) Km= Θ4 × EXP(IIV)	1	84.063	0	Additive error fixed to 0.0001
3	Two-compartment with linear elimination	CL = Θ1 × EXP(IIV) Vc = Θ2 × EXP(IIV) Q = Θ3 × EXP(IIV) Vp = Θ4	2	57.611	-26.45	Additive error fixed to 0.0001
4	Two-compartment with linear elimination + IIV V2	CL = Θ1 × EXP(IIV) Vc = Θ2 × EXP(IIV) Q = Θ3 × EXP(IIV) Vp = Θ4 × EXP(IIV)	3	-12.41	-70.02	Additive error fixed to 0.0001 Worse VPC (see Figure S4)
4	Two-compartment with linear elimination + OMEGA BLOCK between IIV CL and V1	CL = Θ1 × EXP(IIV) Vc = Θ2 × EXP(IIV) Q = Θ3 × EXP(IIV) Vp = Θ4	3	44.027	-13.58	Additive error fixed to 0.0001
5	Two-compartment with linear elimination + OMEGA BLOCK between IIV CL and V1 + different proportional error ≥60AU/mL and <60AU/mL	CL = Θ1 × EXP(IIV) Vc = Θ2 × EXP(IIV) Q = Θ3 × EXP(IIV) Vp = Θ4	4	34.705	-9.322	**Final model** Additive error fixed to 0.0001 IIV CL: 43.1% IIV Vc: 52% IIV Q: 143.2%
6	Two-compartment with linear elimination + OMEGA BLOCK between IIV CL and V1 + different proportional error ≥60AU/mL and <60AU/mL + bodyweight as covariate	CL = Θ1 × EXP(IIV) × ((WT/MWT)**Θ5) Vc = Θ2 × EXP(IIV) × ((WT/MWT)**Θ6) Q = Θ3 × EXP(IIV) Vp = Θ4	5	35.505	0.8	Additive error fixed to 0.0001 IIV CL: 45.2% IIV Vc: 50.8% IIV Q: 145.9%

Model number	Description	Model	Compared against	OFV	ΔOFV	Comments
7	Two-compartment with linear elimination + OMEGA BLOCK between IIV CL and V1 + different proportional error ≥60AU/mL and <60AU/mL + lymphocyte count pre-ATGAM as covariate	CL = Θ1 × EXP(IIV) × (1+(LYMPH/MLYMPH)*Θ5) Vc = Θ2 × EXP(IIV) Q = Θ3 × EXP(IIV) Vp = Θ4	5	36.813	2.108	Additive error fixed to 0.0001 IIV CL: 42.9% IIV Vc: 50.7% IIV Q: 144.2%
8	Two-compartment with parallel linear and non-linear elimination	CL = Θ1 × EXP(IIV) Vc= Θ2 × EXP(IIV) Vp= Θ3 Vmax= Θ4 × EXP(IIV) Km= Θ5 × EXP(IIV)	-	Model unstable	Model unstable	Additive error fixed to 0.0001

CL indicates clearance; IIV: inter-individual variability; Km: Michaelis-Menten contant; LYMPH: lymphocyte count pre-ATGAM; MLYMPH: median lymphocyte count pre-ATGAM; MWT: median population weight; OFV: objective function value; Q: intercompartmental clearance; V: volume of distribution; Vc: volume of distribution central compartment; Vp: volume of distribution peripheral compartment; Vmax: maximum elimination rate; WT: bodyweight.

Table S3. Model building process for total ATGAM.

Model number	Description	Model	Compared against	OFV	ΔOFV	Comments
1	One-compartment with linear elimination	CL = Θ1 × EXP(IIV) V= Θ2 × EXP(IIV)	-	2026.3	-	Additive error fixed to 0.0001 (rounding errors without fixation)
2	One-compartment with parallel linear and non-linear elimination	CL = Θ1 × EXP(IIV) V= Θ2 × EXP(IIV) Vmax= Θ3 × EXP(IIV) Km= Θ4 × EXP(IIV)	1	2026.4	0.06	Additive error fixed to 0.0001. Model instable.
3	Two-compartment with linear elimination	CL = Θ1 × EXP(IIV) Vc = Θ2 × EXP(IIV) Q = Θ3 × EXP(IIV) Vp = Θ4	1	1937.99	-88.32	Additive error fixed to 0.0001 Model unstable
4	Two-compartment with linear elimination + Vp fixed	CL = Θ1 × EXP(IIV) Vc = Θ2 × EXP(IIV) Vp = Θ4 FIX	3	1940.7	2.72	**Final model** Additive error fixed to 0.0001 IIV CL: 44.0% IIV Vc: 57.2% IIV Q: 290.0%
5	Two-compartment with linear elimination + Vp fixed + OMEGA BLOCK between IIV CL and V1	CL = Θ1 × EXP(IIV) Vc = Θ2 × EXP(IIV) Q = Θ3 × EXP(IIV) Vp = Θ4 FIX	4	1935.9	-4.79	Additive error fixed to 0.0001 IIV CL: 44.2% IIV Vc: 58.1% IIV Q: 303.3%
6	Two-compartment with linear elimination + Vp fixed + bodyweight as covariate	CL = Θ1 × EXP(IIV) × ((WT/MWT)**Θ5) Vc = Θ2 × EXP(IIV) × ((WT/MWT)**Θ6) Q = Θ3 × EXP(IIV) Vp = Θ4	4	1947.2	6.48	Additive error fixed to 0.0001 IIV CL: 50.5% IIV Vc: 59.9% IIV Q: 295.8%

Model number	Description	Model	Compared against	OFV	ΔOFV	Comments
8	Two-compartment with parallel linear and non-linear elimination	CL = Θ1 × EXP(IIV) Vc= Θ2 × EXP(IIV) Vp= Θ3 Vmax= Θ4 × EXP(IIV) Km= Θ5 × EXP(IIV)	-	Model unstable	Model unstable	Additive error fixed to 0.0001

CL indicates clearance; IIV: inter-individual variability; Km: Michaelis-Menten contant; MWT: median population weight; OFV: objective function value; Q: intercompartmental clearance; V: volume of distribution; Vc: volume of distribution central compartment; Vp: volume of distribution peripheral compartment; Vmax: maximum elimination rate; WT: bodyweight.

Table S4. Model estimates for active ATGAM pharmacokinetic parameters.

Parameter	Median (range)	Mean	RSE (%)	Shrinkage	1000 bootstrap run results	
					Median	95% CI
Clearance (CL in L/day)	6.5 (3.4-24.0)	6.97	11%		7.02	5.07 - 9.80
Volume of distribution of central compartment (V_c in L)	1.5 (0.6-4.2)	1.51	17%		1.51	0.88 - 2.86
Intercompartmental clearance (Q in L/day)	2.3 (0.5-65.2)	3.2	38%		3.32	1.32 - 9.18
Volume of distribution of peripheral compartment (V_p in L)	11.3	11.2	12%		11.56	6.51 - 22.94
Inter-individual variability (IIV)						
Clearance (IIV CL, %)		43.1	13%	9%	41.98	31.01 - 53.62
CL ~ V_c (%)		-	-	-	39.26	15.72 - 56.14
Volume of distribution of central compartment (IIV Vc, %)		52	16%	22%	49.48	28.36 - 68.12
Intercompartmental clearance (IIV Q, %)		143.2	17%	8%	141.75	102.51 - 194.50
Random residual variability						
Proportional error (CV%)		0.3	12%		0.30	0.23 - 0.57
Additional error (AU/mL)		0.0001	fixed		0.0001	0.0001 - 0.0001
Half-life distribution phase (days)	0.09 (0.02-0.25)					
Half-life elimination phase (days)	4.5 (0.5-16.1)					
Peak concentration (C_{max} in AU/mL)	668.1 (208.6-1595.9)					
Total exposure (AUC_{0-inf})	1801.2 (583.9-4218.7)					

Table S5. Model estimates for total ATGAM pharmacokinetic parameters.

Parameter	Median (range)	Mean	RSE (%)	Shrinkage	1000 bootstrap run results	
					Median	95% CI
Clearance (CL in L/day)	0.4 (0.2-1.4)	0.426	8%		0.42	0.36 - 0.50
Volume of distribution of central compartment (V_c in L)	3.3 (0.9-8.7)	3.22	8%		3.17	2.65 - 3.67
Intercompartmental clearance (Q in L/day)	0.1 (0.0006-2.7)	0.032	12%		0.03	0.01 - 0.15
Volume of distribution of peripheral compartment (V_p in L)	0.9	0.949	fixed		0.95	0.95 - 0.95
Inter-individual variability (IIV)						
Clearance (IIV CL, %)		44	14%	10%	43.10	28.65 - 55.37
Volume of distribution of central compartment (IIV Vc, %)		57.2	10%	4%	57.10	46.13 - 69.76
Intercompartmental clearance (IIV Q, %)		290	17%	41%	276.86	137.16 - 402.10
Random residual variability						
Proportional error (CV%)		0.355	10%		0.35	0.28 - 0.42
Additional error (ug/mL)		0.0001	fixed		0.0001	0.0001 - 0.0001
Half-life distribution phase (days)	4.3 (0.2-8.9)					
Half-life elimination phase (days)	16.8 (1.8-1015.9)					
Peak concentration (C_{max} in µg/mL)	2500.7 (1175.4-7649.0)					
Total exposure ($AUC_{0\text{-}inf}$)	28160.5 (9761.4-90999.0)					

Table S6. Patient characteristics by active ATGAM exposure groups.

Characteristic	Low active ATGAM exposure (n=15)	Medium active ATGAM exposure (n=14)	High active ATGAM exposure (n=15)	P-value
Age at diagnosis (median in years)	40	60	57	0.21
Sex (n)				0.32
Male	7	8	11	
Female	8	6	4	
Disease severity at diagnosis (n)				0.91
Non-severe AA	2	3	2	
Severe AA	7	7	9	
Very severe AA	6	4	4	
Weight at diagnosis (median in kg)	71	75	88	0.003
Height (median in cm)	170	173	180	0.003
Body mass index at diagnosis (median)	22.4	24.5	26.0	0.33
Neutrophils pre-ATGAM (median in 10^9/L)	0.33	0.24	0.31	>0.9
Reticulocytes pre-ATGAM (median in 10^9/L)	17.5	8.4	10	0.6
Lymphocytes pre-ATGAM (median in 10^6/L)[a]	1625	1485	1315	0.75
Eltrombopag added to IST (n)	5	3	8	0.11
Eltrombopag added with start ATGAM	3	2	2	
Eltrombopag added 20-180 days post-ATGAM	2: Day 96 Day 100	1: Day 92	7: Day 69 Day 86 Day 138 Day 160 Day 163 Day 165	
Other second-line treatment ≤180 days post-ATGAM	0	0	0	1.0
Ciclosporin discontinued ≤180 days post-ATGAM	0	0	1	0.40
Deaths ≤180 days post-ATGAM	2	1	1	0.78

[a]Data missing for 2 AA patients (1 in low and 1 in high exposure groups). Statistical differences between continuous variables calculated by Kruskal Wallis test. Statistical differences between categorical variables calculated by Fisher's Exact test. Statistical differences in addition of eltrombopag to IST, ciclosporin discontinuation and death calculated by log-rank (survival) test.

Final active ATGAM pharmacokinetic model code

```
$PROBLEM PK

$INPUT ID TIME DV TAD ATGNR C AMT RATE MDV EVID WEIGHT HEIGHT LYMPHO CD4
CD8 NK B MONO dose_code ATGMgKg DaysATG ATGMgKgDay DayATGStart AGE GENDER
RESPONSE_3M RESPONSE_6M BMI

$DATA PK_ATGAM_data_ACTIVE.csv  IGNORE=@

$SUBROUTINES ADVAN6 TOL=3

$MODEL
COMP=(CENTRAL DEFOBS DEFDOSE)
COMP=(PERIPH)
COMP= AUC

$PK
CL = THETA(1) * EXP(ETA(1))
V1 = THETA(2) * EXP(ETA(2))
Q  = THETA(3) * EXP(ETA(3))
V2 = THETA(4)
S1 = V1
K10=CL/V1
K12=Q/V1
K21=Q/V2

$DES
C1=A(1)/V1
DADT(1)=-K10*A(1)-K12*A(1)+K21*A(2)
DADT(2)=-K21*A(2)+K12*A(1)
DADT(3)= C1

$ERROR
IPRED = F
IF(DV.GE.60) W = SQRT(THETA(5)**2*IPRED**2 + THETA(6)**2)
IF(DV.LT.60) W = SQRT(THETA(7)**2*IPRED**2 + THETA(6)**2)
   Y = IPRED + W*EPS(1)
 IRES = DV-IPRED
IWRES = IRES/W
AUC = A(3)
AUCCL = AMT/CL
```

```
$THETA
(0, 6.97) ; CL
(0, 1.51) ; V1
(0, 3.2) ; Q
(0, 11.2) ; V2
(0, 0.3) ; Prop.RE (sd)
(0.0001) FIX ; Add.RE (sd)
(0, 0.579) ; Prop.RE (sd)
$OMEGA BLOCK(2)
 0.186  ; IIV CL
 0.18 0.27  ; IIV V1
$OMEGA
 2.05 ; IIV Q

$SIGMA
 1 FIX  ; Proportional error PK

$EST METHOD=1 INTER MAXEVAL=2000 NOABORT SIG=2 PRINT=1 POSTHOC
$COV

; Xpose
$TABLE CL V1 V2 Q ID TIME DV MDV EVID PRED IPRED IWRES CWRES ETA1 ETA2 ETA3
LYMPHO CD4 CD8 B NK MONO AGE GENDER WEIGHT HEIGHT BMI AUCCL AUC Response_3M
Response_6M ONEHEADER NOPRINT FILE=sdtab002
$TABLE CL V1 ID TIME DV MDV EVID PRED IPRED IWRES CWRES ETA1 ETA2 ETA3 LYMPHO
CD4 CD8 B NK MONO AGE GENDER WEIGHT HEIGHT AUCCL AUC Response_3M Response_6M
ONEHEADER NOPRINT FIRSTONLY FILE=patab002
```

Final total ATGAM pharmacokinetic model code

```
$PROBLEM PK

$INPUT ID TIME DV TAD ATGNR C AMT RATE MDV EVID WEIGHT HEIGHT LYMPH CD4
CD8 NK B MONO dose_code ATGMgKg DaysATG ATGMgKgDay DayATGStart AGE GENDER
RESPONSE_3M RESPONSE_6M

$DATA PK_ATGAM_data_TOTAL.csv  IGNORE=@

$SUBROUTINES ADVAN6 TOL=3

$MODEL
COMP=(CENTRAL DEFOBS DEFDOSE)
COMP=(PERIPH)
COMP= AUC

$PK
TVCL = THETA(1)
CL = TVCL * EXP(ETA(1))

TVV1 = THETA(2)
V1 = TVV1 * EXP(ETA(2))

TVQ = THETA(3)
Q  = TVQ * EXP(ETA(3))

TVV2 = THETA(4)
V2 = TVV2

S1 = V1

K10=CL/V1
K12=Q/V1
K21=Q/V2

$DES
C1=A(1)/V1
DADT(1)=-K10*A(1)-K12*A(1)+K21*A(2)
DADT(2)=-K21*A(2)+K12*A(1)
DADT(3)= C1
```

```
$ERROR
IPRED = F
   W = SQRT(THETA(5)**2*IPRED**2 + THETA(6)**2)
   Y = IPRED + W*EPS(1)
 IRES = DV-IPRED
IWRES = IRES/W
AUC = A(3)
AUCCL = AMT/CL

$THETA
(0, 0.424) ; CL
(0, 3.23) ; V1
(0, 0.0299) ; Q
(0.949) FIX ; V2
(0, 0.353) ; Prop.RE (sd)
(0.00001) FIX ; Add.RE (sd)

$OMEGA
 0.194 ; IIV CL
 0.318 ; IIV V1
 8.74 ; IIV Q

$SIGMA
 1 FIX  ; Proportional error PK

$EST METHOD=1 INTER MAXEVAL=2000 NOABORT SIG=2 PRINT=1 POSTHOC
$COV

; Xpose
$TABLE CL V1 V2 Q ID TIME DV MDV EVID PRED IPRED IWRES CWRES ETA1 ETA2 ETA3
LYMPH CD4 CD8 B NK MONO AGE GENDER WEIGHT HEIGHT AUCCL AUC Response_3M
Response_6M ONEHEADER NOPRINT FILE=sdtab005
$TABLE CL V1 V2 Q ETA1 ETA2 ETA3 LYMPH CD4 CD8 B NK MONO AGE GENDER WEIGHT
HEIGHT ONEHEADER NOPRINT FIRSTONLY FILE=patab005
```

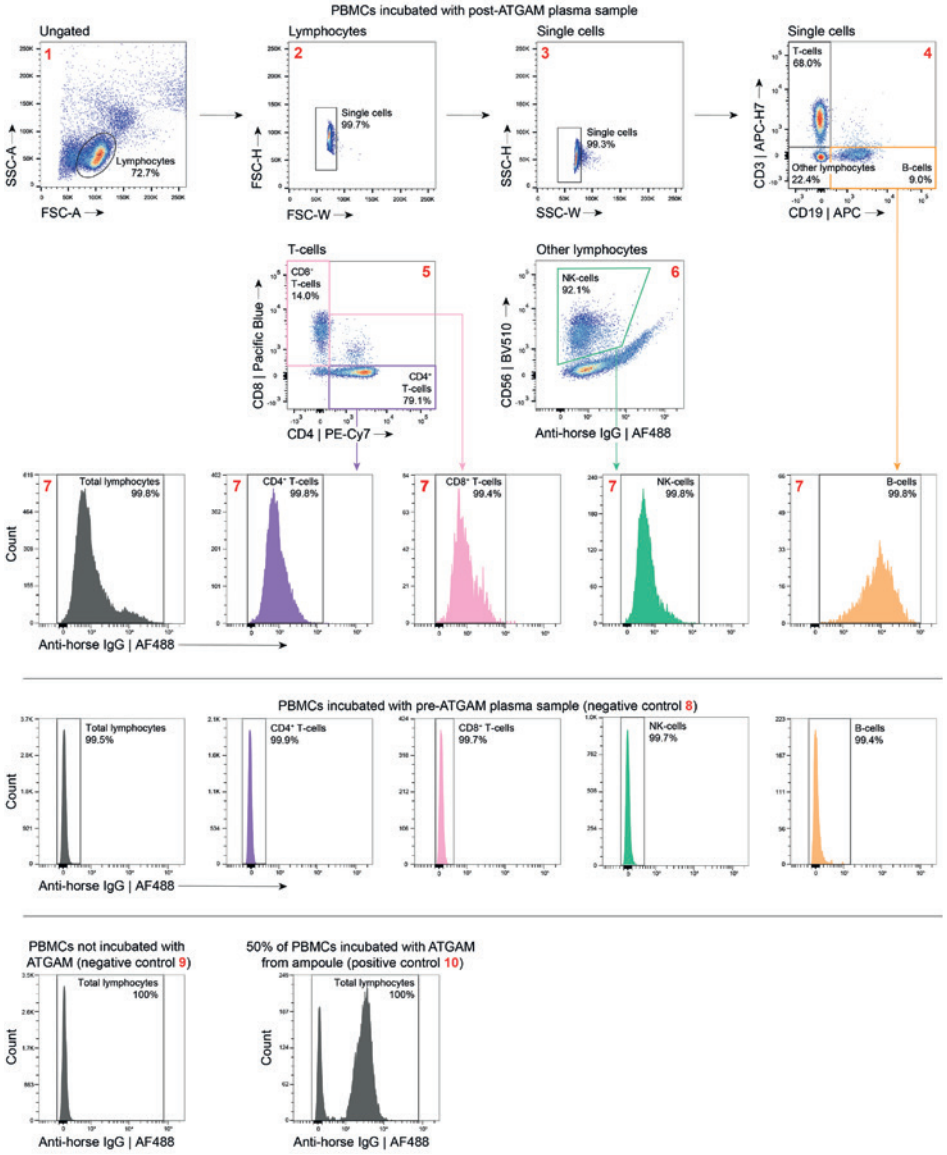


Figure S1. Gating strategy for quantification of active ATGAM plasma concentrations. Lymphocytes were gated using the forward and side scatter (panel 1). Doublets were excluded, and single lymphocytes were selected for further analysis (panels 2-3). Within the single lymphocytes, $CD3^+$ T-cells, $CD19^+$ B-cells or $CD3^-CD19^-$ other lymphocytes were identified (panel 4). $CD4^+$ T-cells and $CD8^+$ T-cells were identified within the T-cell gate (panel 5). $CD56^+$ NK-cells were identified within the 'other lymphocyte' gate (panel 6). The geometric mean fluorescence intensity for the Alexa Fluor 488 anti-horse IgG antibody was determined for each gated population (panels 7). This was used to calculate the active ATGAM concentrations in the patient plasma sample using a reference curve obtained by exposing PBMCs to known concentrations of ATGAM. The gating strategy is shown for PBMCs incubated with a representative post-ATGAM patient plasma sample. Negative controls were included in each experiment and included PBMCs incubated with pre-ATGAM patient plasma samples (panels 8) and PBMCs not exposed to ATGAM (panel 9). Positive controls were PBMCs exposed to known concentrations of ATGAM (panel 10).

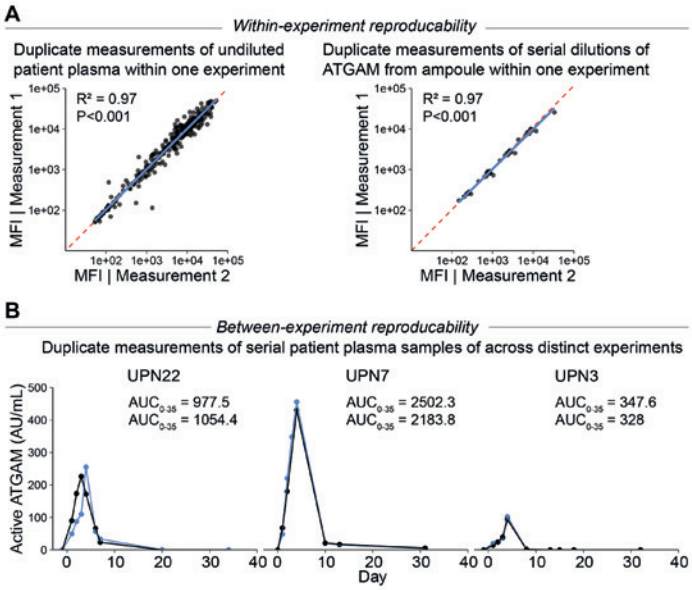


Figure S2. Reproducibility and robustness of the active ATGAM assay. [A] Within-experiment reproducibility, shown by correlation plot of duplicate measurements of undiluted patient plasma within a single experiment (left), or duplicate measurements of serial dilutions of ATGAM (right). [B] Between-experiment reproducibility, shown by duplicate measurements of active ATGAM concentrations in patient plasma in independent experiments.

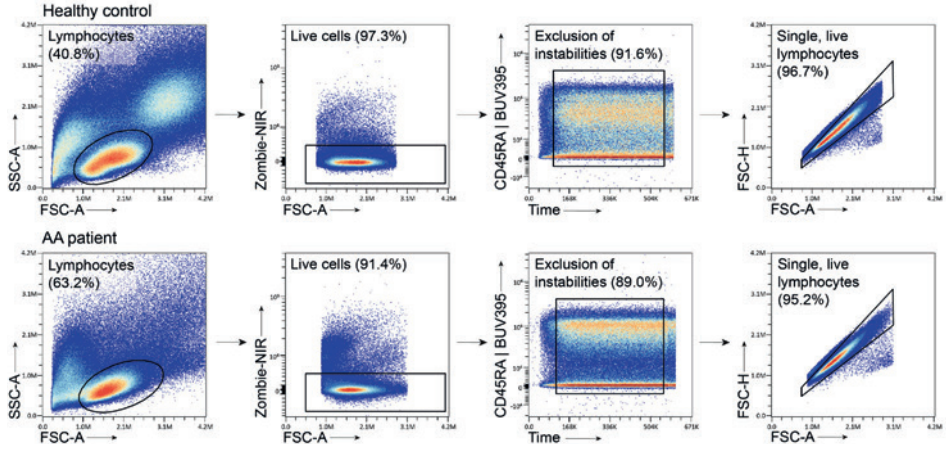


Figure S3. Gating strategy for selection of single, live lymphocytes from spectral flow cytometry data. Lymphocytes were gated in OMIQ based on the forward and side scatter (panel 1). Next, live cells were identified by selecting cells negative for Zombie-NIR (panel 2), and acquisition instabilities were removed by excluding events recorded at the beginning or end of each measurement (panel 3). Finally, doublets were excluded using the forward scatter height (FSC-H) and forward scatter area (FSC-A) parameters (panel 4). Data for a representative healthy control and aplastic anemia patient are shown. Single, live lymphocytes gated in panel 4 were selected for downstream analyses.

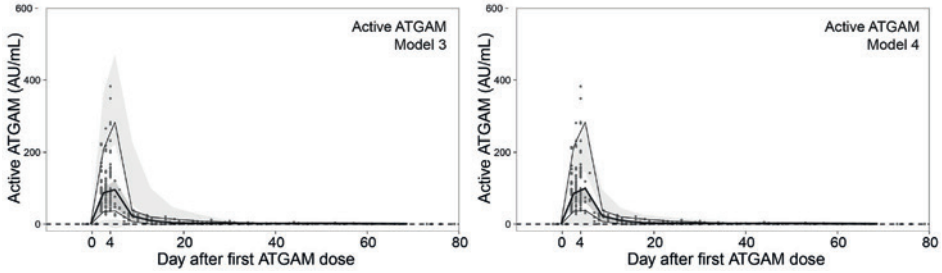
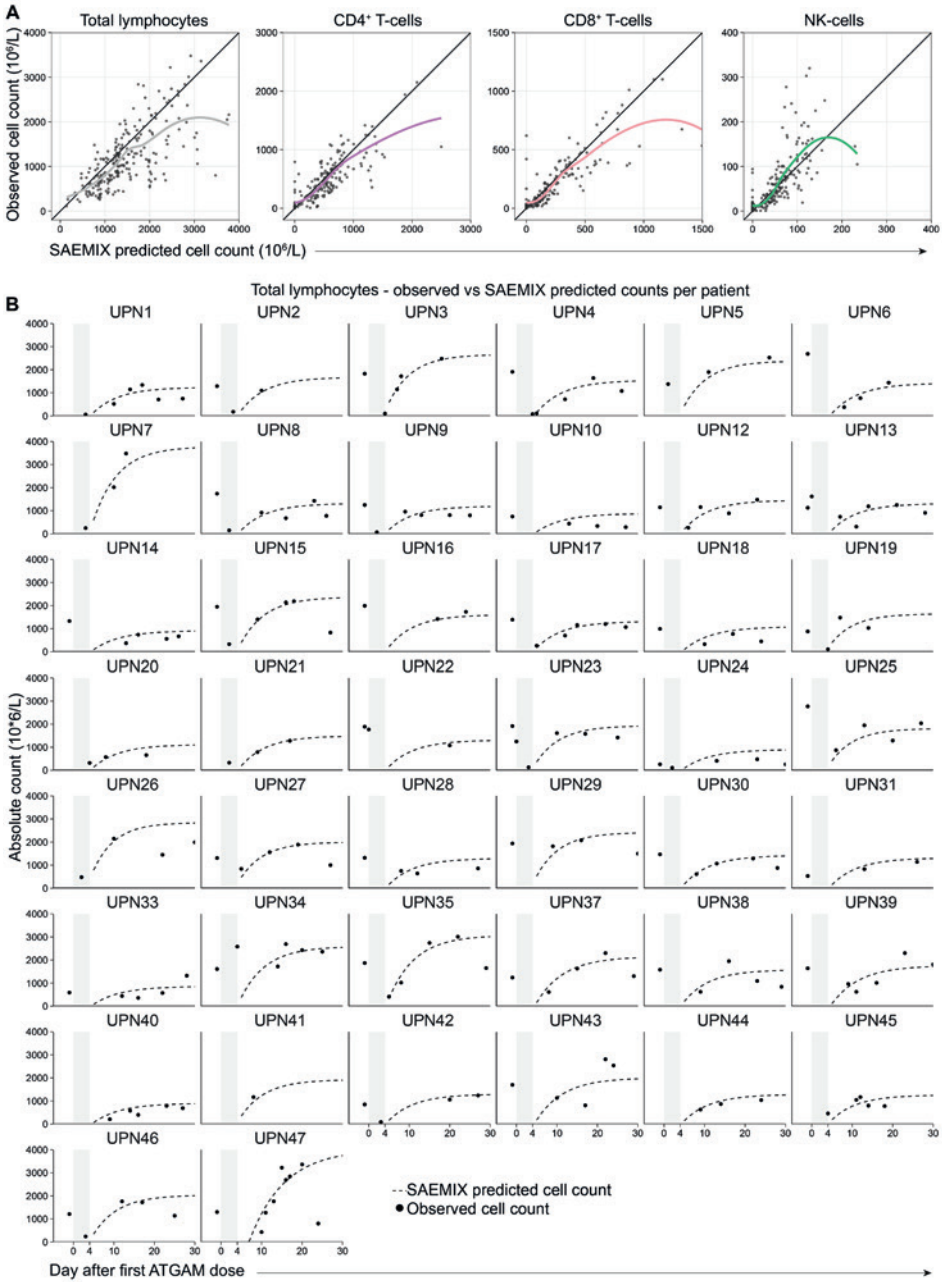
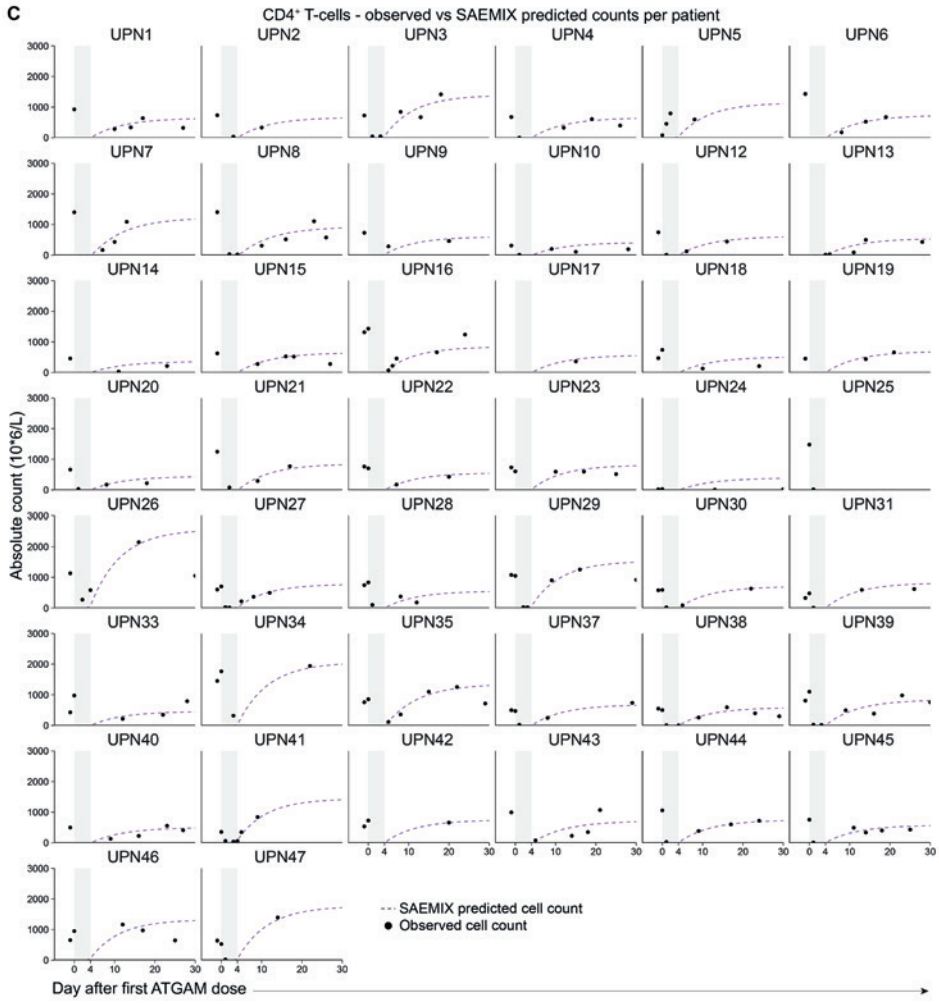
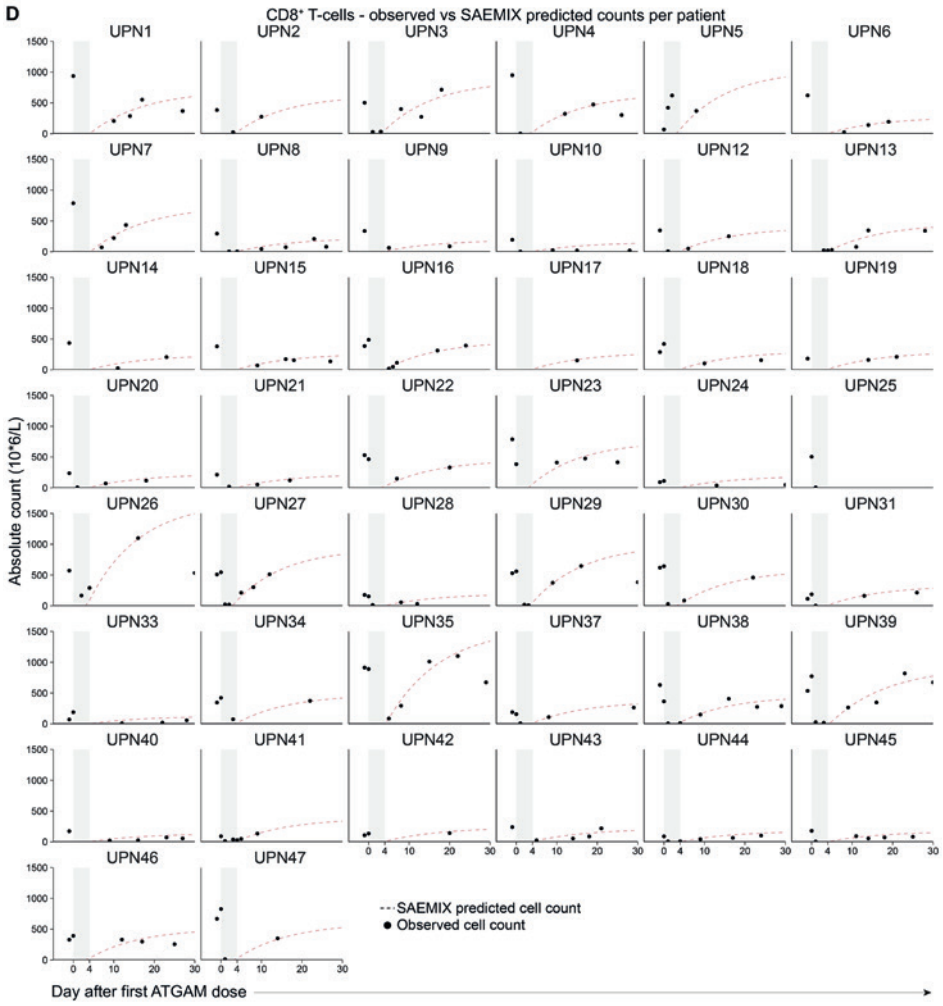


Figure S4. Visual predictive checks for population pharmacokinetic model 3 and model 4 for active ATGAM. Prediction-corrected visual predictive check (VPC) for the final model for active ATGAM. Black lines represent the predicted active ATGAM concentrations at the 95th, 50th, and 5th percentiles. Shaded light gray areas indicate the 95% confidence intervals for the predicted 5th and 95th percentiles, while the dark gray shaded area represents the 95% confidence interval for the predicted 50th percentile. Observed active ATGAM concentrations in all 44 AA patients are shown by black dots.


A
Total lymphocytes
CD4+ T-cells
CD8+ T-cells
NK-cells
Observed cell count (10⁶/L)
SAEMIX predicted cell count (10⁶/L)
B
Total lymphocytes - observed vs SAEMIX predicted counts per patient
UPN1
UPN2
UPN3
UPN4
UPN5
UPN6
UPN7
UPN8
UPN9
UPN10
UPN12
UPN13
UPN14
UPN15
UPN16
UPN17
UPN18
UPN19
UPN20
UPN21
UPN22
UPN23
UPN24
UPN25
UPN26
UPN27
UPN28
UPN29
UPN30
UPN31
UPN33
UPN34
UPN35
UPN37
UPN38
UPN39
UPN40
UPN41
UPN42
UPN43
UPN44
UPN45
UPN46
UPN47
Absolute count (10*6/L)
SAEMIX predicted cell count
Observed cell count
Day after first ATGAM dose


C
CD4+ T-cells - observed vs SAEMIX predicted counts per patient
UPN1
UPN2
UPN3
UPN4
UPN5
UPN6
UPN7
UPN8
UPN9
UPN10
UPN12
UPN13
UPN14
UPN15
UPN16
UPN17
UPN18
UPN19
UPN20
UPN21
UPN22
UPN23
UPN24
UPN25
UPN26
UPN27
UPN28
UPN29
UPN30
UPN31
UPN33
UPN34
UPN35
UPN37
UPN38
UPN39
UPN40
UPN41
UPN42
UPN43
UPN44
UPN45
UPN46
UPN47
Absolute count (10^6/L)
0
1000
2000
3000
0 4 10 20 30
SAEMIX predicted cell count
Observed cell count
Day after first ATGAM dose


D
CD8⁺ T-cells - observed vs SAEMIX predicted counts per patient
UPN1
UPN2
UPN3
UPN4
UPN5
UPN6
UPN7
UPN8
UPN9
UPN10
UPN12
UPN13
UPN14
UPN15
UPN16
UPN17
UPN18
UPN19
UPN20
UPN21
UPN22
UPN23
UPN24
UPN25
UPN26
UPN27
UPN28
UPN29
UPN30
UPN31
UPN33
UPN34
UPN35
UPN37
UPN38
UPN39
UPN40
UPN41
UPN42
UPN43
UPN44
UPN45
UPN46
UPN47
Absolute count (10*6/L)
SAEMIX predicted cell count
Observed cell count
Day after first ATGAM dose

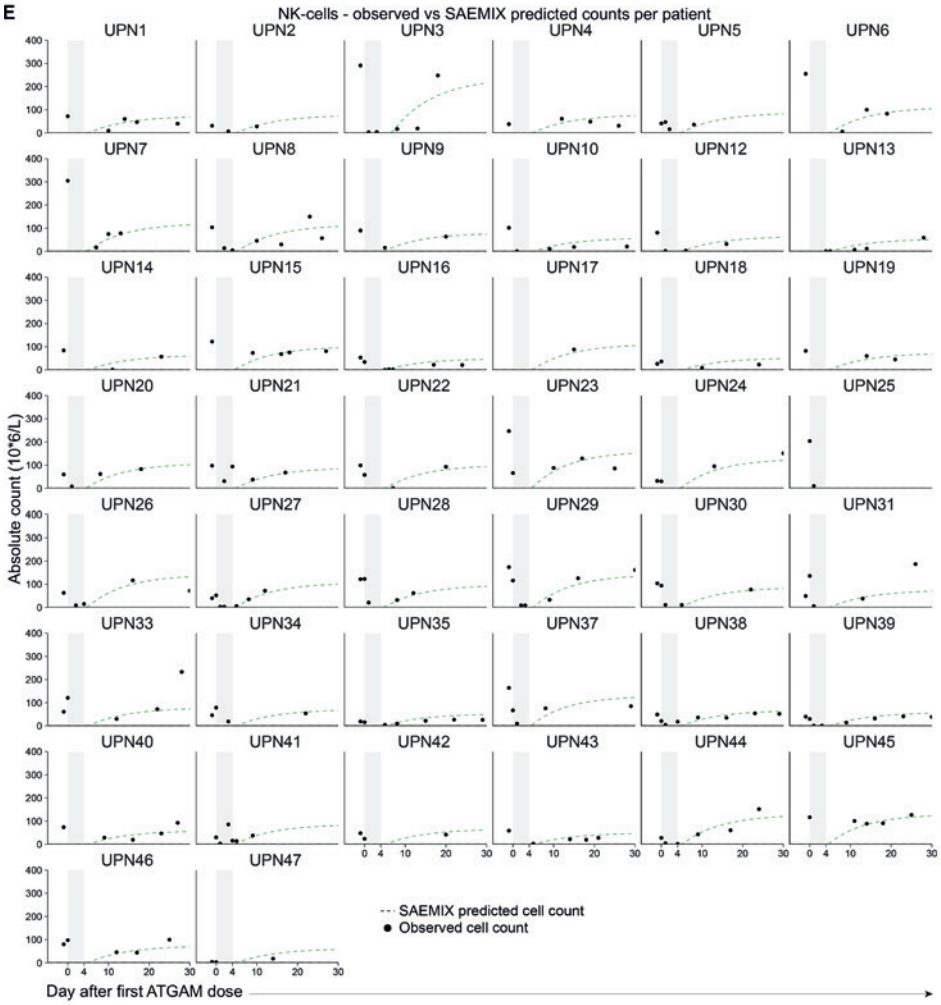


Figure S5. Observed versus predicted immune reconstitution data. [A] Observed versus SAEMIX-predicted total lymphocyte, $CD4^+$ T-cell, $CD8^+$ T-cell and NK-cell counts shown for all patients. The trend between observed and predicted counts are shown using loess regression. [B-D] Observed versus SAEMIX-predicted total lymphocyte [B], $CD4^+$ T-cell [C], $CD8^+$ T-cell [D] and NK-cell [E] counts per patient. Dots in present observed lymphocyte counts; dotted lines present predictions.

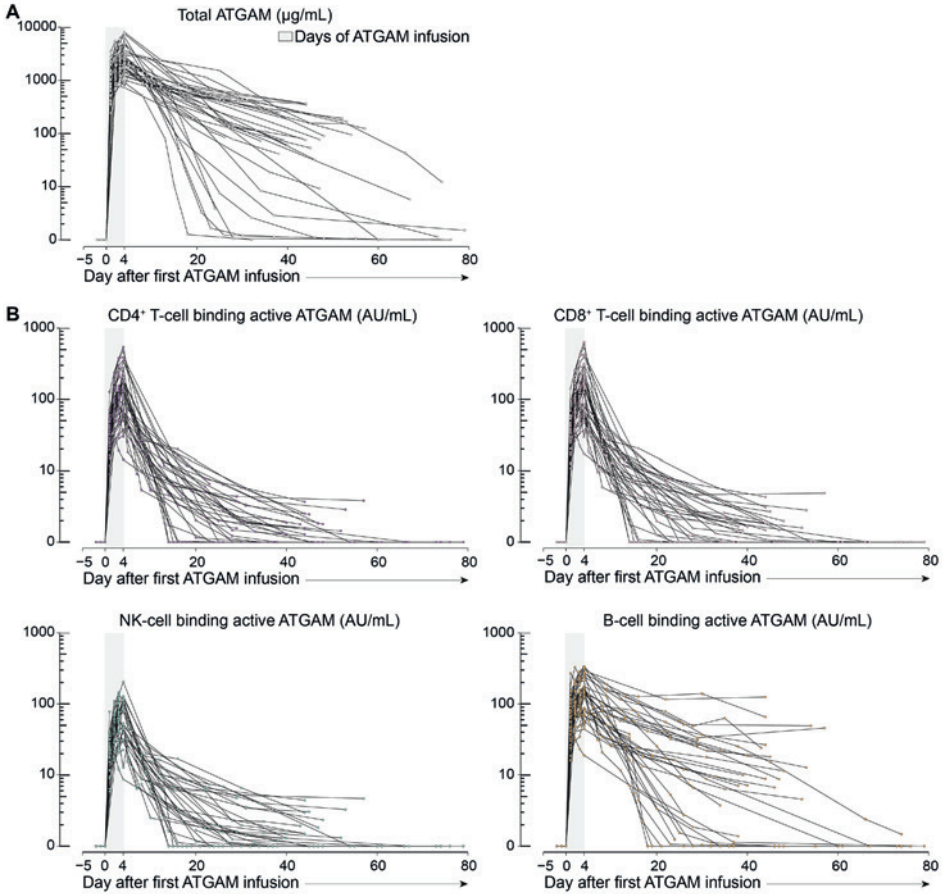


Figure S6. Concentration-time profile of total ATGAM and lineage-binding active ATGAM in patient plasma. [A] Measured total ATGAM, or [B] measured $CD4^+$ T-cell-binding active ATGAM, $CD8^+$ T-cell-binding active ATGAM, $CD19^+$ B-cell-binding active ATGAM, and NK-cell binding active ATGAM concentrations in patient plasma (in µg/mL or arbitrary units/mL; n=44 patients) over time before, during and after ATGAM infusion on days 0-4, shown on a logarithmic scale.

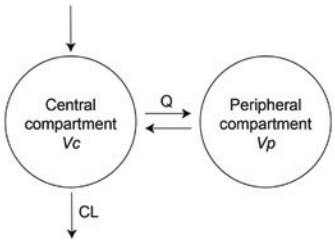


Figure S7. Population pharmacokinetic model overview. A two-compartment population pharmacokinetic model best described the total and active ATGAM concentration-time data. CL: linear clearance, Q: intercompartmental clearance between central compartment with volume Vc, and peripheral compartment with volume Vp.

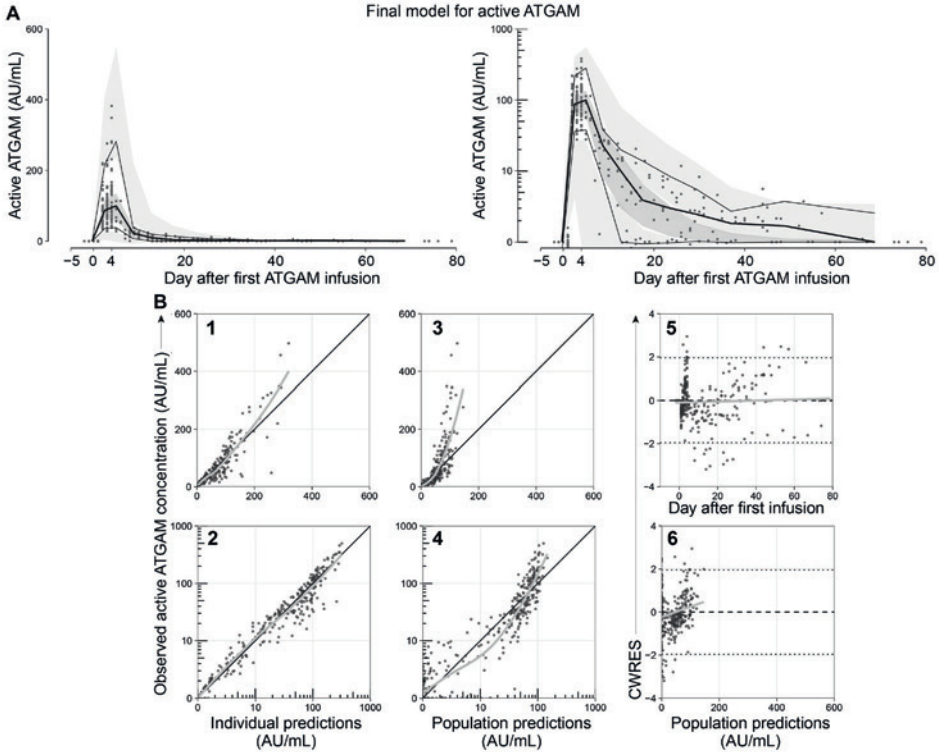


Figure S8. Prediction-corrected visual predictive check and goodness of fit plots for the final pharmacokinetic model for active ATGAM. [A] Prediction-corrected visual predictive check (VPC) for the final model for active ATGAM. Black lines represent the predicted active ATGAM concentrations at the 95th, 50th, and 5th percentiles. Shaded light gray areas indicate the 95% confidence intervals for the predicted 5th and 95th percentiles, while the dark gray shaded area represents the 95% confidence interval for the predicted 50th percentile. Observed active ATGAM concentrations in all 44 AA patients are shown by black dots. VPC is shown on a linear (left) or a logarithmic (right) scale. [B] Goodness of fit plots for the final model for active ATGAM. Observed versus individual predicted (IPRED) active ATGAM concentrations on a linear (1) and logarithmic (2) scale; observed versus population predicted (PRED) active ATGAM concentrations on a linear (3) and logarithmic (4) scale; conditional weighted residuals (CWRES) versus time after ATGAM infusion on days 0-4 (5); conditional weighted residuals (CWRES) versus population predicted active ATGAM concentrations (6). Dotted lines in (5) and (6) present the +/- 1.96 ranges of CWRES (95% confidence interval), which should include 95% of the CWRES values.

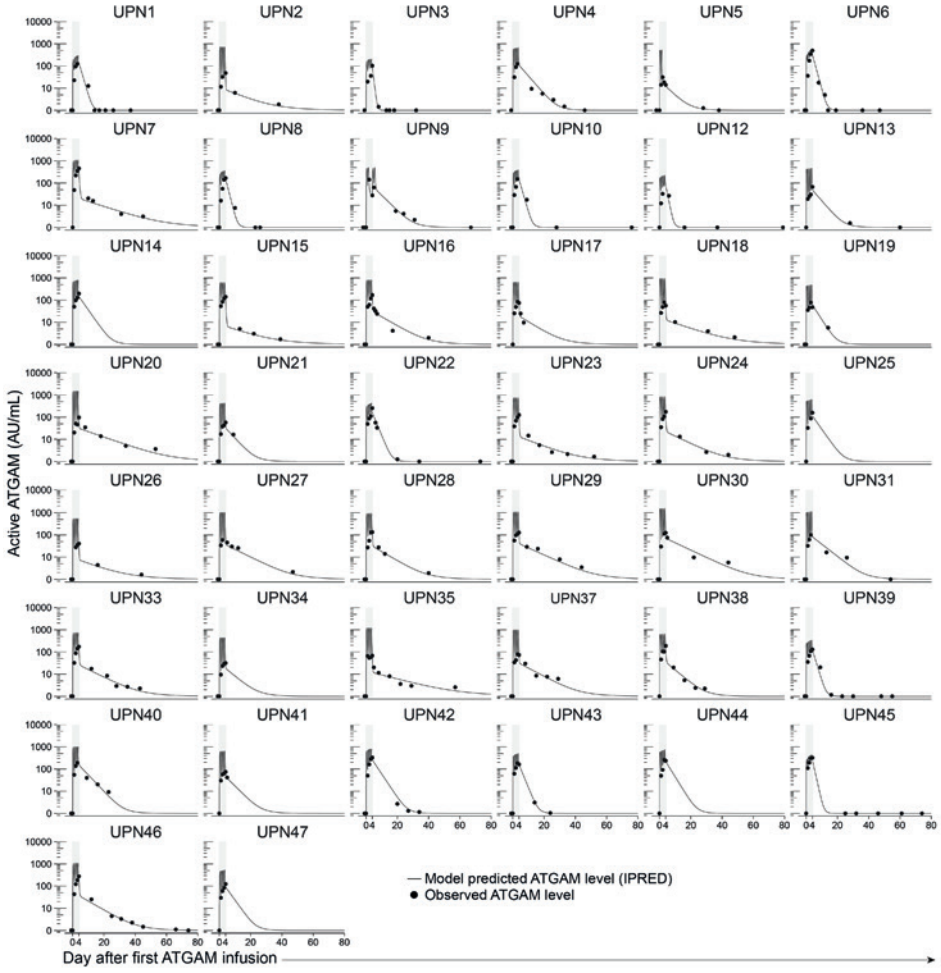


Figure S9. Observed versus model-predicted active ATGAM concentrations per patient. Observed active ATGAM concentrations are shown by black dots, while modelled active ATGAM concentrations in time are shown using black lines. Data are presented on a logarithmic axis.

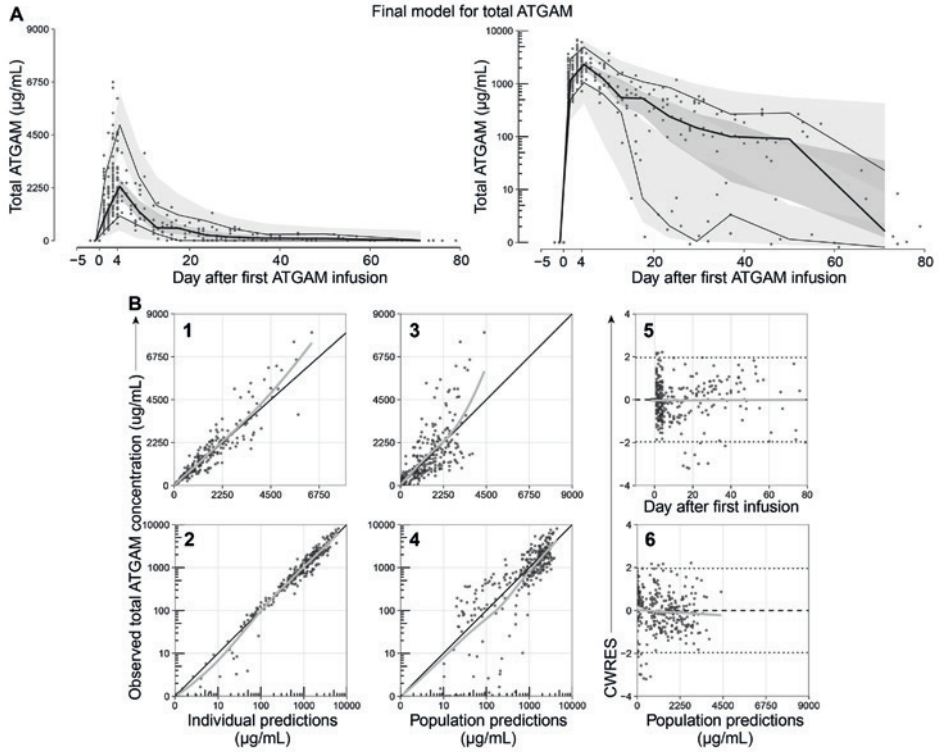


Figure S10. Prediction-corrected visual predictive check and goodness of fit plots for the final pharmacokinetic model for total ATGAM. [A] Prediction-corrected visual predictive check (VPC) for the final model for total ATGAM. Black lines represent the predicted total ATGAM concentrations at the 95th, 50th, and 5th percentiles. Shaded light gray areas indicate the 95% confidence intervals for the predicted 5th and 95th percentiles, while the dark gray shaded area represents the 95% confidence interval for the predicted 50th percentile. Observed total ATGAM concentrations in all 44 AA patients are shown by black dots. VPC is shown on a linear (left) or a logarithmic (right) scale. [B] Goodness of fit plots for the final model for total ATGAM. Observed versus individual predicted (IPRED) total ATGAM concentrations on a linear (1) and logarithmic (2) scale; observed versus population predicted (PRED) total ATGAM concentrations on a linear (3) and logarithmic (4) scale; conditional weighted residuals (CWRES) versus time after ATGAM infusion on days 0-4 (5); conditional weighted residuals (CWRES) versus population predicted total ATGAM concentrations (6). Dotted lines in (5) and (6) present the +/- 1.96 ranges of CWRES (95% confidence interval), which should include 95% of the CWRES values.

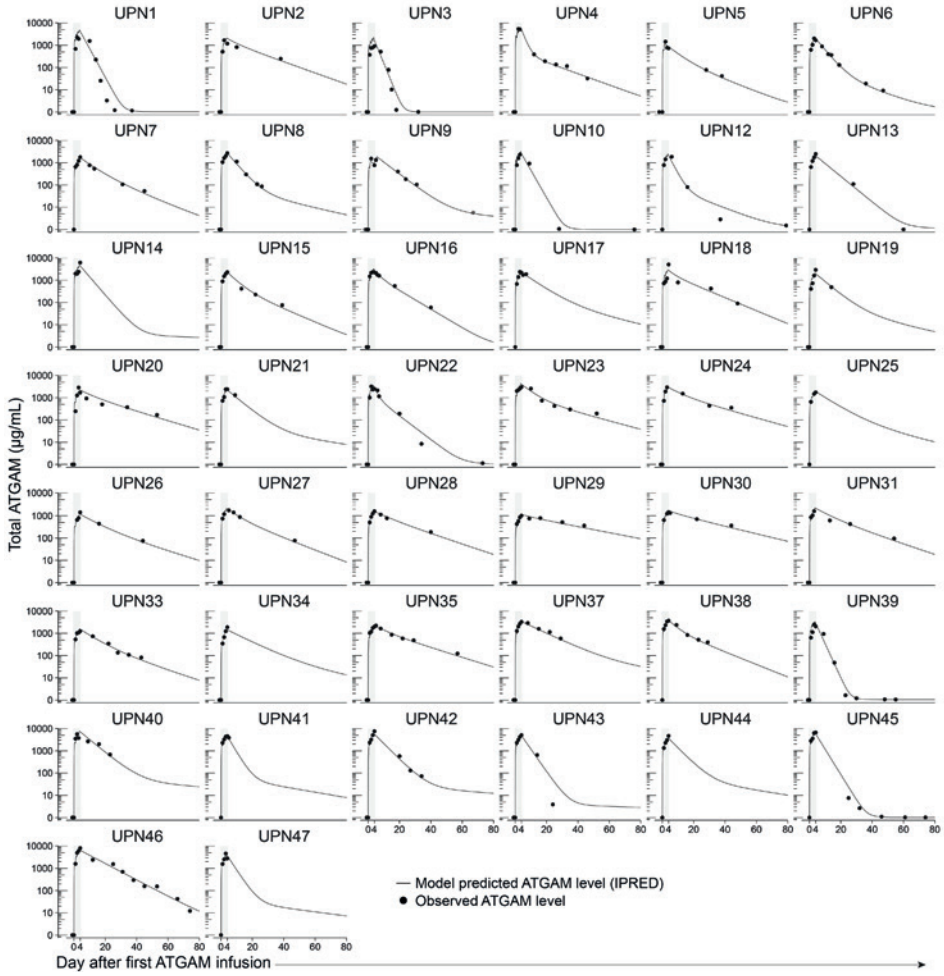


Figure S11. Observed versus model-predicted total ATGAM concentrations per patient. Observed total ATGAM concentrations are shown by black dots, while modelled total ATGAM concentrations in time are shown using black lines. Concentrations are presented on a logarithmic axis.

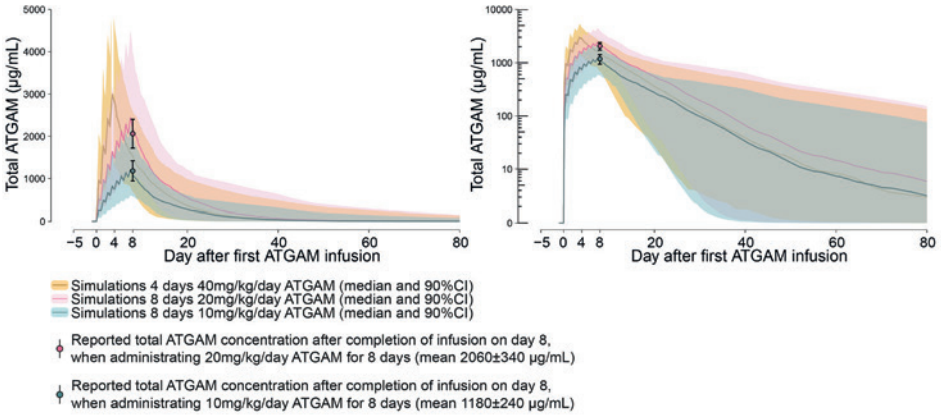


Figure S12. Model simulations for alternative ATGAM dosing schemes. The final pharmacokinetic model for total ATGAM was used to simulate the concentration-time profile of total ATGAM in time after the administration of 8 consecutive days 10mg/kg/day ATGAM, 8 consecutive days 20mg/kg/day ATGAM or 4 consecutive days 40mg/kg/day ATGAM. Lines and shaded areas represent the median and 90% confidence interval obtained from 100 simulations. Dots and error bars represent the mean and range of reported ATGAM peak concentrations following the completion of infusion on day 8 when ATGAM was administered at 10mg/kg/day ATGAM or 20mg/kg/day ATGAM for 8 consecutive days (reported concentrations are described in the manufacturer's brochure by Pfizer).

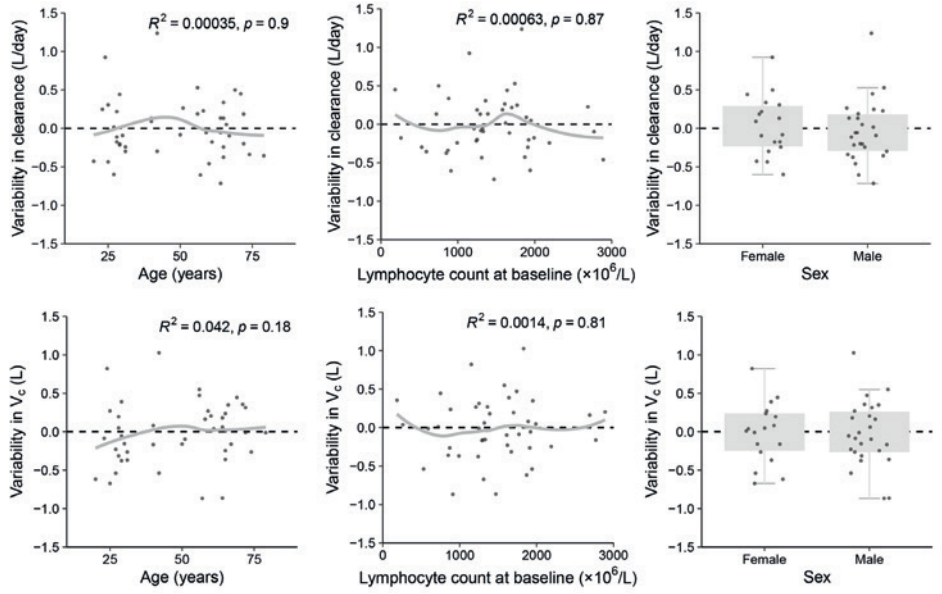


Figure S13. Impact of demographical and clinical covariates on inter-individual variability in pharmacokinetic parameters. Impact of age, lymphocytes pre-ATGAM and sex on inter-individual variability in clearance (row 1) and volume of distribution of the central compartment (row 2) of active ATGAM. Each dot represents a patient.

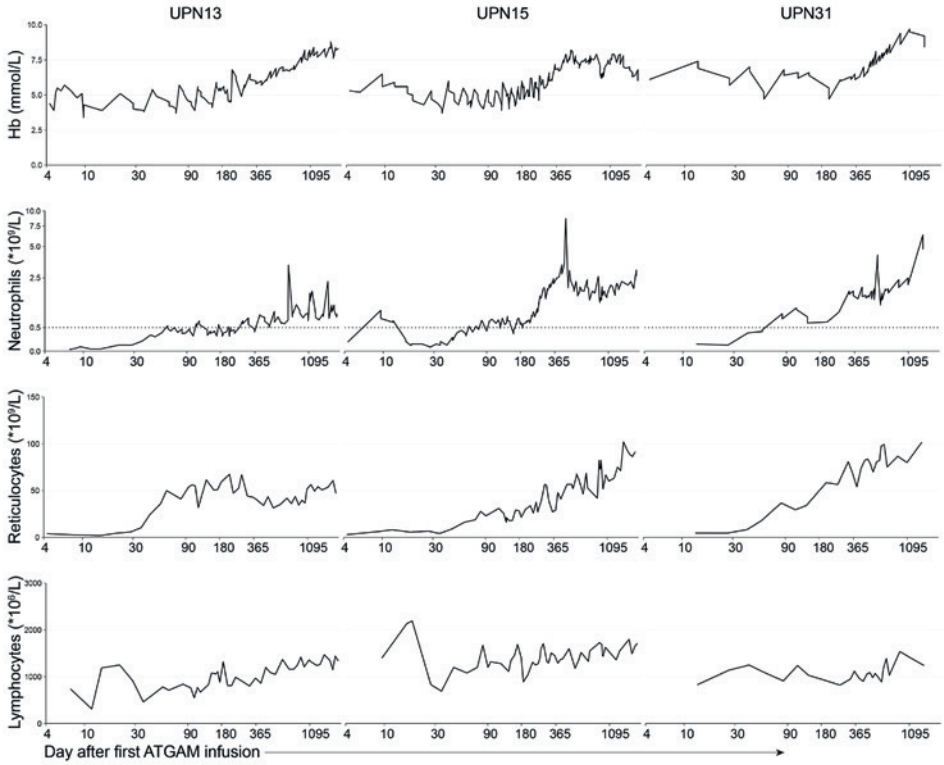


Figure S14. Peripheral blood counts in time after start of ATGAM-based IST. Hemoglobin (Hb), neutrophil, reticulocyte and total lymphocyte counts in patients UPN13, UPN15 and UPN31 over time, up to 3.5 years after start of ATGAM-based IST.

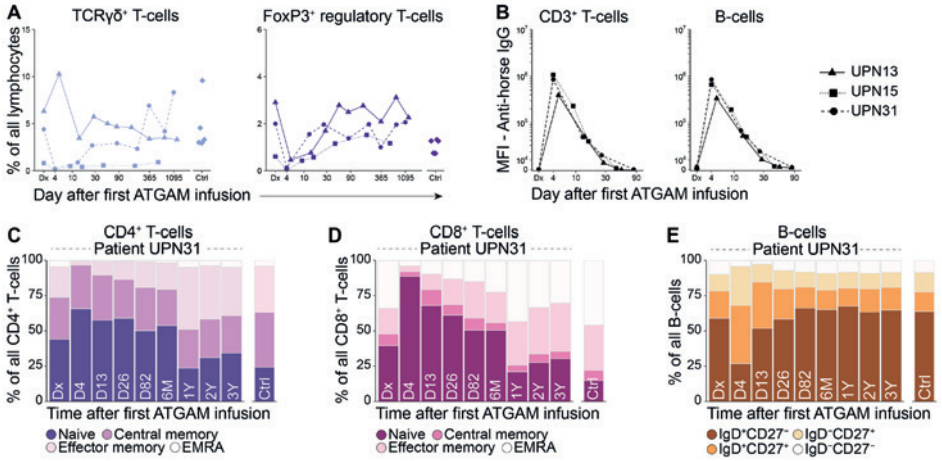


Figure S15. Lymphocyte compartment pre- and over time post-ATGAM. [A] Frequencies of major lymphoid lineages, shown as a percentage of all single, live lymphocytes per time point. Each line represents an individual patient. [B] Presence of ATGAM on the cell surface of T-cells (right) and B-cells (left), quantified over time using the mean fluorescence intensity of the Alexa Fluor 488-conjugated anti-horse IgG antibody. Each line represents an individual patient. [C-E] Bar plots quantifying the frequencies of subpopulations identified within the CD4⁺ T-cell, CD8⁺ T-cell and B-cell compartments from the representative patient UPN31. Flow cytometry plots are shown in Figure 4.

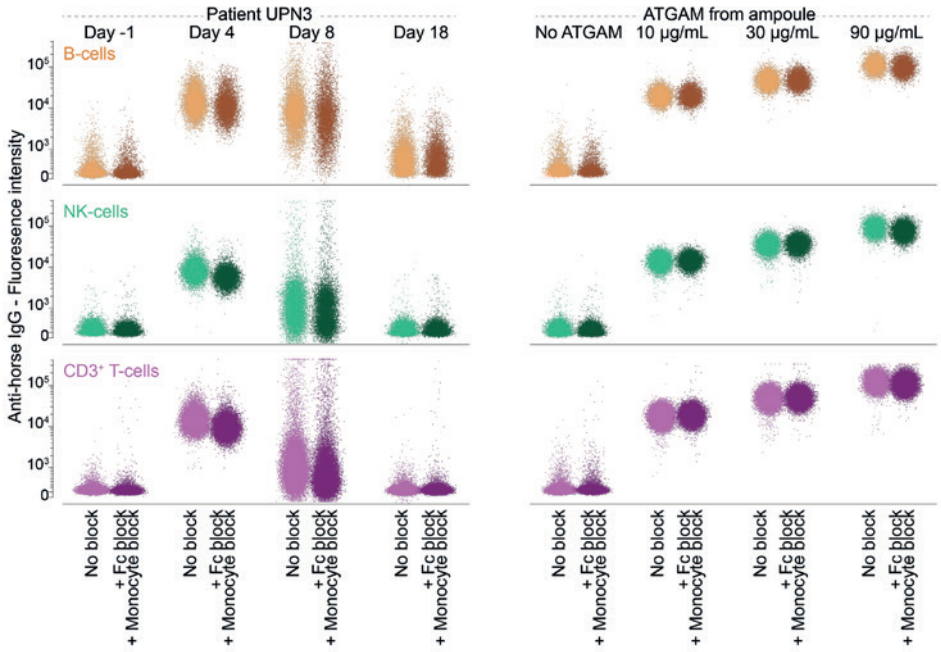


Figure S16. Impact of Fc-receptor blockade on ATGAM binding to lymphoid lineages. PBMCs from a healthy donor were pre-incubated without or with Fc-receptor block (Invitrogen, cat 14-9161-73) and monocyte block (Biolegend, cat 426103) for 30 minutes. Subsequently, cells were washed, co-incubated with undiluted plasma samples collected pre- and post-ATGAM infusion from patient UPN3 (right), or known ATGAM concentrations (right), and stained as described in the methods section (see 'Quantification of active ATGAM concentrations').

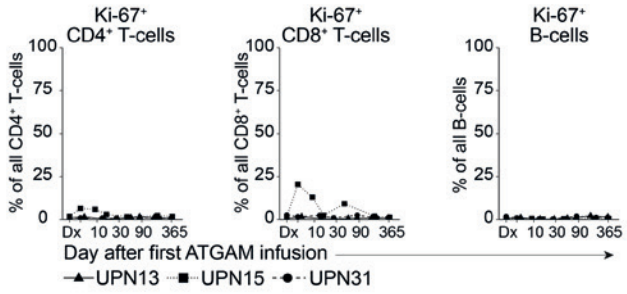


Figure S17. Proliferating CD4⁺ T-cells, CD8⁺ T-cells and B-cells after start of ATGAM-based IST. Ki-67⁺ cells were gated within the CD4⁺ T-cell, CD8⁺ T-cell and B-cell compartments. Data are shown for patients UPN13, UPN15 and UPN31.

References

1. Young NS. Aplastic Anemia. *N Engl J Med*. 2018;379(17):1643-1656.
2. Kulasekararaj A, Cavenagh J, Dokal I, et al. Guidelines for the diagnosis and management of adult aplastic anaemia: A British Society for Haematology Guideline. *Br J Haematol*. 2024;204(3):784-804.
3. Halkes CJ, Veelken H, Falkenburg JH. Horse versus rabbit antithymocyte globulin in aplastic anemia. *N Engl J Med*. 2011;365(19):1842-1843; author reply 1843-1844.
4. Scheinberg P, Nunez O, Weinstein B, et al. Horse versus rabbit antithymocyte globulin in acquired aplastic anemia. *N Engl J Med*. 2011;365(5):430-438.
5. Peffault de Latour R, Kulasekararaj A, Iacobelli S, et al. Eltrombopag Added to Immunosuppression in Severe Aplastic Anemia. *N Engl J Med*. 2022;386(1):11-23.
6. Genestier L, Fournel S, Flacher M, Assossou O, Revillard JP, Bonnefoy-Berard N. Induction of Fas (Apo-1, CD95)-mediated apoptosis of activated lymphocytes by polyclonal antithymocyte globulins. *Blood*. 1998;91(7):2360-2368.
7. Mohty M. Mechanisms of action of antithymocyte globulin: T-cell depletion and beyond. *Leukemia*. 2007;21(7):1387-1394.
8. Elliott JF, Lin Y, Mizel SB, Bleackley RC, Harnish DG, Paetkau V. Induction of interleukin 2 messenger RNA inhibited by cyclosporin A. *Science*. 1984;226(4681):1439-1441.
9. Heidt S, Roelen DL, Eijsink C, et al. Calcineurin inhibitors affect B cell antibody responses indirectly by interfering with T cell help. *Clin Exp Immunol*. 2010;159(2):199-207.
10. Popow I, Leitner J, Grabmeier-Pfistershammer K, et al. A comprehensive and quantitative analysis of the major specificities in rabbit antithymocyte globulin preparations. *Am J Transplant*. 2013;13(12):3103-3113.
11. Bourdage JS, Hamlin DM. Comparative polyclonal antithymocyte globulin and antilymphocyte/antilymphoblast globulin anti-CD antigen analysis by flow cytometry. *Transplantation*. 1995;59(8):1194-1200.
12. Raefsky EL, Gascon P, Gratwohl A, Speck B, Young NS. Biological and immunological characterization of ATG and ALG. *Blood*. 1986;68(3):712-719.
13. Feng X, Scheinberg P, Biancotto A, et al. In vivo effects of horse and rabbit antithymocyte globulin in patients with severe aplastic anemia. *Haematologica*. 2014;99(9):1433-1440.
14. Pool ES, Kooy-Winkelaar Y, van Unen V, et al. Mass cytometric analysis unveils a disease-specific immune cell network in the bone marrow in acquired aplastic anemia. *Front Immunol*. 2023;14:1274116.
15. Pool ES, Luk SJ, Ijsselsteijn ME, et al. Imaging mass cytometry reveals the order of events in the pathogenesis of immune-mediated aplastic anemia. *Blood*. 2025;146(8):951-963.
16. Tjon JM-L, Hussen-Dassen LGMv, Nur E, et al. Dutch guidelines for diagnostics and treatment of acquired aplastic anemia in adults. *Nederlands Tijdschrift voor Hematologie*. 2024.
17. Rebello P, Hale G. Pharmacokinetics of CAMPATH-1H: assay development and validation. *J Immunol Methods*. 2002;260(1-2):285-302.
18. Van Gassen S, Callebaut B, Van Helden MJ, et al. FlowSOM: Using self-organizing maps for visualization and interpretation of cytometry data. *Cytometry A*. 2015;87(7):636-645.
19. Comets E, Lavenu A, Lavielle M. Parameter Estimation in Nonlinear Mixed Effect Models Using saemix, an R Implementation of the SAEM Algorithm. *Journal of Statistical Software*. 2017;80(3):1-41.
20. Pfizer. ATGAM (anti-thymocyte globulin (equine) sterile solution) Perscribing Information. New York, USA: Pfizer; 2026.

21. Scott A, Morris K, Butler J, Mills AK, Kennedy GA. Treatment of aplastic anaemia with lower-dose anti-thymocyte globulin produces similar response rates and survival as per standard dose anti-thymocyte globulin schedules. *Intern Med J*. 2016;46(10):1198-1203.

22. Young N, Griffith P, Brittain E, et al. A multicenter trial of antithymocyte globulin in aplastic anemia and related diseases. *Blood*. 1988;72(6):1861-1869.

23. Admiraal R, van Kesteren C, Jol-van der Zijde CM, et al. Population pharmacokinetic modeling of Thymoglobulin((R)) in children receiving allogeneic-hematopoietic cell transplantation: towards improved survival through individualized dosing. *Clin Pharmacokinet*. 2015;54(4):435-446.

24. Oostenbrink LVE, Von Asmuth EGJ, Jol-van der Zijde CM, et al. Anti-T-lymphocyte globulin exposure is associated with acute graft-versus-host disease and relapse in pediatric acute lymphoblastic leukemia patients undergoing hematopoietic stem cell transplantation: a multinational prospective study. *Haematologica*. 2024;109(9):2854-2863.

25. Walter J, Rolles B, Schumacher Y, et al. Analysis of the Impact of Body Mass Index (BMI) on the Durability of Response in Patients with Aplastic Anemia Treated with Weight-Adjusted Horse Anti-Thymocyte Globulin (hATG). *Blood*. 2023;142.

26. Scheinberg P, Wu CO, Nunez O, Young NS. Predicting response to immunosuppressive therapy and survival in severe aplastic anaemia. *Br J Haematol*. 2009;144(2):206-216.

27. Yoshizato T, Dumitriu B, Hosokawa K, et al. Somatic Mutations and Clonal Hematopoiesis in Aplastic Anemia. *N Engl J Med*. 2015;373(1):35-47.

28. Narita A, Muramatsu H, Sekiya Y, et al. Paroxysmal nocturnal hemoglobinuria and telomere length predicts response to immunosuppressive therapy in pediatric aplastic anemia. *Haematologica*. 2015;100(12):1546-1552.

29. Zhao X, Zhang L, Jing L, et al. The role of paroxysmal nocturnal hemoglobinuria clones in response to immunosuppressive therapy of patients with severe aplastic anemia. *Ann Hematol*. 2015;94(7):1105-1110.

30. Sugimori C, Chuhjo T, Feng X, et al. Minor population of CD55-CD59- blood cells predicts response to immunosuppressive therapy and prognosis in patients with aplastic anemia. *Blood*. 2006;107(4):1308-1314.

31. Zaimoku Y, Patel BA, Kajigaya S, et al. Deficit of circulating CD19(+) CD24(hi) CD38(hi) regulatory B cells in severe aplastic anaemia. *Br J Haematol*. 2020;190(4):610-617.

32. Kordasti S, Costantini B, Seidl T, et al. Deep phenotyping of Tregs identifies an immune signature for idiopathic aplastic anemia and predicts response to treatment. *Blood*. 2016;128(9):1193-1205.

33. Huang AT, Mold NG, Zhang SF. Antithymocyte globulin stimulates human hematopoietic progenitor cells. *Proc Natl* Acad *Sci U S A*. 1987;84(16):5942-5946.

34. Nimer SD, Golde DW, Kwan K, Lee K, Clark S, Champlin R. In vitro production of granulocyte-macrophage colony-stimulating factor in aplastic anemia: possible mechanisms of action of antithymocyte globulin. *Blood*. 1991;78(1):163-168.

35. Lundgren S, Huuhtanen J, Keranen M, et al. Single-cell analysis of aplastic anemia reveals a convergence of NK and NK-like CD8(+) T cells with a disease-associated TCR signature. *Sci Transl Med*. 2025;17(787):eadl6758.

36. Wu Z, Gao S, Feng X, et al. Human autoimmunity at single cell resolution in aplastic anemia before and after effective immunotherapy. *Nat Commun*. 2025;16(1):5048.

37. Wu Z, Young NS. Single-cell genomics in acquired bone marrow failure syndromes. *Blood*. 2023;142(14):1193-1207.

38. de Latour RP, Visconte V, Takaku T, et al. Th17 immune responses contribute to the pathophysiology of aplastic anemia. *Blood*. 2010;116(20):4175-4184.

39. Kordasti S, Marsh J, Al-Khan S, et al. Functional characterization of CD4+ T cells in aplastic anemia. *Blood*. 2012;119(9):2033-2043.

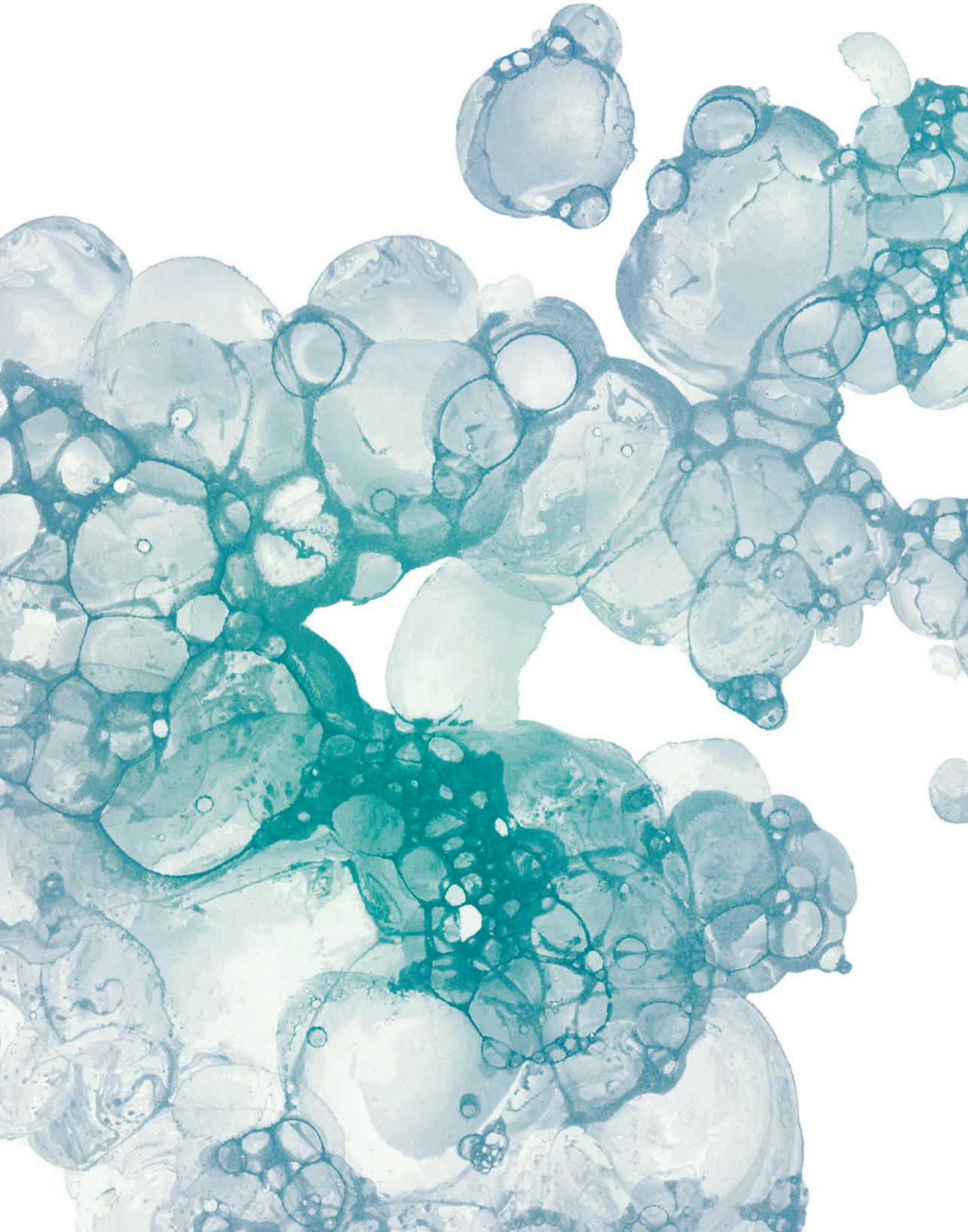
40. Jenkins MK, Schwartz RH, Pardoll DM. Effects of cyclosporine A on T cell development and clonal deletion. *Science*. 1988;241(4873):1655-1658.

41. Havenith SH, Remmerswaal EB, Bemelman FJ, et al. Rapid T cell repopulation after rabbit anti-thymocyte globulin (rATG) treatment is driven mainly by cytomegalovirus. *Clin Exp Immunol*. 2012;169(3):292-301.

42. Regan JF, Lyonnais C, Campbell K, Smith LV, Buelow R, Group USTM-CS. Total and active thymoglobulin levels: effects of dose and sensitization on serum concentrations. *Transpl Immunol*. 2001;9(1):29-36.

43. Jol-van der Zijde CM, Bredius RG, Jansen-Hoogendijk AM, et al. IgG antibodies to ATG early after pediatric hematopoietic SCT increase the risk of acute GVHD. *Bone Marrow Transplant*. 2012;47(3):360-368.

44. Bergstrand M, Hooker AC, Wallin JE, Karlsson MO. Prediction-corrected visual predictive checks for diagnosing nonlinear mixed-effects models. *AAPS J*. 2011;13(2):143-151.



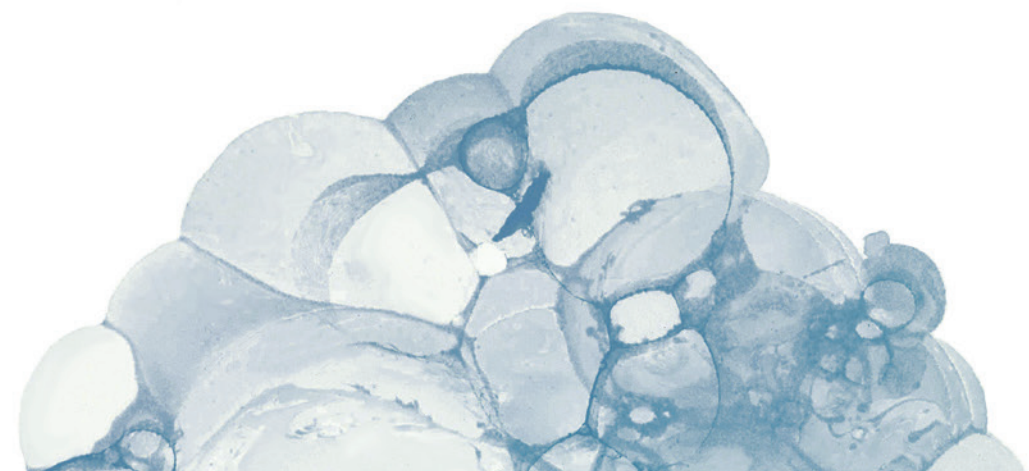
5

Longitudinal spatial mapping of the bone marrow in an aplastic anemia patient progressing to acute myeloid leukemia

Emma S. Pool[1], Georgia Koutsoumpli[1], M. Willy Honders[1], Bert A. van der Reijden[2], Mirjam H.M. Heemskerk[1], Marieke Griffioen[1] and Jennifer M-L. Tjon[1]

[1] Department of Hematology, Leiden University Medical Center, Leiden, The Netherlands
[2] Department of Laboratory Medicine, Laboratory of Hematology, Radboud University Medical Center, Nijmegen The Netherlands

Manuscript in preparation



To the editor,

Immune-mediated aplastic anemia (AA) is a bone marrow failure syndrome caused by an autoimmune response targeting the hematopoietic stem and progenitor cells in the bone marrow[1,2]. This results in bone marrow hypocellularity and severe peripheral cytopenias. Approximately 70% of AA patients show hematologic recovery within six months after start of immunosuppressive therapy (IST), with horse-derived anti-thymocyte globulin (hATG) plus long-term ciclosporin[3]. However, in 10-15% of patients responsive to IST, the development of secondary clonal disorders including acute myeloid leukemia (AML) remains a concerning long-term complication with poor prognosis[4,5]. Reported risk factors for clonal evolution to AML include age, shortened telomere lengths, and loss of HLA class I risk alleles[4,6]. Furthermore, a role for somatic mutations in genes including *ASXL1*, *DNMT3A*, *RUNX1,* and genes encoding splicing factors has been implicated[4,6-8]. However, predicting clonal evolution to AML remains challenging, and the precise mechanisms by which malignant clones emerge, as well as the microenvironmental changes in the bone marrow, have not been defined. Therefore, clonal evolution to AML is typically only detected at a later stage, after clinical symptoms have developed.

In this study, we performed a multi-modal analysis on a unique series of bone marrow samples from a patient with AA-to-AML progression to investigate clonal evolution to AML at the site of its emergence. It concerns a 64-year-old male without additional underlying disease, who was diagnosed with severe AA and progressed to secondary AML 29 months after the start of first-line IST. Diagnosis of AA followed standard Dutch guidelines[9], and was based on bone marrow hypocellularity and pancytopenia, without dysplasia (peripheral blood counts in Table 1). IST consisted of four days 40 mg/kg/day hATG (ATGAM®) and ciclosporin for 14 months. Seven months post-hATG, eltrombopag (Revolade®) was added because of insufficient hematologic response with continuing transfusion dependency. After reaching a partial response nine months post-hATG, eltrombopag and ciclosporin were stopped at 11 and 14 months post-hATG, respectively. The patient had normal peripheral blood counts 24 months post-hATG. However, 29 months post-hATG peripheral blood counts declined (Table 1). Bone marrow analysis showed the presence of 10% $CD45^{dim}$ blasts, and the patient was diagnosed with secondary myelodysplasia-related AML containing *RUNX1* and *IDH1* mutations with variant allele frequencies (VAFs) of 4% and 3%, respectively, according to current WHO/ICC classification[10,11].

Table 1. Peripheral blood counts

Timepoint	Hb (mmol/L)	Reticulocytes (x10^9/L)	Thrombocytes (x10^9/L)	Neutrophils (x10^9/L)
Diagnosis	6.4	20.7	22.0	0.8
6M post-hATG	6.4	58.9	29.5	1.0
24M post-hATG	8.2	64.7	215.0	1.4
29M post-hATG (AML)	7.7	43.9	86.0	0.6
32M post-hATG (AML)	6.2	NA	20.0	0.3

AA: aplastic anemia; AML: acute myeloid leukemia; hATG: anti-thymocyte globulin; Hb: hemoglobin

To map the cellular landscape of the bone marrow during clonal evolution to AML, formalin-fixed paraffin-embedded bone marrow biopsies were analyzed using imaging mass cytometry (IMC). We recently demonstrated that IMC, with a 37-marker antibody panel, provides a detailed visualization of the cellular interactions within the spatial bone marrow architecture in a cohort of AA patients[1]. Here, we applied IMC to characterize the complete series of bone marrow biopsies collected from our patient with AA-to-AML progression at AA diagnosis, and 6, 24, 29 (AML diagnosis) and 32 months post-hATG. Six and 24 month post-hATG biopsies were collected during routine clinical assessment for AA, and both AML biopsies were taken before start of chemotherapy. As a reference, bone marrow biopsies from three age-matched diffuse large B-cell lymphoma patients without bone marrow localization were included.

Sixteen regions of interest (ROIs) with a median surface area of 2.1 mm^2 were imaged. Our patient presented with a characteristically hypocellular bone marrow at AA diagnosis, that still contained sites of active hematopoiesis, as indicated by the presence of CD71$^+$ erythroid precursors (Figure 1A; all ROIs in Figure S1). Between 6 and 24 months post-hATG, bone marrow recovery was accompanied by an increase of precursor cells diffusely distributed throughout the tissue, similar to that seen in controls. The diagnosis of AML 29 months post-hATG was characterized by spatial reorganization of the bone marrow tissue, marked by the formation of concentrated islands of precursor cells (Figure 1A). This was not accompanied by any considerable changes in tissue cellularity, which, together with the low VAFs of the *RUNX1* and *IDH1* mutations, suggested that AML was diagnosed at an early stage in our monitored patient.

To fully capture the microenvironmental changes occurring during clonal evolution from AA to AML, cell segmentation was applied to extract single-cell information from the acquired images as previously described[1]. Visualization of all 0.2·10^6 segmented cells using a tSNE analysis identified five major annotated hematopoietic and stromal cell clusters. In addition, three remaining clusters of Ki-67$^-$ cells were identified (Figure 1B). These Ki-67$^-$ clusters were classified as 1) Ki-67$^-$CD45$^+$CD38$^{+/-}$ cells clustering with mature B-cells that lack all

markers, likely representing a group of early B-cells; 2) Ki-67^{-}CD45^{dim}CD38^{+} cells resembling immature myeloid cells; and 3) an unclassifiable population that expressed vimentin while lacking all other IMC markers (all markers in Figure S2). Visualization of all samples in the tSNE analysis revealed a shift in the cellular composition of the bone marrow over time, with clear differences compared to the controls (Figure 1C). At AA diagnosis, the bone marrow contained lymphoid, stromal and progenitor cells, but reduced numbers of mature myeloid cells, consistent with disease characteristics[1]. Notably, the progression to AML 29 months post-hATG co-occurred with the expansion of Ki-67^{-}CD45^{dim}CD38^{+} cluster 2 cells (yellow circle in Figure 1C). To study the dynamics of this population, we quantified the absolute cell counts of all identified cell clusters over time, corrected for bone marrow cellularity as previously described[1] (Figure 1D). This confirmed that the Ki-67^{-}CD45^{dim}CD38^{+} cells progressively expanded and replaced normal hematopoiesis from the time of AML diagnosis onwards.

To confirm the Ki-67^{-}CD45^{dim}CD38^{+} cells as malignant blasts, we compared their marker expression profile to the phenotype of the leukemic blasts analyzed by 28-marker flow cytometry 29 months post-hATG. In the IMC data, the cells highly expressed CD38, dimly expressed CD45, partially expressed CD15 and HLA-DR, and did not express CD7, CD11b, CD14, CD34, CD56 and CD71 (Figure 1B). This was highly similar to the leukemic blast phenotype observed by flow cytometry, with minor differences attributable to variation in detection sensitivities between the two techniques (Figure 1E, all markers in Figure S3). Flow cytometry further revealed that the blasts lacked a distinctive leukemia-associated phenotype, consistent with the fact that Ki-67^{-}CD45^{dim}CD38^{+} cells were also observable in controls, but in smaller numbers (Figure 1C-D). Importantly, in the AA-to-AML patient, the Ki-67^{-}CD45^{dim}CD38^{+} cells were already detectable at AA diagnosis, and persisted following IST while maintaining a similar phenotype, suggesting that preleukemic clones had been present before the onset of AML (Figure 1C-D).

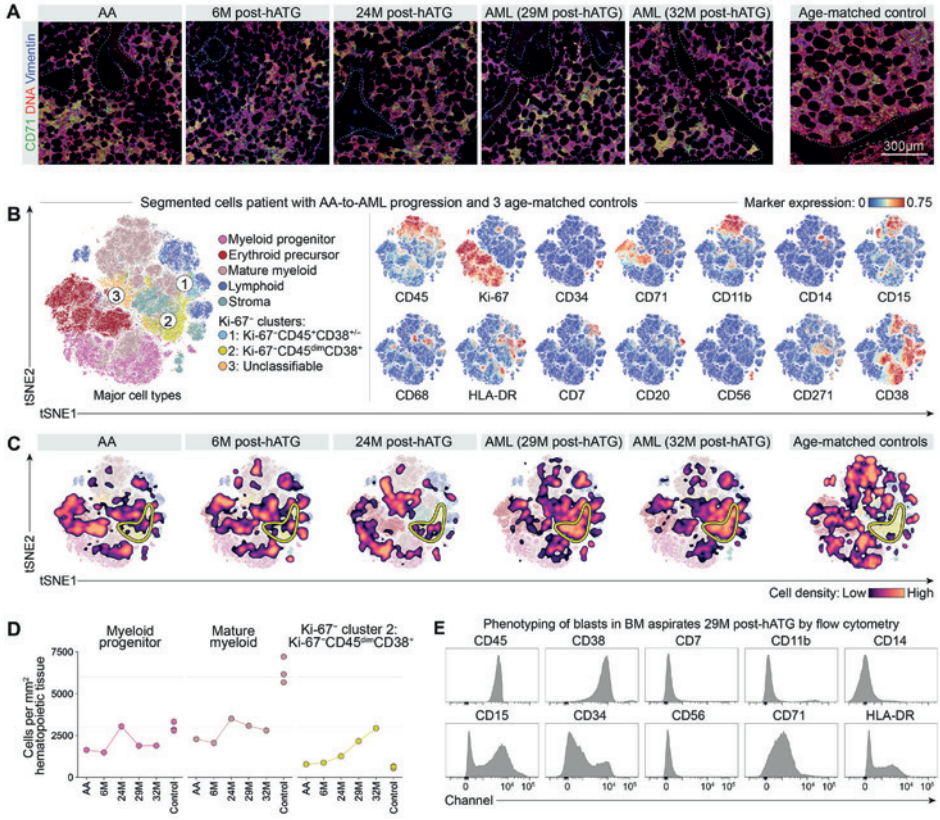


Figure 1. Longitudinal profiling of bone marrow samples from the AA-to-AML patient. A) Global histology of the bone marrow from the AA-to-AML patient across all studied time points, and a representative age-matched control. DNA (red) stains all cellular nuclei, Vimentin (blue) stains all hematopoietic cells and their microenvironment, and CD71 (green) stains erythroid precursors. B) $0.2{\cdot}10^6$ cells segmented from 16 ROIs visualized using a tSNE analysis. C) Contour plots showing the cellular composition of the bone marrow at each time point in the AA-to-AML patient, and three controls. D) Abundance of myeloid progenitors, mature myeloid cells, and Ki-67$^-$CD45^{dim}CD38$^+$ cells across all time points. To correct for differences in bone marrow cellularity, abundances are shown as an absolute cell count per mm^2 of hematopoietic compartment as previously described1. E) Marker expression profile of leukemic blasts in fresh bone marrow aspirates collected 29 months post-hATG, analyzed by flow cytometry.

To understand how the Ki-67$^-$CD45^{dim}CD38$^+$ cells identified as immature blasts expanded within the bone marrow, we mapped spatial 'clusters' of at least five Ki-67$^-$CD45^{dim}CD38$^+$ cells and their immediate microenvironment across all time points with previously described methods[12,13] (Figure 2A). As a reference, we analyzed bone marrow biopsies from the 12 other AA patients from our previous IMC analysis[1] who responded to IST and did not progress to a secondary hematological malignancy. Similar to the AA-to-AML patient, six of these 12 patients had a hypocellular bone marrow that still contained pockets of active hematopoiesis. At AA diagnosis, we observed spatial clusters of Ki-67$^-$CD45^{dim}CD38$^+$ cells in the AA-to-AML patient, which were found in similar numbers in controls, but not in other AA patients (Figure

2A-B). Six months post-hATG, these spatial clusters were detected in all AA patients with the most pronounced bone marrow recovery, but only in the AA-to-AML patient their abundance further increased 24 months post-hATG, and continued to expand after the diagnosis of AML at 29 months post-hATG. This suggested that while the formation of spatial clusters of Ki-67^{-} CD45^{dim}CD38^{+} cells is a normal feature of bone marrow recovery, their continued expansion over time may indicate clonal evolution to AML.

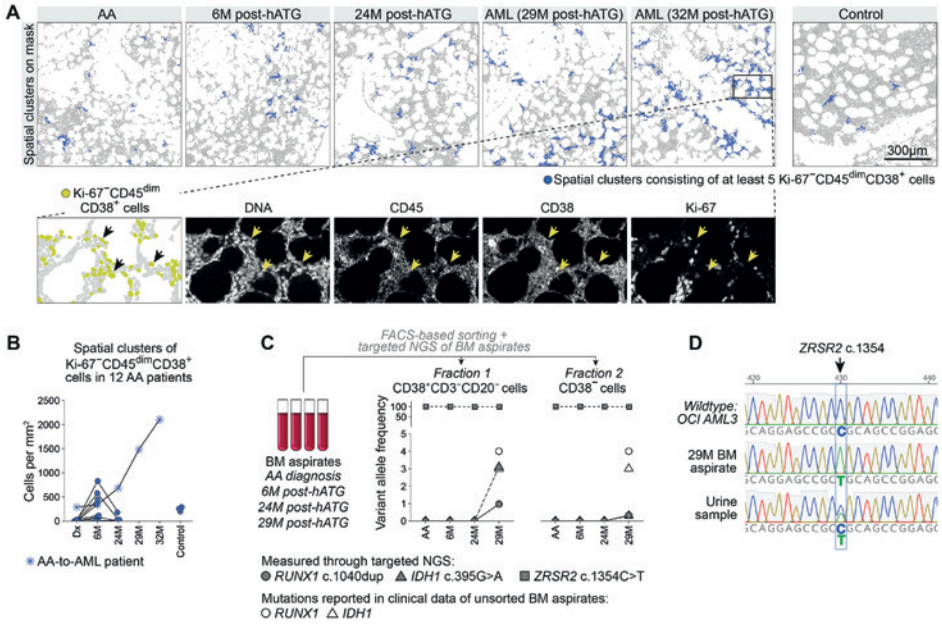


Figure 2. Spatial and genetic analysis of Ki-67^{-}CD45^{dim}CD38^{+} cells from the AA-to-AML patient. A) Top row: Identified spatial clusters of Ki-67^{-}CD45^{dim}CD38^{+} cells (blue) projected on the cell segmentation mask, with all remaining segmented cells shown in gray. Spatial clusters were identified by constructing a spatial interaction graph, where each segmented cell was connected to its neighboring cells within a 25-pixel (µm) distance. Subsequently, connected sets of at least five Ki-67^{-}CD45^{dim}CD38^{+} cells were detected and clusters were expanded by 1 pixel to include their direct microenvironment. Bottom row: Visualization of Ki-67^{-}CD45^{dim}CD38^{+} cells (green) on the cell segmentation mask, with raw IMC images confirming their marker expression profile as CD45^{dim}, CD38^{+} and Ki-67^{-}. B) Total number of the identified spatial clusters of Ki-67^{-}CD45^{dim}CD38^{+} cells across all time points, shown as an absolute cell count per mm^{2} of hematopoietic compartment. C) Variant allele frequencies of RUNX1, IDH1 and ZRSR2 mutations, determined by targeted sequencing on sorted CD38^{+}CD3^{-}CD20^{-} or CD38^{-} cell fractions from bone marrow aspirates. D) Analysis of a 1) wildtype OCI AML3 sample, 2) bone marrow aspirate sample taken from the AA-to-AML patient 29 months post-hATG and 3) a urine sample collected from the AA-to-AML patient to study the presence of the ZRSR2 mutation.

Since these findings indicate a shift in the bone marrow architecture prior to the clinical diagnosis of AML, we questioned how this shift correlated to the underlying genetic changes driving progression to AML. For this purpose, targeted next generation sequencing (NGS) was performed on cryopreserved bone marrow aspirates collected from our patient at AA

diagnosis, and 6, 24, and 29 months post-hATG using a panel of genes recurrently mutated in AML. 32 months post-hATG samples were not available. Sorting enriched for $CD38^{+}CD3^{-}CD20^{-}$ cells, which included the identified $Ki\text{-}67^{-}CD45^{dim}CD38^{+}$ cells and other $CD38^{+}$ hematopoietic populations to meet sequencing requirements (Figure 2C; sorting strategy in Figure S4). Targeted sequencing confirmed the *RUNX1* frameshift (c.1040dup; p.Met347Ilefs*253) and *IDH1* hotspot (c.395G>A; p.R132H) mutations at AML diagnosis 29 months post-hATG, at low VAFs, consistent with the clinical data (Figure 2C). Importantly, higher VAFs of the *RUNX1* and *IDH1* mutations were observed in the $CD38^{+}CD3^{-}CD20^{-}$ fraction compared to the $CD38^{-}$ fraction. As the $CD38^{+}CD3^{-}CD20^{-}$ fraction included the $Ki\text{-}67^{-}CD45^{dim}CD38^{+}$ cells, this provided further support to their identity as leukemic blasts. At all earlier time points, the *RUNX1* and *IDH1* mutations could not be detected by targeted NGS, despite additional higher-sensitivity screening below the initially set threshold of 1%. Interestingly, we did observe a missense mutation in the X-linked splicing factor *ZRSR2* (c.1354C>T; p.R452C) already present at AA diagnosis. Remarkably, this mutation was detected at a VAF of 100%, and also predominated in the $CD38^{-}$ sorted fraction, which included lymphocytes with a lifespan of several years (Figure S4). Additional sequencing on a urine sample ruled out a possible germline mutation in *ZRSR2*: both wildtype (c.1354C) and mutant *ZRSR2* (c.1354T) were found, with the mutant likely derived from leukocytes present in the urine since *ZRSR2* heterozygosity was not possible in our male patient due to its location on the X-chromosome (Figure 2D). Together, these data suggested that the observed *ZRSR2* mutation reflected an early somatic event in a hematopoietic stem cell that had reshaped the entire hematopoietic compartment.

By identifying this somatic *ZRSR2* mutation in the bone marrow at AA diagnosis, our study expands the mutational landscapes reported in AA and provides further evidence that clonal evolution to AML can occur across patients with heterogeneous mutational profiles[8]. Spliceosome mutations, such as mutations in *ZRSR2*, can result in aberrant RNA splicing and are closely related to hematological malignancies, with *ZRSR2* mutations occurring particularly in males due to its X-linked position[14,15]. In AA, *ZRSR2* mutations have been detected at low VAFs in some cases[8], with only one study reporting a VAF of 100% in an AA patient with an extensive medical history[16]. Accordingly, our data on a previously healthy patient raise questions about both the significance of this mutation and how it could have reached such dominance. In this context, it is particularly interesting that the *ZRSR2* mutation also occurred in lymphocytes, which can persist for several years, suggesting that the mutation may have dominated long before the diagnosis of AA. While AA remains a diagnosis of exclusion and an initial myelodysplastic syndrome cannot fully be ruled out, the absence of dysplasia and the presence of the features of immune-mediated AA with T-cell involvement[1] support the diagnosis of immune-mediated AA accompanied by clonal hematopoiesis. We believe this clonal hematopoiesis may have contributed to, or resulted

from, primary bone marrow failure. Following the depletion of the immune response with IST, clonal hematopoiesis persisted, thereby increasing the risk of the development of AML[17].

Our study confirms the close link between clonal hematopoiesis and the development of late clonal disorders[17], and offers unique insight into the underlying processes. It has been postulated that clonal evolution to AML may be the result of environmental selection, where mutant clones are more resistant to the autoimmune attack in the bone marrow and therefore expand as dominant clones in size and time. Alternatively and additionally, stem cell clones may acquire somatic mutations that confer a proliferative advantage as compared to other remaining stem cell clones in the hypocellular bone marrow post-hATG[17]. This model is largely based on indirect evidence from next-generation sequencing on peripheral blood or bone marrow samples, which tracks changes in stem cell clone size over time[8]. Our case study confirms that clonal evolution to AML can occur through a dynamic, multistep process, and additionally provides the first visualization of the possible order of events within the bone marrow. In the described patient, the first detectable clonal event was the expansion of a *ZRSR2*-mutated stem cell clone occurring prior to the diagnosis of AA. This was followed by the expansion of the malignant blasts harboring the *RUNX1* and *IDH1* driver mutations, most likely within the Ki-67$^-$CD45^{dim}CD38$^+$ population. When these driver mutations were exactly acquired remains debatable since the applied targeted NGS has a detection limit of 1-2% VAF, which means that somatic mutations in small cell populations below 2-4% cannot be reliably detected. Resolving this question will require ultra-sensitive sequencing techniques or the development of mutation-specific antibodies for flow-cytometry based screening. Based on our data, two possible models can be proposed. First, the fact that Ki-67$^-$CD45^{dim}CD38$^+$ cells identified as leukemic blasts were detectable at AA diagnosis and expanded post-hATG, could indicate that mutant clones were present in the bone marrow prior to AML diagnosis but missed by targeted NGS. This would support the notion that AA and hematological malignancies lie along a closely related spectrum of diseases[2]. Alternatively, the *RUNX1* and *IDH1* driver mutations could have been acquired post-hATG, due to cellular stress caused by defective splicing through the *ZRSR2* mutation. This is corroborated by the low VAFs and blast percentages observed at AML diagnosis. In either scenario, uncontrolled expansion of the Ki-67$^-$CD45^{dim}CD38$^+$ cells within the bone marrow presents as a key driver of clonal evolution to AML. Although a similar increase in Ki-67$^-$CD45^{dim}CD38$^+$ cells was also initially observed in other AA patients post-hATG, their continued expansion was unique to our AA-to-AML patient. Overall, this illustrates that the initial bone marrow failure may create a microenvironment that both favors and triggers preleukemic clones that survive the autoimmune attack, but that an additional cell-intrinsic event may be required for their continued expansion. In our patient, we believe this could have been the somatic *ZRSR2* mutation, which may have provided such a growth advantage, and thereby promoted the progression to AML.

References

1. Pool ES, Luk SJ, ME IJ, et al. Imaging Mass Cytometry Reveals the Order of Events in the Pathogenesis of Immune-Mediated Aplastic Anemia. *Blood*. 2025.
2. Young NS. Aplastic Anemia. *N Engl J Med*. 2018;379(17):1643-1656.
3. Scheinberg P, Nunez O, Weinstein B, et al. Horse versus rabbit antithymocyte globulin in acquired aplastic anemia. *N Engl J Med*. 2011;365(5):430-438.
4. Babushok DV. A brief, but comprehensive, guide to clonal evolution in aplastic anemia. *Hematology Am Soc Hematol Educ Program*. 2018;2018(1):457-466.
5. Sun L, Babushok DV. Secondary myelodysplastic syndrome and leukemia in acquired aplastic anemia and paroxysmal nocturnal hemoglobinuria. *Blood*. 2020;136(1):36-49.
6. Kulasekararaj AG, Jiang J, Smith AE, et al. Somatic mutations identify a subgroup of aplastic anemia patients who progress to myelodysplastic syndrome. *Blood*. 2014;124(17):2698-2704.
7. Negoro E, Nagata Y, Clemente MJ, et al. Origins of myelodysplastic syndromes after aplastic anemia. *Blood*. 2017;130(17):1953-1957.
8. Yoshizato T, Dumitriu B, Hosokawa K, et al. Somatic Mutations and Clonal Hematopoiesis in Aplastic Anemia. *N Engl J Med*. 2015;373(1):35-47.
9. Tjon JM-L, Hussen-Dassen LGMv, Nur E, et al. Dutch guidelines for diagnostics and treatment of acquired aplastic anemia in adults. *Nederlands Tijdschrift voor Hematologie*. 2024.
10. Khoury JD, Solary E, Abla O, et al. The 5th edition of the World Health Organization Classification of Haematolymphoid Tumours: Myeloid and Histiocytic/Dendritic Neoplasms. *Leukemia*. 2022;36(7):1703-1719.
11. Arber DA, Orazi A, Hasserjian RP, et al. International Consensus Classification of Myeloid Neoplasms and Acute Leukemias: integrating morphologic, clinical, and genomic data. *Blood*. 2022;140(11):1200-1228.
12. Windhager J, Zanotelli VRT, Schulz D, et al. An end-to-end workflow for multiplexed image processing and analysis. *Nat Protoc*. 2023;18(11):3565-3613.
13. Hoch T, Schulz D, Eling N, Gomez JM, Levesque MP, Bodenmiller B. Multiplexed imaging mass cytometry of the chemokine milieus in melanoma characterizes features of the response to immunotherapy. *Sci Immunol*. 2022;7(70):eabk1692.
14. Gomez-Redondo I, Pericuesta E, Navarrete-Lopez P, et al. Zrsr2 and functional U12-dependent spliceosome are necessary for follicular development. *iScience*. 2022;25(2):103860.
15. Madan V, Kanojia D, Li J, et al. Aberrant splicing of U12-type introns is the hallmark of ZRSR2 mutant myelodysplastic syndrome. *Nat Commun*. 2015;6:6042.
16. Thurlapati A, Boudreaux K, Guntupalli S, Mansour RP, Bhayani S. A Case of Aplastic Anemia and Colon Cancer With Underlying Spliceosome Mutation: Is It an Incidental Finding or a Novel Association? *Cureus*. 2022;14(2):e22632.
17. Ogawa S. Clonal hematopoiesis in acquired aplastic anemia. *Blood*. 2016;128(3):337-347.

Supplemental figures

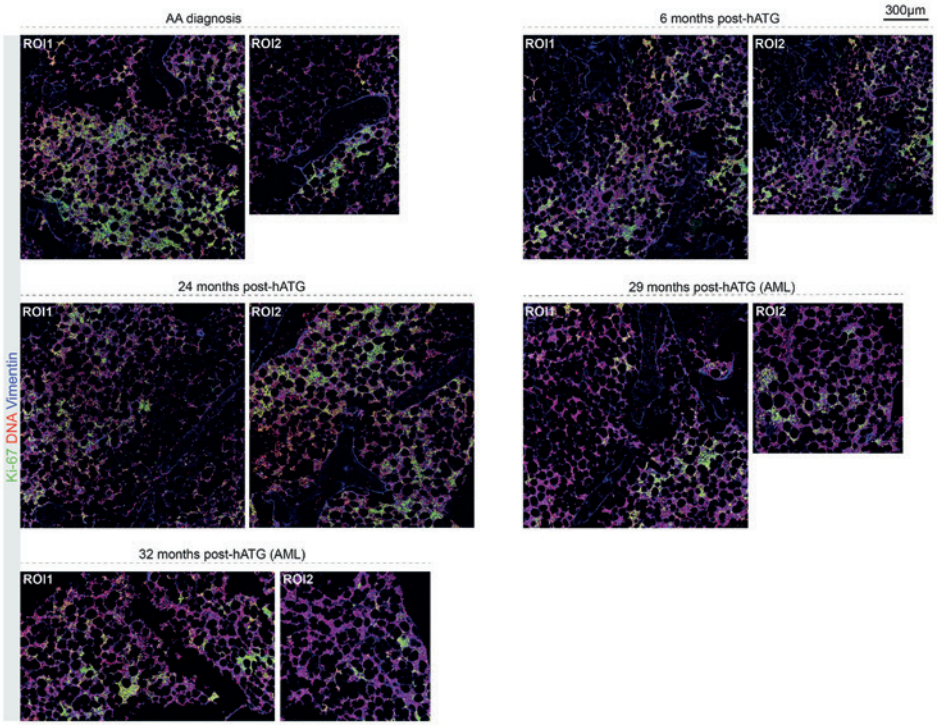


Figure S1. Bone marrow histology over time. DNA stains cellular nuclei; Vimentin stains hematopoietic cells and their microenvironment; Ki-67 stains proliferating cells.

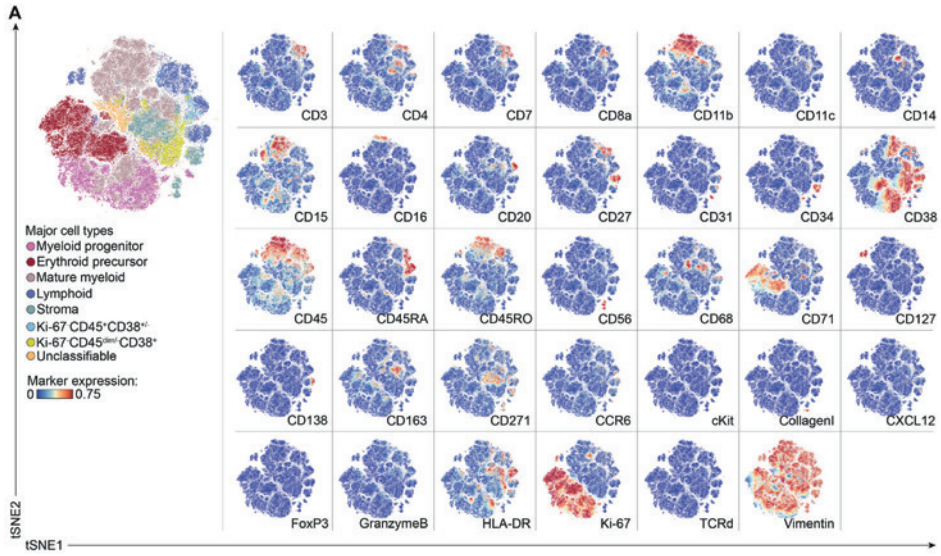


Figure S2. Marker expression profile of all segmented cells from the ROIs collected for the patient with AA-to-AML progression and all controls. A total of $0.2 \cdot 10^6$ cells segmented from 16 ROIs are visualized using a tSNE analysis. cKit (CD117) could only be detected on cells highly expressing cKit through IMC.

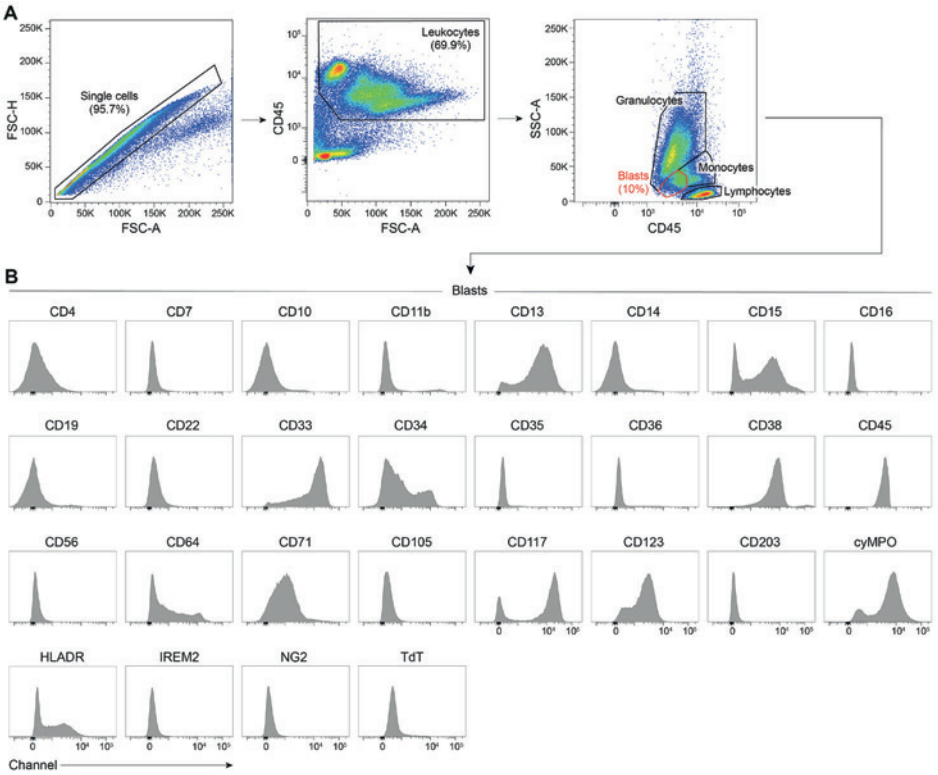


Figure S3. Phenotyping of leukemic blasts 29 months post-hATG by 28-marker flow cytometry. (A) After gating of single cells using the forward scatter (panel 1) and selection of $CD45^{+}$ leukocytes (panel 2), blasts were gated by excluding granulocytes, monocytes and lymphocytes using the side scatter and CD45. (B) Marker expression profile of the blasts, shown using histograms.

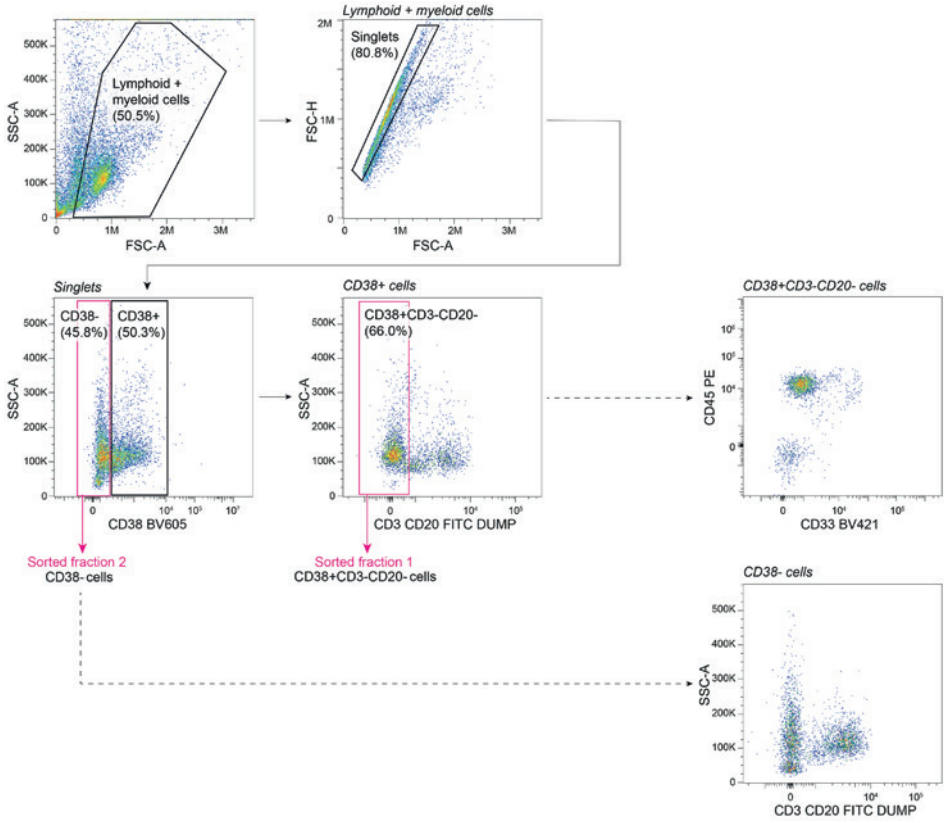
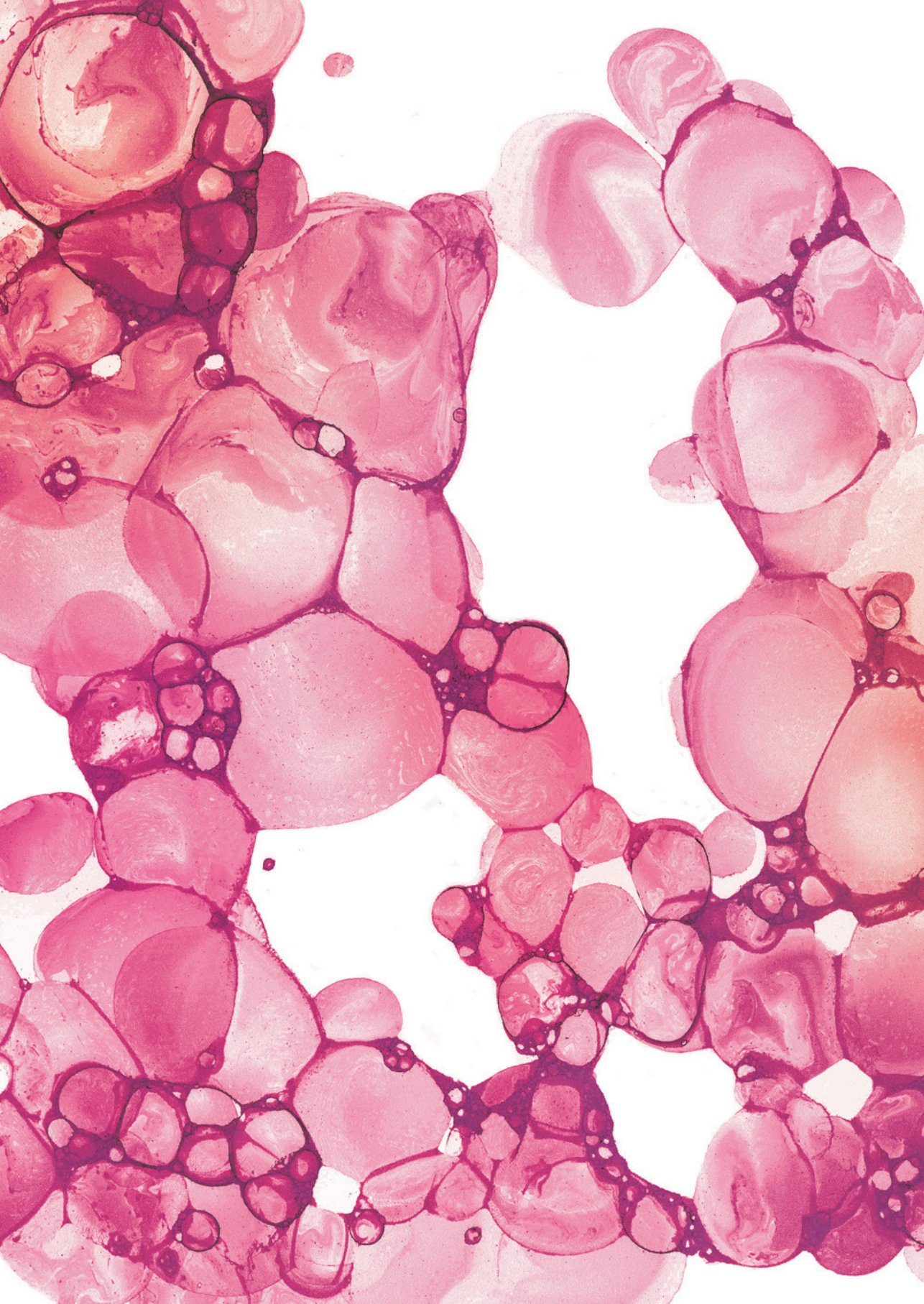
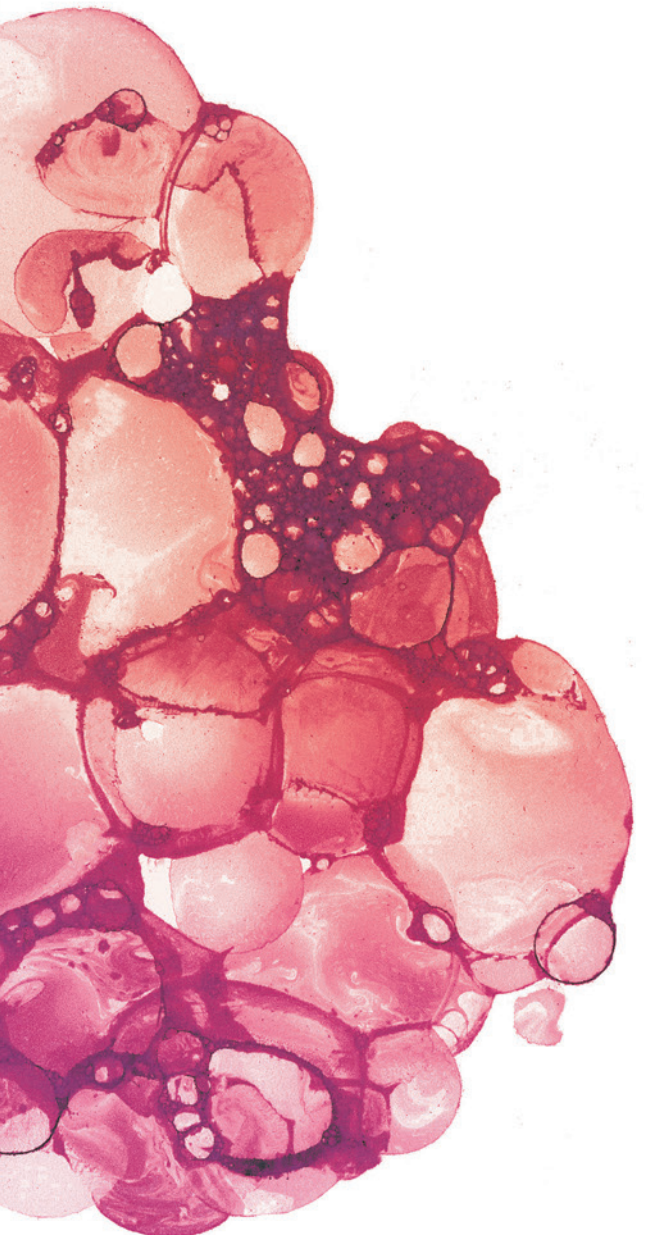


Figure S4. Gating strategy for sorting of bone marrow aspirates. Lymphoid and myeloid cells were gated using the forward and side scatters (panel 1), and single cells were selected using the forward scatters (panel 2). Subsequently, single lymphoid and myeloid cells were split based on the expression of CD38 to sort a $CD38^-$ cell fraction (fraction 2), and a $CD38^-$ cell fraction that further lacked expression of CD3 and CD20 (fraction 1) (panels 3-4). Additional phenotyping confirmed that the $CD38^+CD3^-CD20^-$ fraction expressed the hematopoietic cell marker CD45 and the myeloid cell marker CD33.



Summary and general discussion

6



Summary

Aplastic anemia (AA) is a rare bone marrow failure syndrome that is most often classified as 'idiopathic', despite a long history with the first case described in the late 19th century by Paul Ehrlich[1]. In the 1980s it was discovered that AA patients can respond to immunosuppressive therapy (IST)[2-4]. Therefore, AA is typically viewed as an immune-mediated disease, with T-cells playing a central role[5]. However, IST remains a suboptimal treatment since only 70% of patients respond to first-line IST with horse-derived anti-thymocyte globulin (hATG, ATGAM®) and long-term ciclosporin[6,7]. Therefore, there is a need for improved therapies that specifically target the pathogenic immune cell populations driving stem cell destruction in the bone marrow. However, a comprehensive understanding of the immune response in AA has been hampered by limitations in the number of cellular phenotypes that could be studied simultaneously. Furthermore, spatial analysis of the bone marrow microenvironment has not been possible due to technical limitations caused by tissue decalcification and the lack of spatially-resolved imaging platforms that can map the full complexity of its cellular communities. Therefore, the behavior of potentially pathogenic immune cells within the affected bone marrow has remained unclear.

In this thesis we provide the first atlas of the immune landscape in AA with the aim to unravel the immune response underlying the pathogenesis of AA. We profiled bone marrow and peripheral blood samples collected from AA patients using high-dimensional immunophenotyping techniques. This enabled detailed analyses of all major immune lineages at the immune subpopulation level. We identified potentially pathogenic immune cell subpopulations associated with chronic inflammation, and deciphered their spatial context within the affected bone marrow across different stages of bone marrow tissue destruction. To confirm their relevance, we elucidated the impact of hATG-based IST and demonstrated that these subpopulations were selectively depleted with successful treatment while other memory immune cell subpopulations persisted. Building on these findings, this thesis also includes a case study that explores the long-term biology within the bone marrow following initial AA diagnosis. We demonstrated the added value of analyzing bone marrow tissue samples over bone marrow aspirates, and gained insight into the mechanisms underlying the development of secondary clonal disorders.

Mass cytometry is a high-dimensional phenotyping technique that has pushed the analysis of both common and rarer cell populations forward. Consequently, it has deepened the understanding of immunology in health and disease[8-13]. In the setting of AA, mass cytometry was used to perform detailed analyses of the T-cell compartment in peripheral blood[14,15] but was not used to interrogate the presence of all immune populations within the bone

marrow simultaneously. In **Chapter 2**, we applied mass cytometry on cryopreserved bone marrow aspirates samples from AA patients before and six months after start of IST, and healthy controls with the aim to delineate which immune cell populations may be involved in the pathogenesis of AA. An antibody panel for 39 cell surface markers enabled broad immunophenotyping of all major immune lineages and hematopoietic stem and progenitor cells for the first time. Using dimensionality reduction analyses, we demonstrate that the bone marrow from AA patients pre-IST features a distinct immune cell composition compared to healthy controls, and is characterized by significantly decreased frequencies of hematopoietic stem and progenitor cells, myeloid cells and B-cells. In contrast, $CD4^+$ and $CD8^+$ T-cell frequencies are increased. Further analysis at the immune subpopulation level demonstrated the differential presence of both innate and adaptive immune clusters in AA patients pre-IST. Using correlation network analyses of these cell clusters, we identified a disease-specific immune cell network including $CD16^+$ myeloid cells, $CCR6^{++}$ B-cells, Th17-like $CCR6^+$ memory $CD4^+$ T-cells and $KLRG1^+$ terminally differentiated effector memory $CD8^+$ T-cells, compatible with a state of chronic inflammation. This network is more abundant in AA patients pre-IST compared to healthy controls, and its presence shows a trend towards normalization with successful IST. This suggests a potential pathogenic role. Collectively, our results provide a unique, single-cell view of the immune landscape in the bone marrow in AA that contributes to our understanding of AA as an immune-mediated disease. These findings reveal possible new players in the pathogenesis of AA and identify the chemokine receptor CCR6 as a potential therapeutic target.

In **Chapter 3**, we studied the immune response underlying the pathogenesis of AA in further detail within its native microenvironment in the bone marrow. Because the precise interactions between potentially pathogenic immune cells as well as the chronological order of events leading to AA development cannot be deducted from studying bone marrow aspirates, we performed an analysis of bone marrow tissue biopsies using imaging mass cytometry. Our results reveal that the active immune response in AA is concentrated in immune 'hotspots' within bone marrow tissue regions that still harbor pockets of $Ki\text{-}67^+$ hematopoietic progenitor cells. We propose that AA development begins in 'lymphoid-dominant' immune hotspots, where interactions between pro-inflammatory T- and B-cells, including the previously identified $CCR6^+$ B- and $CD4^+$ T-cells from **Chapter 2**, initiate the immune cascade. As the disease progresses, we observed the development of 'macrophage-enriched' immune hotspots. These hotspots are characterized by the presence of activated and enlarged $CD68^-CD163^+CD4^+$ macrophages along with activated T- and B-cells in close proximity to $Ki\text{-}67^+$ hematopoietic progenitor cells. These findings suggest that macrophages are involved in the pathogenesis of AA through the phagocytosis of dead and apoptotic

cells, while T- and B-cells orchestrate a targeted immune response by cytokine secretion and a cytotoxic attack. After the depletion of all Ki-67$^+$ hematopoietic progenitor cells, terminally differentiated effector memory T-cells and plasma cells remain in the hypocellular bone marrow, fitting with a more advanced stage of the disease where the active immune response has waned. These data, together with the findings from **Chapter 2**, underscore that the autoimmune response resulting in stem cell destruction is more diverse than previously recognized, and likely involves a broad spectrum of innate and adaptive immune cells rather than being only T-cell mediated. In addition, we generate a hypothesis on how the immune response evolves during disease development that illustrates which pro-inflammatory immune cells may contribute to each stage of bone marrow destruction.

To improve the treatment of AA by targeted therapy, more knowledge is needed about the immunomodulatory mechanisms underlying successful treatment. In **Chapter 4**, we investigated the effects of first-line IST with four days of ATGAM and long-term ciclosporin. We focused on active ATGAM, the fraction of this polyclonal antibody preparation capable of binding human lymphocytes and mediating its immunomodulatory effects. We demonstrate there is substantial variability in active ATGAM exposure among AA patients, caused by weight-based dosing, and reveal that higher exposure associates with earlier hematologic recovery. At high plasma levels, ATGAM binds all major lymphoid lineages and profoundly reduces CD4$^+$ T-, CD8$^+$ T-, and NK-cell counts. Remarkably, although ATGAM also binds B-cells, it does not induce B-cell depletion but instead promotes an increase of CD27$^+$ B-cells in peripheral blood, potentially reflecting redistribution of memory B-cells from the lymphoid organs into the circulation post-ATGAM. Deep immunophenotyping on series of peripheral blood samples collected up to three years after start of IST demonstrated that ATGAM induced rapid depletion of memory T-cells, including the potentially pathogenic KLRG1$^+$ terminally differentiated CD8$^+$ T-cells and Th17-like CCR6$^+$CD4$^+$ T-cells identified in **Chapter 2**. Although naïve and virus-specific T-cells were also depleted, they recovered quickly, indicating preservation of protective immunity post-ATGAM. Notably, CCR6^{++} B-cells from **Chapter 2** escaped ATGAM depletion but reduced gradually over time along with residual potentially pathogenic T-cells, including the CCR6$^+$CD4$^+$ T-cells. This could explain the crucial contribution of long-term ciclosporin to successful IST. Collectively, our results identify ATGAM exposure as a factor influencing hematologic recovery, and indicate that the therapeutic effect of IST goes beyond total lymphodepletion but is rather the result of selective depletion and suppression of key lymphocyte subpopulations including the T- and B-cell subpopulations from **Chapter 2**. This underscores the pathogenicity of these lymphocyte populations in the development of AA and highlights their potential as possible therapeutic targets.

In 10-15% of patients who survive AA, the development of secondary clonal disorders including acute myeloid leukemia (AML) remains a concerning long-term complication post-IST. Prediction and prevention remain challenging since the underlying mechanism driving clonal evolution to acute myeloid leukemia is unknown. It has been postulated that clonal evolution to AML may be the result of environmental selection, where mutant clones are more resistant to the autoimmune attack in the bone marrow and therefore expand as dominant clone in size and time[16,17]. Alternatively and additionally, stem cell clones may acquire somatic mutations that confer a proliferative advantage as compared to other remaining stem cell clones in the hypocellular bone marrow post-hATG. Evidence supporting these models is, however, indirect. To address this knowledge gap, in **Chapter 5**, we performed a multi-modal analysis of bone marrow samples from an AA-to-AML patient to track the development of secondary AML following the initial diagnosis of AA at the site of its development. Using imaging mass cytometry, we demonstrate that, in our described patient, the clinical diagnosis of AML was preceded by a shift in the bone marrow architecture. This shift was characterized by the expansion of Ki-67$^-$CD45^{dim}CD38$^+$ preleukemic clones post-hATG. Although the expansion of these Ki-67$^-$CD45^{dim}CD38$^+$ cells was also observable in non-evolving AA patients post-hATG, their continued expansion was unique to our AA-to-AML patient. These data suggest that the initial bone marrow failure could create a microenvironment that both favors and triggers preleukemic clones that survive the autoimmune attack, but that an additional cell-intrinsic event may be required for their continued expansion. By performing targeted next generation sequencing on sorted bone marrow aspirates from the AA-to-AML patient, we further investigated the genetic factors that possibly contributed to clonal evolution to AML. We found that leukemic driver mutations were only detectable at AML diagnosis 29 months post-hATG. Strikingly, we further observed a somatic mutation in the splicing factor *ZRSR2*, which was present in all hematopoietic cells in the bone marrow from AA diagnosis onwards. Overall, these data provide support to the close link between clonal hematopoiesis and the development of clonal disorders. In addition, our results support a model in which clonal evolution to AML is determined by both microenvironmental and genetic factors, and highlight a possible role for the identified *ZRSR2* mutation in this process.

General discussion

Paradigm of immune-mediated AA

AA is generally perceived as an immune-mediated form of bone marrow failure if no other causes of pancytopenia are found[5,18]. The widely accepted paradigm suggests that AA is the result of a T cell-mediated autoimmune response[19]. The disease is thought to develop when an antigen(s) expressed on the surface of hematopoietic stem and progenitor cells triggers

the activation and expansion of T-cells, which subsequently acquire a cytotoxic effector profile and cause damage to the bone marrow[19]. Evidence supporting this paradigm is mostly indirect. Bone marrow recovery after IST with hATG plus long-term ciclosporin suggests T-cell involvement[5]. Furthermore, there are reports of oligoclonal T-cell expansion and T-cell infiltration into the bone marrow in AA[20-24]. More recently, studies have identified patient-derived T-cells capable of killing stem cells *in vitro*[25,26]. Despite these findings, however, the precise mechanisms underlying AA development remain unknown, and two main elements require further exploration. The first relates to the identity of the targeted antigen(s) on the surface of the hematopoietic stem and progenitor cells, which has not yet been determined. The second element concerns the identity of the pathogenic immune cells involved in the autoimmune response, which remains largely elusive. Although there are indications that macrophages[27-29] and NK-cells[26,30,31] may contribute, a potential role of other immune cells besides T-cells has largely been neglected. In addition, in the absence of biomarkers to reliably diagnose the disease, it remains uncertain whether AA is immune-mediated in all patients, and if so, whether the same immune cell subpopulations are involved in all cases. Non-response to IST, defects in the function of the bone marrow niche[32], and frequent detection of somatic mutations[33] could indicate an alternative, non-immune mediated pathogenesis in some patients.

This thesis aimed to decipher the autoimmune response leading to AA development by using high-dimensional single-cell technologies to map the immune landscape in AA patients. By identifying potentially pathogenic immune cell populations, our results advance our understanding of AA as an immune-mediated form of bone marrow failure. Importantly, our findings further challenge the existing paradigm by revealing that AA is driven by an immune response involving a broad spectrum of innate and adaptive immune cells, instead of just T-cells alone. In **Chapter 2**, we propose that AA may be mediated by a disease-specific immune cell network of potentially pathogenic $CCR6^{++}$ B-cells, Th17-like $CCR6^{+}$ memory $CD4^{+}$ T-cells, $KLRG1^{+}$ terminally differentiated effector memory $CD8^{+}$ T-cells, and $CD16^{+}$ myeloid cells, all compatible with a state of chronic inflammation. In **Chapter 3**, we extend the findings from **Chapter 2** by visualizing a phenotypically diverse immune response involving all major immune lineages across different stages of bone marrow destruction. Finally, in **Chapter 4**, we show that bone marrow recovery after successful IST depends on the selective removal of both the pro-inflammatory T- and B-cell subpopulations from our immune cell network identified in **Chapter 2**. It is noteworthy that the immune landscape in all studied patients showed strong similarities, and was characterized by the expansion of the same pro-inflammatory immune cell subpopulations that show a trend toward normalization with successful IST. This implies that all studied patients had immune-mediated AA with involvement of the same

immune cell subpopulations, even though our analyses were performed on a heterogeneous patient population that ranges in age, sex, clinical disease severity, cytomegalovirus (CMV) status and response to IST. These findings are reassuring, as they suggest that the current treatment guidelines are successful in distinguishing patients with immune-mediated AA, despite the fact that AA remains a diagnosis of exclusion[18]. These novel insights into the pathogenesis of AA were made possible by our distinct approach, which differs from seminal papers in the field by 1) studying the immune response at the site of stem cell destruction in the bone marrow instead of in peripheral blood; 2) enabling a simultaneous analysis of all major immune lineages by broad immunophenotyping; 3) visualizing the interactions of in-depth phenotyped cells within the bone marrow architecture; 4) capturing the morphology of immune cells within the bone marrow tissue and 5) delineating the immunomodulatory effects associated with successful IST.

Proposed immunological model of AA

The most important contribution of this thesis is the generation of a hypothesis on the chronological order of events in AA development. By identifying 'lymphoid-dominant' immune hotspots with high densities of pro-inflammatory lymphocytes within the bone marrow tissue in **Chapter 3**, we believe to have captured the initial phase of immune activation in AA for the first time. Our data confirm involvement of ($CCR6^+$) $CD4^+$ and $CD8^+$ T-cells and additionally highlight a previously unappreciated role for ($CCR6^+$) B-cells in this process. As the immune response progresses, 'macrophage-enriched' immune hotspots develop, where a spectrum of pro-inflammatory immune cells including T-cells, B-cells and activated $CD68^-$ $CD163^+CD4^+$ macrophages is colocalized with progenitor cells. We interpreted these tissue areas as sites of peak immune activity, where T- and B-cells may coordinate targeted immune responses through antigen-specific T-cell receptor and B-cell receptor signaling, cytokine secretion, antigen presentation and cytotoxic attack. In contrast, activated $CD68^-CD163^+CD4^+$ macrophages may phagocytose dead and apoptotic cells. In the hypocellular bone marrow regions depleted of progenitor cells, terminally differentiated $CD8^+$ T-cells and plasma cells remain after the immune response has waned, suggesting accumulation of these cells in the bone marrow after repeated antigenic stimulation.

Distinguishing autoreactive immune cells from bystander cells in AA

The findings from this thesis together provide an immunological model of AA development that, for the first time, unravels the distinct roles of immune cell subpopulations during each phase of bone marrow destruction. This enables us to distinguish potentially autoreactive immune cells from bystander cells in AA. As illustrated in Figure 1, we propose that the early

immune environment leading to AA development is created by interactions between ($CCR6^+$) T- and B-cell within the 'lymphoid-dominant' immune hotspots. This develops following T- and/or B-cell activation by recognition of an autoantigen presented by the hematopoietic stem cell (Figure 1, Steps 1-3). We believe these T- and B-cell interactions sustain an antigen-specific immune response. The observation that pro-inflammatory innate immune cells including activated $CD68^-CD163^+CD4^+$ macrophages or NK-cells only come in later, with the development of the 'macrophage-enriched' immune hotspots, suggests that these cells play a secondary role in the pathogenesis of AA. Our findings thereby place the presence of macrophages and NK-cells in a new perspective. In previous studies, it was postulated that macrophages and NK-cells are recruited to the bone marrow in AA to enhance the killing of stem cells by stimulating effector cell function via the production of pro-inflammatory cytokines[26-28]. In this thesis, we demonstrate that macrophages and NK-cells are present in similar numbers between control bone marrow and the macrophage-enriched hotspots in AA. Importantly, we further show that macrophages are already observable within the lymphoid-dominant immune hotspots, but have not yet obtained an activated state. We therefore do not believe that the $CD68^-CD163^+CD4^+$ macrophages and NK-cells are actively recruited to the bone marrow in AA. Instead, it is more likely that these cells are pre-existing tissue-resident populations that are activated in response to the inflammatory signals within the bone marrow microenvironment (Figure 1, Step 4). This interpretation downplays the presumed importance of NK-cells in AA, which could still secrete pro-inflammatory cytokines and/or kill stressed cells within the macrophage-enriched hotspots, but are unlikely to be one of the main effector cell populations.

In contrast, for $CD68^-CD163^+CD4^+$ macrophages we consider a distinct role in phagocytosing the dead and apoptotic cells in the bone marrow (Figure 1, Step 5). Based on the findings from **Chapter 2**, we speculate that these macrophages are activated in the lymphoid-dominant immune hotspots, and subsequently start to engulf debris and dead hematopoietic cells targeted by the pathogenic T- and B-cells. Interestingly, we also found that these macrophages contained activated T- and B-cells, indicating that these lymphocytes possibly are phagocytosed after they have exerted their effector function. This uptake likely leads to the enlarged morphology of the macrophages observed in the macrophage-enriched immune hotspots. Once the active immune response has waned and their phagocytic function is no longer needed, the activated $CD68^-CD163^+CD4^+$ macrophages return to a resting state and recover to their normal size (Figure 1, Steps 6-7). Whether these $CD68^-CD163^+CD4^+$ macrophages are pro- or anti-inflammatory in AA will require further functional studies. Their expression of the scavenger receptor CD163, typically associated with anti-inflammatory M2 phenotype[34,35], strongly supports an immunosuppressive role in AA. However, various studies show that CD163 is not exclusive to an anti-inflammatory state[36,37]. Therefore, both scenarios are plausible: the $CD68^-CD163^+CD4^+$ macrophages could attempt to dampen inflammation

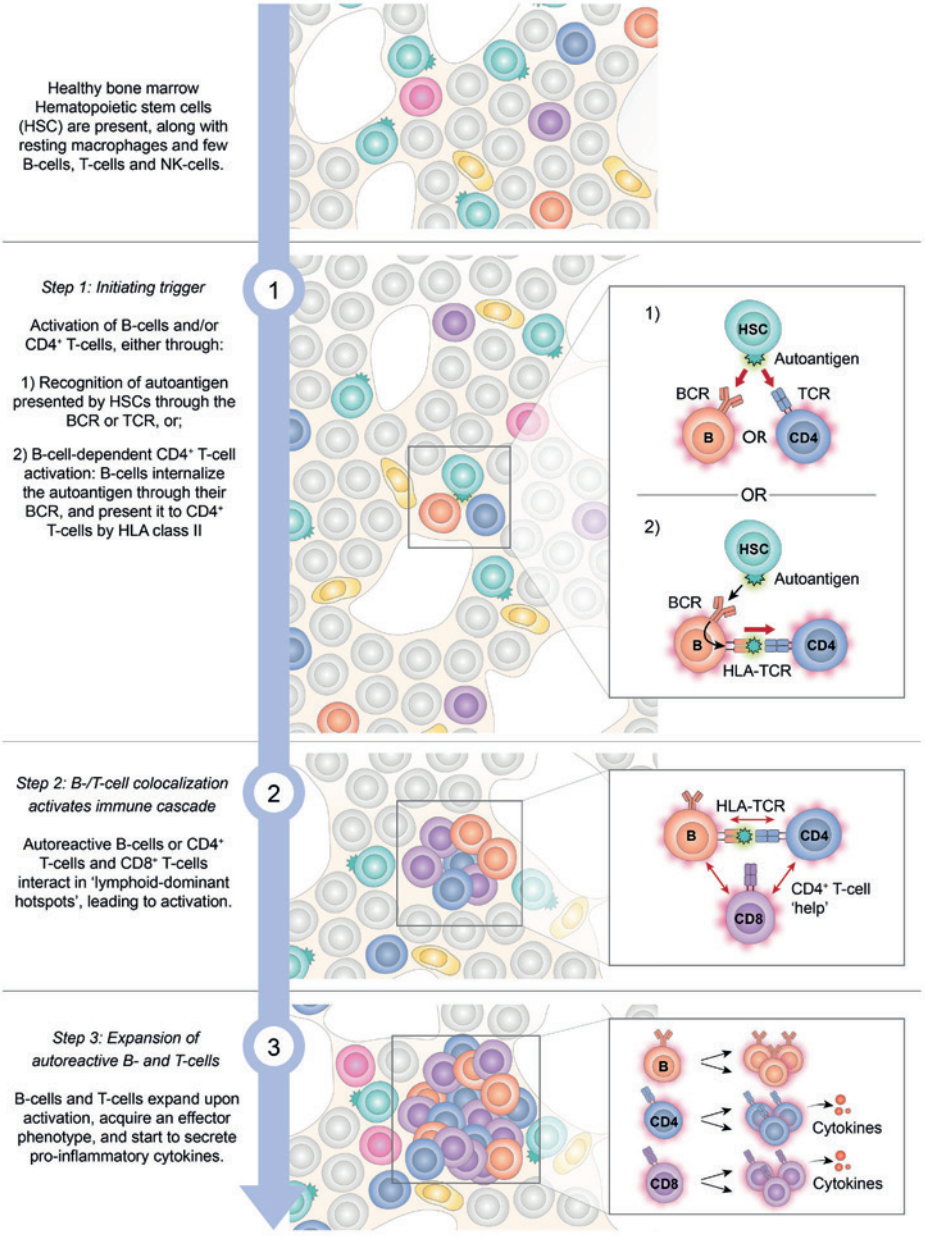
and damage induced by T- and B-cells. Alternatively, they might support inflammation by the production of reactive oxygen species and secretion of pro-inflammatory cytokines that support effector cell function.

Understanding the central role of T- and B-cells in AA

The central role of T- and B-cells and their interactions in our proposed immunological model of AA development calls for further discussion of their potential function. We focus on CCR6$^+$ B-cells, Th17-like CCR6$^+$ CD4$^+$ T-cells and KLRG1$^+$ terminally differentiated CD8$^+$ T-cells, as we consider these cells to be the most important players. This is based on their presence in the identified AA-specific immune cell network from **Chapter 2**, their detection in the affected bone marrow tissue in **Chapter 3**, and their selective removal following successful IST in **Chapter 4**. It is interesting that these subpopulations are frequently described in autoimmunity, and that the combined involvement of T- and B-cells drives many autoimmune diseases, including multiple sclerosis and rheumatoid arthritis[38-40]. This suggests that the observed immune response in AA may not be 'disease-specific', but may in fact be similar to the inflammatory state broadly observed in autoimmunity. Our findings, therefore, add direct evidence that AA shares pathophysiological features with other autoimmune diseases, corroborating previous observations[41-44]. These parallels support the idea that we have identified pathogenic immune cell subpopulations, even though further research is needed to elucidate their functional role and antigenic specificity. Based on prior reports, we speculate that CCR6$^+$ B-cells, Th17-like CCR6$^+$ CD4$^+$ T-cells and KLRG1$^+$ terminally differentiated CD8$^+$ T-cells may contribute to AA development through two distinct mechanisms.

CCR6$^+$ T- and B-cells in the pathogenesis of AA

For CCR6$^+$ B-cells and Th17-like CCR6$^+$ CD4$^+$ T-cells, we consider a role early in the immune response leading to bone marrow destruction. CCR6 has become a well-described marker in autoimmunity[45,46]. This chemokine receptor is found on the membrane of several immune cell types, with the highest expression observed on T- and B-cells[47], and levels increasing on B-cells after activation[48]. In line with its broad expression, CCR6 has been implicated as an important marker in mediating immune cell migration, mostly through the CCR6/CCL20 axis[45]. In this axis, CCL20, secreted in response to inflammatory signals, can attract pro-inflammatory CCR6$^+$ lymphocytes including CCR6$^+$ Th17 cells. This shifts the ratio between Th17 cells and regulatory T-cells to a pro-inflammatory state[49,50]. Numerous studies have highlighted the importance of the CCR6/CCL20 axis in autoimmunity, particularly in sustaining the autoimmune response by mediating immune cell recruitment to the inflamed tissues[45]. This includes renal inflammation, where this axis facilitates the development of lymphoid infiltrates that function as sites of T- and B-cell activation[51].


Healthy bone marrow
Hematopoietic stem cells (HSC) are present, along with resting macrophages and few B-cells, T-cells and NK-cells.
Step 1: Initiating trigger
Activation of B-cells and/or CD4+ T-cells, either through:
1) Recognition of autoantigen presented by HSCs through the BCR or TCR, or;
2) B-cell-dependent CD4+ T-cell activation: B-cells internalize the autoantigen through their BCR, and present it to CD4+ T-cells by HLA class II
1
1)
HSC
Autoantigen
BCR
TCR
B
OR
CD4
OR
2)
HSC
Autoantigen
BCR
B
CD4
HLA-TCR
Step 2: B-/T-cell colocalization activates immune cascade
Autoreactive B-cells or CD4+ T-cells and CD8+ T-cells interact in 'lymphoid-dominant hotspots', leading to activation.
2
HLA-TCR
B
CD4
CD4+ T-cell 'help'
CD8
Step 3: Expansion of autoreactive B- and T-cells
B-cells and T-cells expand upon activation, acquire an effector phenotype, and start to secrete pro-inflammatory cytokines.
3
B
CD4
Cytokines
CD8
Cytokines

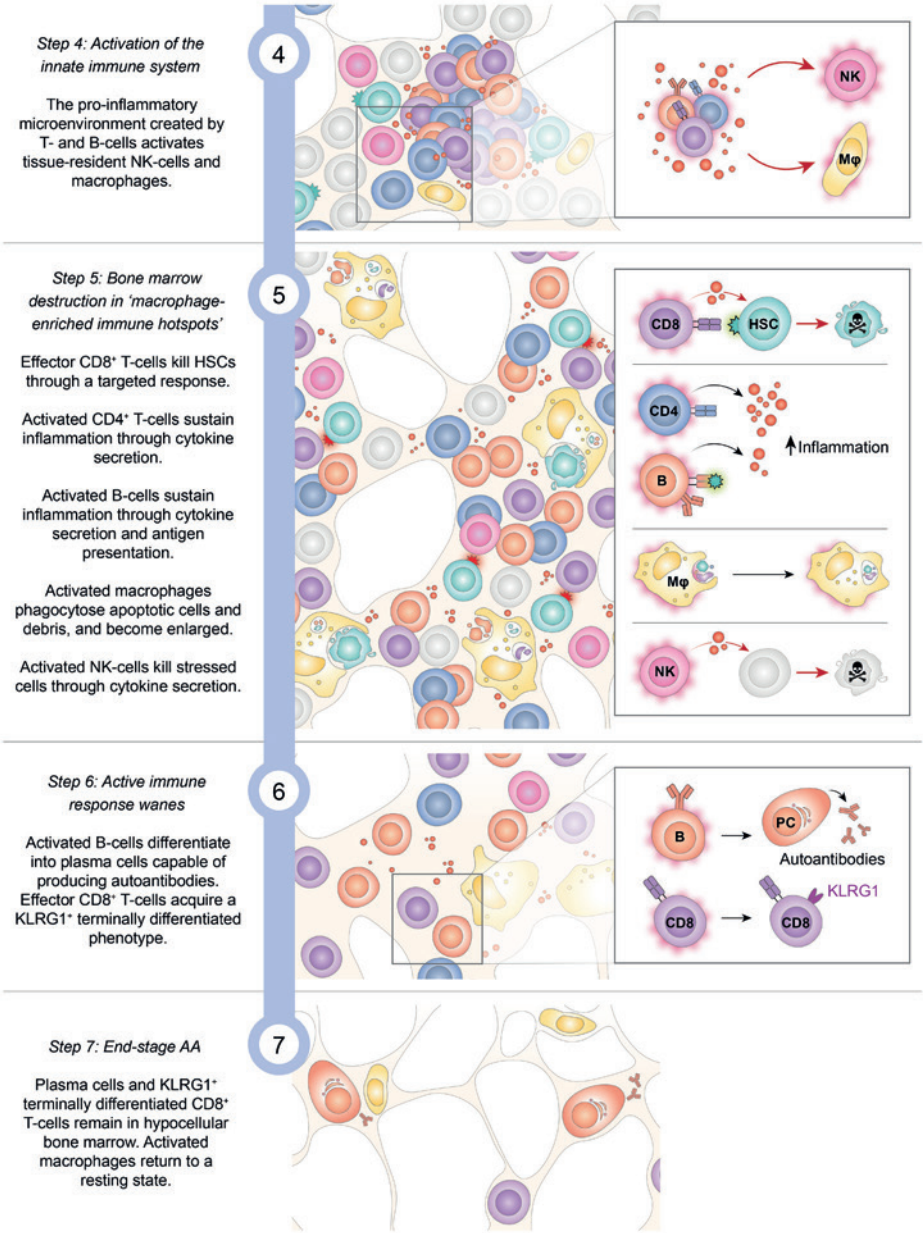


Figure 1. Visualization of the proposed immunological model of AA. BCR: B-cell receptor; HSC: hematopoietic stem cell; Mφ: macrophage; PC: plasma cell; TCR: T-cell receptor.

In the context of AA, we are the first to report on the importance of CCR6. We found that CCR6$^+$ B-cells and Th17-like CCR6$^+$ CD4$^+$ T-cells are prominent populations within the 'lymphoid-dominant' immune hotspots in the bone marrow, where these cells may interact through engagement of their T- and B-cell receptors. The fact that these CCR6$^+$ B-cells and Th17-like CCR6$^+$ CD4$^+$ T-cells were so closely colocalized that they could not be separated by cell segmentation supports that these cells interact within the bone marrow. We believe that these CCR6$^+$ B- and/or T-cells are the autoreactive immune cells that initiate the immune cascade in AA. The activation of these CCR6$^+$ B- and/or T-cells could either occur 1) directly, through recognition of an autoantigen presented by hematopoietic stem cells by the B- or T-cell receptor, or 2) through B-cell dependent T-cell activation, where B-cells take up the autoantigen through the B-cell receptor and activate the CD4$^+$ T-cells by presenting the antigen in HLA class II (e.g. HLA-DR) (Figure 1, Step 1). Following their activation, the interactions of these B- and CD4$^+$ T-cells may amplify the immune response: CCR6$^+$ CD4$^+$ T-cell 'help' to CD8$^+$ T-cells could drive CD8$^+$ T-cell activation, while interactions between CCR6$^+$ B-cells and CCR6$^+$ CD4$^+$ T-cells may promote their local expansion in the bone marrow (Figure 1, Steps 2-3).

These possible mechanisms of the CCR6$^+$ B-cells and CCR6$^+$ CD4$^+$ T-cells are supported by unpublished data on a tertiary lymphoid structure (TLS) from our group, which therefore warrant further discussion. This TLS was detected within a hypocellular bone marrow region from one of our AA patients at diagnosis using imaging mass cytometry (Figure 2). Because of its singular detection, the TLS was examined separately from the cohort-wide analysis presented in **Chapter 3**. Interestingly, the analysis revealed the TLS contained high densities of CCR6$^+$ CD4$^+$ T-cells in close proximity to zones of CCR6$^+$ B-cells, all located between CD11c$^+$HLA-DR$^+$ dendritic cells and/or CD8$^+$ T-cells. Given that TLS are defined as local hubs where autoreactive T- and B-cells are concentrated[52], this provides strong support for identifying the CCR6$^+$ B-cells and CCR6$^+$ CD4$^+$ T-cells as the autoreactive immune cells driving inflammation in AA. Furthermore, the observation that CCR6$^+$ CD4$^+$ T-cells were colocalized with CD8$^+$ T-cells in the TLS illustrates that these CD4$^+$ T-cells may indeed provide the "help" needed to activate cytotoxic CD8$^+$ T-cells in AA. In contrast, CCR6$^+$ B-cells may form germinal center-like structures with follicular helper T-cells, where they undergo clonal expansion, class switching and differentiation to autoantibody-secreting plasma cells. This could expand the autoreactive B-cell pool. It is interesting that TLS serve as sites of T- and B-cell differentiation and expansion, since this implies that CCR6$^+$ B-cells and CCR6$^+$ CD4$^+$ T-cells are not (only) recruited to the bone marrow in AA following clonal expansion in the draining lymph node, but (also) expand locally within it. In this context, the role of CCR6 may not be to facilitate CCL20-dependent immune cell recruitment as described in other autoimmune disorders[45], but to facilitate the retention of autoreactive T- and B-cells within the AA bone marrow microenvironment, where CCL20 levels are high[53].

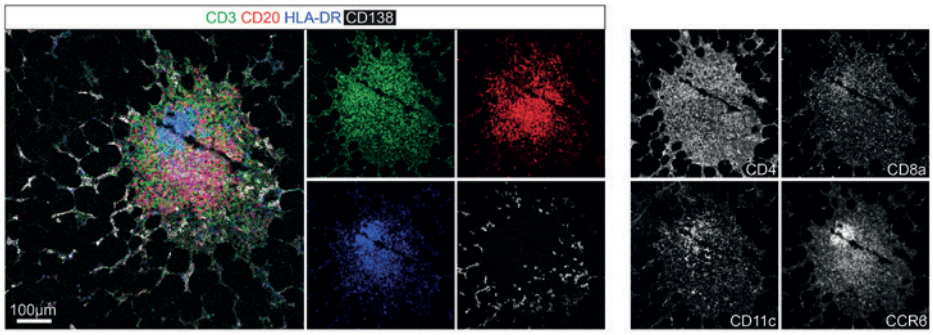


Figure 2. Tertiary lymphoid structure detected within the hypocellular bone marrow from an AA patient (AA13 from Chapter 2) at diagnosis by imaging mass cytometry. Stainings demonstrate high densities of CCR6$^+$ B- and CCR6$^+$ CD4$^+$ T-cells, located in close proximity to CD11c$^+$ dendritic cells, CD8$^+$ T-cells and CD138$^+$ plasma cells.

KLRG1$^+$ terminally differentiated CD8$^+$ T-cells in AA

For terminally differentiated CD8$^+$ T-cells we hypothesize a distinct role in maintaining chronic inflammation. CD8$^+$ T-cells are the most thoroughly studied immune cell population in AA, and have been described to be clonally expanded[22,25,54], express cytotoxic molecules[24-26], and kill hematopoietic stem cells *in vitro*[25,26]. This thesis adds important insight by demonstrating that terminally differentiated CD8$^+$ T-cells are present in the immune hotspots of peak immune activity. In addition, we show that these CD8$^+$ T-cells accumulate in the hypocellular bone marrow after all progenitors have been cleared (Figure 1, Step 6-7). We therefore believe that these cells represent the highly cytotoxic and terminally differentiated state of the activated CD8$^+$ T-cells that are capable of killing the hematopoietic stem cells in the bone marrow. Interestingly, we found that these cells express KLRG1 in **Chapter 2**. This could provide further insight into their cellular state. KLRG1 is a cell surface marker broadly expressed T- and NK-cells that was long considered a marker of T-cell senescence, but has more recently been recognized as a marker for highly activated and short-lived effector cells[55,56]. As an immune checkpoint molecule, KLRG1 can regulate immune responses by interacting with cadherins on the surface of antigen-presenting cells to elevate the activation threshold of T-cells. This process involves dephosphorylation of signaling molecules downstream of the T-cell receptor[55,57]. Therefore, KLRG1$^+$ terminally differentiated CD8$^+$ T-cells are reported to be in a balanced state between cytotoxicity and reduced functionality, which provides a protective mechanism against excessive immune activity[55].

The inhibitory role of KLRG1 is well-described in aging and infection with viruses including CMV, where KLRG1$^+$ terminally differentiated T-cells accumulate in the bone marrow and KLRG1 function increases after repeated antigenic stimulation[55,58]. In this thesis, the antigenic

specificity of the KLRG1$^+$ terminally differentiated CD8$^+$ T-cells was not evaluated, and this should be topic of future studies. However, our data strongly suggest that the expansion of KLRG1$^+$ terminally differentiated CD8$^+$ T-cells in AA is more likely to be the result of the autoimmune response driving stem cell destruction, than to aging or CMV infection. In **Chapter 2**, KLRG1$^+$ terminally differentiated CD8$^+$ T-cells were identified in CMV-negative healthy donors, illustrating that their antigenic specificities go beyond CMV. Furthermore, in **Chapter 3**, we showed that terminally differentiated CD8$^+$ T-cells are more abundant in the bone marrow from AA patients compared to age- and CMV status-matched controls. As a result, we speculate that the KLRG1$^+$ terminally differentiated CD8$^+$ T-cells accumulate in the hypocellular bone marrow to sustain immune memory of the targeted autoantigen in AA. The fact that KLRG1$^+$ terminally differentiated CD8$^+$ T-cells are highly abundant in the most severely damaged tissue regions and correlate with disease severity[55,59-61] in other autoimmune diseases supports this idea.

Identity of the progenitor-specific effector cell in AA

Given that our model implies a central role for both T- and B-cells, it is reasonable to question whether the immune response in AA is initiated by autoreactive T-cells or B-cells. Addressing this subject is incredibly complex, since T- and B-cells can activate each other, and AA is only diagnosed after severe immune damage to the bone marrow has occurred. For now, we can only speculate. Our findings provide no evidence that refutes the widely accepted view that AA is the result of a T-cell mediated immune response[5]. We still consider this a possibility, also because previous reports 1) have identified patient-derived T-cells capable of eliminating hematopoietic progenitor cells *in vitro*[25,26], and 2) have demonstrated loss of HLA expression on hematopoietic stem cells, suggesting their escape from T-cell mediated destruction[62,63]. Our model does support a more prominent role for CD4$^+$ T-cells, in addition to CD8$^+$ T-cells, than has been appreciated to date. At the same time, the recent success of B-cell depleting cellular therapies (e.g. CD19 CAR-T) in other autoimmune diseases traditionally considered T-cell mediated cannot be overlooked, since it suggests a more central role for B-cells than just a supportive function[64]. Whether B-cells could also drive AA development through antigen presentation, autoantibody production and/or cytokine secretion remains an open question that warrants further investigation. Given the close proximity of B- and T-cells within the bone marrow (e.g. lymphoid-dominant immune hotspots and the identified TLS), it is imaginable that B-cells present antigens to CD4$^+$ T-cells, leading to CD4$^+$ T-cell activation and an amplification of the immune response by cytokine production which could support the B-cells as well as the CD8$^+$ T-cells. In support of a possible involvement of autoantibodies, we discovered that bone marrow destruction is accompanied by B-cell differentiation into plasma cells, corroborating previous reports that identified potential autoantibodies[65,66] and

demonstrated deposition of IgG antibodies and complement factors within the bone marrow tissue in AA[67].

To fully elucidate the roles of T- and B-cells in AA development, it would be essential to isolate the CCR6$^+$ B-cells, CCR6$^+$ CD4$^+$ T-cells and KLRG1$^+$ EMRA CD8$^+$ T-cells from bone marrow samples for in-depth analyses of their functional state and clonality. Co-culture experiments of these T- and B-cells with autologous hematopoietic stem cells could shed light on potential autoreactivity by measuring T- and B-cell activation and cytokine secretion. On the other hand, analysis of their T- and B-cell receptor repertoires could offer more direct evidence of whether AA is T- and/or B-cell mediated, through the detection of oligoclonal expansion and the identification of their antigenic target(s). As part of the follow-up research on this thesis, we have already isolated CCR6$^+$ B-cells, CCR6$^+$ CD4$^+$ T-cells and KLRG1$^+$ EMRA CD8$^+$ T-cells from bone marrow aspirates collected from AA patients at diagnosis through flow cytometry-based cell sorting. This illustrates that such approaches are feasible. Preliminary data further show that downstream T- and B-cell receptor sequencing can be conducted successfully. Although this strategy is accompanied by several advantages including the large number of cells that can be assessed simultaneously to detect clonally expanded T- or B-cells, it precludes analyses of the entire B-cell compartment due to the loss of plasma cells during aspiration and sample processing. In addition, it hampers immune repertoire analyses within specific bone marrow tissue regions due to the loss of spatial context. Therefore, T- and B-cell receptor sequencing on bone marrow biopsies could be of added value. Bulk T-cell receptor beta sequencing is a currently available option. A pilot experiment from our group demonstrates that this technique can successfully be applied on technically challenging formalin-fixed paraffin embedded bone marrow biopsies to detect expanded T-cell clones within pre-specified tissue regions. However, joint T- and B-cell receptor sequencing on such bone marrow biopsies remains impossible at a single-cell resolution. Furthermore, combined T-cell receptor alpha and beta chain analysis cannot be done, but is necessary to identify the targeted antigen. Looking ahead, the further development of single-cell T- and B-cell receptor sequencing at a subcellular resolution *in situ* is therefore promising[68].

Clinical implications of the proposed immunological model of AA

It should be underscored that our proposed immunological model of AA also has important clinical implications. hATG-based IST, the first-line treatment for most AA patients, is limited by several issues, including the fact that it is a non-specific therapy with low response rates of approximately 70%[18]. Therefore, the overarching aim of this thesis was to decipher the immune-mediated pathogenesis of AA to identify new therapeutic targets for improved therapy. Based on **Chapters 3 and 4** we conclude that successful treatment for AA depends on

two major processes: 1) the disruption of the coordinated immune cell interactions driving AA development in the bone marrow and 2) the selective depletion of pro-inflammatory immune cell subpopulations including the CCR6$^+$ B-cells, Th17-like CCR6$^+$ CD4$^+$ T-cells and KLRG1$^+$ terminally differentiated CD8$^+$ T-cells discussed above. This presents two distinct therapeutic approaches, each with its own advantages and limitations, that may be applied to tackle both aspects.

First, the use of receptor-targeted therapies more broadly applied in the setting of autoimmunity could be successful since the immune response in AA seems to share pathophysiological features with other autoimmune diseases. This is interesting since AA is such a rare disorder and the development of orphan drugs remains a challenge. CCR6 antagonists have already been reported to be effective in reducing inflammation in autoimmunity in a preclinical setting[45,55]. Furthermore, targeting of KLRG1$^+$ lymphocytes has become a topic of interest in the field of tumor immunology[55], and may be adapted in order to permanently remove KLRG1$^+$ terminally differentiated CD8$^+$ T-cells.

A disadvantage of such receptor-targeted therapies is the inevitable depletion of healthy, non-autoreactive CCR6$^+$ or KLRG1$^+$ immune cells besides the potentially pathogenic populations. The second, and preferred, therapeutic approach would therefore be to specifically deplete the autoreactive T- and B-cells based on their antigenic specificity. This underscores the need of future studies on the T- and B-cell receptor repertoires of the CCR6$^+$ B-cells, Th17-like CCR6$^+$ CD4$^+$ T-cells, and KLRG1$^+$ terminally differentiated CD8$^+$ T-cells in order to identify the targeted antigen in AA. Whether successful treatment of AA depends on the elimination of autoreactive T- or B-cells, or relies on a combination of both, is a relevant question that warrants further investigation. Cellular therapies mediating either approach are emerging. For example, engineered T-cells expressing a chimeric autoantigen receptor (CAAR), containing the targeted autoantigen, hold promise in specifically killing autoreactive B-cells[69].

High-dimensional techniques to study the bone marrow at a single-cell resolution

Beyond these new insights into the pathogenesis of AA, this thesis provides an overview of the experimental and computational workflows that can be used when applying high-dimensional techniques to study the bone marrow at a single-cell resolution. **Chapters 2 and 3** offer an important comparison of two proteomics-based approaches, which demonstrates that suspension-based and spatially-resolved techniques provide complementary data and are most powerful when performed side by side. In **Chapter 2**, suspension-based mass cytometry was useful in screening the large numbers of cells needed to detect potentially pathogenic phenotypes in both common and rarer populations based on differential abundance. This technique therefore is useful for the generation of new hypotheses on the

mechanisms of disease. In **Chapters 3 and 5**, imaging mass cytometry offered insight into the biological processes occurring within the bone marrow tissue. Although this technique is not suitable for analyzing large numbers of cells or rare populations, it preserves spatial context to unravel the cellular interactions and morphologies that were lost in suspension.

It is worth discussing two discrepancies between our data from bone marrow aspirates (**Chapter 2**) and biopsies (**Chapter 3**), as they provide important considerations for future studies. The first discrepancy concerns the activated $CD68^{-}CD163^{+}CD4^{+}$ macrophages, which were found to be involved in AA development based on their distinct morphology in **Chapter 3**, but were not enriched in the bone marrow in absolute numbers. This indicates that cellular abundance is not always an indication of importance, and that relevant subpopulations can be missed when cells are studied outside of their native spatial context. The second discrepancy relates to the stark differences in the composition of the myeloid compartment between bone marrow biopsies and aspirates. For example, $CD16^{+}$ myeloid cells were not identified within bone marrow biopsies in **Chapter 3**, but accounted for a median 30% of myeloid cells in bone marrow aspirates from AA patients in **Chapter 2**. In contrast, myeloid cell subpopulations including macrophages, mast cells and granulocytes were identified in biopsies, but hardly found in aspirates. These data illustrate that analyses of bone marrow aspirates can be biased through selective cell loss: granulocytes and mast cells can be lost with cryopreservation[70,71], while macrophages are underrepresented in aspirates due to their "stickiness" during collection. This could explain why $CD16^{+}$ myeloid cells were the predominant myeloid cell population in bone marrow aspirates from AA patients. Together, these two discrepancies support broader implementation of spatially-resolved tissue profiling techniques for a more accurate analysis of the cellular processes within the bone marrow, either independently, or to validate results found in suspension. This does not only apply to AA, but also to other hematological disorders where myeloid, stromal and progenitor cells are a prominent feature and cannot be studied in their full complexity in suspension.

Recommendations for the analysis of spatial bone marrow datasets

Despite the importance of analyzing bone marrow biopsies, there are few reports that have provided an in-depth analysis of the bone marrow tissue through spatial proteomics (analysis of protein expression) or transcriptomics (analysis of gene expression). This is largely attributable to the challenges introduced by the bone marrow biopsies themselves. On the one hand, the processing of bone marrow tissue samples involves a relatively harsh procedure that can result in protein, DNA and RNA degradation. For example, tissue decalcification is required to enable bone marrow tissue sectioning, but can alter proteins and therefore affect tissue staining[72]. Furthermore, decalcified bone marrow biopsies require embedding

in formalin-fixed paraffin-embedded (FFPE) blocks, which can further dissociate proteins, DNA and RNA. On the other hand, the bone marrow microenvironment consists of a broad spectrum of both hematopoietic and non-hematopoietic cells that is far more heterogeneous than most other tissues[73]. Accordingly, proper profiling of bone marrow biopsies can only be performed when applying the most advanced techniques to distinguish all cell types based on their distinct phenotypes and morphologies.

This thesis provides a technically relevant contribution through the optimization of imaging mass cytometry that overcomes both issues. **Chapter 3** presents a 37-marker imaging mass cytometry panel that was designed by carefully screening more than 100 antibodies and confirming their performance on decalcified bone marrow tissue. This panel can visualize the full spectrum of bone marrow cell types in their true morphological shapes and is not limited by issues of autofluorescence and the need for cyclic staining[74]. Therefore, imaging mass cytometry is a useful alternative to fluorescence-based imaging (e.g. CODEX or CyCIF imaging platforms) and spatial transcriptomics (e.g. Xenium or CosMx techniques), which can be affected by spectral overlap and the lack of a direct visualization of cell morphology, respectively[75,76]. It is worth noting that our imaging mass cytometry panel can be adapted to study other hematological disorders by replacing AA-specific markers including CCR6, while keeping its backbone. Like with other antibody-based approaches, however, several challenges warrant consideration. This includes the limited availability of suitable antibody clones for decalcified FFPE bone marrow tissue, and the fact that the analyses are not fully unbiased. Yet, with the increasing number of antibody-based studies on bone marrow biopsies, imaging mass cytometry is a promising technique for research driven by a clear question on specific cell subpopulations.

A prominent, but less recognized, hurdle in spatial profiling besides data acquisition are the downstream data analyses that require tailoring to each tissue type. To appropriately extract single-cell data from the acquired images, we established a data analysis pipeline that provides a detailed guideline on how to handle spatially-resolved datasets of the bone marrow, from cell segmentation to spatial analysis. We showed that cell segmentation should always be based on multiple cell markers, beyond the nuclear DNA stain. This is particularly important for segmenting megakaryocytes, which are large in size and lack the markers typically used (e.g. CD45, Vimentin)[77]. In addition, unlike previous reports[73], we found that stromal cells can be segmented appropriately, but only when a suitable marker that captures their complex shape (e.g. CD271) is included. We do recommend that the number of markers should be selected carefully based on the research question, since every additional marker increases the risk of data loss due to overlapping features in the cell segmentation mask. These segmentation errors can be expected to wane as imaging resolution continues to improve.

For the downstream subpopulation and spatial analyses several approaches were evaluated. The major difficulty here was to overcome the obstacles introduced by AA itself, which were 1) depletion of the myeloid compartment and 2) bone marrow hypocellularity. We found that both challenges could best be addressed by analyzing cell abundance as an absolute cell count, normalized to the tissue area of the hematopoietic compartment. This helped avoid analyzing skewed data of cell frequencies, and thereby facilitated a fair comparison between AA and control bone marrow tissue. As a result, our approach differed from previous spatial analyses of tissue microenvironments[71,73,78]. We envision that this approach will be of interest to future studies of normal and diseased bone marrow, as the cellular composition of the bone marrow shifts with age[73,79] and displacement of healthy hematopoietic cells is a hallmark of hematological malignancies[34].

For the spatial analyses, we recommend another customized approach. We discovered that the 'traditional' pairwise interaction analysis between all cell types as proposed by Schapiro *et al*[80] was inadequate when comparing tissues with heterogeneous cellularities. The Schapiro approach calculates the average number of cell-cell interactions an returns an estimate of the interaction or avoidance of cell subpopulations, corrected for randomness. In the context of AA, however, the reduced number of cellular interactions hampered comparison to a normal, cellular bone marrow architecture. Therefore, we applied the spatial cellular neighborhood analysis proposed by Schürch *et al*[81], which clusters cells based on the information contained in their direct microenvironment. The main advantages of this approach were that it 1) enables analysis of all segmented cells simultaneously, 2) provides a visualization of the identified neighborhoods, and 3) considers a maximum distance in its calculations to control for differences in tissue cellularity. Spatial cellular neighborhood analyses have recently become an increasingly applied approach in studies of the tissue microenvironment, and can be extended to detect spatial niches or trajectories[82,83]. We confirm their value and advocate that cellular neighborhood analyses should be used in future studies of the bone marrow microenvironment as well. These analyses could be particularly useful in unraveling the distinct pathophysiologies of bone marrow failure syndromes, or the heterogeneity in the immune landscape in acute myeloid leukemia subtypes that is reported to influence clinical outcome[84].

Given that our analyses set the stage for further exploration of bone marrow biopsies through spatially-resolved profiling techniques, it is important to consider when such techniques may be applied. The work performed in this thesis revealed several bottlenecks that limit their widespread use. The first concerns the large quantities of data that these techniques provide, which are time-consuming to analyze and require knowledge on both basic biology and bioinformatics. It can be expected that the complexity of these datasets will only increase as the number proteins or genes that can be measured increases, or as methods

are combined[76,85]. The second relates to the low throughput of most spatially-resolved profiling techniques, as data acquisition can take several hours or even days[86]. Therefore, these techniques are primarily useful in exploratory research, where to provide a platform to both test existing hypothesis and generate new ones in health and disease. This limits their clinical applicability. In patient care, however, such detailed information is hardly needed. There, it would be more relevant to detect key findings from exploratory research with more accessible techniques such as immunohistochemistry or immunofluorescence.

Future perspectives: towards identifying the antigenic target in AA

Collectively, this thesis illustrates the feasibility and power of applying high-dimensional single-cell analysis techniques on bone marrow samples to investigate the pathogenesis of AA. Using (imaging) mass cytometry, we successfully identified potentially pathogenic immune cell populations, and thereby address a major gap in the current knowledge on AA. We recognize that our findings, although significant, require further functional studies to confirm the relevance of the immune cell populations identified in **Chapters 2 to 4**. Therefore, continued research is essential. This thesis highlights that identifying the antigenic specificities of these cells should be the next step forward.

Despite the increasing number of TCR sequencing studies[21,25,26], the targeted antigen in AA remains unknown. Recent evidence suggests that AA may result from cross-reactivity, where virus-specific T-cells mistakenly attack the hematopoietic stem cells in the bone marrow[25]. However, it is probable that the origin of the autoimmune response is not so 'simple'. First, the lack of strong HLA-associations[62,87] could suggest that the antigenic target differs between AA patients. Second, it is conceivable that a committed progenitor population(s) instead of the hematopoietic stem cell is the primary target of the immune response. In this scenario, hematopoietic stem cells, which are susceptible to environmental stress[88], could be destructed as a consequence of the development of the inflammatory environment.

The data from this thesis support a more targeted approach than previously applied. Specifically, we propose selecting the $CCR6^{++}$ B-cells, $CCR6^{+}$ $CD4^{+}$ T-cells and $KLRG1^{+}$ terminally differentiated memory $CD8^{+}$ T-cells identified in **Chapters 2 and 3** and screening these cells for reactivity towards autologous stem cells. While this idea appears straightforward, its execution is complicated by the limited availability of materials collected from AA patients at diagnosis. To overcome this issue, a model could be developed to mimic AA *in vitro*. This would involve isolating the $CCR6^{++}$ B-cells, Th17-like $CCR6^{+}$ $CD4^{+}$ T-cells and $KLRG1^{+}$ terminally differentiated memory $CD8^{+}$ T-cells in order to analyze their T- and B-cell receptor repertoire to identify clonally expanded populations that may predominate the T- and B-cell compartments following antigen recognition in AA (Figure 3, top row). These T- and B-cell

receptors could then be transduced into cell lines to generate large numbers of potentially autoreactive T- and B-cells. In parallel, induced pluripotent stem cell (iPSC) technology could be applied to reprogram peripheral blood cells from the same patient, in order to produce sufficient numbers of target cells for coculture experiments (Figure 3, middle row). This model would allow functional testing of potentially autoreactive T- and B-cell receptors and would set the stage for further identification of their targeted antigen.

Another interesting approach is to identify the targeted antigen from the side of the target cell (Figure 3, bottom row). In AA, the autoimmune attack could cause a shift in the hematopoietic stem and progenitor cell compartment, in which stem cells expressing the targeted antigen are depleted but progenitor cells lacking the antigen survive. This phenomenon would explain clonal hematopoiesis, often observed in AA at diagnosis[16]. Detecting this possible shift in the hematopoietic stem and progenitor cell compartment by single-cell RNA sequencing could provide important insight into the identity of the targeted antigen(s). This approach does not need to stand on its own but can complement T- and B-cell receptor sequencing data to provide strong evidence of the antigen(s) involved in AA[25,26].

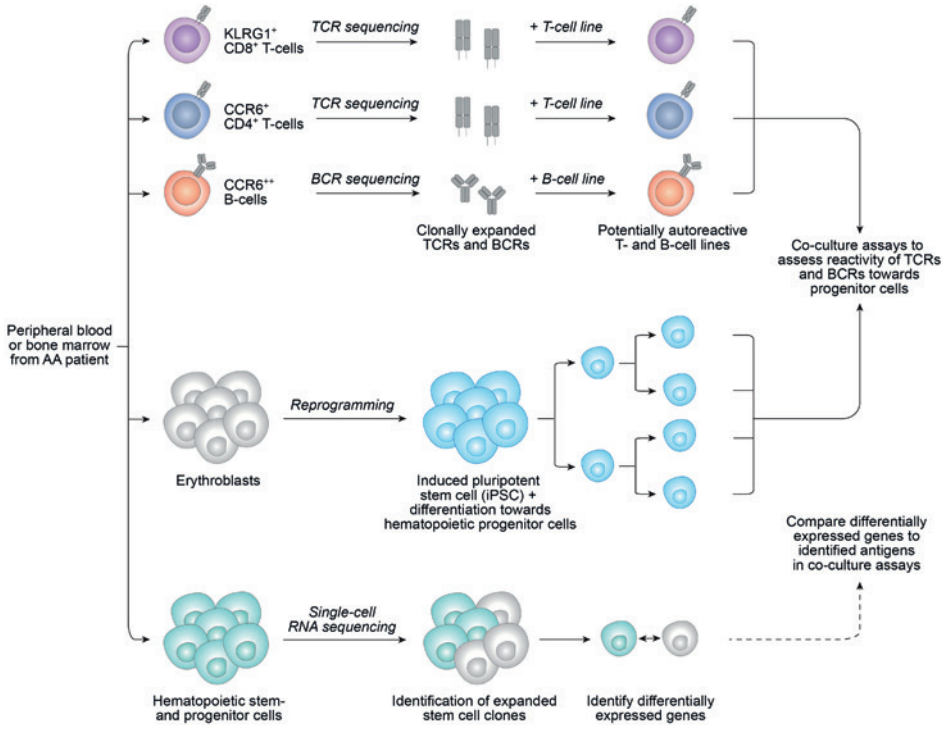


Figure 3. Proposed strategy and experimental workflow towards identifying the targeted autoantigen(s) in AA. BCR: B-cell receptor; TCR: T-cell receptor.

References

1. Ehrlich P. Ueber einen Fall von Anämie mit Bemerkungen über regenerative Veränderungen des Knochenmarks. Vol. 13: Charité-Annalen; 1888.
2. Gluckman E, Devergie A, Poros A, Degoulet P. Results of immunosuppression in 170 cases of severe aplastic anaemia. Report of the European Group of Bone Marrow Transplant (EGBMT). *Br J Haematol*. 1982;51(4):541-550.
3. Speck B, Gluckman E, Haak HL, van Rood JJ. Treatment of aplastic anaemia by antilymphocyte globulin with and without allogeneic bone-marrow infusions. *Lancet*. 1977;2(8049):1145-1148.
4. Young N, Griffith P, Brittain E, et al. A multicenter trial of antithymocyte globulin in aplastic anemia and related diseases. *Blood*. 1988;72(6):1861-1869.
5. Young NS. Aplastic Anemia. *N Engl J Med*. 2018;379(17):1643-1656.
6. Scheinberg P, Nunez O, Weinstein B, et al. Horse versus rabbit antithymocyte globulin in acquired aplastic anemia. *N Engl J Med*. 2011;365(5):430-438.
7. Halkes CJ, Veelken H, Falkenburg JH. Horse versus rabbit antithymocyte globulin in aplastic anemia. *N Engl J Med*. 2011;365(19):1842-1843; author reply 1843-1844.
8. de Vries NL, van de Haar J, Veninga V, et al. gammadelta T cells are effectors of immunotherapy in cancers with HLA class I defects. *Nature*. 2023;613(7945):743-750.
9. Jia L, Li N, Abdelaal TRM, et al. High-Dimensional Mass Cytometry Reveals Emphysema-associated Changes in the Pulmonary Immune System. *Am J Respir Crit Care Med*. 2024;210(8):1002-1016.
10. Li N, van Unen V, Hollt T, et al. Mass cytometry reveals innate lymphoid cell differentiation pathways in the human fetal intestine. *J Exp Med*. 2018;215(5):1383-1396.
11. van der Zwan A, van Unen V, Beyrend G, et al. Visualizing Dynamic Changes at the Maternal-Fetal Interface Throughout Human Pregnancy by Mass Cytometry. *Front Immunol*. 2020;11:571300.
12. van Unen V, Li N, Molendijk I, et al. Mass Cytometry of the Human Mucosal Immune System Identifies Tissue- and Disease-Associated Immune Subsets. *Immunity*. 2016;44(5):1227-1239.
13. van Unen V, Ouboter LF, Li N, et al. Identification of a Disease-Associated Network of Intestinal Immune Cells in Treatment-Naive Inflammatory Bowel Disease. *Front Immunol*. 2022;13:893803.
14. Kordasti S, Costantini B, Seidl T, et al. Deep phenotyping of Tregs identifies an immune signature for idiopathic aplastic anemia and predicts response to treatment. *Blood*. 2016;128(9):1193-1205.
15. Zhang L, Mao J, Lian Y, et al. Mass cytometry analysis identifies T cell immune signature of aplastic anemia and predicts the response to cyclosporine. *Ann Hematol*. 2023;102(3):529-539.
16. Ogawa S. Clonal hematopoiesis in acquired aplastic anemia. *Blood*. 2016;128(3):337-347.
17. Babushok DV. A brief, but comprehensive, guide to clonal evolution in aplastic anemia. *Hematology Am Soc Hematol Educ Program*. 2018;2018(1):457-466.
18. Kulasekararaj A, Cavenagh J, Dokal I, et al. Guidelines for the diagnosis and management of adult aplastic anaemia: A British Society for Haematology Guideline. *Br J Haematol*. 2024;204(3):784-804.
19. Risitano AM. (Auto-)immune signature in aplastic anemia. *Haematologica*. 2018;103(5):747-749.
20. Melenhorst JJ, van Krieken JH, Dreef E, Landegent JE, Willemze R, Fibbe WE. T cells selectively infiltrate bone marrow areas with residual haemopoiesis of patients with

acquired aplastic anaemia. *Br J Haematol*. 1997;99(3):517-519.

21. Risitano AM, Kook H, Zeng W, Chen G, Young NS, Maciejewski JP. Oligoclonal and polyclonal CD4 and CD8 lymphocytes in aplastic anemia and paroxysmal nocturnal hemoglobinuria measured by V beta CDR3 spectratyping and flow cytometry. *Blood*. 2002;100(1):178-183.

22. Risitano AM, Maciejewski JP, Green S, Plasilova M, Zeng W, Young NS. In-vivo dominant immune responses in aplastic anaemia: molecular tracking of putatively pathogenetic T-cell clones by TCR beta-CDR3 sequencing. *Lancet*. 2004;364(9431):355-364.

23. Enache A, Carty SA, Babushok DV. Origins of T-cell-mediated autoimmunity in acquired aplastic anaemia. *Br J Haematol*. 2025;206(4):1035-1053.

24. Giudice V, Feng X, Lin Z, et al. Deep sequencing and flow cytometric characterization of expanded effector memory CD8(+)CD57(+) T cells frequently reveals T-cell receptor Vbeta oligoclonality and CDR3 homology in acquired aplastic anemia. *Haematologica*. 2018;103(5):759-769.

25. Ben Hamza A, Welters C, Stadler S, et al. Virus-reactive T cells expanded in aplastic anemia eliminate hematopoietic progenitor cells by molecular mimicry. *Blood*. 2024.

26. Lundgren S, Huuhtanen J, Keranen M, et al. Single-cell analysis of aplastic anemia reveals a convergence of NK and NK-like CD8(+) T cells with a disease-associated TCR signature. *Sci Transl Med*. 2025;17(787):eadl6758.

27. Sun W, Wu Z, Lin Z, et al. Macrophage TNF-alpha licenses donor T cells in murine bone marrow failure and can be implicated in human aplastic anemia. *Blood*. 2018;132(26):2730-2743.

28. Vaht K, Brenner J, Ednersson SB, Ljungman P, Brune M, Andersson PO. Bone marrow expression of CD68/CD163 macrophages, IL-17 and FOXP3 cells in aplastic anemia and their relation to prognosis. *Eur J Haematol*. 2023;110(3):313-321.

29. Glass J, Feng X, Chen J, et al. Macrophage polarization, inflammatory monocytes, and impaired MDSCs are associated with murine and human immune aplastic anemia. *J Leukoc Biol*. 2025;117(6).

30. Vissers LTW, van Ostaijen-Ten Dam MM, Melsen JE, et al. Potential role of B- and NK-cells in the pathogenesis of pediatric aplastic anemia through deep phenotyping. *Front Immunol*. 2024;15:1328175.

31. Liu C, Li Z, Sheng W, et al. Abnormalities of quantities and functions of natural killer cells in severe aplastic anemia. *Immunol Invest*. 2014;43(5):491-503.

32. Medinger M, Drexler B, Lengerke C, Passweg J. Pathogenesis of Acquired Aplastic Anemia and the Role of the Bone Marrow Microenvironment. *Front Oncol*. 2018;8:587.

33. Yoshizato T, Dumitriu B, Hosokawa K, et al. Somatic Mutations and Clonal Hematopoiesis in Aplastic Anemia. *N Engl J Med*. 2015;373(1):35-47.

34. Parham P. The Immune System (ed 4). New York: Garland Science, Taylor & Francis Group, LLC; 2014.

35. Chen S, Saeed A, Liu Q, et al. Macrophages in immunoregulation and therapeutics. *Signal Transduct Target Ther*. 2023;8(1):207.

36. Chinju A, Moriyama M, Kakizoe-Ishiguro N, et al. CD163+ M2 Macrophages Promote Fibrosis in IgG4-Related Disease Via Toll-like Receptor 7/Interleukin-1 Receptor-Associated Kinase 4/NF-kappaB Signaling. *Arthritis Rheumatol*. 2022;74(5):892-901.

37. Fuentes-Duculan J, Suarez-Farinas M, Zaba LC, et al. A subpopulation of CD163-positive macrophages is classically activated in psoriasis. *J Invest Dermatol*. 2010;130(10):2412-2422.

38. Shah K, Leandro M, Cragg M, et al. Disrupting B and T-cell collaboration in autoimmune disease: T-cell engagers versus CAR T-cell therapy? *Clin Exp Immunol*. 2024;217(1):15-30.

39. Rao DA. The rise of peripheral T helper cells in autoimmune disease. *Nat Rev Rheumatol*. 2019;15(8):453-454.

40. van Langelaar J, Rijvers L, Smolders J, van Luijn MM. B and T Cells Driving Multiple Sclerosis: Identity, Mechanisms and Potential Triggers. *Front Immunol*. 2020;11:760.

41. Wu Z, Gao S, Feng X, et al. Human autoimmunity at single cell resolution in aplastic anemia before and after effective immunotherapy. *Nat Commun*. 2025;16(1):5048.

42. Kordasti S, Marsh J, Al-Khan S, et al. Functional characterization of CD4+ T cells in aplastic anemia. *Blood*. 2012;119(9):2033-2043.

43. de Latour RP, Visconte V, Takaku T, et al. Th17 immune responses contribute to the pathophysiology of aplastic anemia. *Blood*. 2010;116(20):4175-4184.

44. Solomou EE, Kattamis A, Symeonidis A, et al. Increased age-associated B cells in patients with acquired aplastic anemia correlate with IFN-gamma. *Blood Adv*. 2024;8(2):399-402.

45. Gomez-Melero S, Caballero-Villarraso J. CCR6 as a Potential Target for Therapeutic Antibodies for the Treatment of Inflammatory Diseases. *Antibodies (Basel)*. 2023;12(2).

46. Meitei HT, Jadhav N, Lal G. CCR6-CCL20 axis as a therapeutic target for autoimmune diseases. *Autoimmun Rev*. 2021;20(7):102846.

47. Ponten F, Jirstrom K, Uhlen M. The Human Protein Atlas--a tool for pathology. *J Pathol*. 2008;216(4):387-393.

48. Elgueta R, Marks E, Nowak E, et al. CCR6-dependent positioning of memory B cells is essential for their ability to mount a recall response to antigen. *J Immunol*. 2015;194(2):505-513.

49. Ranasinghe R, Eri R. Modulation of the CCR6-CCL20 Axis: A Potential Therapeutic Target in Inflammation and Cancer. *Medicina (Kaunas)*. 2018;54(5).

50. Harper EG, Guo C, Rizzo H, et al. Th17 cytokines stimulate CCL20 expression in keratinocytes in vitro and in vivo: implications for psoriasis pathogenesis. *J Invest Dermatol*. 2009;129(9):2175-2183.

51. Welsh-Bacic D, Lindenmeyer M, Cohen CD, et al. Expression of the chemokine receptor CCR6 in human renal inflammation. *Nephrol Dial Transplant*. 2011;26(4):1211-1220.

52. Sato Y, Silina K, van den Broek M, Hirahara K, Yanagita M. The roles of tertiary lymphoid structures in chronic diseases. *Nat Rev Nephrol*. 2023;19(8):525-537.

53. Ge M, Zheng Y, Li X, et al. Differential expression profile of Th1/Th17/Th2-related chemokines and their receptors in patients with acquired bone marrow failure syndromes. *Hum Immunol*. 2013;74(2):176-180.

54. Melenhorst JJ, Fibbe WE, Struyk L, van der Elsen PJ, Willemze R, Landegent JE. Analysis of T-cell clonality in bone marrow of patients with acquired aplastic anaemia. *Br J Haematol*. 1997;96(1):85-91.

55. Zhang Y, Chen S, Tang X, et al. The role of KLRG1: a novel biomarker and new therapeutic target. *Cell Commun Signal*. 2024;22(1):337.

56. Henson SM, Akbar AN. KLRG1--more than a marker for T cell senescence. *Age (Dordr)*. 2009;31(4):285-291.

57. Greenberg SA, Kong SW, Thompson E, Gulla SV. Co-inhibitory T cell receptor KLRG1: human cancer expression and efficacy of neutralization in murine cancer models. *Oncotarget*. 2019;10(14):1399-1406.

58. Ouyang Q, Wagner WM, Voehringer D, et al. Age-associated accumulation of CMV-specific CD8+ T cells expressing the inhibitory killer cell lectin-like receptor G1 (KLRG1). *Exp Gerontol*. 2003;38(8):911-920.

59. Li Y, Li B, You Z, et al. Cytotoxic KLRG1 expressing lymphocytes invade portal tracts in primary biliary cholangitis. *J Autoimmun*. 2019;103:102293.

60. Kalim H, Wahono CS, Permana BPO, Pratama MZ, Handono K. Association between senescence of T cells and disease activity in

patients with systemic lupus erythematosus. *Reumatologia*. 2021;59(5):292-301.

61. Goyal NA, Coulis G, Duarte J, et al. Immunophenotyping of Inclusion Body Myositis Blood T and NK Cells. *Neurology*. 2022;98(13):e1374-e1383.

62. Zaimoku Y, Patel BA, Adams SD, et al. HLA associations, somatic loss of HLA expression, and clinical outcomes in immune aplastic anemia. *Blood*. 2021;138(26):2799-2809.

63. Tsuji N, Hosokawa K, Urushihara R, et al. Frequent HLA-DR loss on hematopoietic stem progenitor cells in patients with cyclosporine-dependent aplastic anemia carrying HLA-DR15. *Leukemia*. 2022;36(6):1666-1675.

64. Muller F, Taubmann J, Bucci L, et al. CD19 CAR T-Cell Therapy in Autoimmune Disease - A Case Series with Follow-up. *N Engl J Med*. 2024;390(8):687-700.

65. Hirano N, Butler MO, Von Bergwelt-Baildon MS, et al. Autoantibodies frequently detected in patients with aplastic anemia. *Blood*. 2003;102(13):4567-4575.

66. Kelkka T, Tyster M, Lundgren S, et al. Anti-COX-2 autoantibody is a novel biomarker of immune aplastic anemia. *Leukemia*. 2022;36(9):2317-2327.

67. Fidanza CA, Bortolotti M, Croci GA, Barcellini W, Fattizzo B. Characterization of Complement and Immunoglobulin Deposition in Bone Marrow Trephine Biopsies of Patients with Cytopenias. *Blood*. 2024;144:5666-5666.

68. Zhan X, Liu Y, Guo Y, et al. Single cell resolved spatial immune repertoire unveils spatial heterogeneity of lymphoid aggregates in human immune disorders. *bioRxiv*. 2025:2025.2001.2016.630222.

69. Ellebrecht CT, Bhoj VG, Nace A, et al. Reengineering chimeric antigen receptor T cells for targeted therapy of autoimmune disease. *Science*. 2016;353(6295):179-184.

70. Takaku T, Malide D, Chen J, Calado RT, Kajigaya S, Young NS. Hematopoiesis in 3 dimensions: human and murine bone marrow architecture visualized by confocal microscopy. *Blood*. 2010;116(15):e41-55.

71. Krop J, van der Zwan A, Ijsselsteijn ME, et al. Imaging mass cytometry reveals the prominent role of myeloid cells at the maternal-fetal interface. *iScience*. 2022;25(7):104648.

72. Miquelestorena-Standley E, Jourdan ML, Collin C, et al. Effect of decalcification protocols on immunohistochemistry and molecular analyses of bone samples. *Mod Pathol*. 2020;33(8):1505-1517.

73. Bandyopadhyay S, Duffy MP, Ahn KJ, et al. Mapping the cellular biogeography of human bone marrow niches using single-cell transcriptomics and proteomic imaging. *Cell*. 2024;187(12):3120-3140 e3129.

74. Giesen C, Wang HA, Schapiro D, et al. Highly multiplexed imaging of tumor tissues with subcellular resolution by mass cytometry. *Nat Methods*. 2014;11(4):417-422.

75. Black S, Phillips D, Hickey JW, et al. CODEX multiplexed tissue imaging with DNA-conjugated antibodies. *Nat Protoc*. 2021;16(8):3802-3835.

76. Janesick A, Shelansky R, Gottscho AD, et al. High resolution mapping of the tumor microenvironment using integrated single-cell, spatial and in situ analysis. *Nat Commun*. 2023;14(1):8353.

77. Ijsselsteijn ME, Somarakis A, Lelieveldt BPF, Hollt T, de Miranda N. Semi-automated background removal limits data loss and normalizes imaging mass cytometry data. *Cytometry A*. 2021;99(12):1187-1197.

78. Salie H, Wischer L, D'Alessio A, et al. Spatial single-cell profiling and neighbourhood analysis reveal the determinants of immune architecture connected to checkpoint inhibitor therapy outcome in hepatocellular carcinoma. *Gut*. 2025;74(3):451-466.

79. Ogawa T, Kitagawa M, Hirokawa K. Age-related changes of human bone marrow: a histometric estimation of proliferative cells, apoptotic cells, T cells, B cells and macrophages. *Mech Ageing Dev*. 2000;117(1-3):57-68.

80. Schapiro D, Jackson HW, Raghuraman S, et al. histoCAT: analysis of cell phenotypes and interactions in multiplex image cytometry data. *Nat Methods*. 2017;14(9):873-876.

81. Schurch CM, Bhate SS, Barlow GL, et al. Coordinated Cellular Neighborhoods Orchestrate Antitumoral Immunity at the Colorectal Cancer Invasive Front. *Cell*. 2020;182(5):1341-1359 e1319.

82. Windhager J, Zanotelli VRT, Schulz D, et al. An end-to-end workflow for multiplexed image processing and analysis. *Nat Protoc*. 2023;18(11):3565-3613.

83. Pham D, Tan X, Balderson B, et al. Robust mapping of spatiotemporal trajectories and cell-cell interactions in healthy and diseased tissues. *Nat Commun*. 2023;14(1):7739.

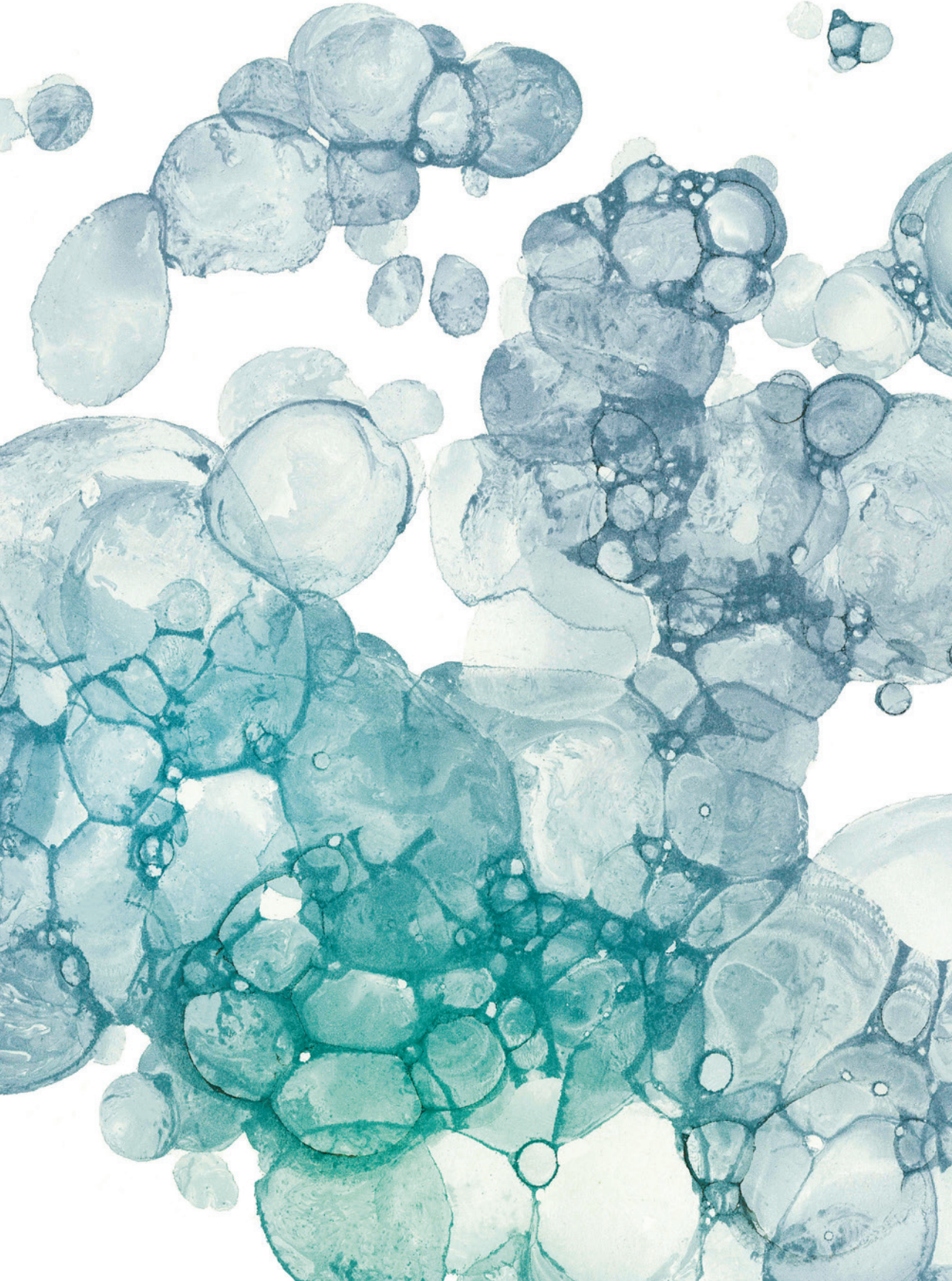
84. van Galen P, Hovestadt V, Wadsworth Ii MH, et al. Single-Cell RNA-Seq Reveals AML Hierarchies Relevant to Disease Progression and Immunity. *Cell*. 2019;176(6):1265-1281 e1224.

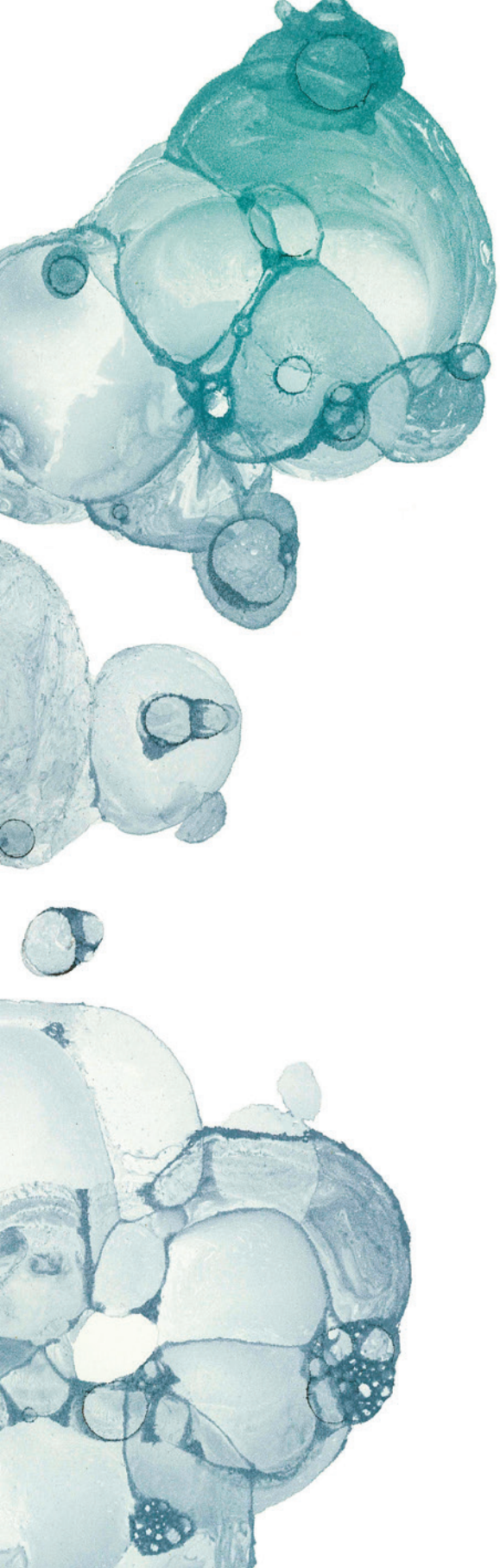
85. Takano Y, Suzuki J, Nomura K, et al. Spatially resolved gene expression profiling of tumor microenvironment reveals key steps of lung adenocarcinoma development. *Nat Commun*. 2024;15(1):10637.

86. Bressan D, Battistoni G, Hannon GJ. The dawn of spatial omics. *Science*. 2023;381(6657):eabq4964.

87. Olson TS, Frost BF, Duke JL, et al. Pathogenicity and impact of HLA class I alleles in aplastic anemia patients of different ethnicities. *JCI Insight*. 2022;7(22).

88. Tower J. Stress and stem cells. *Wiley Interdiscip Rev Dev Biol*. 2012;1(6):789-802.





Appendices

A

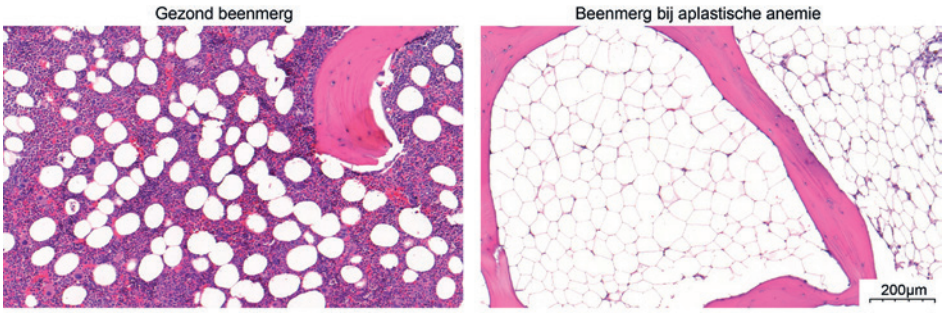
Nederlandse samenvatting
About the author
List of publications
Acknowledgements / Dankwoord

Nederlandse samenvatting

Immuun-gemedieerde aplastische anemie: een zeldzame ziekte met veel vraagtekens

Het beenmerg is het belangrijkste orgaan voor de productie van bloed. Het beenmerg produceert rode bloedcellen, witte bloedcellen en bloedplaatjes, die respectievelijk belangrijk zijn voor zuurstoftransport, afweer tegen ziekteverwekkers en wondheling. Aan de basis van de bloedproductie staan de hematopoietische stamcellen; de 'oercellen' waaruit alle typen bloedcellen ontstaan.

Indien het beenmerg onvoldoende rode bloedcellen, witte bloedcellen en/of bloedplaatjes produceert, kan er sprake zijn van beenmergfalen. Immuun-gemedieerde aplastische anemie (AA) is een ernstige, verworven vorm van beenmergfalen dat op elke leeftijd kan ontstaan. AA wordt gekenmerkt door een beenmerg met een gatenkaasstructuur. In dit 'lege' beenmerg is het bloedproducerende (hematopoietische) weefsel (roze/paars vlakken) vervangen door vet (witte bollen; zie figuur hieronder). Deze lege structuur lijkt met wat fantasie op de afbeelding die is weergegeven op de kaft van dit proefschrift. Het gevolg van dit lege beenmerg is een sterk verminderde productie van alle bloedcellen, wat kan leiden tot vermoeidheid, kortademigheid en potentieel levensbedreigende infecties en bloedingen.



AA is een zeldzame aandoening en treft in Nederland jaarlijks ongeveer 50 volwassenen. Een groot deel van deze patiënten wordt behandeld in het nationaal expertisecentrum voor zeldzaam beenmergfalen in het Leids Universitair Medisch Centrum. Voor de meeste patiënten bestaat de standaardbehandeling uit afweeronderdrukkende medicatie: een korte kuur met anti-thymocytenglobuline, gevolgd door langdurig gebruik van ciclosporine. Deze behandeling kan leiden tot herstel van het beenmerg, maar het is nog niet duidelijk hoe de therapie precies werkt. Daarnaast is de behandeling niet specifiek, gaat het gepaard met bijwerkingen en leidt het slechts bij een minderheid van de patiënten tot volledig herstel. Hierdoor bestaat er een grote behoefte aan betere en gerichtere behandelingen.

Wat veroorzaakt immuun-gemedieerde aplastische anemie?

Vanwege de zeldzaamheid van AA wordt er wereldwijd relatief weinig onderzoek gedaan naar deze aandoening. Hierdoor is de exacte oorzaak van de ziekte nog steeds onbekend en is het momenteel niet mogelijk om nieuwe, gerichte behandelingen te ontwikkelen. Omdat een deel van de patiënten herstelt na behandeling met afweeronderdrukkende medicatie, wordt aangenomen dat AA een auto-immuunziekte is. Hierbij valt het immuunsysteem vermoedelijk per ongeluk de stamcellen in het beenmerg aan.

Vooral T-cellen lijken hierbij een belangrijke rol te spelen. Dit zijn afweercellen die normaal gesproken helpen bij de bestrijding van ziekteverwekkers, maar in sommige gevallen ook onbedoeld lichaamseigen cellen kunnen aanvallen. Daarnaast zijn er aanwijzingen dat ook andere typen afweercellen betrokken kunnen zijn bij het ontstaan van AA. Zo zouden B-cellen, die ons normaal gesproken beschermen tegen ziekteverwekkers door het maken van antilichamen, mogelijk kunnen bijdragen aan het doden van de stamcellen in het beenmerg.

Hoewel deze aanwijzingen bestaan, ontbreekt tot op heden een volledig beeld van de auto-immuunrespons bij AA. Dit wordt deels veroorzaakt door het beperkte beschikbare onderzoeksmateriaal. Patiënten met AA hebben sterk verlaagde bloedwaarden, waardoor slechts kleine hoeveelheden bloed kunnen worden afgenomen voor onderzoek. Beenmergmateriaal is nog schaarser en moeilijker te verkrijgen. Hierdoor zijn de enkele gepubliceerde studies noodgedwongen uitgevoerd met het perifere bloed, terwijl de ziekteprocessen zich juist in het beenmerg afspelen. Daarnaast maken de gangbare onderzoekstechnieken het slechts mogelijk om een beperkt aantal typen afweercellen tegelijk te bestuderen, waardoor belangrijke onderdelen van de immuunrespons buiten beeld zijn gebleven. Als gevolg hiervan is de aanwezigheid en rol van mogelijk ziekmakende afweercellen in het doelwitorgaan zelf, het beenmerg, grotendeels onbekend gebleven.

Doel van dit proefschrift

Het doel van dit proefschrift was om beter te begrijpen hoe de auto-immuunreactie bij AA verloopt en welke afweercellen daarbij betrokken zijn. Hiermee werd een basis gelegd voor het identificeren van mogelijke aanknopingspunten voor de ontwikkeling van meer specifieke behandelingen voor AA in de toekomst.

Om dit te bereiken, maakten we gebruik van geavanceerde laboratoriumtechnieken, zoals (imaging) massacytometrie en (spectrale) flowcytometrie. Deze methoden maken het mogelijk om veel verschillende typen afweercellen gelijktijdig te bestuderen. In tegenstelling tot gangbare analysemethoden kunnen met deze technieken tot wel 40 celeigenschappen tegelijk worden gemeten, waardoor zowel veelvoorkomende als zeldzamere afweercelpopulaties

gedetailleerd in kaart kunnen worden gebracht. In dit proefschrift pasten we deze methoden toe op zowel vloeibare beenmergmonsters als vaste beenmergbiopten van patiënten met AA. Dit unieke materiaal was beschikbaar dankzij de rol van het Leids Universitair Medisch Centrum als nationaal expertisecentrum. Hierdoor kon voor het eerst de auto-immuunreactie in het beenmerg bij AA uitgebreid worden bestudeerd.

Welke afweercellen zijn betrokken bij het ontstaan van aplastische anemie?

In **Hoofdstuk 2** onderzochten we met behulp van massacytometrie hoe het afweersysteem in vloeibare beenmergmonsters van patiënten met AA eruitziet. Dit maakte het mogelijk om voor het eerst een gedetailleerd overzicht te krijgen van het immuunsysteem bij deze ziekte.

We vonden dat de samenstelling van het immuunsysteem in het beenmerg van AA patiënten duidelijk afwijkt van die van gezonde donoren. Zo waren de cellen die nodig zijn voor een normale bloedproductie sterk verminderd, terwijl bepaalde afweercellen juist vaker voorkwamen. Door het immuunsysteem vervolgens verder in detail te analyseren, konden we een netwerk aan afweercellen identificeren dat mogelijk een rol speelt in het ziekteproces van AA. Specifiek bestond dit netwerk uit $CD16^{+}$ myeloïde cellen, $CCR6^{++}$ B-cellen, $CCR6^{+}$ geheugen $CD4^{+}$ T-cellen en $KLRG1^{+}$ terminaal gedifferentieerde geheugen $CD8^{+}$ T-cellen. Deze afweercellen zijn bekend uit andere auto-immuunziekten en worden geassocieerd met chronische ontstekingsreacties. Zij kwamen vooral voor bij patiënten op het moment van diagnose en namen af na succesvolle behandeling. Dit suggereert dat deze afweercellen betrokken zijn bij het ontstaan of in stand houden van AA. Samenvattend bieden onze resultaten een unieke atlas van het immuunsysteem in het beenmerg bij AA en identificeren we het celoppervlakeiwit CCR6 als mogelijke aangrijpingspunt voor toekomstige therapieën. Deze bevindingen vormden de basis voor nieuwe onderzoeksvragen die in **Hoofdstuk 3** en **Hoofdstuk 4** verder zijn onderzocht.

Hoe verloopt het ontstaan van aplastische anemie precies?

Hoewel de analyse van vloeibare beenmergmonsters in **Hoofdstuk 2** essentieel is om ziekmakende afweercellen bij AA te identificeren, blijft hierbij onbekend hoe deze afweercellen zich tot elkaar verhouden en met elkaar communiceren binnen het beenmergweefsel.

In **Hoofdstuk 3** onderzochten we daarom de autoimmuunreactie bij AA in een ruimtelijke context, door afweercellen in de ruimtelijke architectuur van het beenmergweefsel in beeld te brengen. Met behulp van imaging massacytometrie konden we bestuderen waar in het beenmerg de immuunreactie plaatsvindt en hoe verschillende celtypen met elkaar in contact staan. We zagen dat de actieve immuunreactie zich concentreert in zogeheten

immuun 'hotspots': specifieke gebieden in het beenmerg waar voorlopercellen nog aanwezig zijn. Onze resultaten suggereren dat de ziekte begint in immuun hotspots die verrijkt zijn in lymfoïde afweercellen. Hier brengen interacties tussen T- en B-cellen, waaronder de $CCR6^+$ B-cellen en $CCR6^+$ geheugen $CD4^+$ T-cellen geïdentificeerd in **Hoofdstuk 2**, de immuunreactie op gang. Naarmate de ziekte vordert, veranderen deze hotspots van samenstelling en verschijnen er ook geactiveerde macrofagen. Deze afweercellen hebben de unieke taak om beschadigde of dode cellen op te ruimen en lijken betrokken te zijn bij het verwijderen van afgestorven cellen. Wanneer uiteindelijk alle voorlopercellen zijn verdwenen en de actieve immuunreactie is uitgedoofd, blijven de terminaal gedifferentieerde geheugen $CD8^+$ Tcellen uit **Hoofdstuk 2** en plasmacellen achter in het lege beenmerg.

Samenvattend visualiseert dit hoofdstuk voor het eerst de immuunrespons tijdens de ontwikkeling van AA, en toont het aan welke afweercellen bij ieder ziektestadium betrokken zijn. Deze bevindingen bevestigen de relevantie van de afweercellen geïdentificeerd in **Hoofdstuk 2**. Daarnaast illustreren deze resultaten dat de immuunreactie in AA wordt gevormd door een spectrum aan afweercellen, met een rol voor meer typen afweercellen dan alleen T-cellen.

Waarom werkt afweeronderdrukkende medicatie soms bij aplastische anemie?

Om de behandeling van AA in de toekomst te verbeteren, is het naast het identificeren van mogelijke aangrijpingspunten ook belangrijk om te begrijpen hoe en waarom de huidige behandeling bij een deel van de patiënten effectief is. Het wordt verondersteld dat de afweeronderdrukkende therapie werkt door het uitschakelen van afweercellen die het beenmerg aanvallen. De vierdaagse behandeling met paarden antithymocytenglobuline leidt hierbij mogelijk tot een snelle afname van afweercellen, met name T-cellen. Het langdurige gebruik van ciclosporine zou vervolgens voorkomen dat overgebleven ziekmakende afweercellen opnieuw actief worden. Het exacte werkingsmechanisme van deze behandeling bij AA is echter onbekend. Hierdoor is het op dit moment onduidelijk welke afweercellen de meest geschikte doelwitten zijn voor meer specifieke therapieën.

In **Hoofdstuk 4** brachten we het effect in kaart van de afweeronderdrukkende therapie, bestaande uit een korte kuur paarden antithymocytenglobuline (commercieel verkrijgbaar als ATGAM), gevolgd door langdurig gebruik van ciclosporine. ATGAM is een geneesmiddel dat bestaat uit antilichamen die in paarden worden aangemaakt nadat zij zijn blootgesteld aan cellen van een menselijke thymus (zwezerik). Omdat dit middel van dierlijke oorsprong is en de thymus naast afweercellen ook andere typen cellen bevat, kan slechts een klein deel van deze antilichamen aan menselijke afweercellen binden en uitschakelen.

Met behulp van (spectrale) flowcytometrie onderzochten we in **Hoofdstuk 4** specifiek het effect van dit actieve deel van ATGAM dat kan binden aan menselijke afweercellen. We vonden dat de blootstelling aan actief ATGAM sterk verschilt tussen patiënten ondanks dosering volgens de internationale richtlijnen. Deze verschillen lijken van invloed te zijn op hoe snel de bloedproductie herstelt na de start van de behandeling. Daarnaast vonden we dat ATGAM direct na toediening leidt tot een snelle, maar kortdurende afname van afweercellen, met verschillende effecten per type afweercel. Hoewel actief ATGAM kan binden aan alle typen lymfoïde cellen, leidt dit alleen tot een afname van T- en NK-cellen. Opmerkelijk is dat B-cellen niet worden verminderd, maar juist tekenen van activatie vertonen.

Om het langdurige therapeutische effect van ATGAM plus ciclosporine op te helderen, analyseerden we de T-, NK- en B-cellen in meer detail op subpopulatieniveau. We vonden dat ATGAM verantwoordelijk is voor een snelle depletie van T-celtypen, waaronder de $KLRG1^+$ terminaal gedifferentieerde geheugen $CD8^+$ T-cellen uit **Hoofdstuk 2**. Het daaropvolgende langdurige gebruik van ciclosporine leidt tot een selectieve vermindering van de $CCR6^+$ Bcellen en $CCR6^+$ geheugen $CD4^+$ T-cellen uit **Hoofdstuk 2**. Opmerkelijk is dat andere T-cellen die verantwoordelijk zijn voor de bescherming tegen virusinfecties na de start van de behandeling deels behouden lijken te blijven. Deze bevindingen suggereren dat succesvolle behandeling van AA niet afhankelijk is van een volledige herstart van het immuunsysteem, maar eerder het gevolg is van een combinatie van depletie en onderdrukking van resterende, potentieel ziekte veroorzakende afweercellen, waaronder de afweercellen geïdentificeerd in **Hoofdstuk 2**. Dit bevestigt deze celtypen als potentiële aangrijpingspunten voor de ontwikkeling van meer specifieke therapieën voor AA.

Hoe kan leukemie ontstaan na aplastische anemie?

Zelfs bij patiënten met AA die goed reageren op de afweeronderdrukkende behandeling, kunnen op de lange termijn ernstige complicaties optreden. Eén van deze mogelijke complicaties is het ontstaan van leukemie. Leukemie is een vorm van bloedkanker die ontstaat uit afwijkende bloedvormende stamcellen in het beenmerg en ontwikkelt zich bij ongeveer 10-15% van de AA patiënten binnen tien jaar na behandeling.

Er zijn verschillende verklaringen voorgesteld voor het verhoogde risico op het ontstaan van leukemie na AA. Ten eerste kan het zijn dat afwijkende stamcellen een groeivoordeel hebben ten opzichte van andere stamcellen in het lege beenmerg van AA patiënten na behandeling. Ten tweede wordt gedacht dat afwijkende stamcellen de autoimmuunreactie bij AA mogelijk beter kunnen overleven, waardoor zij het beenmerg na verloop van tijd kunnen overnemen.

Waarom slechts een deel van de AA patiënten leukemie ontwikkelt is echter nog onbekend. Ook is het onduidelijk hoe deze ziekte zich in een vroeg stadium in het beenmerg ontwikkelt. Hierdoor is het niet mogelijk om dit verloop te voorspellen en wordt leukemie doorgaans pas gediagnosticeerd wanneer klachten optreden.

In **Hoofdstuk 5** is aan de hand van een patiëntcasus de ontwikkeling van leukemie na succesvolle behandeling van AA in detail bestudeerd. Met behulp van imaging massacytometrie analyseerden we een unieke reeks beenmergbiopten van één patiënt, afgenomen bij de diagnose van AA, na start van de afweeronderdrukkende behandeling en bij de latere diagnose van leukemie. Hierdoor konden we voor het eerst de ontwikkeling van leukemie stap voor stap visualiseren in het beenmergweefsel.

We vonden dat het ontstaan van leukemie in de beschreven patiënt gepaard ging met een sterke toename van onrijpe myeloïde cellen, die geleidelijk de normale bloedproductie verdrongen. Opmerkelijk was dat deze afwijkende cellen gebaseerd op hun uiterlijk (fenotype) al aanwezig leken te zijn op het moment van de oorspronkelijke diagnose van AA. Hun abnormale groei in het beenmerg kon bovendien worden waargenomen ruim voordat de genetische veranderingen die kenmerkend zijn voor leukemie aantoonbaar waren.

Daarnaast liet aanvullend genetisch onderzoek zien dat deze patiënt al bij de diagnose van AA een verworven genetische verandering had in het spliceosoomgen *ZRSR2*, dat betrokken is bij de verwerking van RNA en de aanmaak van eiwitten. Dit wijst mogelijk op een kwetsbaarheid in de bloedvormende stamcellen. Op basis van deze observaties veronderstellen wij dat de ontwikkeling van leukemie in deze casus mogelijk het gevolg was van veranderingen in de micro-omgeving van het beenmerg na succesvolle afweeronderdrukkende behandeling en/of van een verhoogde instabiliteit van de stamcellen als gevolg van de *ZRSR2* mutatie. Deze bevindingen suggereren dat het ontstaan van leukemie na AA in sommige gevallen anders kan verlopen dan tot nu toe werd aangenomen, en bieden aanknopingspunten voor toekomstig onderzoek naar het vroeg herkennen en voorkomen van bloedkanker na AA.

Conclusie en toekomstperspectief

Wat hebben we geleerd door dit proefschrift?

Samenvattend biedt dit proefschrift tot op heden het meest gedetailleerde overzicht van het immuunsysteem bij AA, zowel voor als na behandeling met afweeronderdrukkende medicatie. Door geavanceerde technieken toe te passen op het beenmerg van AA patiënten, hebben we aangetoond dat AA het gevolg is van een gecoördineerde immuunreactie die wordt gevormd door meerdere typen afweercellen. Daarmee laten onze resultaten zien dat AA niet uitsluitend wordt aangedreven door T-cellen, maar door een breder spectrum aan afweerceltypen.

Op basis van onze bevindingen beschouwen wij met name $CCR6^{++}$ B-cellen, $CCR6^{+}$ geheugen $CD4^{+}$ T-cellen en $KLRG1^{+}$ terminaal gedifferentieerde geheugen $CD8^{+}$ T-cellen als belangrijke effectorcellen in het ziekteproces. Deze subpopulaties vormen daarmee veelbelovende aanknopingspunten voor de ontwikkeling van meer gerichte en mogelijk effectievere therapieën voor AA.

Hoe nu verder?

Hoewel dit proefschrift belangrijke nieuwe inzichten oplevert, is aanvullend onderzoek nodig om de precieze functionele rol van deze B- en T-celpopulaties beter te begrijpen. Met name het bestuderen van hun antigeenspecificiteit kan helpen om te achterhalen welke structuren op de bloedvormende stamcellen precies door het immuunsysteem worden herkend. Dit onderzoek vormt een logische vervolgstap op de bevindingen uit dit proefschrift en is essentieel voor de ontwikkeling van meer specifieke therapieën. Het vervolgonderzoek wordt momenteel uitgevoerd op het laboratorium van de afdeling Hematologie van het Leids Universitair Medisch Centrum.

About the author

Emma Pool was born on August 4, 1996 in Terneuzen, The Netherlands. She lived in Midland, Michigan, USA, with her family for six years during her childhood, before returning to the Netherlands in 2006. In 2014, she graduated from Stedelijk Scholengemeenschap De Rede and began her bachelor's studies in Bio-Pharmaceutical Sciences at Leiden University. That same year, she also enrolled in the Honors College 'Beta and Life Science'.

After completing both programs in 2017, and serving a year on the board of the study association, she continued with her master's studies in Bio-Pharmaceutical Sciences. Fascinated by clinical research and immunology, she completed her first research internship at the Willem-Alexander Childrens' Hospital of the Leiden University Medical Center. Here, she studied the effects of rabbit-derived anti-thymocyte globulin and post-transplant cyclophosphamide in pediatric allogeneic stem cell transplantation for non-malignant hematological diseases. *This is when she first heard of aplastic anemia.*

For her second research internship, she joined the Oxford Vaccine Group at the University of Oxford to study immune responses in typhoid fever. Her project combined laboratory work with mass cytometry data analyses to explore the role of dendritic cells in this disease. *It sparked her interest in complex single-cell analyses and in integrating wet- and dry-lab research.*

In 2020, she obtained her master's degree and started her PhD project at the Department of Hematology of the Leiden University Medical Center under the supervision of Jennifer Tjon, Mirjam Heemskerk and Frits Koning. As described in this thesis, her project focused on deciphering the immune-mediated pathogenesis of acquired aplastic anemia using advanced single-cell techniques. This research was performed in collaboration with the Departments of Immunology, Pathology, and Clinical Pharmacy & Toxicology of the Leiden University Medical Center. In 2024, she extended her PhD contract to study the spatial bone marrow architecture in acute myeloid leukemia in collaboration with the Prinses Máxima Center for Pediatric Oncology in Utrecht. During her PhD, she presented her research at several (inter) national conferences, with one highlight being the selection of her work as a Best of ASH research highlight at the 64th Annual Meeting of the American Society of Hematology.

Since September 2025, Emma has continued to explore the complex architecture of tissue microenvironments as a postdoctoral researcher at the Department of Internal Medicine (Nephrology) of the Leiden University Medical Center.

List of publications

Included in this thesis

Mass cytometric analysis unveils a disease-specific immune cell network in the bone marrow in acquired aplastic anemia (included in this thesis as Chapter 2)

Pool ES, Kooy-Winkelaar Y, van Unen V, Falkenburg JHF, Koning F, Heemskerk MHM, Tjon JML (2023). *Frontiers in Immunology*. 14, 1274116. PMID: 38094307

Imaging Mass Cytometry Reveals the Order of Events in the Pathogenesis of Immune-Mediated Aplastic Anemia (included in this thesis as Chapter 3)

Pool ES, Luk SJ, Ijsselsteijn ME, van Unen V, de Miranda NFCC, Falkenburg JHF, Koning F, Heemskerk MHM, Tjon JML (2025). *Blood*. 146(8): 951-963. PMID: 40403228

Selective lymphodepletion underlies the efficacy of horse anti-thymocyte globulin-based immunosuppressive therapy in aplastic anemia (included in this thesis as Chapter 4)

Pool ES, Pothast CR, Gennesse SM, van Egmond HM, Giezen JM, Veld SAJ, Toes REM, Halkes CJM, Heemskerk MHM, Tjon JML (2026). *Haematologica*. PMID: 41609027

Other publications

Proceedings of the European Group for Blood and Marrow Transplantation (EBMT) congress on sickle cell disease, 16-17 May 2019, Regensburg, Germany: What is the impact of antithymocyte globulin pharmacokinetics on haploidentical hematopoietic stem cell transplantation?

Oostenbrink LVE, Jol-van der Zijde CM, Jansen-Hoogendijk AM, **Pool ES**, van Halteren AGS, Moes DJAR, Bredius RGM, Mohseny AB, Smiers FJW, van Tol MJD, Schilham MW, Lankester AC (2020). *Hematology/Oncology and Stem Cell Therapy.* 13(2), 61-65. PMID: 32202242

Successful mismatched hematopoietic stem cell transplantation for pediatric hemoglobinopathy by using ATG and post-transplant cyclophosphamide.

Oostenbrink LVE, **Pool ES**, Jol-van der Zijde CM, Jansen-Hoogendijk AM, Vervat C, van Halteren AGS, Bredius RGM, Smiers FJW, van Tol MJD, Schilham MW, Lankester AC, Mohseny AB (2021). *Bone Marrow Transplantation*. 56(9), 2203-2211. PMID: 33941871

SARS-CoV-2 mRNA vaccination of aplastic anemia patients is safe and effective.

Pothast CR*, van Dijk K*, **Pool ES**, Halkes CJM, Heemskerk MHM, Tjon JML (2023). *American Journal of Hematology.* 98(2), E20-E23. PMID: 36371670

Local administration of mesenchymal stromal cells is safe and modulates the immune compartment in ulcerative proctitis.

Ouboter LF, Barnhoorn MC, Verspaget HW, Plug L, **Pool ES**, Szuhai K, Hawinkels LJ, van Pel M, Zwaginga JJ, Roelen D, Koning F, Pascutti MF, van der Meulen-de Jong AE (2023). *JCI Insight.* 8(9). PMID: 36951952

Optimal genetic feeder cell-expanded and engineered NK cell products are composed of CD56(bright) and CD56(dim) NK cells.

van Hees EP, Pothast CR, **Pool ES**, Falkenburg JHF, Melsen JE, Heemskerk MHM (2026). Cancer Immunology, Immunotherapy. 75(2): 57. PMID: 41591514

Spatial proteomics defines an immune signature with T-cell colocalization in bone marrow of pediatric aplastic anemia.

Vissers LTW*, **Pool ES***, Koudijs KKM, Ihlow J, Penter L, Lankester AC, van den Burg M, Tjon JML#, Mohseny AB#. *Submitted*

Spatial multi-omics uncovers targetable immunosuppressive macrophage-T cell interactions in pediatric and adult acute myeloid leukemia.

van der Meulen M*, **Pool ES***, Perzolli A*, Koedijk JB; Argiro E, Chen LT, de Jonge WJ, Schweighart E, Vermeulen MA, Nierkens S, Ihlow J, Horst D, Lissat A, Vormoor HJ, Belderbos ME, Veelken H, Penter L, Goemans BF, van den Akker E, Margaritis T, Zwaan CM#, Griffioen M#, Tjon JML#, Heidenreich O#. *Submitted*

* Shared first authorship

Shared last authorship

Conference presentations

2022

High-Dimensional Mass Cytometric Analysis of the Bone Marrow Compartment Identifies a Disease-Specific Immune Cell Network in Aplastic Anemia

Oral presentation at the 64th American Society for Hematology Annual Meeting | New Orleans, Louisiana, United States

Oral presentation at the 2nd ESH-EBMT Translational Research Conference: Bone Marrow Failure Syndromes: From the Cell to the Cure of the Disease | Paris, France

2023

High-Dimensional Imaging of the Bone Marrow in Acquired Aplastic Anemia

Oral presentation at the 15th Dutch Hematology Congress | Papendal, The Netherlands

2024

Dissecting the spatial bone marrow immune cell composition in aplastic anemia with high-dimensional imaging

Oral presentation at the 16th Dutch Hematology Congress | Papendal, The Netherlands

Poster presentation at the ESH-EBMT-EHA-IPIG 3rd Translational Research Conference: Bone Marrow Failure and Leukemia Predisposition Syndromes | Paris, France

Impact of anti-thymocyte globulin-based immunosuppressive therapy in acquired aplastic anemia patients

Poster presentation at the Dutch Society for Immunology Winter School | Noordwijkerhout, The Netherlands

2025

In vivo effects of ATGAM in immune-mediated aplastic anemia patients

Poster presentation at the 51st Annual Meeting of the European Society for Blood and Marrow Transplantation | Florence, Italy

Dankwoord

Aan het einde van mijn promotietraject kijk ik met een warm gevoel terug op de afgelopen zes jaar. Ik dank iedereen die, op welke manier dan ook, aan dit proefschrift heeft bijgedragen en deze periode zoveel kleur heeft gegeven. Een aantal van hen wil ik hier in het bijzonder noemen.

Mijn eerste dank gaat uit naar mijn (co-)promotores **Jennifer, Mirjam en Frits**; dankzij jullie werd dit onderzoek mogelijk en kreeg ik het vertrouwen om mij te ontwikkelen als onderzoeker. Samen zijn we gestart met het onderzoek naar aplastische anemie, waarin toenemend enthousiasme ons steeds verder bracht. Jullie verschillende perspectieven en brede kennis hielpen om ideeën te verdiepen, de rode lijn te bewaken en complexe data tot de essentie terug te brengen. Wat ik bijzonder waardeer, is jullie oog voor ieders kwaliteiten, altijd met aandacht voor de persoon achter de onderzoeker. Ik ben dankbaar dat ik mijn promotieonderzoek onder zulke fijne begeleiding heb mogen doen.

Vanaf het eerste moment voelde de afdeling Hematologie als thuis. De betrokkenheid, het voor elkaar klaarstaan, de positieve sfeer en de vele sociale activiteiten maakten dat elke werkdag met plezier begon. Dank aan alle collega's voor deze fijne werkomgeving.

Ook hebben velen van jullie inhoudelijk bijgedragen aan dit proefschrift. **Esther**, dankzij jou verloopt alles op het lab gestructureerd, en werd samenwerken aan ATGAM een groot plezier. **Renate, Sabrina en Willy**, jullie hulp bij de experimenten was onmisbaar, evenals de kennis en labvaardigheden die jullie met me deelden. **Sietse**, dankzij jou kreeg ik weefselkleuringen en spatial data-analyse in de vingers; jouw bijdrage aan het IMC-project was van grote waarde. **Cilia and Georgia**, your willingness to help makes a difference; thank you for the fun and efficiency you brought to the experiments we performed together. **Fred en Stijn**, veel dank voor jullie scherpe feedback op de manuscripten die een grote rol hebben gespeeld in mijn ontwikkeling als onderzoeker. **Henk en Gerrie**, geweldig dat jullie altijd klaarstaan om te helpen. **Marieke**, met jou is samenwerken altijd prettig, dank voor je waardevolle input op de AML-projecten. **Shannah**, veel dank voor je inzet tijdens je stage.

Mijn PhD en postdoc collega's: **Cilia, Els, Eva, Eva, Fleur, Georgia, Hannah, Ilse, Janneke, Johannes, Joost, Miranda, Nadine, Renée, Rosa, Ruben, Sietse, Tassilo en Teuntje**. Van congressen in New Orleans tot lunches buiten de deur, van karaoke tot C5, en van discolichten tot (post-congres) reizen; jullie maakten alles leuker. We leren van elkaar, steunen elkaar en vieren mijlpalen met elkaar. Zo'n hechte groep is alles waard. Ik ben ontzettend blij dat ik jullie heb leren kennen.

The mucosal immunology group has truly been a second home since the first day of my PhD. **Ciska, Fernanda, Jia Li, IJsbrand, Juliette, Laura, Mette, Nannan, Natasja, Qinyue, Sanne, Tessa, Veerle and Vincent**: our Friday meetings, filled with t-SNE plots and colorful IMC-images, were among the most visually striking at the LUMC. I am grateful for all your advice and the opportunity to broaden my knowledge of bioinformatics and immunology. I also look back with joy on the many dinners, CyTOF experiments, dumpling workshops and days spent working at L3. Thank you for the always warm welcome to the team.

Ik vind het bijzonder dat ik, buiten de afdelingen Hematologie en Immunologie om, ook met veel andere onderzoekers heb mogen samenwerken en van hen heb mogen leren. Dank aan een aantal van hen in het bijzonder:

Marieke, Noel en Manon, dank voor het delen van jullie onmisbare inzichten in het opzetten van IMC-panels en data-analyse waardoor dit proefschrift aanzienlijk kleurrijker is geworden.

Dirk Jan, dank dat we na mijn masterstage opnieuw konden samenwerken aan de farmacokinetiek van anti-thymocytenglobuline. Jouw begeleiding en expertise maakten dit project erg leerzaam.

Alex en Mirjam, dank voor de fijne samenwerking en de kans om, naast het onderzoek beschreven in dit proefschrift, ook beenmergfalen bij kinderen te bestuderen. **Lotte**, met jou samenwerken aan aplastische anemie is altijd een groot plezier; ons gezamenlijke enthousiasme maakte dat we veel van elkaar konden leren over zo'n zeldzame ziekte.

Julia, dankzij de extra B-cel flow experimenten werd het ATGAM stuk echt compleet; veel dank voor je snelle bijdrage hieraan.

Merel, bij het spatial AML-project bleef je me, zelfs bij het vierde IMC-cohort, uitdagen om het maximale uit de analyses te halen. Veel dank voor de vele leuke discussies waar ik steeds van leerde.

Inmiddels werk ik al bijna een jaar samen met een fantastische nieuwe groep collega's bij de Interne Geneeskunde, die opnieuw zorgen voor veel werkplezier en van wie ik elke dag blijf leren. Veel dank voor jullie support bij de laatste loodjes.

Lieve vriendinnen en vrienden, jullie betekenen heel veel voor mij. Jullie geven me energie, staan altijd klaar met een luisterend oor en zorgen voor veel plezier en ontspanning naast het onderzoek. Met jullie is het altijd feest. Veel van jullie ken ik al jaren, en juist dat maakt het heel speciaal. Van het zwemmen in dezelfde baan tot het lachen op het Gorlaeus en het wonen aan de Boerhaavelaan: zelfs de gewone momenten zijn leuk met jullie, net als de vele

etentjes, borrels, weekendjes weg en reizen van de afgelopen jaren. Ook al zien we elkaar niet altijd dagelijks of wekelijks, het voelt altijd meteen vertrouwd. Zo fijn dat we al het moois met elkaar blijven delen en vieren.

Lieve familie, wat een geluk dat ik jullie heb. Dank voor jullie onvoorwaardelijke steun. **Nora en Victor**, wij delen dezelfde nieuwsgierigheid; van onze fascinatie voor Pompeï en Egypte als kinderen tot waar we nu staan, met een diploma in de (bio)chemie. Ik ben trots op jullie, en dankbaar voor alles wat we delen, de afgelopen jaren ook met **Teun**. **Papa en mama**, jullie creëerden een warme plek om te leren; te ontdekken; te groeien. Jullie gaven mij het vertrouwen om mijn eigen pad te kiezen en kansen te zien én te creëren. Het moment waarop jullie ons na elk bezoek uitzwaaien, herinnert me telkens hoe waardevol thuisthuis is, en voor altijd zal blijven. Wat mooi dat de kaft van dit proefschrift een herinnering is aan één van de vele leuke dagen samen.

